Open Research Online

The Open University's repository of research publications
and other research outputs

The Attenuation of Sunlight by Airborne Dust Particles on Earth and Mars

Thesis

How to cite:

Mason, Jonathon Peter (2013). The Attenuation of Sunlight by Airborne Dust Particles on Earth and Mars. PhD thesis The Open University.

For guidance on citations see FAQs.

© 2013 The Author

Version: Version of Record

Copyright and Moral Rights for the articles on this site are retained by the individual authors and/or other copyright owners. For more information on Open Research Online's data policy on reuse of materials please consult the policies page.

oro.open.ac.uk

UNRESTRICTED

The Attenuation of Sunlight

by Airborne Dust Particles on Earth and Mars

Jonathon P. Mason

September 2012

The Open University

Department of Physical Sciences

A THESIS SUBMITTED TO THE OPEN UNIVERSITY IN THE

SUBJECT OF PLANETARY SCIENCES FOR THE

DEGREE OF DOCTOR OF PHILOSOPHY

DATE of SUBMISSION : 21 SEPTEMBER 2012
DATE of AWARD : 30 APRIL 2013

ProQuest Number: 13835946

All rights reserved

INFORMATION TO ALL USERS
The quality of this reproduction is dependent upon the quality of the copy submitted.

In the unlikely event that the author did not send a complete manuscript
and there are missing pages, these will be noted. Also, if material had to be removed,
a note will indicate the deletion.

ProQuest 13835946

Published by ProQuest LLC (2019). Copyright of the Dissertation is held by the Author.

All rights reserved.
This work is protected against unauthorized copying under Title 17, United States Code
Microform Edition © ProQuest LLC.

ProQuest LLC.
789 East Eisenhower Parkway
P.O. Box 1346
Ann Arbor, MI 48106 – 1346

Dedicated to the loving memory of Grandad Peter

Acknowledgements

First and foremost I would like to express my sincere gratitude to my supervisors Dr. Manish Patel and Dr. Stephen Lewis for giving me the opportunity to undertake this PhD project. The journey was arduous at times and I would like to show my appreciation for their patience and supporting me during the hardships of this PhD. A big thank you also goes out to them for commenting and reviewing thesis drafts which came at short notice towards the end. I would like to thank Dr. Jon Merrison at the University of Aarhus for allowing me to use the Mars Simulation Wind Tunnel Facility and answering endless streams of email.

I am also indebted to my friends in the Mars corner, Euan Monaghan, Samantha Rolfe, Adam Stevens and Daniel Dawson for proof reading multiple thesis drafts and endlessly correcting what could only be described as some questionable English grammar.

I would like to express my thanks to my family and friends that supported me in the decision to study for my PhD. Most importantly a special thanks to Zoe Wathen for her love and unwavering support during this endeavour and I would just like to acknowledge that without her I'm not sure I would have made it.

Finally I would like to show my appreciation to my friends in PSSRI for helping me see that there is life outside the office, even if it did take dragging me away from my desk. A special acknowledgement goes out to Farrer's™ coffee for creating their fabulous No. 1 blend, without which this thesis would never have been completed.

Abstract

This thesis details an investigation into how dust and ice aerosols in the atmosphere of Earth and Mars affect the solar spectrum from the ultraviolet to the near infrared, allowing the characterisation of the aerosols using broad band surface measurements.

A Monte Carlo Light Scattering Model (MCLSM) was developed to predict the optical signature of terrestrial and martian dust devils. The MCLSM was applied to measurements taken in the Eldorado Valley, U.S.A. Transit signatures were found to be dependent on the method of observation. The transit signature measured in scattered light depends on the dust concentration and distribution in contrast to the total light transit signature, which depends primarily on the column-integrated dust optical depth. On Mars the high diffuse irradiance provides better definition of the vortex interior within the transit signature, with wavelengths between 600–750 nm optimal for detecting a transit. To determine the vortex size and dust concentration, both the total *and* the scattered light must be measured. Retrieval of the dust optical properties showed that spectral measurements and the calculated mass concentration were sensitive to the presence of small particles (0.5–5.0 μm).

A comparison of the downward irradiance for two distinct dust components suggests that dust with a higher absorption at visible wavelengths causes increased heating at higher altitudes, leading to a more statically-stable atmosphere, which may result in more rapid decay of large-scale dust storms. The investigations have also shown that variations in single scattering properties can lead to ~20% difference in the daily UV-C dose.

A method was devised to distinguish compositional changes in the ubiquitous martian dust haze and validated against wind tunnel experiments. This technique is applicable to determine the size of water-ice crystals in clouds and the optical depth of the dust haze at the time of the cloud passage.

Publications

As an outcome of this study, the following *manuscript* has been accepted for publication:

J.P Mason, M.R Patel and S.R Lewis. (2013). *Radiative Transfer Modelling of Dust Devils.* Icarus, 233, pp. 1-10

The following are *conference presentations* given over the course of this study:

J.P Mason, M.R Patel and S.R Lewis. *Retrieving Dust Properties by Radiative Transfer Modelling of Dust Devils on Earth and Mars*. European Planetary Science Congress, Madrid, Spain, 23rd – 28th September, 2012.

J.P Mason, M.R Patel and S.R Lewis. *Effects of Aerosols on the Observed Irradiance from the Ultraviolet to Near-Infrared at the Surface of Mars*. Fourth International Workshop on the Mars Atmosphere: Modelling and Observations, Paris, France, 8th – 11th February, 2011.

J.P Mason, M.R Patel and S.R Lewis. *Airborne Dust and Water Vapour at Visible Wavelengths in the Martian Atmosphere*. European Workshop on Astrobiology, Brussels, Belgium, 12rd – 14th October, 2009.

Table of Contents

1 Chapter One: Introduction 1

1.1 Aim of the thesis 1

1.2 The planet Mars 2

1.3 History of optical depth measurements from the surface of Mars 2

1.4 The atmosphere of Mars 6

1.5 Aeolian mineral dust 9

1.5.1 Sources of aerosol dust 10

1.5.2 Seasonal variation 11

1.6 Condensate clouds 12

1.6.1 Physical characteristics of martian H_2O aerosols 14

1.7 Vertical distribution of dust and water-ice aerosols 14

1.8 Diurnal variation of optical depth: Morning fogs 15

1.9 Thesis outline 16

2 Chapter Two: Dust aerosols in the martian atmosphere 19

2.1 Light scattering by aerosols 20

2.1.1 Single scattering theory 21

2.1.2 Spherical particles (Mie theory) 25

2.1.3 Non-spherical particles (discrete dipole approximation) 29

2.2 Optical properties of martian aeolian dust 34

2.2.1 Overview of the different observations 35

2.2.2 Single scattering albedo 36

2.2.3 Asymmetry parameter and extinction efficiency 38

2.2.4 Complex refractive index 40

2.3 Dust devil phenomena 42

2.3.1 Dust devil formation 43

2.3.2 Lower dust devil structure 45

2.3.3 Dust devils on Mars 47

2.4 Previous radiative transfer modelling of dust devils 50

3 Chapter Three: Monte Carlo modelling of dust devil vortices 51

3.1 Radiative transfer in dusty environments 52

3.1.1 Model description 52

3.1.2 Dust scattering and absorption 54

3.1.3 Directional change and photon classification 56

3.1.4 Spatial variation in dust distribution 57

3.1.5 Error analysis of coordinate system transformation 59

3.2 Dust devil simulations 60

3.2.1 Model parameters 60

3.2.2 Photon propagation 60

3.3 Simulated dust devil transits 63

3.3.1 Effect of dust loading 65

3.3.2 Effect of dust distribution 67

3.3.3 Effect of core size 69

3.3.4 Effect of transit direction 71

3.3.5 Effect of single scattering properties 72

3.4 Discussion of the MCLSM simulations 75

4. Chapter Four: Spectral measurements of terrestrial dust devils 79

4.1 Experimental setup and execution 79

4.2 Dust devil measurements 82

4.2.1 Data reduction 83

4.2.2 Estimation of dust devil parameters 89

4.3 Possible sources of error and uncertainties 96

4.3.1 Presence of a dust haze 96

4.3.2 Uncertainty in dust devil dimensions and non-uniformity 97

4.3.3 Interference from the chase vehicle 98

4.4 Retrieval of the dust single scattering properties 98

4.4.1 Dust particle size distribution 100

4.4.2 Retrieval method 106

4.4.3 Retrieval results 110

4.5 Determination of the dust devil structure and vertical mass fluxes 114

4.6 Summary of results 121

5. Chapter Five: Effects of dust and ice aerosols on the downward irradiance at the martian surface 123

5.1 Mars radiative transfer model 123

5.2 Effect of martian airborne dust on the downward irradiance at the surface 125

5.2.1 Impact of dust on the downward surface flux 127

5.2.2 Effect of Q_{ext}, ω_0, and g on the irradiance spectrum 132

5.2.3 UV radiation at the surface of Mars for different dust properties 135

5.2.4 Dust-dependent UV dose: Implications for astrobiology 142

5.2.5 Differentiating between different dust species 146

5.3 Transits of martian dust devils 151

5.3.1 Modelling the diffuse component 153

5.3.2 Transit signatures of martian dust devils 157

5.3.3 Single scattering properties for the entrained dust 161

5.4 The effect of water-ice clouds on the downward irradiance at the surface 165

5.4.1 Attenuation of the irradiance spectrum 165

5.4.2 Retrieval of water- ice aerosol characteristics 167

6. Chapter Six: Wind tunnel measurements of suspended dust 171

6.1 The Mars Simulation Wind Tunnel Facility and experimental setup 171

6.1.1 Spectroscopic instrumentation 172

6.1.2 Light sources 174

6.1.3 Determination of LED radiant flux 175

6.1.4 Dust samples 178

6.1.5 Effect of dust particle shape 180

6.2 Experimental procedure 184

6.2.1 Detection of the scattered light component 187

6.3 Adaptations to the Monte Carlo Light Scattering Model 190

6.3.1 Photon initial position and trajectory 190

6.3.2 Boundary conditions 191

6.3.3 Photon detection 192

6.4 Discussion on the retrieval of optical properties 192

6.5 Differentiating between two dust samples 194

6.6 Summary 197

7 Chapter Seven: Discussion and further work 201

7.1 Retrieval of the dust optical properties of dust devil vortices 201

7.2 Predicted and measured transit signatures of terrestrial dust devils 204

7.2.1 MCSLM predictions 204

7.2.2 Transit signature of terrestrial dust devils 205

7.3 Transit signatures of martian dust devils 207

7.4 Effects of martian dust and ice aerosols on the surface irradiance spectrum 209

7.5 Differentiating between different dust compositions and ice particle size 212

7.6 Further work 213

7.7 Final remarks 214

8 References 217

List of figures

Figure 1-1: The descent profiles for pressure (solid lines) and temperature (dashed lines) 8

Figure 1-2: The atmospheric opacity at different wavelengths as a function of L_s,..... 12

Figure 2-1: Image from the martian surface by Curiosity..... 19

Figure 2-2: Effect of a dust particle on a plane electromagnetic wave. 20

Figure 2-3: ω_0 and g as a function of x for a selection of n_i for a single particle. 27

Figure 2-4: ω_0 and g as a function of x for a selection of n_i for a distribution of particle sizes. . 28

Figure 2-5: The real and imaginary parts of the complex refractive index for kaolinite, grey line, (Egan and Hilgeman, 1979) and hematite, black line, (Sokolik and Toon, 1999)..... 30

Figure 2-6: Comparison between the calculated single scattering properties a) Q_{ext}, b) Q_{abs}, c) ω_0 and d) the g for non-spherical shaped kaolinite particles with an effective radius of 0.5 μm. ... 32

Figure 2-7: Same as figure 2-4 but for a randomly orientated and irregular hematite particle... 33

Figure 2-8: The retrieved ω_0 of martian aeolian dust from various instruments..... 38

Figure 2-9: (a) The retrieved g of martian dust from various instruments and (b) The retrieved Q_{ext} of martian dust. 40

Figure 2-10: The retrieved values of n_i for martian aeolian dust 41

Figure 2-11: Image of a dust devil in the Nevada desert. (a)..... 42

Figure 2-12: Schematic of a dust devil moving from right to left 45

Figure 2-13: Thermal images taken of a dust devil with a low dust density in the Eldorado Valley, Nevada..... 46

Figure 2-14: Image taken in the Eldorado Valley of a dust devil with secondary vortices present in the primary dust column. 47

Figure 2-15: Two examples of dust devils on the surface of Mars;..... 48

Figure 3-1: Global coordinate system of the MCLSM. 53

Figure 3-2: Rotation of a photon vector onto the τ_c grid..... 58

Figure 3-3: The photon positions after one scattering event in a dust devil of (a) high and (b) low dust concentration, and after four scattering events, (c) high and (d) low dust concentration. 62

Figure 3-4: Photon positions after six scattering events for: (a) $g = 0.98$ and (b) $g = 0.7$..... 63

Figure 3-5: Φ_T and Φ_S during a transit of a dust devil with $R_{dd} = 2$ m and $\tau_c = 0.6$ for: (a) NV case and (b) FS case. 64

Figure 3-6: NV dust devil transits from Scenario 1 (black lines) and uniform Scenario (grey lines) for different τ. 66

Figure 3-7: As fig.6, but showing the FS simulated transits. 67

Figure 3-8: The observed Φ_S in the core relative to the illuminated wall as a function of the N_{core} / N_{wall}. 68

Figure 3-9: Transit signatures of dust devils with core radii of 0.5 m, 1.0 m and 1.5 m..... 70

Figure 3-10: The variation in the dust devil transit signature for different trajectories over the PoM: (a) NV model (b) FS model. 72

Figure 3-11: Transit of a dust devil moving along the X-axis for different values of g..... 73

Figure 3-12: Number of scattered photons detected as a function of θ_z for dust components with different g. 74

Figure 3-13: Transit of a dust devil moving along the X-axis for different ω_0 values 75

Figure 4-1: The experimental setup for the dust devil measurements..... 80

Figure 4-2: Illustration of the measurement process performed by the chase vehicle 80

Figure 4-3: Diagrams showing the different viewing geometries for the two optical setups..... 81

Figure 4-4: Location of the dust devil encounters considered for further analysis. 83

Figure 4-5: An example of a typical dataset obtained for a dust devil encounter. 84

Figure 4-6: An example of the reduced data for a dust devil encounter. 85

Figure 4-7: Correlation of the UV-VIS and PICO datasets..... 87

Figure 4-8: Comparison of T_a measured by the UV-VIS using the NV setup with the PCIO dataset for encounter E6. 88

Figure 4-9: Illustration of how the dust devil dimensions were approximated for each encounter. 90

Figure 4-10: (a) Uncertainty in the dust devil attitude during a dust devil encounter, (b) enhanced image showing the vertical extent of the vortex with the highest dust loading confined to an altitude of 12 m above the surface..... 91

Figure 4-11: The apparent transmission at the core of a 4m dust devil with an height of 12 m and 38 m. 92

Figure 4-12: (a) The apparent transmission spectrum measured during the dust devil transits E4 and E5 and through the dust devil shadow. (b) T_a at 450nm as a function time. 93

Figure 4-13: Encounter correlation for E4 and E5. 94

Figure 4-14: Enhanced colour image showing the dust haze that was present during the first two days of the experiments. 96

Figure 4-15: Enhanced images taken during a dust devil transit illustrating the evolution of the dust devil structure over short time scales. 97

Figure 4-16: (a) The measured reference and attenuated solar spectrum normalised to the peak irradiance 99

Figure 4-17: The volume size distribution as a function of particle radius for different model radii. 102

Figure 4-18: (a) Q_{ext} (b) ω_0 and (c) g as a function of wavelength for various particle size distributions 103

Figure 4-19: The effect on the size distribution as a result of increasing the volume occupied by the fine particles. 104

Figure 4-20: The effect of increasing the fraction of total volume occupied by the fine particle on (a) Q_{ext}, (b) ω_0 and (c) g. 105

Figure 4-21: T_a as a function of ω_0 and g 107

Figure 4-22: T_a as a function of wavelength for the different dust devil encounters. 108

Figure 4-23: The retrieved $\omega_0(\lambda)$ and $g(\lambda)$ for encounters E1, E2, E3, E4 and E5. 111

Figure 4-24: The retrieved refractive index as a function of wavelength for dust suspended in dust devil vortices in the Nevada desert 113

Figure 4-25: The transmission and normalised scattered light over the model surface 114

Figure 4-26: Model fits of the dust devil transit signatures for E1, E2, E3, E4 and E5 116

Figure 4-27: The best fit for different dust concentrations for E6. 120

Figure 5-1: Illustration of how the incident light interacts with the layered atmosphere of the delta-Eddington approximation. 124

Figure 5-2: Simulated irradiance at the martian surface for an atmosphere with $\tau = 0.3$. 125

Figure 5-3: Optical depth measured by the Spirit rover during MY27, MY28 and MY29 126

Figure 5-4: The surface flux at noon as a function of τ at the location of the Spirit rover. 127

Figure 5-5: As figure 5-4 except for 9am local time. 129

Figure 5-6: The total (black lines), visible (green lines), NIR (red lines) and UV (blues lines) noon surface flux as a function of L_s for MY27 and MY28 130

Figure 5-7: Comparison of the single scattering properties derived for martian aeolian dust including that produced by Mie theory for spherical particles. 133

Figure 5-8: a) Surface irradiance spectrum for different dust components b) the irradiance ratio between the different dust components to O97. 135

Figure 5-9: The latitudinal and seasonal variation of local noon UV flux for, (a) W09 and (b) O97 dust components. 136

Figure 5-10: a) Total UV daily dose as a function of τ for O97 and W09. b) The UV daily from the received from the direct component (solid lines) and diffuse component (dashed lines). .. 137

Figure 5-11: Difference in UVC dose as a function of L_s for O97 and W09 during MY27 and MY28. 139

Figure 5-12: Same as figure 5-11 except for UVB 140

Figure 5-13: Same as figure 5-11 except for UVA. 140

Figure 5-14: $\Re_I$ as a function of L_s for O97 (grey line) and W09 (black line) during MY27 and MY28. 147

Figure 5-15: $\Re_I$ as a function of L_s for the hypothetical MY27 and MY28 scenario 148

Figure 5-16: $\Re_I$ as a function of τ for MY27 and MY28 149

Figure 5-17: As Figure 5-16 but for $\Re_D$ for W09 and O97. 150

Figure 5-18: The relative contributions to the total surface irradiance from the direct (solid lines) and diffuse (dashed lines) components 153

Figure 5-19: The θ_{pz} probability distribution for photons incident on the model surface. 155

Figure 5-20: Direct and diffuse photon positions after 1-5 scattering events for a high dust background component and low and high opacity dust devils. 156
Figure 5-21: The spectral signature at 388 nm during a transit of a martian dust devil..... 158
Figure 5-22: As figure 6-21, but at a wavelength of 750 nm. 160
Figure 5-23: The variation in the transit signatures at 388 nm and 750 nm of dust devils with different dust components 162
Figure 5-24: $\Re_I$ and $\Re_D$ as a function of the τ_a for dust devils with different dust components 163
Figure 5-25: $\Re_{Dir}$ as a function of the τ_a for dust devils with different dust components 164
Figure 5-26: The variation in the surface irradiance spectrum during the passage of a H_2O ice cloud..... 166
Figure 5-27: $\Re_I$ as a function of the atmospheric optical depth. 168
Figure 5-28: Dust and ice optical depth as a function of L_s. 168
Figure 5-29: $\Re_I$ as a function of atmospheric optical depth for a varying τ_{bg} 169
Figure 6-1: Image of the Mars Simulation Wind Tunnel Facility. 172
Figure 6-2: (a) experimental setup showing the MSWTF and the positions of the spectrometers and light sources and (b) the approximate chamber volume observed by the UV-VIS spectrometer. 172
Figure 6-3:The measured the irradiance spectrum by the UV-VIS spectrometer (black line) and the validation spectrometer (red line) produced by (a) the halogen bulb and (b) the LED arrays. 173
Figure 6-4: (a) Image of the halogen bulb used in the experiments. (b) The measured irradiance spectrum of the halogen bulb. (c) Layout of one of the LED arrays. There were 20 identical arrays along each side of the MSWTF. (d) An example of the irradiance spectrum produced by the LED arrays. 174
Figure 6-5 Determination of the output power of the individual LED arrays..... 175
Figure 6-6: Relative intensity as a function of angular displacement for the individual wavelengths..... 176

Figure 6-7: Slices through the modelled chamber showing the irradiance at each node from a single (a) blue and (b) red LED highlighting the differences in angular displacement..... 177
Figure 6-8: The particle size distributions of the various dust samples. 179
Figure 6-9: The approximated size distribution for the hematite dust sample using two log-normal distributions..... 180
Figure 6-10: SEM images of (a) Mars JSC-1, (b) quartz and (c) hematite. 181
Figure 6-11: The scattering process that takes place at each node in the model. 181
Figure 6-12: Scattering angles for (a) the facing LED arrays and (b) back wall LED arrays. The sources (yellow dots) and fibre (red dot) are shown in the plot for prospective. 182
Figure 6-13: Scattering irradiances for (a) the facing LED arrays and (b) back wall LED arrays. The sources (yellow dots) and fibre (red dot) are shown in the plot for prospective. 183
Figure 6-14: The experimental procedure for the experiments. 185
Figure 6-15: Transmission as a function of time for experiment M2 showing the different stages of the experiment and the locations where the reference and attenuated spectra are measured.186
Figure 6-16: The measured transmission for different dust samples for τ of (a) 0.09, (b) 0.15 and (c) 0.5. 187
Figure 6-17: Transmission values for the Salten Skov 1 dust sample for τ of 0.09, 0.15, and 0.3 for the different light sources. 188
Figure 6-18: Attenuated irradiance spectrum for experiment M9 (hematite) at different τ..... 189
Figure 6-19: The initial trajectory of the photons entering the modelled MSWTF..... 191
Figure 6-20: Illustration of the direct and scattered photons detected in the modelled MSWTF. 192
Figure 6-21: The measured and model spectrum for experiment M10. 193
Figure 6-22: The time-series showing the simulated passage of a dust cloud containing particles of different composition super imposed on a ubiquitous background dust haze..... 195
Figure 6-23: $\Re_I$ as a function of τ within the MSWTF for the two cloud simulations 196

List of Tables

Table 1-1: Past and present spectroscopic and imager instruments, on the surface of Mars, to study the atmosphere. 5

Table 1-2: Same as Table 1-1 except for martian orbiters 6

Table 2-1. The x, y and z dimensions of the different aerosol particle shapes 31

Table 3-1: The k_{ext} in the core and walls for non-uniform dust devils under the different scenarios considered for each τ. 65

Table 4-1: Estimated dust devil parameters from the visual references and UV-VIS data. 95

Table 4-2: The best fit model parameters for encounter E4 and E5. 117

Table 4-3: The retrieved k_{ext} at 386 nm, mass concentration, assumed vertical velocities and the calculated vertical mass flux. 118

Table 5-1: Parameters used in the radiative transfer model. 126

Table 5-2: Summary of the cumulative UVC, UVB and UVA dose for the two different dust components O97 and W09 during MY27 and MY28. 141

Table 5-3: Time required to accumulate the lethal (LD_{99}) UVC+UVB doses for dust components O97 and W09 at the Spirit rover location. 143

Table 5-4: Time required to accumulate the lethal (LD_{99}) UVC+UVB doses for dust components O97 and W09 at the Curiosity landing site. 143

Table 5-5: Time required to accumulate the lethal (LD_{99}) UVC+UVB doses for dust components O97 and W09 at the Phoenix lander 144

Table 5-6: Time required to accumulate LD_{99} for *B. subtilis* endospores exposed to 100% of the diffuse irradiance for dust components O97 and W09 at the Curiosity and Phoenix locations. 145

Table 6-1: List of the experiments carried out, showing total mass of each sample and the light source used. 184

Abbreviations and Acronyms

FoV = Field of View

FS = Full Sky field of view

GCM = Global Climate Model

IR = Infrared

LED = Light Emitting Diode

MCLSM = Monte Carlo Light Scattering Model

MSWTF = Mars Simulation Wind Tunnel Facility

NV = Optical setup with a narrow field of view

NIR = Near Infrared

O97 = Optical properties for martian dust from Ockert-Bell *et al* (1997)

PoM = Point of Measurement

RTM = Radiative Transfer Model

ToA = Top of the Atmosphere

UV = Ultraviolet

UV-VIS = Ultraviolet and Visible spectrometer

VIS = Visible

W09 = Optical properties for martian dust from Wolff (2009)

List of terms

a_{eff} = Volume equivalent radius

C_{abs} = Absorption cross-section

C_{ext} = Extinction cross-section

C_{sca} = Scattering cross-section

g = Asymmetry parameter

k_{ext} = Extinction coefficient

L = Path length through the dust devil

L_s = Areocentric solar longitude

I_a = Ambient surface irradiance on Mars

I_{dd} = Irradiance within dust devil interior

I_{ref} = Reference irradiance spectrum

m = Complex refractive index

n_i = Imaginary refractive index

n_r = Real part of the complex refractive index

N = Dust concentration

Nt = Number of data point fitted in dust devil transit signature

N_λ = Number of fitted wavelengths

r_{vc} = Median volume radius for coarse particles

r_{vf} = Median volume radius for fine particles

V_f = Volume fraction of fine particles

V_c = Volume fraction of coarse particles

S = Path length travelled by a photon

r = Particle radius

R_{core} = Dust devil core radius

R_{dd} = Dust devil outer radius

r_{eff} = Effective radius

r_m = Median radius

Q_{ext} = Extinction efficiency

Q_{sca} = Scattering efficiency

Q_{abs} = Absorption efficiency

T_a = Apparent transmission

$T_{dd}(t,\lambda)$ = Measured transmission during a dust devil transit

$T_m(t,\lambda)$ = Modelled transmission during a dust devil transit

$T_{dd}(0,\lambda)$ = Measured transmission spectrum at the dust devil centre

$T_m(0,\lambda)$ = Modelled transmission spectrum at the dust devil centre

T_{end} = Measurement end time

$T_{integration}$ = Spectrometer integration time

Tsc = Time taken for the spectrometer to make 1 scan

$T\varepsilon$ = Time correction factor

T_{30} = Thirty seconds after encounter E4

u_x, u_y, u_z = Directional cosine

v_{eff} = Effective variance

Z_{dd} = Dust devil height

α_{dd} = Dust devil bearing relative to the sun illuminated wall

β_{dd} = Dust devil trajectory relative to north

θ_z = Solar zenith angle

θ_{pz} = photon zenith angle

Θ = Scattering angle

ϕ_s = Scattering azimuth angle

Φ_S = Scattered photon flux

Φ_T = Total photon flux

σ_{vf} = Variance of the fine particle volume distribution

σ_{vc} = Variance of the coarse particle volume distribution

$\Re_I$ = Ratio of total irradiances at two widely spaced wavelengths

$\Re_D$ = Ratio of diffuse irradiances at two widely spaced wavelengths

$\Re_{Dir}$ = Ratio of direct irradiances at two widely spaced wavelengths

τ = Optical depth

τ_a = Apparent optical depth

T_{bg} = Background dust haze optical depth

τ_c = Cumulative optical depth

τ_{cld} = Water-ice cloud optical depth

ω_0 = Single scattering albedo

χ^2 = Merit factor

LD_{99} = Effective lethal dose rate for a 99.9% kill of Bacillus subtilis endospores in UV radiation

1 Chapter One: Introduction

1.1 Aim of the thesis

This thesis aims to investigate the following research questions:

1) What are the critical factors required for successful retrieval of the optical properties of dust particles in suspension around dust devil vortices?
2) What can we determine from spectral measurements of dust devil vortices in order to constrain the internal characteristics and the mass concentration?
3) What are the observed differences between martian and terrestrial dust devil spectral signatures and what are the implications?
4) How do compositional changes to the dust background component of the martian atmosphere affect observations of dust devils and is there a method for differentiating between different dust and ice aerosol components?

These aims form a scientific case for sending a spectrometer to the surface of Mars, observing the atmosphere in the ultraviolet, visible and near-infrared wavelength region for the purpose of improving our knowledge of the optical properties of martian dust and determining the effect of dust devils on the martian climate. This will further our understanding of the influence of dust on the martian atmosphere.

1.2 The planet Mars

The planet Mars has played an iconic part in many different cultures and religions throughout human history, most notably representing the 'god of War' in Roman mythology. Less than a century ago it was believed that Mars could be habitable and that the dark areas were vegetation. This idea was not so far-fetched for the time as observations showed seasonal variation in these dark areas (Schiaparelli, 1899, Lowell, 1906). While we may look back with mild amusement at these outdated ideas, at the time there was no reason to believe that Mars would not be habitable like the Earth. It was not until the space age began, and the first probes arrived to study the red planet, that Mars was found to be a cold, barren, dusty desert apparently incapable of supporting life like that found on Earth (Klein *et al.*, 1992).

Regardless that we have yet to discover life on Mars, space agencies continue to send robotic explorers in an effort to understand this iconic planet. Beyond Earth it has become a major focus of scientific research within the Solar System with over thirty missions sent to study the planet.

1.3 History of optical depth measurements from the surface of Mars

History has shown that exploring the martian surface is no easy feat, with nearly half of the missions sent to the surface to date suffering failure. However, overshadowing this fact are the successful missions, some operating many years past their planned mission lifetime. These missions have provided, and indeed continue to provide, a large volume of data, allowing better understanding of the martian surface, atmosphere and history.

The initial attempts to land a surface probe on the surface of Mars were plagued with failure. The Soviet built Sputnik 24 was the first spacecraft designed to land on the martian surface, but failed to escape low earth orbit due to a problem with the launch vehicle (Shelton,

1968). It took nearly a decade before the Soviets attempted another landing in 1971, with both spacecraft Mars 2 and Mars 3 successfully entering orbit around Mars (Harvey, 1996). Unfortunately, the Mars 2 lander element crashed on the surface and, while Mars 3 did successfully land, it ceased all transmissions within a minute of landing. Two more attempts were made by the Soviet Union in 1973 with Mars 6 & 7 (Harvey, 1996). Mars 6 was a partial success, returning data during the descent through the martian atmosphere but subsequently failed on landing. A fault with Mars 7 led to the premature separation of the lander probe which entered a heliocentric orbit (Harvey, 1996).

In 1976 a new era of martian exploration began with the successful landing and operation of the NASA Viking 1 and Viking 2 (VL1 and VL2) spacecraft (Soffen, 1977). Both missions were a success and provided the first surface observations of the martian atmosphere and surface environment. In situ measurement of the Sun by the lander imaging cameras enabled the determination of atmospheric dust opacity from the surface. Pollack *et al.* (1977) analysed sky brightness data to determine the optical properties of the airborne dust and to provide an estimated particle radius of 1.8 μm, important for understanding the radiative effects of the dust and its impact on the atmosphere.

Following Viking, it took a further 20 years before another successful landing on the martian surface by NASA's Mars Pathfinder (MPF) in 1996 (Golombek, 1997). Previous attempts to land on Mars between Viking and MPF were fraught with failure, with Phobos 1 and 2 (Galeev, 1996) failing to deploy their lander elements and Mars 96 failing to escape Earth orbit (Sagdeev *et al.*, 1988). The MPF surface probe contained a rover named Sojourner that had the capability of exploring the local vicinity of the lander. Images of the horizon captured by the Imager for Mars Pathfinder (IMP) were the first surface images to observe directly the presence of dust devils (dust laden convective vortices) on Mars (Metzger *et al.*, 1999). The IMP allowed in-situ measurements of sky brightness which were used to refine the particle size and optical properties of the martian dust background (Markiewicz *et al.*, 1999). In the late nineties and entering the following decade, Mars once again confirmed its status as a

challenging destination with the failure of the NASA Mars Polar Orbiter, and its accompanying lander Deep Space 2 (Smrekar *et al.*, 1999), and the British Beagle 2 probe (Sims *et al.*, 1999).

In 2004, the Mars Exploration Rovers (MER), Spirit and Opportunity arrived at Mars (Squyres *et al.*, 2004a; b); these were a resounding success story in the exploration of Mars. The two rovers were a significant improvement over MPF, each carrying almost twenty times the mass of Sojourner. The initial mission lifetime of MER was 90 sols (a sol is defined as one martian solar day with duration of 24 hours and 37 minutes), but eight years on Opportunity is still operating on the martian surface, currently returning data from Greeley Haven. The last communication from Spirit was received in March 2010 after six years of operations on the martian surface. During its operational life, Spirit produced an extensive library of dust devil images at Gusev crater, which was used by Greeley *et al.* (2010) to produce statistical data on the characteristics of martian dust devils. Observations of the Sun by the panoramic camera (PANCAM) on MER have provided detailed insight into the daily and seasonal variation in atmospheric opacity at the Rover locations (Lemmon, 2004). The infrared spectrum measured by the Miniature Thermal Emission Spectrometer (mini-TES) on the MER rovers was used by Wolff *et al.* (2006) to determine a dust particle size distribution with an effective radius (the mean radius weighted by the geometrical cross–section, r_{eff}) between 1.3-1.8 μm.

The landing of the Phoenix Mars Lander inside the Arctic circle of Mars on 25th May 2008 further enhanced our understanding of the martian atmosphere and surface (Smith *et al.*, 2008). Phoenix landed during martian northern spring and successfully survived 65 sols past its mission lifetime of 90 sols. One of the mission goals was to verify the existence of subsurface water-ice, which was inadvertently accomplished, during landing, when one of the thrusters exposed the ice table (Smith *et al.*, 2009). On-board Phoenix was the first Light Detection and Ranging (LIDAR) instrument sent to the planet (Whiteway *et al.*, 2008). The LIDAR observed water ice clouds in the atmosphere, analogous to cirrus clouds on Earth and detected precipitation of ice crystals within the cloud structure (Whiteway *et al.*, 2009). Phoenix

performed synchronised experiments with the Mars Reconnaissance Orbiter (MRO) and discovered discrete vertical layers of water ice and dust (Tamppari *et al.*, 2010).

During the writing of this thesis, the Curiosity rover successfully landed on the surface of Mars ushering in a new era of martian exploration (Grotzinger *et al.*, 2012). Curiosity is the most sophisticated rover to land on Mars to date and the results from its science payload may provide new insights into the history of Mars and whether its climate was ever conducive to being habitable. Table 1-1 provides a summary of the past and current spectroscopic and imaging instruments, on the martian surface, used to study the martian atmosphere. Spectroscopic and imager instruments used to study the martian atmosphere from orbit are given in Table 2-1. The wavelength region observed and mission duration is given for each instrument.

Instrument	Acronym	Wavlength region	Mission Duration
Viking 1 & 2			**1976 – 1982**
Imaging Cameras	-	VIS	
Mars Pathfinder			**1996***
Imager for Mars Pathfinder	IMP	VIS	
Mars Exploration Rovers			**2004 - present****
Minature Thermal Emission Spectrometer	Mini-TES	IR	
The Panoramic Camera	PANCAM	VIS - NIR	
Phoenix			**05/2008 - 11/2008**
Surface Stero Imager	SSI	VIS - NIR	
Light Detection and Ranging	LIDAR	VIS - NIR	
Curiosity			**07/2012 - present**
The Mast Camera	MASTCAM	VIS	
Rover Enviroment Monitoring Station	REMS	UV	
* The duration on the surface was 84 days	UV = Ultraviolet	VIS = Visible	
** Spirit ceased operations in 2009, Opportunity is still operational	NIR - near-infrared	IR = Infrared	

Table 1-1: Past and present spectroscopic and imager instruments, on the surface of Mars, to study the atmosphere. For mission duration, the years of operation are given except in the case of operation within one year only, in which case the months of operation are also given.

Instrument	Acronym	Wavlength region	Mission Duration
Mariner 9			**1971 – 1972**
Ultraviolet Spectrometer	UVS	UV	
Infrared Spectrometer	IRIS	IR	
Viking 1 & 2			**1976 – 1982**
Orbiter imager		VIS	
Infrared Thermal Mapper	IRTM	IR	
Mars Atmospheric Water Detector	MAWD	NIR	
Phobos 2			**01/1989 - 03/1989**
Combined Radiometer and spectrophometer for Mars	KRFM	VIS	
Infrared Spectrometer	ISM	IR	
Mars Global Surveyor			**1996 – 2006**
Thermal Emission Spectrometer	TES	IR	
Mars Orbital Camera	MOC	VIS	
2001 Mars Odyssey			**2001 - present**
Thermal Emission Imaging System	THEMIS	VIS & IR	
Mars Express			**2003 - present**
Spectroscopy for Investigation of Characteristics of the Atmosphere of Mars	SPICAM	UV &NIR	
High-Resolution Stero camera	HRSC		
Planetary Fourier Spectrometer	PFS	NIR & IR	
Mars Reconnaissance Orbiter			**2005 - present**
Context imager		VIS	
Mars Climate Sounder	MCS	UV, VIS & IR	
Mars Color Imager	MARCI	UV - VIS	
Compact Reconnaissance Imaging Spectrometer	CRISM	VIS-IR	
High Resolution Imaging Science Experiment	HiRISE	VIS & NIR	
UV = Ultraviolet	VIS = Visible	NIR - near-infrared	IR = Infrared

Table 1-2: Same as Table 1-1 except for martian orbiters

1.4 The atmosphere of Mars

The primary constituent of the martian atmosphere is carbon dioxide (CO_2) with a volume abundance of 95.32%. Other main components include nitrogen (2.70%), argon (1.60%), oxygen (0.13%), carbon monoxide (0.07%), ozone (O_3, seasonally dependent) and seasonally dependent water vapour (H_2O, ~ 0.03%) (Owen, 1992). Measurements by the Planetary Fourier

Spectrometer (PFS) on Mars Express (Formisano *et al.*, 2004) and Earth based measurements (Mumma *et al.*, 2009) have reported the presence of methane in the martian atmosphere. However the validity of these measurements is still a matter of debate (Zahnle *et al.*, 2011).

Observations and studies of Mars have revealed many similarities with the Earth. The diurnal cycle is similar between the two planets, with a typical Martian day (or sol) lasting 24.7 hours. The obliquity of Mars is 25.2°, comparable to 23.4° for the Earth, leading to Earth-like seasonal cycles. Differences do exist however, the higher eccentricity of the Mars orbit results in approximately 30% less incident solar radiation at aphelion, areocentric solar longitude (L_s) of 90°, in comparison to perihelion, (L_s = 270°). Mars also possesses a significantly thinner atmosphere, with a surface pressure approximately 100 times less than Earth. The surface pressure was observed to vary between 6 and 10 mb at the Viking 1 landing site over the mission duration (Hess *et al.*, 1977). The low pressure at the surface prevents the existence of liquid water and results in water-ice subliming directly into the atmosphere. The pressure and temperature structure of the martian atmosphere, measured by VL1 and VL2, MPF and MER during their descents is shown in Figure 1-1 (Nier *et al.*, 1972, Schofield *et al.*, 1997, Withers and Murphy, 2009). All profiles contain long wavelength oscillations except Spirit's, which exhibits a relatively smooth temperature profile. As suggested by Withers and Smith (2006), the moderate dust storm event which occurred prior to the descent of Spirit and Opportunity may explain the smoother temperature profile measured by Spirit and the warmer temperatures experienced by both rovers compared to the Viking landers and MPF below 30 km. This is because dust storms can result in broad vertical warming of the atmosphere (Smith *et al.*, 2001). The MPF temperature profile shows the coldest temperature of 92 K (below the condensation temperature of CO_2) at approximately 80 km likely indicating presence of CO_2 condensate clouds. A strong thermal inversion is observed in the lower atmosphere in the MPF profile at around 10 km, with a minimum temperature below the condensation temperature of water vapour in the martian atmosphere. As noted by Schofield *et al.* (1997), this temperature inversion may indicate the altitude of the water-ice clouds observed by the IMP before sunrise.

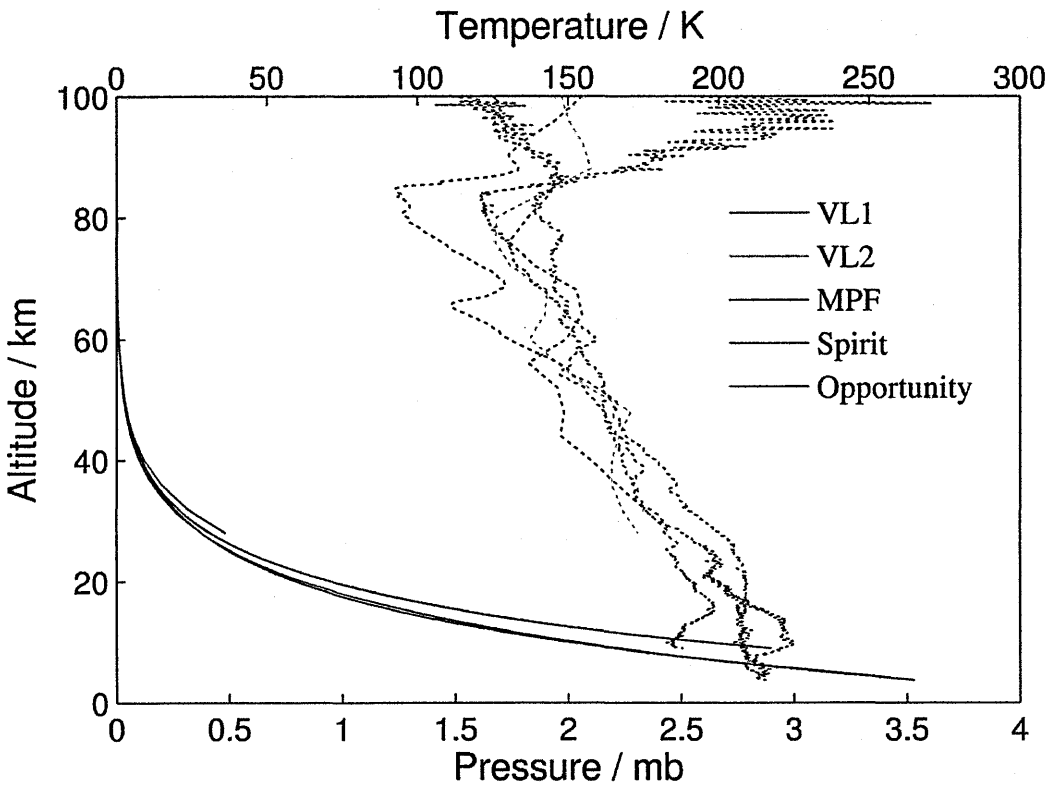

Figure 1-1: The descent profiles for pressure (solid lines) and temperature (dashed lines) by VL1 (green), VL2 (grey), MPF (black) and MER (red-Spirit, blue-Opportunity).

The presence of ozone in the Earth's atmosphere prevents 90% of high energy UVC (200–280) and UVB (280–315) from reaching the surface. The thin martian atmosphere contains a significantly lower abundance of ozone, exposing the martian surface to a greater proportion of the high energy ultraviolet photons (Cockell *et al.*, 2000, Patel *et al.*, 2004). Under simulated martian conditions, Schuerger *et al.* (2003) have shown UVC irradiation to be the primary factor that determines the survivability of microorganisms.

Another major difference between Earth and Mars is the ubiquitous presence of suspended dust particles in the martian atmosphere. Chemical and physical weathering over millions of years has led to micron-sized mineral dust particles dominating the atmospheric aerosol component, and gives rise to the red/pink hue to the martian sky seen in images returned by Viking, MPF, MER and Phoenix. At this point it is useful to introduce the parameter optical depth (τ), which defines how opaque the atmosphere is to the incident radiation. Optical depth is dimensionless and is defined as the product of a species' extinction cross-section with its

column abundance. The extinction cross-section is a measure of the likelihood of a photon-particle interaction and is analogous to the projected area of the species as seen by the photons.

1.5 Aeolian mineral dust

Aeolian (windblown) dust is a major component of the martian atmosphere with variations in dust loading reflecting major interannual climate variability (Haberle *et al.*, 1982, Haberle *et al.*, 1993, Read and Lewis, 2004). The martian dust cycle has been investigated extensively since the mid–20th century with Gierasch and Goody (1968) being the first to identify clearly the fundamental role of dust aerosols in modifying the structure and evolution of the martian atmosphere. Using a simplified radiative convective model, Gierasch and Goody (1968) showed that a CO_2 atmosphere fails to reproduce the general thermal structures of the martian atmosphere as observed by the Mariner 9 spacecraft. By adding an absorbing component which removed 10% of the incoming solar radiation they showed that the model atmosphere could create temperature profiles in the lower atmosphere consistent with those observed. Subsequent studies up to the present day have presented an ever more detailed picture of the effect of the airborne dust on the martian climate (Leovy and Mintz, 1969, Gierasch and Goody, 1972, Pollack *et al.*, 1976, Conrath, 1975, Leovy, 1985, Zurek *et al.*, 1992, Clancy *et al.*, 1995, Haberle *et al.*, 1999, Smith *et al.*, 2001, Bell *et al.*, 2007).

The suspended dust is radiatively active and the large temporal and spatial variations in the atmospheric dust distribution significantly impact the atmospheric state. The suspended dust is strongly coupled to the atmosphere with positive and negative feedback existing between dust lifting by near surface wind stress and the atmospheric heating rate (Newman *et al.*, 2002). The injection of dust into the atmosphere causes greater and more vertically-extended solar heating leading to stronger circulation within the atmosphere. This in turn increases the near surface winds, lifting more dust into the atmosphere and resulting in the formation of dynamical meteorological phenomena such as dust clouds and local and planet-encircling dust storms.

Once a dust storm becomes large, the higher vertical extent of the dust component leads to the absorption of solar radiation higher in the atmosphere. This leads to a warming and cooling of the atmosphere at higher and lower altitudes respectively. As a result the static stability of the atmosphere increases, leading to a more stable atmosphere (Andrews, 2000). The more statically-stable atmosphere leads to less small scale instabilities, such as gravity waves and convective motions, while large scale phenomena tend towards larger spatial scales. This reduces the near-surface wind stress, which will reduce the amount of dust lifted into the atmosphere. This mechanism is what eventually results in the decay of large dust storms.

Dust storms have been observed from martian orbit (Cantor *et al.*, 2001, 2002, 2007),on the martian surface (Smith *et al.*, 2006), from Earth based telescopes (Capen and Martin, 1971, Parkinson and Hunten, 1972, Boyce, 1973) and from Earth orbit (Wolff *et al.*, 1999). Local scale dust events occur frequently throughout a martian year and are usually associated with either topographic features or the retreating edge of the seasonal polar ice cap in spring in both hemispheres. Regional dust storms are less frequent, occurring annually but typically observed when Mars is at perihelion (L_s = 225–315°) while planet-encircling dust events occur on average every three martian years and result in the majority of the atmosphere experiencing dust optical depths that exceed unity, obscuring the surface. The last planet-encircling dust event occurred in 2007 and was witnessed by Spirit and Opportunity from the martian surface (Smith, 2009).

1.5.1 Sources of aerosol dust

The entrainment of fine dust (defined as particles with radii between 0.6-2.0 μm) into the martian atmosphere is still not fully understood. Larger particles are more easily lofted, but fall swiftly back to the surface due to gravity. Cohesive forces such as electrostatic forces and intermolecular forces act to stick the dust particles together, making it more difficult for surface winds to lift them from the surface. On Mars the required wind threshold speed to lift micron sized particles was determined by Greeley *et al.* (1992) to be an order of magnitude greater than

those observed at the martian surface. This has led to different hypotheses about how the dust is entrained in the atmosphere with the two main theories being saltation and/or dust devils.

Saltation is a process where large particles are temporarily lifted into the air by surface winds, quickly fall out by sedimentation and on impact with the surface, dislodge and inject smaller particles into the atmosphere (Bagnold, 1941). Bagnold observed wind-blown sand and dust in the northern African desert. He suggested that the resistance of surface particles to be lifted by surface winds could be quantitatively represented by the fluid threshold and the impact threshold. The fluid threshold is the speed required to allow wind stress alone to lift the particles from the surface and the impact threshold takes into account saltation and is approximately 80% of the fluid threshold (Greeley *et al.*, 1992). Experiments conducted in martian surface conditions have demonstrated the suspension of fine dust through the saltation process however, as reported by Greeley *et al.* (1992), the effect is less pronounced than expected.

Dust devils are another mechanism through which micron sized dust particles can be injected into the atmosphere. The low pressure observed at the centre of dust devils (Sinclair, 1973, Greeley *et al.*, 2003) exerts an upward buoyancy force on the surface particles making such phenomena highly efficient at lifting fine dust particles into the atmosphere. Dust devils are discussed in further detail in Chapter 2.

1.5.2 Seasonal variation

The majority of the martian dust activity occurs between L_s = 180–360°, coinciding with the approach of perihelion (martian southern summer). As mentioned earlier, the reduced distance to the Sun increases the solar flux incident on Mars, causing the southern summer to experience warmer surface and atmospheric temperatures and higher dust abundances. When Mars is at aphelion (northern summer) the atmosphere is cooler resulting in reduced dust activity, with τ measured by MER oscillating around 0.2 between L_s = 50° and 150° (Lemmon *et al.*, 2004). The optical depth measured by VL1 and VL2 (Pollack *et al.*, 1977), MPF (Smith and Lemmon, 1999), MER (Lemmon, 2004) and Phoenix (Lemmon, 2008) as a function of L_s is shown in

Figure 1-2. The measurements reveal an annual pattern in τ, with reduced dust activity observed by all landers during northern spring and summer. Southern spring and summer is characterised by an overall increase in τ, associated with the increased dust activity, with larger variations observed in all datasets over short timescales. The large increase in τ measured by Spirit and Opportunity in Mars Year 28 (Martian Years are numbered according to the calendar proposed by R. Todd Clancy (Clancy *et al.*, 2000): Martian Year 1 begins at a time such that $L_s = 0°$ on April 11th, 1955) around $L_s = 270°$ correlates with the 2007 planet encircling dust event where τ, due to dust, was observed to exceed 4.

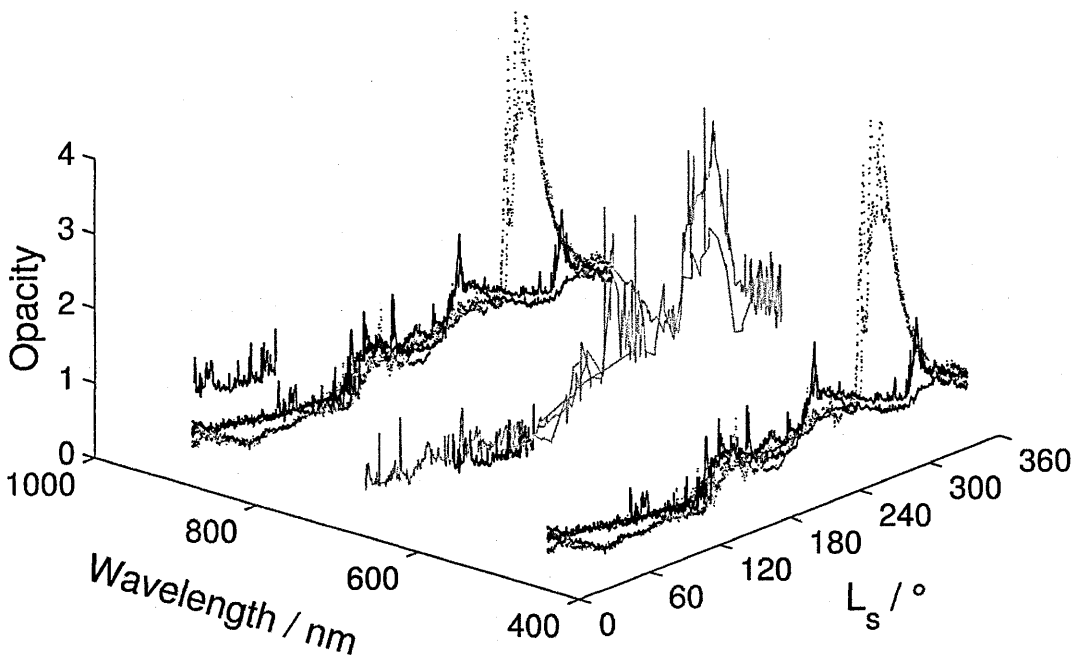

Figure 1-2: The atmospheric opacity at different wavelengths as a function of L_s, measured by: the Viking 1 lander (grey), Spirit (red), Opportunity (blue) and Phoenix (black). The blue and red solid and dashed lines represent Mars Years (MY) 27 and 28 respectively.

1.6 Condensate clouds

Dust is not the only aerosol in the martian atmosphere, condensate clouds of H_2O and CO_2 have been observed to form frequently in the martian atmosphere by Earth-based telescopes (Pettit and Richardson, 1955, Smith and Smith, 1972), orbital spacecraft (Curran *et al.*, 1973, Jakosky and Farmer, 1982, Wang and Ingersoll, 2002) and surface landers (Pollack *et al.*, 1977, Pollack *et al.*, 1979, Smith *et al.*, 1997). Ice clouds of water and CO_2 form when the atmospheric

temperature is low enough to allow either species to condense. The altitude of this condensation can vary considerably and is dependent on the seasonal and diurnal changes in temperature profiles on Mars. Water-ice clouds alter the global transport of water vapour, with the condensation, sedimentation and sublimation processes resulting in a vertical redistribution of water, thus playing a significant part in the martian water cycle (Clancy *et al.*, 1996).

Water-ice aerosols show an anti-correlation with the dust optical depth, with the greatest extent of condensate clouds observed when Mars is at aphelion (low atmospheric temperatures and dust activity) and in the polar regions in the winter hemisphere (Pearl *et al.*, 2001, Wang and Ingersoll, 2002, Liu *et al.*, 2003). The two main cloud features on Mars are the polar hoods and the annual formation of the aphelion cloud belt. The aphelion cloud belt lies between approximately 10°S and 30°N, with the highest ice optical depths observed around large topographic features such as the Tharsis volcanoes. The main belt develops in early northern spring ($L_s = 0°$) and peaks in τ and spatial extent near summer solstice ($L_s = 90°$). The aphelion cloud belt exhibits a rapid non-uniform decay around $L_s = 140°$, with large fluctuations in spatial coverage observed on timescales of a day.

Pure water-ice crystals typically have a single scattering albedo (ω_0) of ~1 indicating that the incident solar radiation is entirely scattered. The reduced absorption decreases the atmospheric heating rate, hence ice aerosols act to cool the atmosphere. The atmospheric circulation responds by decreasing in strength, thus the near surface winds decrease lowering the amount of dust lifted into the atmosphere, further reducing atmospheric heating. Since the majority of the solar radiation is scattered by the ice aerosols, their radiative impact is highly sensitive to how they scatter the radiation (*i.e.* their scattering phase function) which is dependent on the crystal shape and size. Therefore retrieval of ice particle size and shape is crucial, as this will determine how much solar radiation is scattered back to space and how much is scattered toward the surface.

1.6.1 Physical characteristics of martian H_2O aerosols

Modelling the spectral dependence of water-ice absorption in infrared spectra, produced by the Infrared Interferometer Spectrometer (IRIS) on Mariner 9, Curran *et al.* (1973) determined martian ice aerosols to have an effective radius (r_{eff}) of 2 μm. Rodin *et al.* (1997) and Pearl *et al.* (2001) also retrieved ice aerosol distributions with $r_{eff} = 2$ μm using infrared observations from Phobos 2 and Thermal Emission Spectrometer (TES) data respectively. Two distinct populations of water-ice aerosols were discovered by Clancy *et al.* (2003) using emission phase function observations by TES. Type 1 ice aerosols are small with r_{eff} between 1 μm and 2 μm, while type 2 have a distribution with r_{eff} between 3 μm and 4 μm. Type 1 ice aerosols were typically observed in high altitude hazes and in the polar hoods, and are reported to have the scattering behaviour indicative of crystalline shapes. The larger ice aerosols belonging to the type 2 population show scattering characteristics of spheroidal particles and are frequently observed in the aphelion belt. Observations over the Tharsis region, during the Phobos 2 mission, have shown ice particles with $r_{eff} = 0.5$ and 1 μm to exist (Petrova *et al.*, 1996). (Petrova *et al.*, 1996) take into consideration the potential presence of a dust nucleus within each ice particle, and show that over the Tharsis region the dust core will have sizes less than 0.8 μm.

1.7 Vertical distribution of dust and water-ice aerosols

The vertical distribution of solar energy in the martian atmosphere is dependent on the vertical distribution of the dust and ice aerosols. Observations and measurements have shown that the scale height of the dust (defined as the vertical distance over which the dust abundance has decreased by a factor e) is consistent with a CO_2 atmosphere (Pollack *et al.*, 1977, Smith *et al.*, 1997, Lemmon *et al.*, 2004). This fact allows retrieval algorithms to make the simplified assumption that the dust is well-mixed with the CO_2 atmosphere (Conrath *et al.*, 1973, Wolff *et al.*, 2009). However, the actual vertical distribution of dust differs from the well-mixed scenario

with the dust extending to higher altitudes (60 km) during the dustier southern spring and summer and confined to lower altitudes in the relatively dust free northern spring and summer (Jaquin *et al.*, 1986, Chassefière *et al.*, 1992, Cantor, 2007). By analysing measurements of the martian atmosphere by the Mars Climate Sounder (MCS), McCleese *et al.* (2010) have shown that the dust vertical distribution can deviate considerably from the idealized Conrath profile (Conrath, 1975) during northern spring and summer, with a maximum in the dust mixing ratio observed at approximately 15–25 km above the surface. The retrieved dust profiles by McCleese *et al.* (2010) reveal a complex vertical dust distribution in the atmosphere with multiple discrete dust layers.

The vertical distribution of water-ice in the martian atmosphere is highly dependent on the abundance of water vapour and temperature as a function of altitude, and is controlled by the saturation conditions of the atmosphere (Pearl *et al.*, 2001, Richardson *et al.*, 2002). Observations of water-ice clouds are consistent with the idea that the altitude at which water-ice clouds form correlates with the condensation level of the atmosphere, defined as the altitude where atmospheric temperatures are cold enough to allow the condensation of water vapour. The condensation level is highly dependent on latitude and season, being high (> 30 km) during perihelion, when the atmosphere is warmer, and significantly lower (10-20 km) at aphelion. In winter, both polar regions display extremely low condensation levels, with the precipitation of water-ice observed by the Phoenix lander (Whiteway *et al.*, 2009).

1.8 Diurnal variation of optical depth: Morning fogs

To date, measurement of atmospheric optical depth at high temporal resolution over long time-scales has not been performed, leaving a gap in our knowledge and understanding of the diurnal cycle of martian atmospheric dust and water-ice. However low temporal resolution measurements by Viking landers and IMP of atmospheric optical depth have revealed hour by hour variations in τ during a martian day and night (Pollack *et al.*, 1977, Pollack *et al.*, 1979,

Colburn *et al.*, 1989, Smith and Lemmon, 1999). The Viking landers recorded increased τ during the early morning, with τ in the blue filter being consistently higher than the longer wavelength filters. A minimum τ was observed around midday before increasing again in late afternoon. Similar observations were also observed in IMP τ measurements. The mechanism for these variations in τ is the presence of water-ice particles forming a fog near the surface (Pollack *et al.*, 1977, Pollack *et al.*, 1979, Colburn *et al.*, 1989, Smith and Lemmon, 1999). When the temperature at night falls below the frost point of water the dust particles can act as nucleation sites enabling the condensation of water vapour around the dust particle. The growth of the particles due to the accumulation of ice increases the extinction cross-section of the particle resulting in higher τ. Thomas *et al.* (1999) measured τ during the night by observing the bright stars Arcturus and Vega and the martian moons Phobos and Deimos. The optical depth was observed to increase during the martian night, correlating with condensation of water vapour. Wilson *et al.* (2007) compared spatial patterns of Mars Orbiter Laser Altimeter (MOLA) absorptions to the difference between observed and modelled night-time temperatures, and found at aphelion, ice optical depths at night are higher than daytime values, consistent with the development of a surface fog. In the morning the atmospheric temperature increases causing the condensed ice to sublime, reducing the particle size and thus the observed τ. During early afternoon, IMP observed an increase in τ, likely associated with increased dust loading from local phenomena such as dust devils or the formation of water-ice clouds higher in the atmosphere (Smith and Lemmon, 1999). By late afternoon atmospheric temperatures cool enough to re-initiate the condensation of water vapour, indicated by an increase in τ.

1.9 Thesis outline

Chapter 2 gives an introduction into single scattering theory and the single scattering properties of martian aeolian dust retrieved to date are reviewed. The chapter concludes with a discussion on the formation and characteristics of terrestrial and martian dust devils. Chapter 3 provides a detailed description of the Monte Carlo Light Scattering Model (MCLSM), developed

specifically for this work and discusses the predicted optical signatures of terrestrial dust devil transits. In Chapter 4 fieldwork undertaken in Eldorado Valley, Nevada, is described, and the MCLSM is applied to spectral and optical measurements of terrestrial dust devil transits over a spectrometer observing at ultraviolet and visible wavelengths. A retrieval of the single scattering properties of dust entrained in the vortices is performed and compared to similar desert aerosols around the World. Chapter 5 explores the effect of dust and water-ice on the irradiance spectrum encountered at the martian surface (180-1100 nm) using a Mars atmosphere Radiative Transfer Model (RTM), and applies the MCLSM to determine the expected optical signatures of martian dust devils. Chapter 6 investigates the retrieval of dust optical properties from irradiance measurements under controlled laboratory conditions and serves as validation of the optical property retrieval technique applied to terrestrial dust devils. The thesis ends with a discussion and outlines ideas for further work.

2 Chapter Two: Dust aerosols in the martian atmosphere

Images sent back from the surface of Mars, revealed an orange tint to the colour of the sky (Figure 2-1), indicating that the optical properties of the martian atmosphere are quite different from those typically found on the Earth.

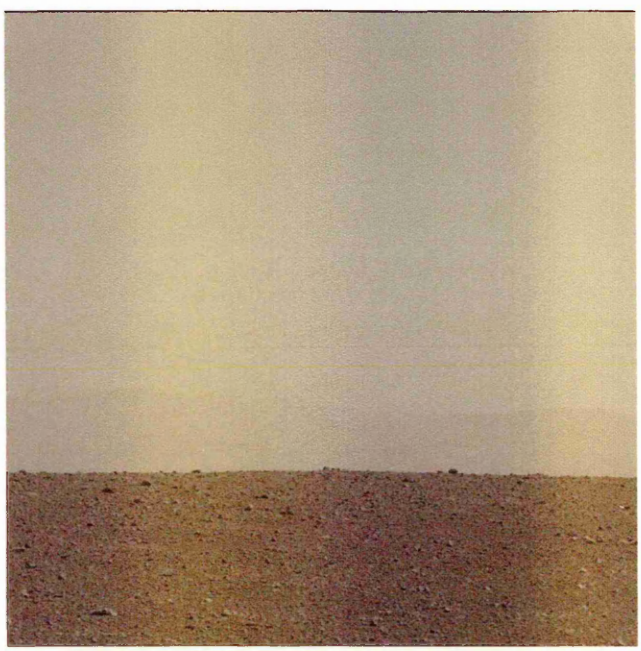

Figure 2-1: Image from the martian surface by Curiosity (NASA/JPL-Caltech/Malin Space Science Systems).

In general the colour of Earth's sky is blue due to the shorter wavelengths of light (violet and blue) being scattered more strongly by the molecules in the Earth's atmosphere. As air molecules are smaller than the wavelength of light ($r_m << \lambda$, where r_m is the radius of the molecule), the angle through which the light is scattered is strongly dependent on wavelength ($\propto \lambda^{-4}$) and leads to shorter wavelengths having larger scattering angles. The scattering of electromagnetic radiation by air molecules can be accurately described by Rayleigh scattering

(Rayleigh, 1918). In the martian atmosphere the primary scattering component is suspended aeolian dust. These dust particles are larger than air molecules, typically comparable to the wavelength of visible light, and scatter light anisotropically (predominately in the forward direction). As a result, their wavelength dependent scattering cannot be described accurately by Rayleigh scattering.

2.1 Light scattering by aerosols

The fundamental concept of electromagnetic scattering used by Mie (1908) is the modification of the total electromagnetic field caused by the presence of a particle. For example, a solution of the macroscopic Maxwell's equations is a plane electromagnetic wave propagating in an infinite non–absorbing medium without a change in its intensity or polarisation state (incident field), Figure 2-2a. When a particle is present the electromagnetic field differs from the incident field (Figure 2-2b). The difference between the total field when the particle is present and the incident field can be thought of as the electromagnetic field scattered by the particle (Figure 2-2c). In terms of a mathematical expression, the total field in the presence of the particle is the sum of the respective incident and scattered fields.

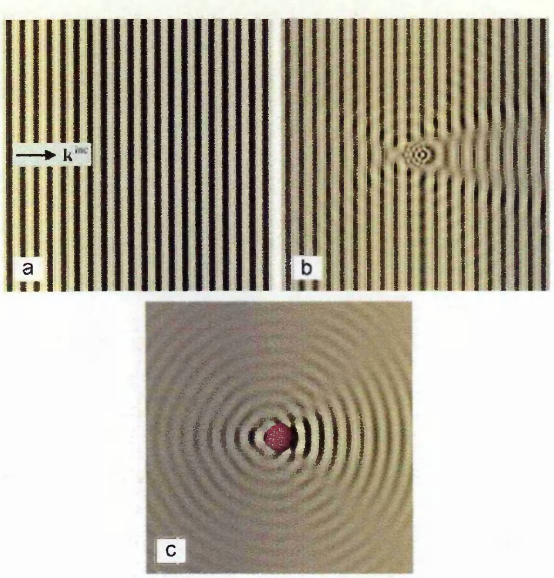

Figure 2-2: Effect of a dust particle on a plane electromagnetic wave. (a) The real part of the vertical component of the electric field vector of a plane electromagnetic wave propagating in the direction of the wave vector k_{inc}, (b) The electric field in the presence of a small homogeneous spherical particle and (c) The difference between the fields shown in (a) and (b). Figure taken from Mishchenko (2009).

Like all materials, mineral dust particles interact with electromagnetic radiation. This interaction results in what we observe as scattering and absorption, and is the mechanism by which dust can alter the distribution of the radiative energy within the atmosphere. The scattering properties of a dust particle are dependent on size, shape, orientation, mineral composition and surface roughness of the particle (Nousiainen, 2009) and are used to describe the fraction of light absorbed and scattered, and the scattering direction.

For an ensemble of dust particles, these properties all form distributions which are inter-dependent on each other and thus, there is no exact analytical solution to Maxwell's equations for light scattering by dust-like particles. Therefore, the simulation of optical scattering by aerosols requires simplifications to the modelled particles and/or the use of non-exact methods. However numerical methods have their limitations and, as a result of the wide range of particle sizes and shapes, different methods and simplifications are often required.

2.1.1 Single scattering theory

In the far-field approximation ($kR >> 1$, where k is the wavenumber and R is the distance from the particle) the scattered electric field can be written as follows.

$$\begin{bmatrix} E_{\vartheta}^{s} \\ E_{\varphi}^{s} \end{bmatrix} = \frac{\exp(ikR)}{R} \mathbf{S}\left(\mathbf{n}^{\mathrm{sca}}; \mathbf{n}^{\mathrm{inc}}; \alpha, \beta, \gamma\right) \begin{bmatrix} E_{\vartheta}^{i} \\ E_{\varphi}^{i} \end{bmatrix} \tag{2.1}$$

where $E_{\vartheta}^{s}, E_{\varphi}^{s}$ and $E_{\vartheta}^{i}, E_{\varphi}^{i}$ describe the scattered and incident electric field parallel and perpendicular to the scattering plane (defined as a plane containing the incident and scattered beam in the direction of observation) and **S** is a 2×2 scattering amplitude matrix which relates the amplitude of the outgoing spherical wave to the incident plane wave. For irregularly shaped particles, the amplitude matrix is a function of the scattering and incidence directions, $\mathbf{n}^{\mathrm{sca}}$ and $\mathbf{n}^{\mathrm{inc}}$, and the particle composition, morphology, size and orientation with respect to the global coordinate system (defined by the Euler angles of rotation[1] α, β and γ). The **S** matrix is the

[1] The Euler angles of rotation transform the global coordinate system into the particle coordinate system .

primary output of single scattering theory, which if known, enables computation of any other light scattering characteristics of the particle.

Optical measurements of light cannot measure the electric field associated with a beam of light, but instead measure quantities that are quadratic combinations of the electric field components (Mishchenko *et al.*, 2000) and define the Stokes parameters *I, Q, U, V* with the Stokes vector given by:

$$\mathbf{I} = \begin{bmatrix} I \\ Q \\ U \\ V \end{bmatrix} \tag{2.2}$$

The first Stokes parameter, *I*, is equal to the net monochromatic energy flux, *Q* and *U* describe the state of linear polarisation and *V* describes the state of circular polarisation of the electromagnetic wave. The condition that the incident electromagnetic wave is unpolarised leads to $Q = U = V = 0$. The transformation of the Stokes vector of the incident wave into those of the scattered spherical wave follows from the definition of the amplitude matrix:

$$\mathbf{I}^{\text{sca}} = \frac{1}{R^2}\mathbf{Z}\left(\mathbf{n}^{\text{sca}};\mathbf{n}^{\text{inc}};\alpha,\beta,\gamma\right)\mathbf{I}^{\text{inc}} \tag{2.3}$$

where **Z** is the 4×4 phase matrix and relates the incident and scattered wave Stokes parameters with respect to the global frame. The elements of **Z** are functions of the elements of the scattering amplitude matrix **S** and expressions for **Z** are summarised by (Mishchenko *et al.*, 2000). The scattering matrix (**F**) differs from the phase matrix in that it relates the incident and scattered wave Stokes parameters with respect to the scattering plane and is proportional to the phase matrix $\mathbf{Z}\left(\vartheta^{\text{sca}}, \varphi^{\text{sca}} = 0; \vartheta^{inc} = 0, \varphi^{\text{inc}} = 0; a; \beta; \gamma\right)$ where $\mathbf{n}^{\text{sca}}$ is defined by the angles ϑ^{sca} and φ^{sca}, and $\mathbf{n}^{\text{inc}}$ by the angles ϑ^{inc} and φ^{inc}.

For isotropic and symmetric media, the scattering matrix is independent of the chosen scattering plane and depends only on the angle between the incident and scattered waves (Θ). In

this case, $\Theta = \vartheta^{sca}$ and the scattering matrix depends solely on Θ (Van de Hulst, 1957) and is defined by:

$$\mathbf{F}(\Theta) = \frac{4\pi}{C_{sca}} \mathbf{Z}(\Theta) \tag{2.4}$$

The proportionality constant $4\pi/C_{sca}$ originates from the normalisation condition on the phase function. C_{sca} is the average scattering cross–section per particle and is calculated from:

$$C_{sca} = 2\pi \int_0^{\pi} Z_{11}(\Theta) \sin\Theta \, d\Theta \tag{2.5}$$

The scattering cross-section is a hypothetical area that quantifies the likelihood that incident electromagnetic radiation will be scattered by a particle. The total amount energy scattered by a collection of similar particles is the product of the particle scattering cross-section and the total number of particles. For isotropic symmetric media, the scattering matrix has the form, (Van de Hulst, 1957):

$$\mathbf{F}(\Theta) = \begin{bmatrix} a_1(\Theta) & b_1(\Theta) & 0 & 0 \\ b_1(\Theta) & a_2(\Theta) & 0 & 0 \\ 0 & 0 & a_3(\Theta) & b_2(\Theta) \\ 0 & 0 & -b_2(\Theta) & a_4(\Theta) \end{bmatrix} \tag{2.6}$$

The (1,1) element of the scattering matrix $a_1(\Theta)$ is the phase function and satisfies the normalised condition:

$$\frac{1}{4\pi} \int_{4\pi} a_1(\Theta) \, d\Omega = \frac{1}{2} \int_0^{\pi} a_1(\Theta) \sin\Theta \, d\Theta = 1 \tag{2.7}$$

where Ω is the solid angle. The asymmetry parameter of the phase function, g (defined as the average cosine of the scattering angle weighted by the phase function) is a measure of the direction towards which the light is favourably scattered. Forward scattering is indicated by a positive value, backward scattering by negative values and zero indicates isotropic scattering.

The asymmetry parameter is defined as:

$$g = \langle \cos\Theta \rangle = \frac{1}{2} \int_{-1}^{1} a_1(\Theta) \cos\Theta \, \mathrm{d}(\cos\Theta) \tag{2.8}$$

Similar to the scattering cross-section, the extinction cross-section (C_{ext}) is the hypothetical area that describes the likelihood that incident electromagnetic radiation will interact with a particle through either scattering or absorption. The absorption cross-section, C_{abs}, is found by subtracting the scattering cross–section from the extinction cross-section. The single scattering albedo (ω_0) is defined as the ratio of the scattering and extinction cross-sections, and is a measure of the probability that a photon incident on a small volume element will be scattered.

$$\omega_0 = \frac{C_{sca}}{C_{ext}} \tag{2.9}$$

Another important set of parameters is the extinction, scattering and absorption efficiencies which are dimensionless ratios of the respective cross–sections to the geometrical cross-section:

$$Q_i = \frac{C_i}{\pi a_{eff}^2}, \qquad i = \text{ext, sca, abs} \tag{2.10}$$

where a_{eff} is defined for non–spherical particles as the radius of an equal volume sphere and for a spherical particles $a_{eff} = r$ with r being the radius of the spherical particle.

Measurements of dusty environments in nature generally observe a distribution of dust particle sizes. At this point it is useful to introduce two parameters, the effective radius, r_{eff} (the mean radius weighted by the geometrical cross-section) and the effective variance, v_{eff} (the spread of the particle size) which are defined by:

$$r_{eff} = \frac{1}{G} \int_{r_1}^{r_2} r \pi r^2 n(r) \mathrm{d}r \tag{2.11}$$

$$v_{eff} = \frac{1}{G r_{eff}^2} \int_{r_1}^{r_2} (r - r_{eff})^2 \pi r^2 n(r) \mathrm{d}r \tag{2.12}$$

where G is the geometric cross-sectional area of particles per unit volume, r is the particle radius and $n(r)$ is the particle size distribution per unit volume. Assuming that each particle scatters independently, the scattering and extinction coefficients are defined as:

$$k_{sca} = \int_{r_1}^{r_2} \pi r^2 Q_{sca}(r) n(r) \mathrm{d}r \tag{2.13}$$

$$k_{ext} = \int_{r_1}^{r_2} \pi r^2 Q_{ext}(r) n(r) \mathrm{d}r \tag{2.14}$$

The extinction coefficient relates the total amount of electromagnetic radiation lost to the distance travelled through the attenuating species. Similarly the scattering and absorption coefficients tell us how much light is lost due to scattering and absorption for a given path length through an attenuating environment.

2.1.2 Spherical particles (Mie theory)

Exact solutions to the Maxwell's equations are only known for special geometries, *e.g.* spheres, spheroids and infinite cylinders. In nature, the physical shape of aerosol particulates is highly irregular and, without an exact solution to Maxwell's equations, approximate methods must be used. At the end of the 19th and beginning of the 20th centuries, numerical solutions to Maxwell's equations for homogeneous spherical particles were produced (Lorenz, 1890, Mie, 1908, Debye, 1909). The Mie solution provides a method for calculating the electric and magnetic fields inside and outside smooth homogeneous spherical objects. The formulism can be used to calculate the total extinction of light incident on a particle (*i.e.* scattering and absorption) and the amount and direction of the scattered light.

The Mie solution to Maxwell's equations provides expressions for two elements of the amplitude matrix S_{11} and S_{22} in the form of two infinite series:

$$S_{11} = \sum_{n=1}^{\infty} \frac{2n+1}{n(n+1)} [a_n \pi_n + b_n \tau_n] \tag{2.1}$$

$$S_{22} = \sum_{n=1}^{\infty} \frac{2n+1}{n(n+1)} [b_n \pi_n + a_n \tau_n] \tag{2.2}$$

The parameters π and τ are functions of the scattering angle (Θ) only, and are calculated by recurrence relations. The full derivation for S_{11} and S_{22} can be found in Bohren and Huffman (1983). The core of the Mie scattering problem is the computation of the coefficients a_n and b_n which are functions of the complex refractive index, $m = n_r - in_i$, and the size parameter, $x = 2\pi r / \lambda$, which describes the ratio of the particle circumference to the incident wavelength, λ. The reader is again referred to Bohren and Huffman (1983) for the full derivation of the scattering coefficients a_n and b_n and the final solutions are given below:

$$a_n = \frac{m\psi_n(mx)\psi'_n(x) - \psi_n(x)\psi'_n(mx)}{m\psi_n(mx)\xi'_n(x) - \xi_n(x)\psi'_n(mx)} \tag{2.15}$$

$$b_n = \frac{\psi_n(mx)\psi'_n(x) - m\psi_n(x)\psi'_n(mx)}{\psi_n(mx)\xi'_n(x) - m\xi_n(x)\psi'_n(mx)} \tag{2.16}$$

The symbols ψ, ξ are Riccati-Bessel functions of the first and third kind respectively. The scattering coefficients a_n and b_n allow the computation of the scattering and extinction efficiencies and the asymmetry parameter from which the extinction and scattering cross–sections can be calculated (Van de Hulst, 1957).

$$Q_{\text{scat}} = \frac{2}{x^2} \sum_{n=1}^{\infty} (2n+1)\left(a_n a_n^* + b_n b_n^*\right) \tag{2.17}$$

$$Q_{\text{ext}} = \frac{2}{x^2} \sum_{n=1}^{\infty} (2n+1)\,\text{Re}\left(a_n + b_n\right) \tag{2.18}$$

$$g = \langle \cos\Theta \rangle = \frac{4}{x^2 Q_{\text{sca}}} \sum_{n=1}^{\infty} \left[\frac{n(n+2)}{n+1} \text{Re}\left(a_n a_{n+1}^* + b_n b_{n+1}^*\right) + \frac{2n+1}{n(n+1)} \text{Re}\left(a_n b_n^*\right) \right] \tag{2.19}$$

In Figure 2-3, ω_0 and g are plotted as a function of x for different values of the imaginary refractive index (n_i) the real refractive index (n_r)was held constant at 1.5. For small values of n_i (< 0.001), ω_0 remains approximately around 0.99 for $x < 100$ indicating that for small n_i the absorption by the particle is more or less unaffected by the particle size. As n_i is

increased ω_0 begins to decrease with increasing x as a result of more of the light refracted into the particle being absorbed. The ripples in ω_0 are directly related to the ripples seen in the Q_{sca} curve and arise from edge rays which graze the sphere (Bryant and Cox, 1966). The convergence of ω_0 to ~ 0.53 at large x is explained by Hansen and Travis (1974), in summary for $n_i = 0$, 50 % of the scattered light is diffracted, 3.3 % is reflected and the remainder is refracted into the particle. Single scattering albedo values below 0.5 are observed for small x and are the result of the Rayleigh region being approached. A weak dependence is seen in ω_0 with particle size for extreme values of n_i (~10) due to the particle tending towards a perfect reflector.

For $x \sim 1$, g is close to the Rayleigh result ($g = 0$) for n_i lower than ≤ 1, converging close to $g = 0.2$. At large n_i, backward scattering dominates at small x and g becomes negative. As the size parameter is increased a corresponding increase in g is observed, with low n_i displaying the oscillatory nature as a result of grazing light rays. For increasingly larger values of n_i, g quickly converges and is constant for $x > 10$.

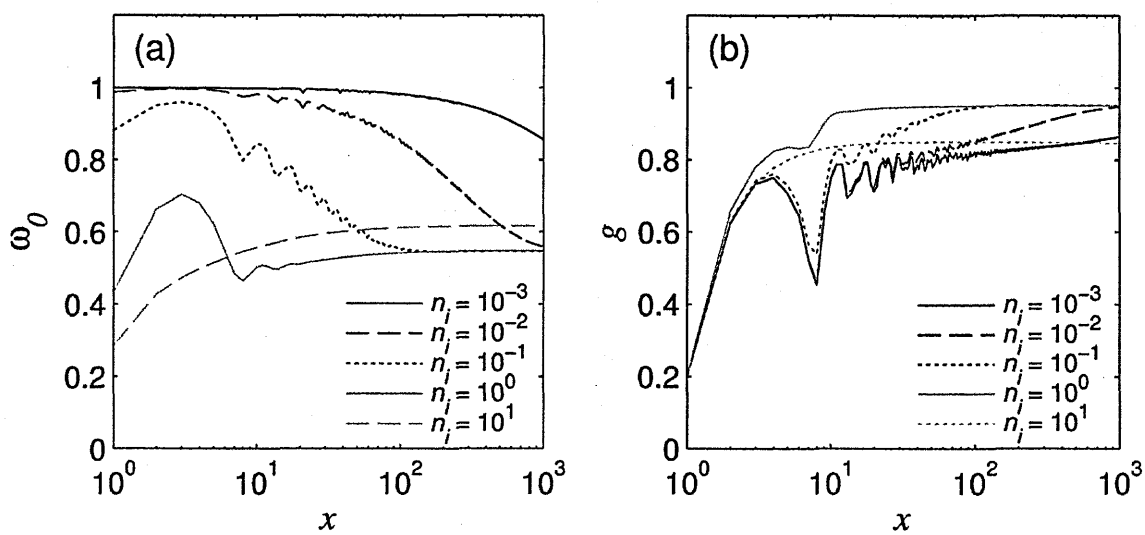

Figure 2-3: ω_0 and g as a function of x for a selection of n_i for a single particle.

Figure 2-4 illustrates the effect of a distribution of particle sizes on ω_0 and g for different n_i values. At $x < 10$, ω_0 shows a small dependence on the effective variance of the size

distribution, At larger x, ω_0 is more or less independent of v_{eff}. It should be noted that this is only true if r_{eff} and v_{eff} are used to describe the particle size distribution. At small x, g displays a larger dependence on v_{eff}, resulting in an increase in g from its single particle value. This indicates that light will be more favourably scattered into the forward direction. At larger x, the size distributions dampen out the oscillations (characteristic of a single particle), however variation in g is still observed up to $x = 10$. Note that for the size distribution cases, $x = 2\pi r_{eff} / \lambda$. The increase in g as x increases is generally observed in measurements of dust aerosols as a decrease in g with increasing λ. Similarly, the dependence of ω_0 on x for a constant n_i and λ indicates that if larger particles are present in the dust aerosol distribution then more of the incident solar radiation will be absorbed. This dependence also signifies that with a constant size distribution, ω_0 will increase with increasing wavelength if n_i is approximately constant over the wavelength range observed.

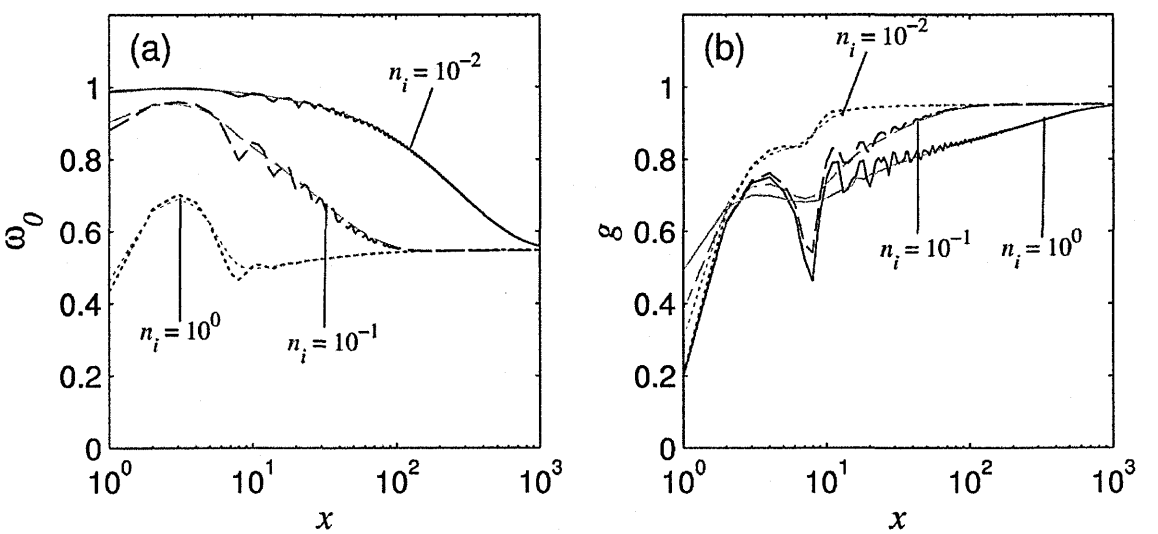

Figure 2-4: ω_0 and g as a function of x for a selection of n_i for a distribution of particle sizes. The black lines denote a single particle and grey lines represent a distribution with $v_{eff} = 0.1$ and light grey for $v_{eff} = 0.25$.

One of the aims of this thesis is to retrieve the single scattering properties of desert dust particles in suspension around dust devil vortices. Evidence suggests (see Section 2.3) that these vortices are more efficient, in comparison to near-surface winds, at lifting large particles

(>10.0 μm) into the atmosphere. This implies that the retrieval of ω_0 for dust particles entrained around dust devils will be lower than equivalent measurements for desert aerosols, and indicates that higher absorption is expected over the visible wavelength region. For g, the presence of larger particles will result in increased forward scattering. It is thus expected that g for dust particles entrained in a dust devil will be higher than those for desert aerosols.

2.1.3 Non-spherical particles (discrete dipole approximation)

One method of calculating the absorption and scattering properties for particles of arbitrary shape is the Discrete–Dipole Approximation (DDA) and was first introduced by DeVoe who studied the optical properties of molecular aggregates (DeVoe, 1964; 1965). However, DeVoe's method did not account for retardation effects (difference in phase between fields propagating from different regions of the particle) and thus, was limited to aggregates which were small compared with the wavelength (the phase within the particle can be assumed uniform). The method was improved by Purcell and Pennypacker (1973), who accounted for retardation effects, enabling the use of DDA to study the scattering nature of interstellar dust grains. The DDA approach replaces the solid particle by an array of polarisable points (dipoles) with the spacing between the dipoles being small compared to the wavelength of light under investigation. Each dipole will adopt an oscillating polarisation in response to both an incident plane wave and the electric fields of the other dipoles in the array. A full description of the DDA method can be found in Draine and Flatau (1994).

DDSCAT, a portable Fortran 95 code developed by Draine and Flatau (1994), was used to compute the single scattering properties of kaolinite and hematite particles of different non-spherical shapes (prolate and oblate spheroids and cylinders) and the results compared to Mie theory for spherical particles. Hematite was used as it has a ω_0 spectrum representative of martian aerosols, with strong absorption at blue wavelengths and highly scattering at red wavelengths. Kaolinite was also simulated to show the variation and sensitivity of the single scattering properties to particles of different composition which exhibit high scattering of light

over the UV, visible and near infrared wavelength region. The refractive indices of hematite (Sokolik and Toon, 1999) and kaolinite (Egan and Hilgeman, 1979) as a function of wavelength are shown in Figure 2-5. The high n_i of hematite indicates that it is highly absorbing, especially at wavelengths less than 550 nm. Kaolinite has a n_i three orders of magnitude smaller than hematite and will result in little absorption at all wavelengths.

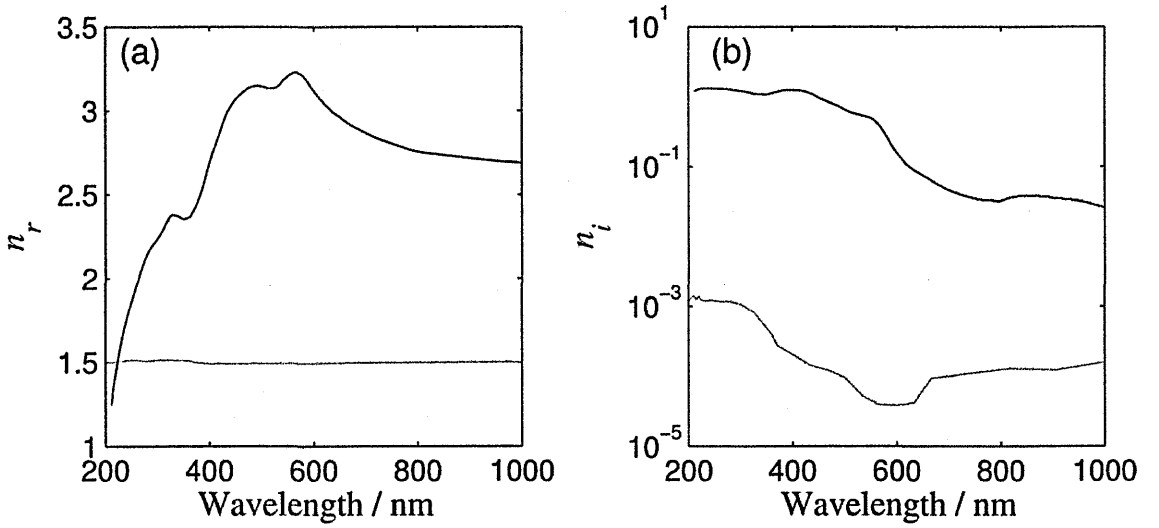

Figure 2-5: The real and imaginary parts of the complex refractive index for kaolinite, grey line, (Egan and Hilgeman, 1979) and hematite, black line, (Sokolik and Toon, 1999).

Using DDSCAT, the single scattering properties for spherical, oblate, prolate and cylindrical kaolinite aerosol particles were calculated. All particles were assumed to be randomly orientated and their sizes selected so that the radius of an equivalent volume sphere (a_{eff}) was 0.5. The dimensions of the particles are given in Table 2-1.

Particle shape	Particle dimensions		
	x / μm	y / μm	z / μm
Sphere	1.00	1.00	1.00
Prolate spheroid	0.794	0.794	1.588
Oblate spheroid	1.258	1.258	0.628
Cylinder	0.742	0.742	1.200

Table 2-1. The x, y and z dimensions of the different aerosol particle shapes, with the particle centre at the origin.

Figure 2-6 shows that the different shapes of kaolinite particles have approximately the same absorption efficiency, with small variation below 500 nm and negligible difference above. All shapes show an increase in scattering towards 700 nm before falling off towards the near-infrared. The scattering profile of prolate spheroids and the cylindrical particles are very similar especially at longer wavelengths. The largest difference is observed with spherical particles, which predict significantly less scattering with a calculated scattering cross-section at 500 nm of 2.15 cm^2 compared to 2.61 cm^2, 2.76 cm^2 and 2.78 cm^2 for oblate, prolate and cylindrical particles respectively (with the particle size known the scattering cross-sections were calculated using Eq. (2.10) with Q_{sca} calculated from Mie theory and DDSCAT). This difference in scattering cross-section will result in approximately 18% to 20 % less light being scattered in a kaolinite scenario, if spherical particles are assumed to approximate the aerosol particles.

As expected, due to the low absorption, very little difference is observed in ω_0. In contrast, g shows variations on the order of 0.3 between non–spherical and spherical particles. Spherical particles consistently predict lower g values except at 350 nm. This indicates that over the majority of the visible wavelength region, spherical particles will scatter more isotropically with less light scattered into the forward lobe. Comparing the non–spherical particles, considerably less variation is observed above 450 nm, but interestingly at wavelengths less than 400 nm the particle shapes show large differences in g. Even prolate spheroids and cylindrical particles which, have been shown to have similar Q_{sca} profiles, see a difference of approximately

0.05 at 350 nm. This indicates that the measured attenuation by kaolinite particles at wavelengths less than 400 nm will be more sensitive to the particle shape, relative to longer wavelengths.

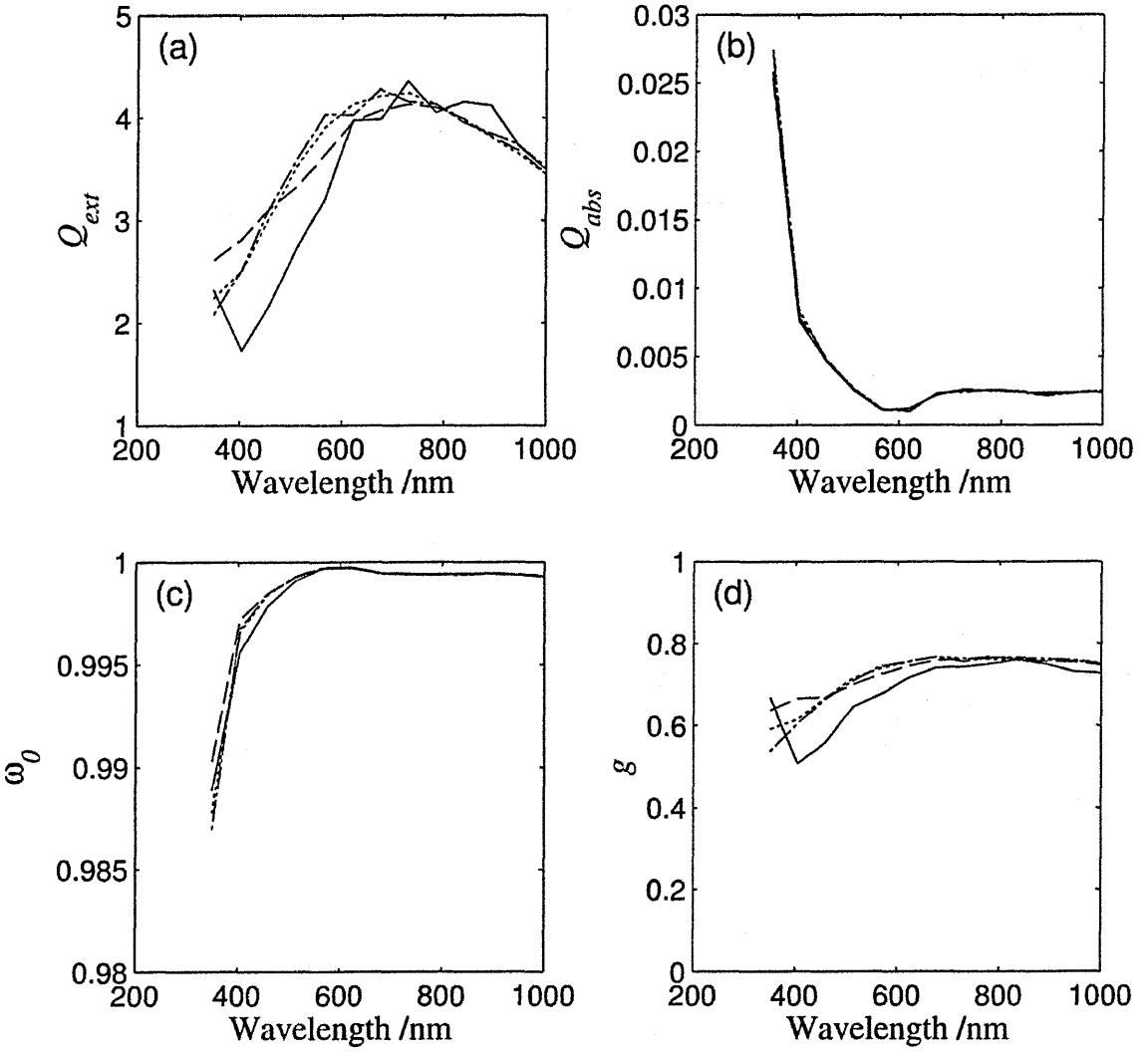

Figure 2-6: Comparison between the calculated single scattering properties a) Q_{ext}, b) Q_{abs}, c) ω_0 and d) the g for non-spherical shaped kaolinite particles with an effective radius of 0.5 μm. The solid line denotes spherical particles, dashed lines represent oblate spheroids, prolate spheroids are shown as dotted lines and dot dashed lines denote cylindrical particles.

The single scattering properties of non-spherical hematite particles are given in Figure 2-7. In comparison to the kaolinite particles, larger variations in ω_0 and g are observed for hematite particles. The assumption of spherical particles will result in an underestimation of the amount of incident light absorbed by the hematite particles. At wavelengths < 560 nm, ω_0

converges to ~0.57 for oblate, prolate and spherical particles but cylindrical particles predict increased scattering at these wavelengths with 6% higher ω_0 values, meaning particles of this shape will observe a higher scattered component if suspended in an atmosphere. Below 560 nm, oblate, prolate and spherical particles show comparable g values, while cylindrical particles diverging to lower values of g. At longer wavelengths, cylindrical and prolate particles show approximately the same wavelength dependence, with the oblate particles diverging to significantly lower g values. Spherical particles exhibit large oscillations in ω_0 and g as a function of wavelength and predict increased and more isotropic scattering over the majority of the 350-1100 nm wavelength range.

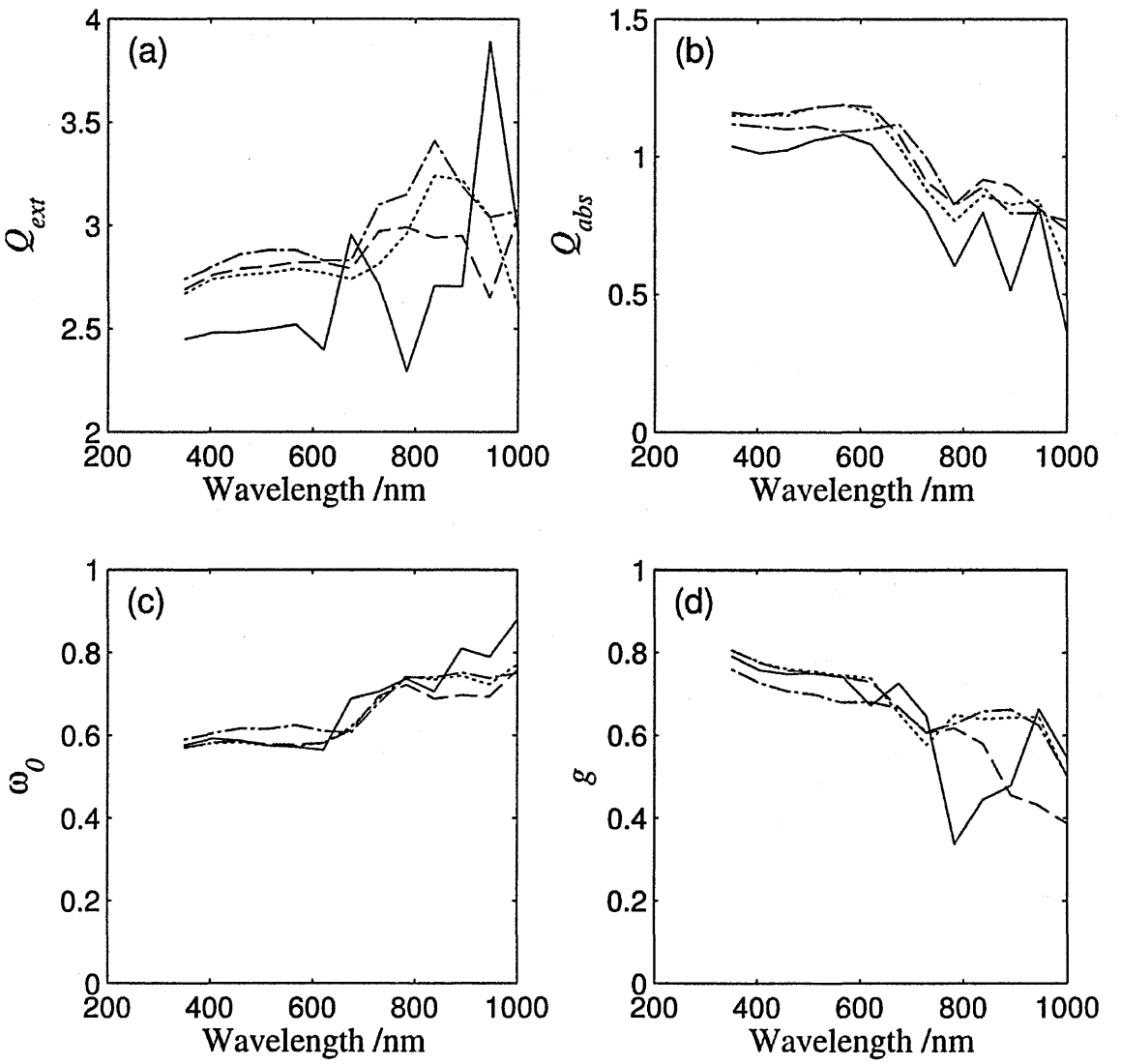

Figure 2-7: Same as figure 2-4 but for a randomly orientated and irregular hematite particle.

While differences in the single scattering properties of individual shapes have been analysed and discussed, it should be noted that any distribution of dust will comprise a variety of irregular shapes, some of which will be far removed from the examples given above, further modifying the particle single scattering properties. Particle shape is not the only parameter that has an effect on the single scattering properties and Nousiainen (2009) provides an in depth study of the effects of other irregular shapes, particle surface roughness and variation in particle composition.

This analysis illustrates the significance of any assumption regarding particle shape. Spherical kaolinite particles result in a lower C_{sca} than non-spherical particles, hence they scatter less light. Therefore, when attempting to retrieve single scattering properties, assuming spherical over non-spherical particles can lead to the overestimation of the number of particles or their size, as more particles or larger sizes are required to observe the same amount of scattering. The ω_0 and g wavelength dependence of hematite has shown that higher n_i results in the single scattering properties being more sensitive to changes in particle shape. The implication is that any assumption on the particle shape can lead to erroneous retrieval of n_i and highlights the need for care when making assumptions on the shape of the dust particle.

In Chapter 4, n_i of dust particles entrained in dust devils are retrieved. Spherical particles are assumed in the retrieval as only a first order approximation and proof of concept. This was because retrievals using more realistic dust particle shapes proved too costly in computer resources). However, the above highlights the importance of particle shape on the retrieval of dust particle optical properties and the difference that might be expected if more realistic particle shapes are considered.

2.2 Optical properties of martian aeolian dust

The optical scattering properties of martian airborne dust have been investigated in a number of studies, yet remain highly debated. Part of the ambiguity is due to the fact that the studies are

based on limited measurements, from remote sensing (Pollack *et al.*, 1977, Pollack *et al.*, 1995, Ockert-Bell *et al.*, 1997, Wolff and Clancy, 2003, Mateshvili *et al.*, 2007, Wolff *et al.*, 2010), *in situ* observations available from the surface from probes such as Viking (Pollack *et al.*, 1977, Pollack *et al.*, 1995), Mars Pathfinder (Tomasko *et al.*, 1999, Smith and Lemmon, 1999, Markiewicz *et al.*, 1999), and the MERs (Lemmon *et al.*, 2004, Wolff *et al.*, 2009). The scattering properties of solid particles are highly dependent on size, shape and composition (cf. Hansen and Travis, 1974, Mishchenko *et al.*, 2000, Bohren and Huffman, 1983, Nousiainen, 2009) and since there has been no attempt to observe directly their composition and shape, their properties are inferred indirectly using optical measurements of extinction, spectral intensity and phase function retrievals. These derived properties are then compared to outputs from Mie theory (Bohren and Huffman, 1983) and other semi-empirical models for spheres and other simple particle shapes such as: cylinders, oblate and prolate discs (Pollack and Cuzzi, 1980, Petrova, 1993, Pollack *et al.*, 1995).

2.2.1 Overview of the different observations

The single scattering properties of martian dust were derived by Pollack *et al.* (1995) from revisited Viking data. They used an improved particle scattering procedure developed by Pollack and Cuzzi (1980) for non-spherical particles, and noted that certain angles of the dust particle phase function are sensitive to different aspects of the dust particles. The authors separated the phase functions into 3 regions; the first region covers the forward scattering peak from 0° to 30° and is most sensitive to the dust particle size distribution, with little variation as a result of changes to the refractive index and particle shape. The second region between 30° and 60° has reduced sensitivity to the particle size distribution and is more dependent on the particles' complex index of refraction. The final region is the side and back scattering region, which is most sensitive to the particle shape. Their analysis showed that ω_0 increases and g decreases with increasing wavelength.

As well as using Viking 1 data, Ockert-Bell *et al.* (1997) incorporated observations from ground based instruments and the Phobos 2 spacecraft, spanning from the ultraviolet to the near infrared. To determine the values of n_i, Ockert-Bell *et al.* (1997) made use of the fact that the complex index of refraction is an intrinsic property of the dust, independent of their distribution and location (*i.e.* the same if they are suspended or on the surface). They used Hapke theory (Hapke, 1981) to relate observations of reflected light and surface albedo in bright regions to n_i.

Clancy and Lee (1991) used emission phase function (EPF) from the Infrared Thermal Mapper (IRTM) data to separate the atmospheric and surface contributions to retrieve an estimate of the solar band ($\overline{\lambda}$ = 0.67 μm, bandwidth of 0.3–3.0 μm) albedo of 0.92. Wolff *et al.* (2009) used retrieved data from the Compact Reconnaissance Imaging Spectrometer (CRISM) and MER during the 2007 dust storm to further refine ω_0 and n_i over the wavelength range 440 – 2920 nm. Observations of Mars by the Wide Field Planetary Camera 2 (WFPC2) and the Faint Object Spectrograph (FOS) on-board the Hubble Space Telescope (HST) were used by Clancy *et al.* (1999) and Wolff *et al.* (1999) to refine the single scattering properties at UV wavelengths. They were further refined by Wolff *et al.* (2010) using observations at 258, 320 and 436 nm of the 2007 planet encircling dust storm, by the Mars Color Imager (MARCI), combined with observations from MER. The high atmospheric dust loading reduced the contribution of the surface reflections in the retrieval, and the low contrast of the surface in the UV and blue wavelengths also reduced the importance of the ground contribution.

2.2.2 *Single scattering albedo*

Pollack *et al.* (1995) used the revisited Viking data to derive values of ω_0 = 0.79 at 490 nm and ω_0 = 0.89 at 860 nm. A similar value for ω_0 was retrieved by Ockert-Bell *et al.* (1997) at 490 nm of 0.76, however at 860 nm a significantly higher ω_0 of 0.95 was found. The higher ω_0 at 860 nm of implies a larger faction of the incident light is scattered resulting in a higher diffuse flux. The culmination of the studies, by Pollack and Ockert-Bell produced values of ω_o that

resulted in a solar irradiance-weighted average of ~ 0.89, close to the value previously proposed by Gierasch and Goody (1968).

However, results from the IRTM and TES (solar band) (Clancy and Lee, 1991, Clancy *et al.*, 2003) show a discrepancy with the irradiance–weighted average albedo calculated to be 0.92-0.94, a difference of 30-45% in the amount of absorbed solar radiation. The solar band albedo derived by Wolff *et al.* (2009) is close to the values proposed by Clancy and Lee (1991), Clancy *et al.* (2003) and Määtänen *et al.* (2009) with a value between 0.92 and 0.94. As suggested by Vincendon *et al.* (2007) this discrepancy in ω_0 maybe a result of the less than ideal observational constraints in the Ockert-Bell *et al.* (1997) data and suggests closer agreement may have been found had they possessed a spectrum with a higher spatial resolution.

Previous work to characterise the dust properties in the UV have yielded ω_0 values in the range of 0.57- 0.60 (Wolff *et al.*, 1999, Clancy *et al.*, 1999). A ω_0 value of 0.64 at 260 nm was retrieved by Goguen *et al.* (2003) using the Space Telescope Imaging Spectrographs (STIS) observations of the 2001 global dust event. Wolff *et al.* (2010) found ω_0 to be between 0.619 – 0.626 at 258 nm and 0.648 at 320 nm for r_{eff} = 1.6 μm and are consistent with the values found by Mateshvili *et al.* (2007) using SPICAM data of 0.60 and 0.64 at 213 and 300 nm respectively. In comparison to the Ockert-Bell *et al.* (1997) dataset, the retrieved ω_0 by Mateshvili *et al.* (2007) and Wolff *et al.* (2010) indicate that the dust is more absorbing at UV wavelengths. The ω_0 values retrieved by the various studies are shown in Figure 2-8.

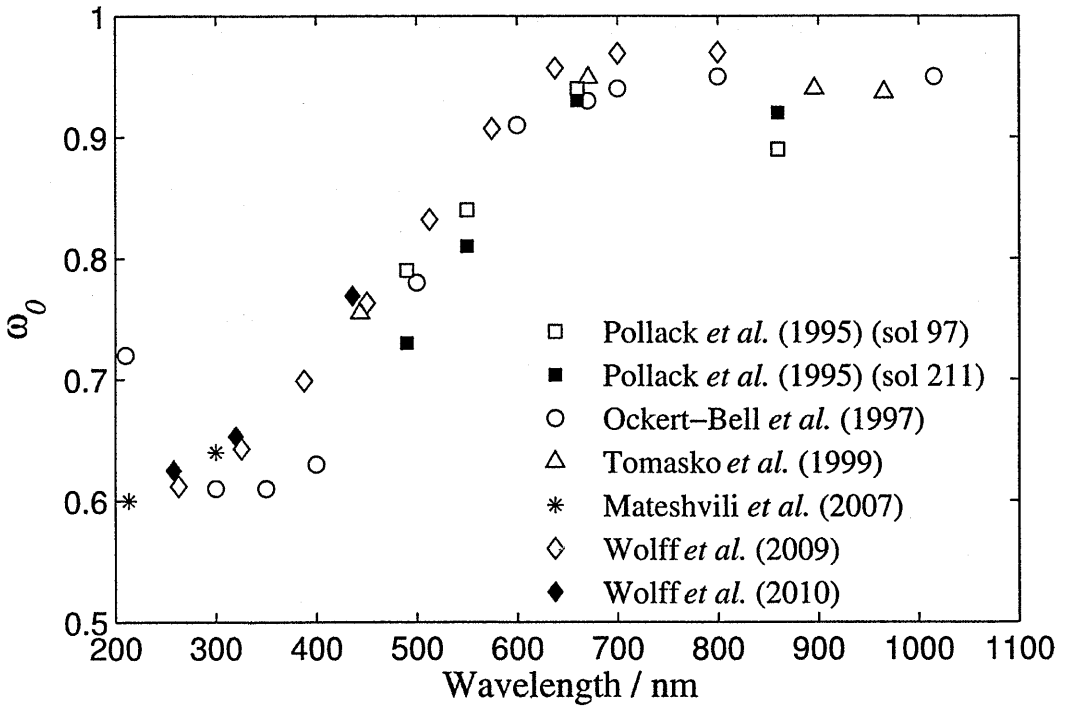

Figure 2-8: The retrieved ω_0 of martian aeolian dust from various instruments.

The injection of dust into the atmosphere causes greater and vertically extended solar heating leading to a strengthening of the Hadley circulation which in turn affects the surface wind stress (Newman *et al.*, 2002). One of the factors determining atmospheric heating rates is the amount of solar incident radiation absorbed by the dust particles and is proportional to $(1-\omega_0)$ in the optically thin limit. Therefore an uncertainty of 5% for a ω_0 of 0.9 at solar wavelengths will result in a 50% error in the heating rate. This will affect the Hadley circulation, surface winds and hence the lifting of additional dust.

2.2.3 *Asymmetry parameter and extinction efficiency*

The investigations discussed in Section 2.2.1 also produced estimates for g of suspended martian dust. In the UV, Ockert-Bell *et al.* (1997) find that g(210 nm) = 0.81 and g(300 nm) = 0.88 and are consistent with Goguen *et al.* (2003), who retrieved a value of 0.84 at 260 nm. An analysis by Mateshvili *et al.* (2007) found g(213 nm) = 0.88 and g(300 nm) = 0.86, while Wolff *et al.* (2010) retrieved g(258 nm) = 0.9 and g(320 nm) = 0.87 for r_{eff} = 1.6 μm.

At visible and near–infrared wavelengths the fitted sky brightness phase functions of Viking lander observations gave g(490 nm) = 0.68 decreasing to 0.63 at 860 nm (Pollack *et al.*, 1995). Using a similar technique, Tomasko *et al.* (1999) and Markiewicz *et al.* (1999) fitted phase functions observed by IMP and retrieved g values between 0.78 and 0.68 for wavelengths between 443 nm and 965 nm with g decreasing with increasing wavelength. All of these analyses are consistent with the Ockert-Bell *et al.* (1997) dataset, which has g = 0.73 and 0.63 at 500 and 1015 nm respectively (Figure 2-9).

Similar to ω_0, small changes in g can affect the heating rate of atmosphere and surface. A decrease in g corresponds to an increase in backscattering which reduces the amount of solar radiation reaching the surface, altering surface temperatures. The scattering of solar radiation back to space also reduces the amount of energy deposited in the atmosphere, lowering the atmospheric heating rate and altering the Hadley circulation and thus surface winds. The extinction efficiency at 670 nm is close to Q_{ext} averaged over the solar spectrum and is used in Mars atmospheric models to scale the dust optical depth with wavelength (Pollack, *et al.*, 1979). Figure 2-9b shows Q_{ext} normalised to 670 nm for the retrieved Q_{ext} of Pollack *et al.* (1995), Ockert-Bell *et al.* (1997), Markiewicz *et al.* (1999) and Wolff *et al.* (2009). Above 600 nm the retrieved values for Q_{ext} as a function of wavelength are consistent, however below 600 nm the profiles diverge, with Wolff *et al.* (2009) predicting an optical depth 10% higher at 350 nm relative to Ockert-Bell *et al.* (1997). This will result in a larger fraction of the incident solar flux being removed by the dust component, leading to a reduced direct irradiance at the surface. The increase in Q_{ext} with wavelength indicates that the particle size is larger than visible wavelengths. A detailed investigation into the effects of different dust components, the irradiance spectrum is given in Chapter 5.

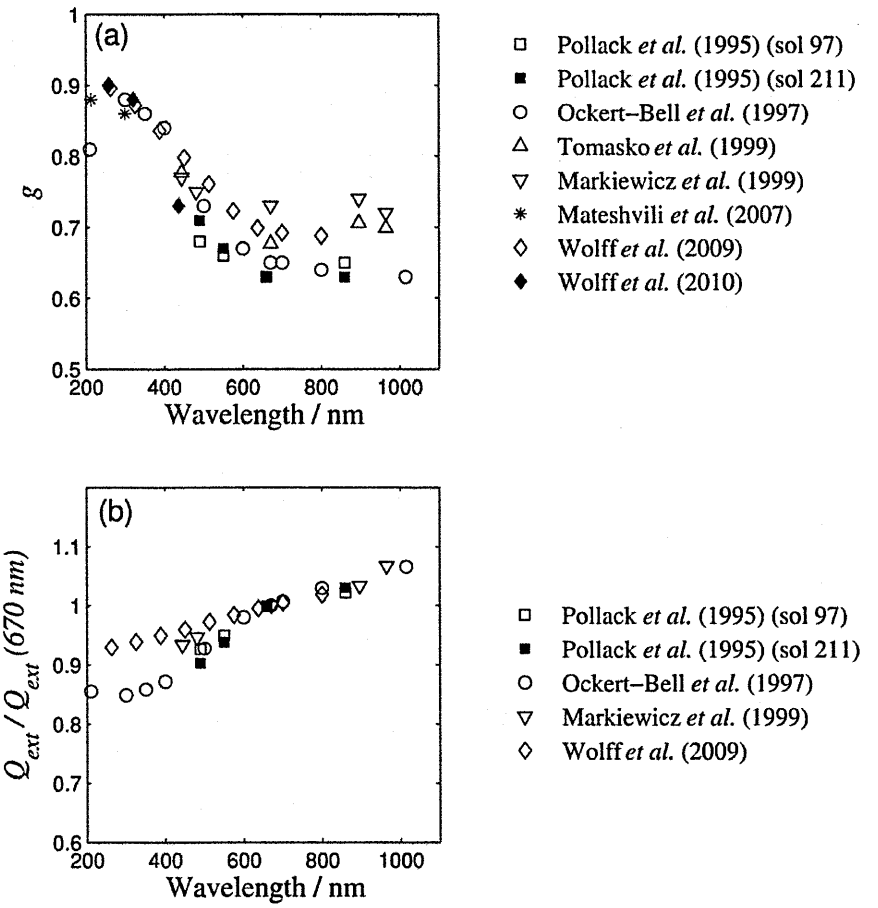

Figure 2-9: (a) The retrieved g of martian dust from various instruments and (b) The retrieved Q_{ext} of martian dust.

2.2.4 *Complex refractive index*

The first analysis and determination of n_i for martian aeolian dust was performed using Viking Lander images of sky brightness at varying solar zenith angles to approximate the phase function of the dust particles. By fitting a semi–empirical phase function to the observed particle phase functions, n_i was determined to be 0.086, 0.074, and 0.041 at 490, 550 and 660 nm respectively (Pollack *et al.*, 1977). However subsequent investigations have shown these values to be extremely high. Using revisited Viking data Pollack *et al.* (1995) determined n_i to be an order of magnitude lower at the same wavelengths. Using midday brightness measurements from IMP, Markiewicz *et al.* (1999) determined n_i to be 0.015 at 443.6 nm with a correlated decrease with wavelength to 0.0024 at 965.3 nm. These results are consistent with the values retrieved by Tomasko *et al.* (1999) and the revisited Viking results. Furthermore, the n_i values

retrieved by Markiewicz *et al.* (1999) provided further refinement of n_i in the near-infrared region which are currently poorly constrained as the comparison in Figure 2-10 demonstrates.

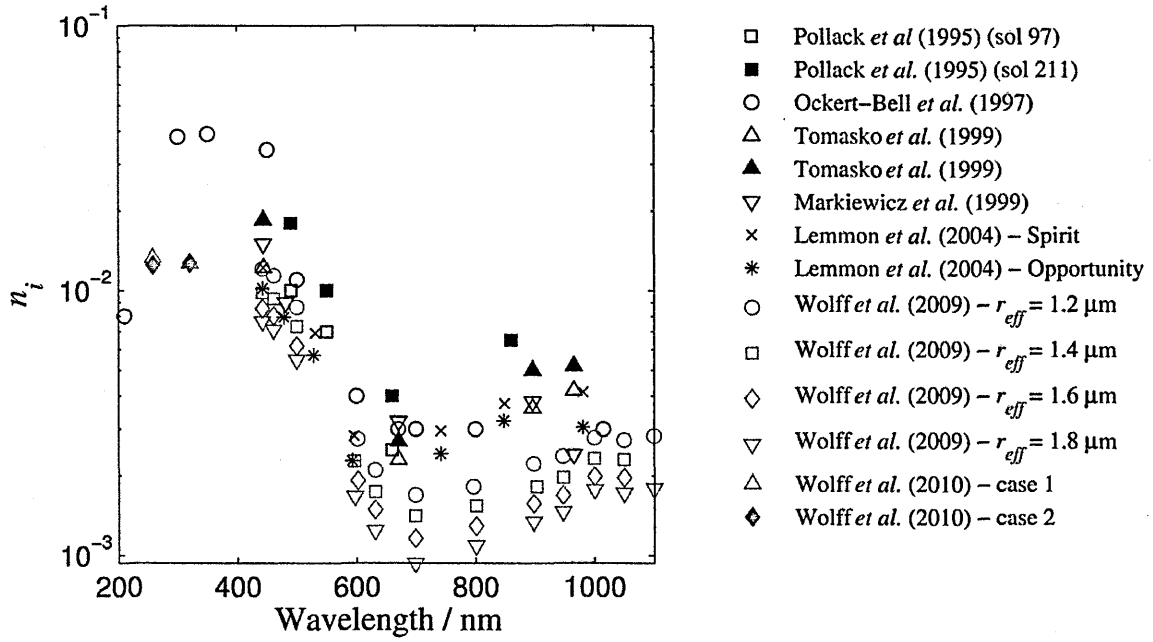

Figure 2-10: The retrieved values of n_i for martian aeolian dust by the authors noted in the legend.

The imaginary refractive index derived by Ockert-Bell *et al.* (1997) and Wolff *et al.* (2009) also agree with the previous investigations with n_i decreasing from 0.011 to 0.003 at 500 and 1000 nm respectively. Below 500 nm, variations in n_i become significant, with the Ockert-Bell *et al.* (1997) values exhibiting a large increase towards 400 nm that is not observed in any of the other datasets. As discussed by Wolff *et al.* (2010) this discrepancy could be an artefact of Rayleigh scattering not being accounted for in the Ockert-Bell analysis. Instead they define an effective surface reflectance in the UV by scaling the data to match a visible spectrum, thus introducing higher uncertainties into their results. The retrieved n_i for martian aeolian dust are illustrated in Figure 2-10. It is important to note that the variations in the retrieved single scattering properties, presented above could be a result of the different techniques and instruments employed and also the different geographical location of the observations.

The single scattering properties of Ockert-Bell *et al.* (1997) have been widely used to describe the radiative effects of martian aeolian dust. More recently Wolff *et al.* (2009) derived

a new set of wavelength dependent single scattering properties for martian dust by fitting the observed phase functions using non–spherical T–matrix calculation (Mishchenko *et al.*, 2000). Both datasets reveal a highly absorbing dust component at wavelengths below 500 nm, with a n_i value of 0.011 ($\omega_0 = 0.78$) at 500 nm. At longer wavelengths n_i quickly reduces to values below 0.001 ($\omega_0 > 0.95$), indicating the dust is highly efficient at scattering incident light. As with ω_0 and g, these two datasets are not in mutual agreement, especially at ultraviolet wavelengths, and a comparison between their effects on the irradiance at the martian surface is explored in Chapter 5.

2.3 Dust devil phenomena

Particle-loaded convective vortices (dust devils) develop from an unstable near-surface layer of air that forms from surface heating. A dust devil consists of a vortex with vertical upward flow forming its core, and lateral inflow of air near the bottom of the vortex (Sinclair, 1966; 1973). Such vortices are common, but not all are strong enough to loft and carry materials and thus remain non-visible. The term 'dust devil' is used to distinguish visible vortices from ones that are not able to sustain a particle-load. An example of a dust devil is shown in Figure 2-11.

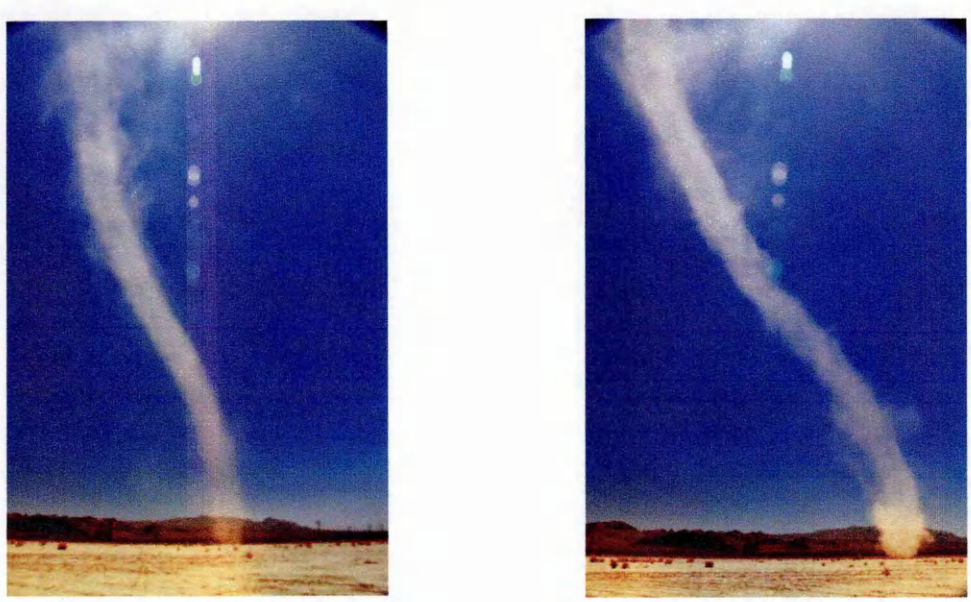

Figure 2-11: Image of a dust devil in the Nevada desert. (a) intensity of the vortex is insufficient to suspend large dust particles (b) formation of a sand/dust 'skirt' as the wind surface shear stress allows entrainment of larger particles.

2.3.1 Dust devil formation

Dust devils are low pressure, warm core vortices which usually occur during the summer season in arid locations around the world (Ives, 1947), however they are not limited to these regions and can occasionally form in all climate regions. Terrestrial dust devils are commonly squat, V–shaped vortices that can last up to several minutes. Well–formed vortices consist of an outer cylinder of high dust concentration exhibiting high rotational velocities, an intermediate cylinder of moderate vertical lift, and a low pressure inner core (~2% below the ambient pressure conditions) that experiences an enhanced temperature excursion up to 20°C above ambient air temperature. A number of studies of terrestrial dust devils have been carried out (Sinclair, 1966, Ryan and Carroll, 1970, Sinclair, 1974, Greeley *et al.*, 2003, Metzger, 1999a, Balme and Greeley, 2006), with evidence suggesting that dust devil formation occurs in the bottom of convective cells (Battan, 1958, Sinclair, 1966, Ryan and Carroll, 1970).

At least two mechanisms are known that could allow convective vortices to lift and entrain dust. The first is analogous to the wind shear that lifts particles in boundary layer winds. Convective vortices can develop tangential wind velocities which have a surface shear stress exceeding that of horizontal turbulent winds. This can result in particle saltation which forms a 'skirt' of windblown sand and dust at the base of the vortex allowing the entrainment of particles from the surface that would otherwise be resistant to turbulent wind shear (Bagnold, 1941). Once suspended, the fine particles remain entrained and enhance the dust load of the vortex. The other lifting mechanism which enhances dust loading is the 'ΔP effect' suggested by Greeley *et al.* (2003) which is related to the pressure drop found at the centre of dust devils and results in an upward force on the particles as the vortex moves along the surface. Measurements carried out by Metzger (1999a) showed that terrestrial rotational and lift velocities as low as 3.8 ms^{-1} and 1.9 ms^{-1} respectively are sufficient to enable dust entrainment within convective vortices. Both of these mechanisms result in saltation that aids further lofting of particles from the surface. Figure 2-11b gives an example of a dust devil in the Nevada

desert, the dust 'skirt' resulting from saltation can be clearly seen around the base of the vortex close to the surface.

Laboratory experiments have also been conducted to investigate different components of dust devil vortices. Greeley *et al.* (2006) constructed a vortex generator (The Arizona State University Vortex Generator, ASUVG) to simulate terrestrial and martian dust devils. Their experiments showed that the pressure drop (ΔP) at the vortex core provides an additional lift component, making dust devils more efficient at removing dust from surfaces than boundary layer winds. Using the ASUVG, Neakrase *et al.* (2006) and Neakrase and Greeley (2010a) conducted dust and sediment flux experiments at Earth and Mars atmospheric pressures and found that the sediment flux is related to the vortex intensity, which itself is dependent on the ΔP at the core. Their experiments showed that vortices of different sizes could yield the same pressure drop at the core and concluded that the vortex size is less important for sediment lifting than the ΔP at the core. The vertical flux of dust (particles < 2 μm in diameter) was found to increase exponentially with increasing tangential velocity but decrease exponentially with increasing core radii. Their results demonstrated that smaller vortices experience higher dust fluxes. A similar relationship to the core pressure drop was also reported with an exponential increase in dust flux for larger ΔP. Furthermore, the effects of surface roughness on dust devil dynamics was explored by Neakrase and Greeley (2010b) for terrestrial and martian dust devils. They found a correlated increase in the vortex size with increasing surface roughness, while the tangential velocity was observed to decrease. The expansion of the vortex reduces the energy available and will eventually impede additional lifting of surface material. However, Neakrase and Greeley (2010b) showed that small increases in surface roughness can reduce the threshold required to lift fine particles (< 100 μm) enhancing the sediment flux of weaker dust devils beyond that which would be expected. For larger increases in surface roughness the ΔP and tangential velocities are reduced, decreasing the vertical flux of surface material.

2.3.2 Lower dust devil structure

The lower structure of dust devils has been well characterised by Kaimal and Businger (1970) and Sinclair (1973) and a schematic is shown in Figure 2-12. The main feature of the temperature distribution is the well-defined temperature increase towards the inner edge of the dust column and the presence of downward moving cooler air within the dust-free core. Figure 2-13 shows thermal images taken of a dust devil transiting across the Eldorado valley in the Nevada desert with the temperature enhancement clearly visible in the dust column. The images also correlate with the rapid temperature decrease with altitude described by Sinclair (1973).

Dust devils are also characterised by a low pressure region coinciding with the warm core, with a typical drop of 2% relative to ambient pressure. The warm, low pressure core can result in the air density at the core being 1-2% lower than ambient conditions (Sinclair, 1973). The nature of dust devils results in the pressure perturbation reaching a maximum a few metres above the ground before rapidly decreasing with altitude and nearly vanishes a few hundred metres above the surface.

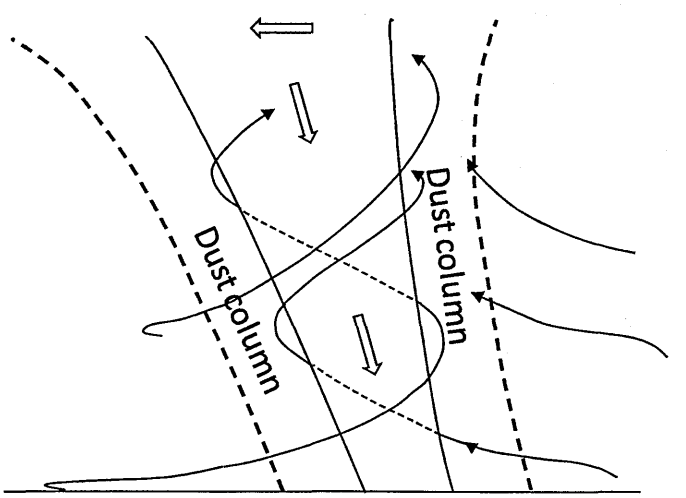

Figure 2-12: Schematic of a dust devil moving from right to left (adapted from Sinclair (1973)).

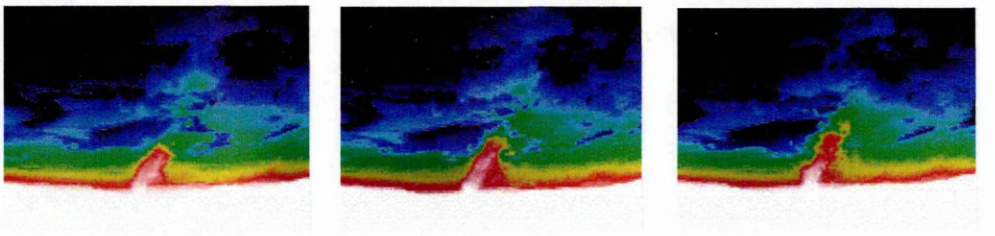

Figure 2-13: Thermal images taken of a dust devil with a low dust density in the Eldorado Valley, Nevada.

Field investigations of terrestrial dust devils by Balme *et al.* (2012) have shown a correlation between the wind speed at 20-30 m above the surface to the horizontal speed of the vortex along the surface. The vertical velocity component is strongly dependent on the distance from the dust devil centre, with vertical velocities reaching speeds of 10 ms^{-1} around the centre, and rapidly decreasing radially outwards. The region of maximum vertical velocity expands radially with altitude, correlated with the radial expansion of the dust devil with altitude. Perhaps the most significant discovery by Kaimal and Businger (1970) and Sinclair (1973) is the presence of a down-current or a region of reduced vertical motion at the core. This result correlates with the detected presence of cooler air embedded within the warm central region of the dust devil, and agrees with the presence of a highly superadiabatic lapse rate within and around the dust devil. It is this downward motion and the centrifugal forces that suppress the presence of dust particles in the vortex core.

Another feature reported by Sinclair (1973) and observed during the dust devil field work carried out as part of this thesis, was the presence of secondary circulations embedded in the primary rotation of the dust devil. Figure 2-14 shows an enhanced image of the dust column of a dust devil encounter in the Eldorado Valley. Clearly visible are several small secondary circulations within the primary rotating dust column. Although the primary and secondary vortices will mutually interact, the wind field of the secondary vortices is locally confined and has little influence on the motion of the main vortex and will follow concentric paths around the dust devil core.

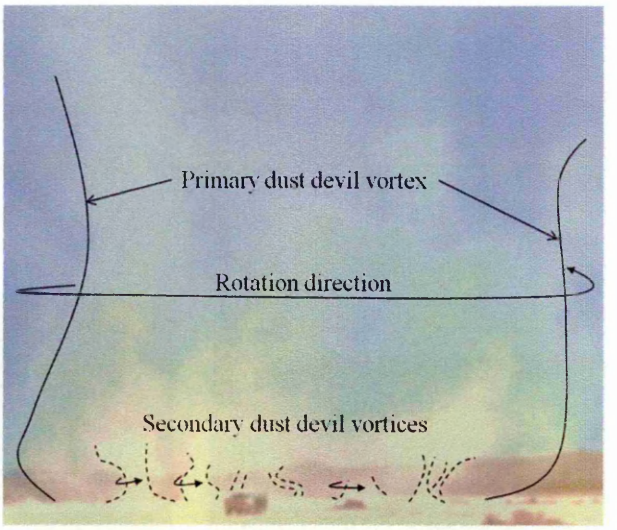

Figure 2-14: Image taken in the Eldorado Valley of a dust devil with secondary vortices present in the primary dust column. Seven secondary rotations are highlighted; however the video capture indicates that in this case the entire surrounding dust column was made up of 10s of small secondary rotations.

2.3.3 Dust devils on Mars

Dust devils are not a phenomenon unique to the Earth; recent observations by the imager for Mars pathfinder (IMP) (Metzger *et al.*, 1999b, Ferri *et al.*, 2003), Mars orbital camera (MOC) on–board Mars global surveyor (Fisher *et al.*, 2005, Cantor *et al.*, 2006), and thermal emission imaging system (THEMIS) on Mars Odyssey (Cushing *et al.*, 2005) among others have shown them to frequently occur on the martian surface, Figure 2-15. While dust devils on the two planets are similar, they play very different roles on their respective planets. On Earth, they are secondary to boundary layer winds and only play a minor role in the dust cycle except possibly in arid regions. In contrast, on Mars they maintain the constant aeolian dust background, especially in northern summer, and play a major role in the rapid transport of fine particulates into the martian planetary boundary layer. As was shown in Chapter 1, the atmospheric dust loading is at a minimum during northern spring and summer, when Mars is at aphelion, and the atmosphere is cooler due to the reduced level of solar insolation. The cooler atmosphere reduces the strength of the atmospheric circulation which in turn decreases the surface wind stress leading to less dust lifted into the atmosphere. However, observations by MOC (Edgett and Malin, 2000) have shown dust devils forming in all seasons and, as suggested by Sinclair

(1973), dust devil formation can occur whenever the conditions are met for superadiatic lapse rates in the local atmosphere. Therefore it is likely that dust devil activity is responsible for maintaining the low level background dust haze that is observed during northern spring and summer.

Figure 2-15: Two examples of dust devils on the surface of Mars; (a) imaged by the NAVCAM on sol 616 by the MER rover (Spirit) in Gusev crater, Greeley *et al.* (2006) and(b) image taken by the HiRISE imager on the Mars Reconnaissance Orbiter (image: NASA/JPL/University of Arizona).

It has also been suggested that dust devils may act as a precursor to the formation of large scale dust storms on Mars (Thomas and Gierasch, 1985). However, Newman *et al.* (2002) has shown that dust devil activity displays a negative feedback with increasing atmospheric dust loading. The dust lifted by the dust devils extends vertically into the atmosphere causing increased heating above the surface and reduces the solar insolation at the surface. This reduces the surface-atmosphere temperature gradient and as a consequence, less energy is available to drive dust devil formation. The negative feedback of dust devil formation with atmospheric dust loading is counterproductive to the formation of dust storms.

The occurrence of dust devils on the martian surface was first suggested by Ryan (1964), and two decades on the first direct observations of dust devils on Mars were performed by the Viking Orbiter (Thomas and Gierasch, 1985). In 1997 IMP observed several dust devils with

estimated diameters of tens of metres to greater than 100 m (Metzger *et al.*, 1999b, Smith and Lemmon, 1999, Ferri *et al.*, 2003). Another indication of dust devil activity on Mars are tracks left on the surface. These tracks are characterised by a change in the surface albedo as a result of small particulate material on the surface being lofted and entrained within the dust devil, exposing a darker (or sometimes lighter) subsurface layer when compared to the surrounding surface (Balme *et al.*, 2003, Fisher *et al.*, 2005, Cantor *et al.*, 2006, Drake *et al.*, 2006). Observations of dust devil have shown a seasonal dependence on the formation of dust devils, with the perihelion (L_s = 270° -360°) showing greater abundance of dust devil tracks, compared to the aphelion (L_s = 60° - 195°) where very few tracks are observed (Balme *et al.*, 2003, Whelley and Greeley, 2006). The widths of the tracks vary significantly from less than 10 m to greater than 200 m. Metzger *et al.* (1999b) used column opacity measurements of dust devils by IMP to determine the particle loading to be 70 mg m^{-3}, and assuming a vertical velocity of 7 ms^{-1} they estimated the vertical flux of material into the atmosphere to be 500 mg m^{-2} s^{-1}. Furthermore, the Spirit Rover observed an entire year of dust devil activity within Gusev crater and, using these data, Greeley *et al.* (2006) calculated the vertical wind speeds of martian dust devils to be between 0.2-8.8 ms^{-1}, similar to the results of Metzger (1999a) for terrestrial dust devils. Three dust devil seasonal cycles at Gusev crater, spanning Mars Years (MY27 - MY29) as observed by the Spirit Rover, were analysed by Greeley *et al.* (2010). Estimation of the dust concentrations within the dust devils were found to range from $2.1 \times 10^{-9} - 2.5 \times 10^{-4}$ kg m^{-3} for MY27, $7.9 \times 10^{-7} - 4.5 \times 10^{-5}$ kg m^{-3} in MY28 and $4.3 \times 10^{-8} - 7.7 \times 10^{-5}$ kg m^{-3} for MY29. Extrapolating the dust mass per dust devil over the Gusev crater they determined that the total mass of dust injected into the atmosphere ranged from 6.6×10^{3} kg to 7.7×10^{8} kg (MY27), $9.9 \times 10^{4} - 1.2 \times 10^{7}$ kg (MY28) and 2.7×10^{5} kg to 2.8×10^{8} kg (MY29). Martian dust devils are not confined to lower latitudes; analysing meteorological data measured at the Phoenix landing site, Ellehoj *et al.* (2010) showed that during its operational lifetime the lander experienced 502 identifiable encounters with convective vortices or dust devils.

2.4 Previous radiative transfer modelling of dust devils

No detailed radiative transfer (RT) model of light transmission through a dust devil vortex has been developed to date. A Monte Carlo scattering model was developed by Metzger *et al.* (1999b) to calculate the dust loading within a dust devil observed by the Mars Pathfinder camera. However, their model was never applied fully to dust devils of different size and internal dust distribution. Furthermore, they did not apply the scattering model as a tool for retrieval of the single scattering properties or size distribution of the entrained dust particles. Accurate determination of the single scattering properties and particle size entrained within dust devils is important for the determination of the dust loading and, hence the vertical flux of material into the atmosphere. Metzger *et al.* (1999b) assumed the entrained dust has the same size distribution and single scattering properties as the background haze. A detailed model, simulating the transmission of light through a dust devil vortex, is therefore required in order to simulate the radiative effect of dust devils and to determine whether the entrained dust particle single scattering properties and size distribution can be retrieved from spectroscopic measurements during dust devil transit. The description of the dust devil model is the subject of the next chapter.

Chapter Three: Monte Carlo modelling of dust devil vortices

Aeolian mineral dust can have a large effect on the radiation budget of planetary atmospheres such as those surrounding the Earth and Mars. This dust can absorb solar and infrared radiation resulting in localised warming of the atmosphere (positive radiative forcing) and scatter incoming light back to space resulting in cooling of the atmosphere (negative radiative forcing). The balance between absorption and scattering determines whether the aeolian dust acts to cool or warm the surrounding atmosphere (Alpert *et al.*, 1998) and highlights the importance of accurate retrieval of the dust particle single scattering properties, specifically ω_0. One method used to retrieve the single scattering properties is to fit radiative transfer model outputs with the observed attenuated spectrum. However, accurate modelling of the light transmission through a dusty environment can be extremely difficult, especially at large τ where the single scattering approximation is inadequate to describe accurately the diffuse component. The Monte Carlo radiative transfer (MCRT) method has been used successfully in many different fields to describe accurately multiple scattering scenarios in significantly different environments. Witt (1977) applied MCRT to interstellar grains by looking at reflectance nebulae and has shown that MCRT can be applied to the multiple scattering problem. MCRT was employed by Vincendon and Langevin (2010) to simulate the impact of aerosols on the remote sensing of the surface of Mars and Titan. More relevant to this study, Metzger *et al.* (1999b) used a MCRT to simulate the scattered diffuse component of martian dust devils observed by the Imager for Mars Pathfinder (IMP).

In this chapter the development of a Monte Carlo Light Scattering Model (MCLSM) to simulate the transmission of sunlight through dust devil vortices is described. The model was created using the Research Systems Inc. Interactive Data Language (IDL) and utilising GPUlib which allows efficient operation of the model code on the graphics processing unit (GPU). The

simulated variation in light during a dust devil transit over a fixed point on the surface is investigated to determine whether the dust load, size and internal structure of the vortex can be estimated from a dust devil transit signature (defined as the observed light curve as a function of distance or time). The transmission of sunlight through the vortex depends on how the dust is distributed internally and the vortex internal structure (in terms of the core diameter). Therefore, using the MCLSM, the internal structure and dust distribution within dust devils is explored explicitly, comparing the assumption of a uniform dust concentration to one with a relatively dust free central vortex surrounded by walls of larger dust concentration. Finally, the effect on the transit signature due to variations in single scattering properties is investigated to determine the possibility of retrieval of the dust particle optical properties.

3.1 Radiative transfer in dusty environments

3.1.1 Model description

The scattering of sunlight by dust grains entrained in a dust devil vortex was modelled using the Monte Carlo method (Cashwell and Everett, 1959, Witt, 1977, Whitney, 2011). The model geometry and coordinate system are illustrated in Figure 3-1. The Cartesian coordinate system (*X, Y, Z*) has its origin at the vortex centre and the vertical Z-axis is directed along the axis of symmetry of the vortex flow, normal to the *X-Y* plane. The positions of the individual photons are given by their (*X, Y, Z*) coordinates while their direction vectors, P_v, are described by the directional cosines (u_x, u_y, u_z), which are calculated from the angles θ and φ. It is assumed that the incident photons are plane-parallel, travelling in the $+X$ and $-Z$ directions depending on the solar zenith angle (θ_z). The line of sight of the modelled spectrometer is normal to the X-Y plane in the $+Z$ direction.

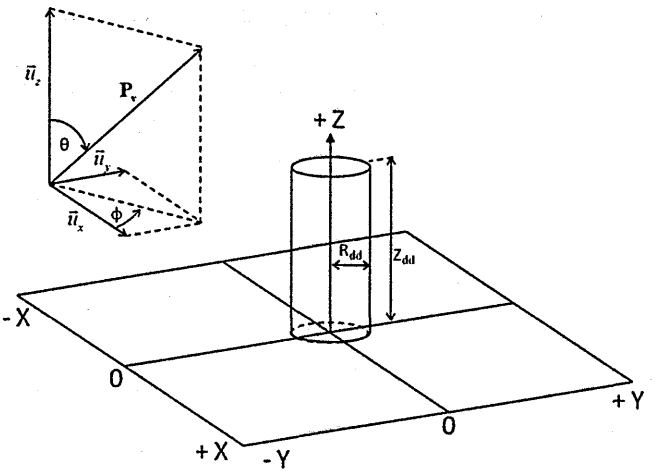

Figure 3-1: Global coordinate system of the MCLSM. (X_0, Y_0) is defined as the centre of the dust devil. Also shown is the decomposition of the photon vector P_v in to its direction cosines.

The quantities describing photon trajectories, for example, direction of travel after a scattering event and the path length between scattering events, may be considered random variables, with each being characterised by a probability density function (PDF) *P(x)*. The heart of the Monte Carlo method is sampling of these PDFs and is known as the 'Fundamental Principle'. For example, to sample the quantity x_i from *P(x)* the cumulative probability distribution (CPD) $\psi(x_i)$, which is the integral of *P(x)*, is inverted to give:

$$\psi(x_0) = \frac{\int_a^{x_0} P(x)\,dx}{\int_a^b P(x)\,dx} \tag{3.1}$$

As the variable x_i is integrated over a to b, $\psi(x_i)$ varies between 0 and 1, therefore to sample the variable x_i a random number, ξ, is selected from a uniform distribution $0 \leq \xi \leq 1$ and Eq. (3.1) is inverted to find x_i. After applying the fundamental principle, the τ travelled by a photon is given by:

$$\tau = -\ln(1-\xi) \tag{3.2}$$

τ is related to the optical free path, S, and is calculated from:

$$S = \tau \frac{L}{k_{\text{ext}}} \tag{3.3}$$

where k_{ext} is the extinction coefficient. The spatial co-ordinates (X, Y, Z) of the point where the photon interacts with a dust particle can be determined from:

$$X = X_0 + Su_{x0} \tag{3.4}$$

$$Y = Y_0 + Su_{y0} \tag{3.5}$$

$$Z = Z_0 + Su_{z0} \tag{3.6}$$

where (X_0, Y_0, Z_0) and (u_{x0}, u_{y0}, u_{z0}) are the previous positions and direction cosines of the photons respectively and τ through the dust devil is defined by:

$$\tau = C_{ext} NL \tag{3.7}$$

where C_{ext} is the extinction cross-section of the particle, N is the dust concentration (number of particles / m^{-3}) and L is the path length (m) through the dust devil. The product $C_{ext}N$ is defined as the extinction coefficient (k_{ext}) which is a measure of the extinction per unit length (m^{-1}) and is used in the model to describe heterogeneities in the dust distribution.

3.1.2 Dust scattering and absorption

For each photon-dust particle interaction there is a chance that the photon will either scatter or be absorbed by the dust grain. The probability of an absorption event occurring is governed by ω_0 and is equal to (1- ω_0). For each interaction a random real number between 0 and 1 is generated and absorption occurs if the random number is greater than ω_0, otherwise the photon scatters. Two methods can be used to describe the absorption by dust particles (Whitney, 2011). The first method removes the photon from the system if an absorption event occurs; the second

incrementally reduces the photon weight by a factor of (1- ω_0). Both methods were applied in the model, though the second method processed scattering events and tracked photons with small weights, significantly increasing the simulation run-time. Due to computational constraints, long run-times were undesirable as this limited the overall number of photons that could be injected into the model volume. The difference in the number of photons detected between the two methods was two orders of magnitude lower than the photon count, therefore the removal method was applied.

If scattering occurs, the angle through which a photon scatters is determined by the phase function of the dust grains. The model has the capability of using both the single and three parameter analytical Henyey-Greenstein phase function (Cashwell and Everett, 1959, Witt, 1977) and phase functions produced by semi-empirical codes used to model spherical particles (Mie theory) and non-spherical particles (T-matrix and Discrete Diploe Approximation). The Henyey-Greenstein parameter description of the phase function is given by:

$$\phi(\mu, g) = \left[\left(1-g^2\right)/4\pi\right]\left(1+g^2-2g\mu\right)^{-\frac{3}{2}} \tag{3.8}$$

Here, $\mu = \cos\Theta$ and Θ is the scattering angle measured with respect to the original photon direction and g is the asymmetry parameter. Using Eq. (3.8) it is possible to produce phase functions ranging from completely forward scattering to completely backward scattering. However, the Henyey-Greenstein function does not allow simultaneous forward and backward scattering lobes which are characteristic of many cases of particulate scattering. To remedy this, a three parameter form of Eq. (3.8) was also incorporated into the model and is the result of the superposition of two Henyey-Greenstein phase functions (Cashwell and Everett, 1959):

$$\phi(\mu, g_1, g_2) = f\phi(\mu, g_1) + (1-f)\phi(\mu, g_2) \tag{3.9}$$

Both functions have the form of Eq. (3.8) and f is a characteristic number between 0 and 1 which describes the proportion of light scattered in the forward and backward directions. Following the methods of Witt (1977) the scattering angle for each scattered photon is found by

setting a number variable equal to the integral of the phase function. After integration the cosine angle (μ) is related to random number κ by:

$$\mu = \frac{\left\{\left(1+g^2\right)-\left[\left(1-g^2\right)/\left(1-g+2g\kappa\right)\right]^2\right\}}{2g} \tag{3.10}$$

Witt (1977) also provides an expression relating μ and κ for the three parameter analytical phase function which is used to supply the model with a table relating μ over the interval -1 to 1 to κ over the range 0 to 1. Thus scattering angles are found by generating random numbers between 0 and 1, equal to the number of scattering events, and interpolated to find the corresponding scattering angle. The assumption of randomly orientated dust particles makes the scattering phase function independent of the scattering azimuth angle (ϕ_s). Thus ϕ_s is determined using:

$$\phi_s = 2\pi\xi_2 \tag{3.11}$$

where ξ_2 is a random number from a uniform distribution in the range $0 < \xi_2 < 1$ and ϕ_s varies from 0 to 2π.

3.1.3 *Directional change and photon classification*

The scattering angle, Θ, and scattering azimuth angle, ϕ_s, are determined in the particle reference frame and must be transformed to the global frame coordinate system. The equations of transformation from the old direction cosines to the new directional cosines are defined as:

$$u_x = \sin(\theta)\frac{\left(u_{x0}u_{z0}\cos(\phi_s)-u_{y0}\sin(\phi_s)\right)}{\left(1-u_{z0}^2\right)^{1/2}}+u_{x0}\cos(\theta) \tag{3.12}$$

$$u_y = \sin(\theta)\frac{\left(u_{y0}u_{z0}\cos(\phi_s)+u_{x0}\sin(\phi_s)\right)}{\left(1-u_{z0}^2\right)^{1/2}}+u_{y0}\cos(\theta) \tag{3.13}$$

$$u_z = -\sin(\theta)\cos(\phi_s)\left(1-u_{z0}^2\right)^{1/2}+u_{z0}\cos(\phi_s) \tag{3.14}$$

As $u_{z0} \rightarrow 1$ ($u_{z0} \geq 0.999$) these equations break down resulting in the need to replace them with:

$$u_x = \sin(\theta)\cos(\phi) \tag{3.15}$$

$$u_y = \sin(\theta)\sin(\phi) \tag{3.16}$$

$$u_z = \cos(\theta)u_{z0} \tag{3.17}$$

After each photon–particle interaction photons remaining in the simulated dust devil are carried forward in the model, with the photon behaviour after subsequent scattering events simulated by repeating the above procedure. From here the term *scattering cycle* refers to one pass through the model, *i.e.* one scattering event. Photons that are outside the vortex and are travelling parallel to or away from the simulated desert floor ($Z = 0$) are removed from the simulation. If the photons are outside the dust devil and travelling toward the desert floor, the interaction point of the line joining the photon along its trajectory and the desert floor is computed before being removed.

3.1.4 Spatial variation in dust distribution

The equations described in Witt (1977) and Whitney (2011) require the assumption of a uniform dust distribution within the dust devil. However, for intense vortices this is a poor approximation, with the majority of the dust entrained in the 'wall' of the vortex which surrounds a central core of significantly lower N (Sinclair, 1973). The non-uniformity in N was modelled as a concentric ring of high k_{ext} around a central cylinder of lower k_{ext}. The cylinders are approximated using the integer grid approximation, creating a uniform grid over the model X-Y plane. To find the distance travelled by a photon within the dust devil, knowledge of the cumulative optical depth (τ_c) in front of the photon direction of travel is required. Lookup tables of τ_c relative to the centre of the vortex are generated for an observer looking along the Y-direction (the X-axis could also have been used since the dust devil is assumed to be a circle

in the *X-Y* plane). The generated τ_c lookup table is required to generate a second lookup table relating τ_c to a distance travelled down each grid path.

Relating the distance travelled by the photon in any given direction to τ requires transformation of the photon *(X,Y)* coordinate and vector (u_x, u_y, u_z) onto the Cartesian coordinates of the τ_c grid, (X',Y') and (u_x',u_y',u_z'), such that the photon direction vector (P_v) is parallel to the $Y'-$axis (*i.e.* $u_x' = 0$). The transformation is illustrated in Figure 3-2 with a photon travelling along vector 1 (dashed line) being equivalent to a photon travelling along vector 2 (solid line). The transformation allows all the photons within the simulation to be placed on a uniform grid for interpolation. The transformation is performed over the individual photon locations and cosines instead of the τ_c grid as this allowed simultaneous calculations over many photons, reducing the computation time. The optical depth associated with the (X',Y') position in the τ_c grid is found by interpolating over the τ_c table. The randomly produced τ is then added or subtracted from this value depending on the direction of travel (*i.e.* the sign of u_y'), with the resulting τ and Y' position interpolated onto the distance lookup table to find the new position of the photon.

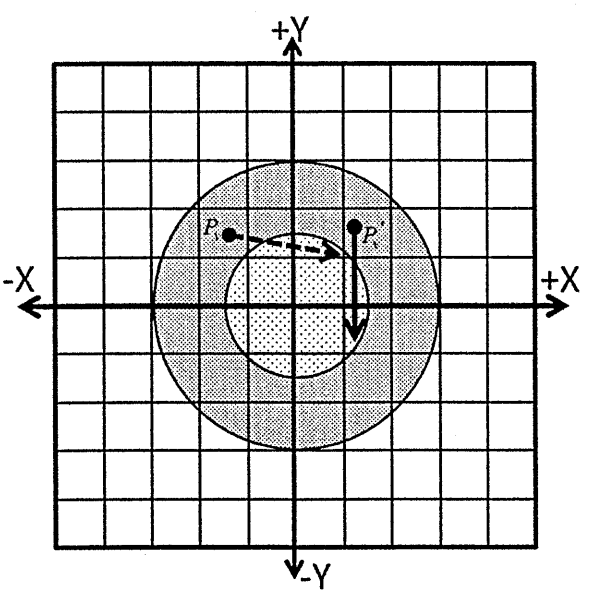

Figure 3-2: Rotation of a photon vector onto the τ_c grid.

The absolute difference between the photon's new distance and current distance is calculated to find the distance travelled in the *X-Y* plane and the new photon position is calculated by modifying the transformation equations defined by Cashwell and Everett (1959) for the *X-Y* plane. As $\sin\theta \rightarrow 0$ (*i.e.* a photon direction vector close to vertical) the transformation equations break down and it is assumed that the *X* and *Y* positions of the photons are unchanged for small $\sin\theta$ values since ΔX and ΔY tend to zero. The new *Z* position is determined from $Z = Z_0 + u_z \tau_c / k_{ext}$ where k_{ext} is determined by interpolation of the photon position on the k_{ext} lookup table.

3.1.5 Error analysis of coordinate system transformation

The large numerical arrays used in the model resulted in the use of single numerical precision for the cosine, sine and interpolation due to memory limitations. This resulted in errors in the photon optical free path and final position at the observation point. To characterise the magnitude of these errors on the final output of the model, the errors at key stages in the model were analysed. Considering the case of no errors, after rotation the photon vectors align vertically on the τ_c grid, giving a value of 0 for the rotated directional cosine, u_{Rx}. Hence the original X' position and the new photon position (X'') in the τ_c grid will be equal. The introduction of errors in the rotation angle results in a departure from the perfect case and $X' \neq X''$. Fifty batches of 10^7 photons (a practical limitation) were injected into the system and the ΔX_R was computed. Of the photons injected, 99% experience a displacement in $X_{RI} < 1\times10^{-5}$ m with the remaining 1% having an error on the order of 10^{-4} m. The impact of the rotation errors on the new (*X, Y, Z*) coordinates of the photons is small with > 85% of all photon interactions having a ΔX between 1×10^{-4} and 1×10^{-5} m, a ΔY between 1×10^{-5} and 1×10^{-6} m. Approximately 99% of the photons had a ΔZ of less than 1×10^{-4} m. A small fraction of the photon interactions have larger positional differences with approximately 0.6% and 0.006% of the interactions exhibiting a ΔZ of 0.001 m and 0.01 m respectively, while one in every two million photons had a ΔZ of approximately 0.1 m. The larger errors are associated with the error

due to the calculation of the new directional cosines at small angles and the new Z position calculated with a division by sin θ. The above analysis demonstrates that the errors introduced by coordinate transformation are negligible. The $\sqrt{N}$ error for the simulations performed was determined to be 1.0%.

3.2 Dust devil simulations

In this section idealised dust devils of different τ are modelled to assess what effect the quantity of dust has on the photon propagation. For these simulations the composition and size of the suspended dust is assumed to be constant, *i.e.* C_{ext} is constant. A second set of simulations investigates the effect of different single scattering properties on the photon propagation with N held constant.

3.2.1 Model parameters

The MCLSM requires specification of: solar zenith angle (θ_z), dust devil height (Z_{dd}), dust devil radius (R_{dd}), location of the point of measurement (PoM), optical properties of the dust entrained in the vortex, the detection plane height (set to the height of the PoM above the surface) and the interpolation lookup tables. Two scenarios are presented; the first assumes the full sky irradiance (FS) is measured by the detector (*i.e.* half-angle field of view, FoV, is equal to 90°) and the second applies a narrow view (NV) such that the solar disc does not enter the detector FoV, meaning that only scattered light is detected. For all simulations in this section, θ_z was held constant at 13.5°, which corresponds to the maximum solar elevation angle before the solar disc enters the FoV in the NV case, assumed to be 12.7°. The dust particle scattering phase function was described by the Henyey-Greenstein approximation.

3.2.2 Photon propagation

Photons are injected into the model volume at random locations. The initial positions of the photons for the FS model are found by generating random numbers so that the photons are

positioned in the *X-Y* plane at the height of the dust devil. The NV case resulted in significantly fewer photons being detected since only scattered photons are detected. To increase the photon density, only photons that intersect the vortex are considered. Increasing the number of photons injected into the system was not a practical solution due to the available computing resources. The initial positions of the photons are randomised on the illuminated edge, described as the Sun-facing edge, by randomly selecting $-R_{dd} \leq Y \leq R_{dd}$ and $0 \leq Z \leq Z_{dd}$, The X position is then determined using Pythagoras' theorem. The photons propagate forward in the model until all photons are either detected or move outside the model volume.

Figure 3-3 shows the propagation of the photon in the *X-Y* plane after one and four consecutive scattering events for a dust devil with a large N in the wall ($k_{ext} = 0.5$ m^{-1}) and a dust devil with small N in the wall ($k_{ext} = 0.05$ m^{-1}). In both scenarios a dust-free core is assumed and the dust devil is assumed to have a core and outer radius of 3.0 m and 6.0 m respectively. The Sun is positioned on the left and the initial vector of the photons is in the $+X$ direction. The black dots mark the positions where the active photons interact with a dust particle only (photons which travelled outside the model volume or were detected on the previous cycle are not shown in consecutive figures). The simulations show what effect varying the dust concentration has on the propagation of the photons through the vortex. After the first cycle the high opacity case shows that the majority of the photons will interact with a dust particle close to the inside edge of the illuminated wall or on the inside edge of the non-illuminated wall. In contrast, after one scattering event the dust devil with small N in the wall has a much more uniform distribution with a significantly higher portion of the photons passing directly through without interacting. As more cycles are performed the photons migrate towards the non-illuminated side. However, this process is 'slower' at large N as a result of the higher probability of photon–dust particle interaction, with the majority of the photon-dust particle interactions still occurring in the illuminated wall and near the core on the non-illuminated wall after four scattering events. At small N the propagation is more clearly seen and after the same number of scattering events the number of photons present inside the vortex is significantly

reduced, with their positions being nearly uniform, albeit with a slight bias towards the non-illuminated edge.

The results of the simulations are physically realistic. The optical free path of the photons is inversely proportional to k_{ext} and from Eq. (3.7) assuming the dust composition constant, the optical free path is also inversely proportional to N. Thus as N increases the photons will travel a shorter distance before interacting with dust particles. This explains the slower migration of the photons from the illuminated wall to the non-illuminated wall in the high τ case compared to the low τ case.

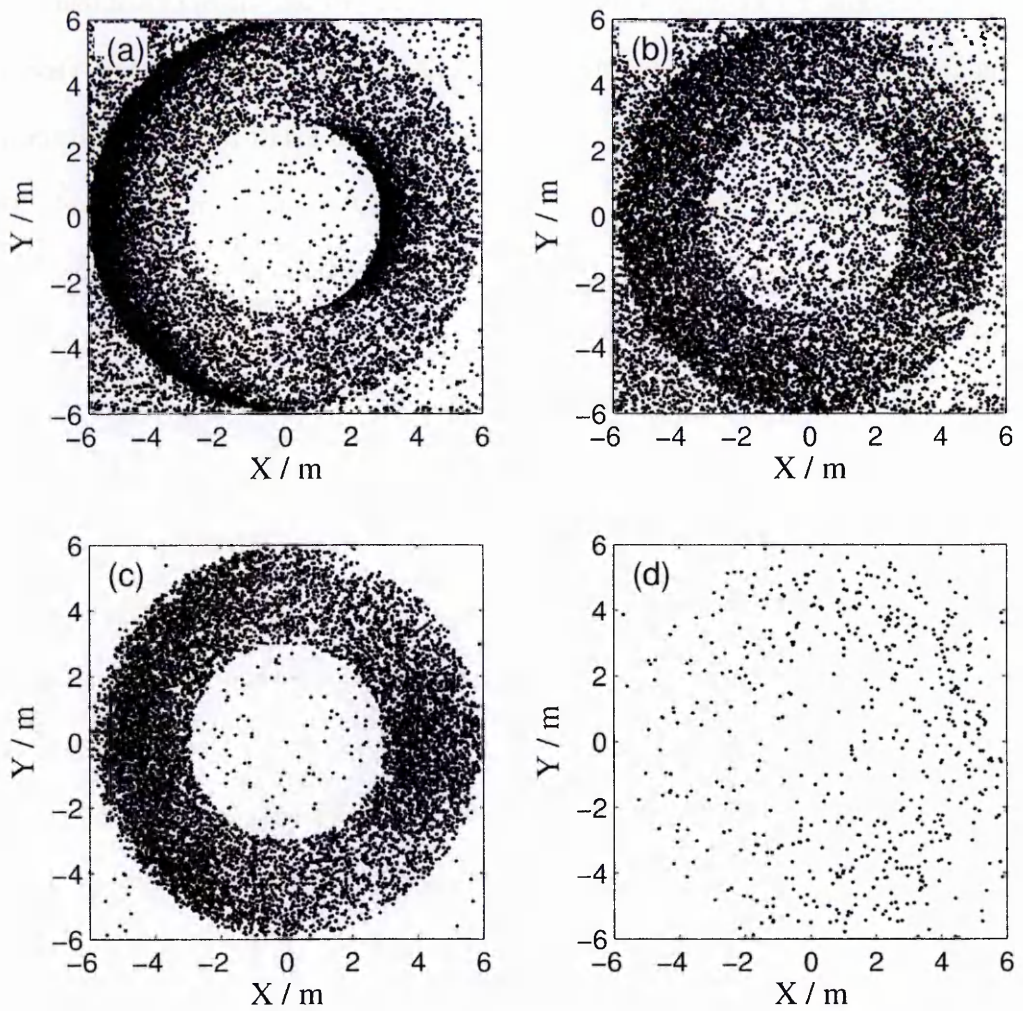

Figure 3-3: The photon positions after one scattering event in a dust devil of (a) high and (b) low dust concentration, and after four scattering events, (c) high and (d) low dust concentration.

To illustrate the effect of changes in the scattering nature of the dust particles on the photon propagation, g was assigned values of 0.70, 0.80, 0.90 and 0.98. The NV model was used for a dust devil with $\tau = 0.6$. The position of the photons after six scattering events is shown in Figure 3-4 for $g = 0.70$ and 0.98. As Figure 3-4 illustrates, for lower values of g, the location where the photons cross the detector plane is more uniformly spread around the vortex. At high g values, the positions where the photons cross the detector plane are highly concentrated in the $+X$ plane and cover an area only slightly larger than the dust devil radius. This result is expected, since as $g \rightarrow 0$ the photon scattering will tend towards isotropic resulting, in a more uniform distribution of photons around the vortex. As $g \rightarrow 1$ the photons will scatter more favourably in the forward direction and the positions where the photons cross the detector plane will be concentrated on the opposite side ($+X$) from where they enter ($-X$).

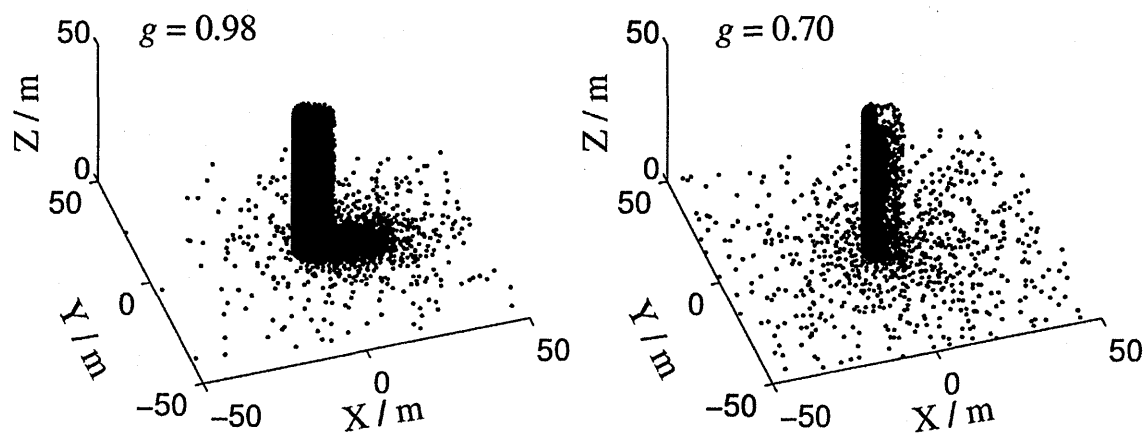

Figure 3-4: Photon positions after six scattering events for: (a) $g = 0.98$ and (b) $g = 0.7$.

3.3 Simulated dust devil transits

The simulations assume a sky that is free of dust and clouds and therefore the direct component forms the majority of the total surface irradiance. The FS case will detect photons which pass directly through the dust without interaction (direct component) and also any photon scattered onto the PoM (scattered component). Since the direct component will comprise the majority of the combined signal as a dust devil transits across the PoM the light received decreases by a

factor of $\exp[-k_{ext}L]$, where L is the path length through the dust. The scattered component increases during the transit, though the increase is small in comparison to the decrease in the direct component. In contrast, when a dust devil transits in the NV case an increase in light should be observed. This is because the FoV in the NV case precludes detection of the direct component and therefore only the scattered component is detected, which increases as N (hence k_{ext}) increases resulting in a net increase in signal over the ambient signal. Figure 3-5 shows the number of photons detected over the model surface for both FoV cases for a dust devil with $R_{dd} = 2$ m and $\tau = 0.6$.

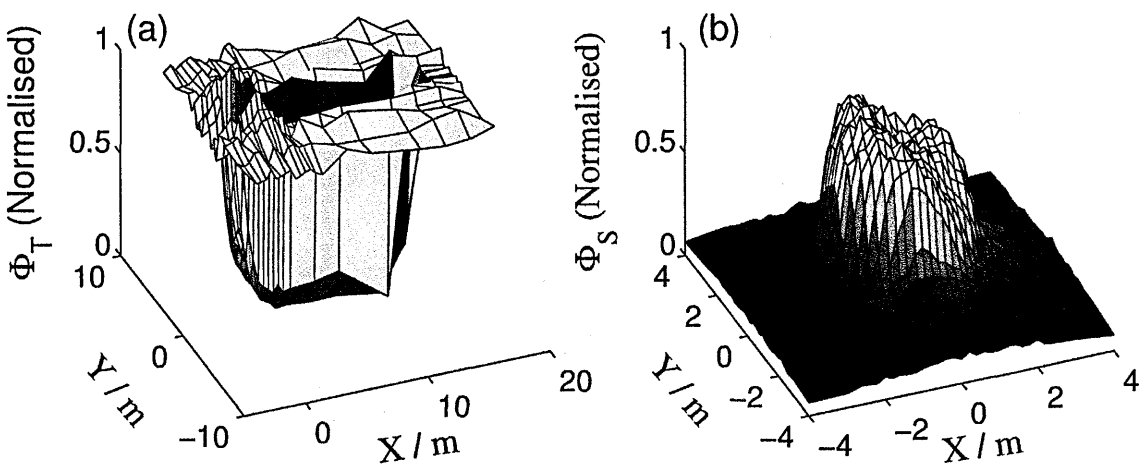

Figure 3-5: Φ_T and Φ_S during a transit of a dust devil with $R_{dd} = 2$ m and $\tau_c = 0.6$ for: (a) NV case and (b) FS case.

In the following sections a transit of a dust devil moving in the $-X$ direction is simulated for $\tau = 0.15$, 0.3, 0.6, 0.9, 1.2, 1.6 and 2.0. For a uniform dust devil with $R_{dd} = 2$ m this results in k_{ext} of 0.0375, 0.075, 0.15, 0.225, 0.3, 0.4 and 0.5 m^{-1} respectively. Note that since the dust devil size and dust composition is fixed the quantity being varied is the dust concentration. For the non–uniform dust devils three scenarios were considered: the first assumes 1/4 of the total dust is in the core with the remainder in the wall. The second and third assume 1/3 and 2/5 of the dust is present in the core leaving 2/3 and 3/5 of the dust in the wall respectively. Table 3-1

provides k_{ext} for each scenario for a non–uniform dust devil with a core radius of 1 m and the same outer radius as the uniform dust devil.

	k_{ext} / m^{-1}					
	Scenario 1		**Scenario 2**		**Scenario 3**	
Dust optical depth	Core	Wall	Core	Wall	Core	Wall
0.15	0.019	0.056	0.025	0.050	0.030	0.045
0.3	0.038	0.113	0.050	0.100	0.060	0.090
0.6	0.075	0.225	0.100	0.200	0.120	0.180
0.9	0.113	0.338	0.150	0.300	0.180	0.270
1.2	0.150	0.450	0.200	0.400	0.240	0.360
1.6	0.200	0.600	0.267	0.533	0.320	0.480
2.0	0.250	0.750	0.333	0.667	0.400	0.600

Table 3-1: The k_{ext} in the core and walls for non-uniform dust devils under the different scenarios considered for each τ.

3.3.1 Effect of dust loading

The transit of a dust devil with the parameters of Scenario 1 is used to investigate the effect of increasing dust loads, Figure 3-6. From examination of the simulated dust devil transits we would expect a dust devil of high dust loading, for the NV case, to be characterised by a significant increase in the scattered light (Φ_S) as the illuminated edge passes over. This would be followed by a sharp decrease in Φ_S through the core and non–illuminated wall. For the dust concentrations considered, Φ_S is approximately 150 and 300% greater in the illuminated wall compared to the dust devil core and non-illuminated wall respectively. Smaller N results in fewer photon–particle interactions, lowering the probability of scattering into the PoM, causing Φ_S in the illuminated wall to decrease. The longer optical free path for small N allows more photons to penetrate into the core and opposite wall and correspondingly Φ_S in the core and non-illuminated wall increases. For vortices with a τ of 0.15 and 0.3, the optical free path far exceeds

the diameter of the dust devil; as a result Φ_S rapidly decreases with ~70 % less light detected in the core for a dust devil with $\tau = 0.15$ compared to vortices with $\tau = 0.6$. At these small values of N the internal distribution of dust becomes important. The uniform case shows a peak in Φ_S at the dust devil centre, while the more heterogeneous dust devils (Scenario 1) show a maximum in detected light near the core–wall boundary of the illuminated and non-illuminated wall, with less scattered light detected in the core.

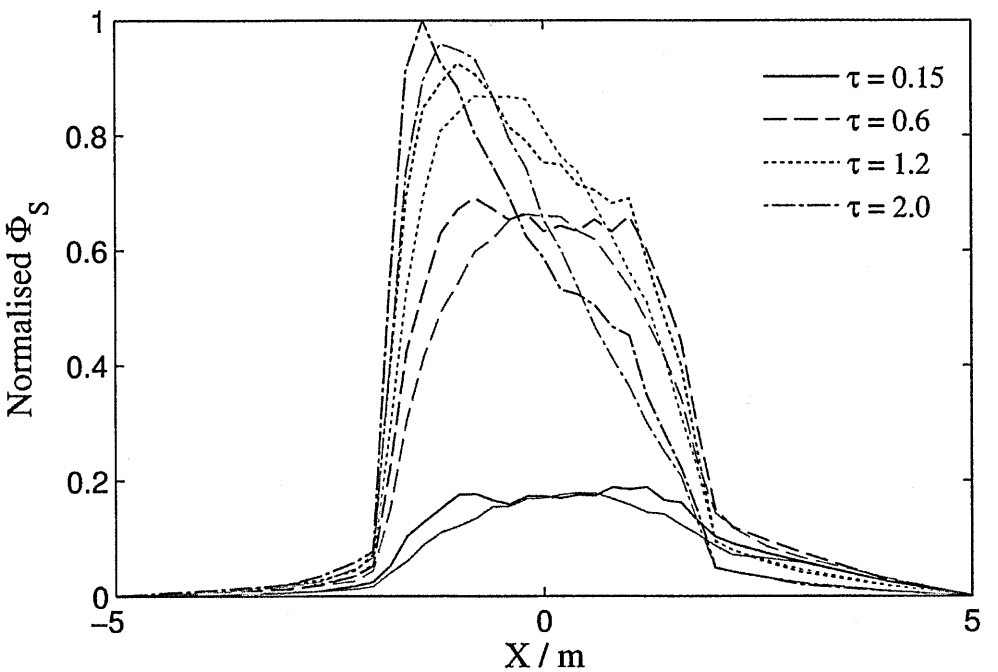

Figure 3-6: NV dust devil transits from Scenario 1 (black lines) and uniform Scenario (grey lines) for different τ.

The total light (Φ_T) transit signatures can generally be characterised by a reduction in Φ_T as the vortex passes over the PoM. When $k_{ext} > 0.24$ m^{-1} in the wall there is an increase in Φ_T as the dust devil approaches the PoM. A peak in Φ_T is observed just inside the illuminated wall, X = -1.8 m, with high τ dust devils showing a 10% increase in Φ_T. Further into the vortex Φ_T decreases depending on τ, with low τ showing a more gradual decline between X = -1.8 m and X = 1.0 compared to high τ. As the PoM passes through the core a slight change in the Φ_T gradient is observed at large N in the heterogeneous dust devils which is not observed in the uniform case. Upon exiting the dust devil the Φ_T gradient reduces significantly and Φ_T reduces

gradually to a minimum at $X \approx 14.0$ m before increasing back to the ambient illumination. This result is significant as it shows that for dust devil transits with this geometry (vortices moving directly towards or away from the Sun) the position of lowest Φ_T does not correlate with the portion of the transit signature associated with the centre of the dust devil but to the location on the surface where τ along the photon incident path is at a maximum. This occurs at the point where the line joining the PoM to the Sun has the longest path length through the dust devil.

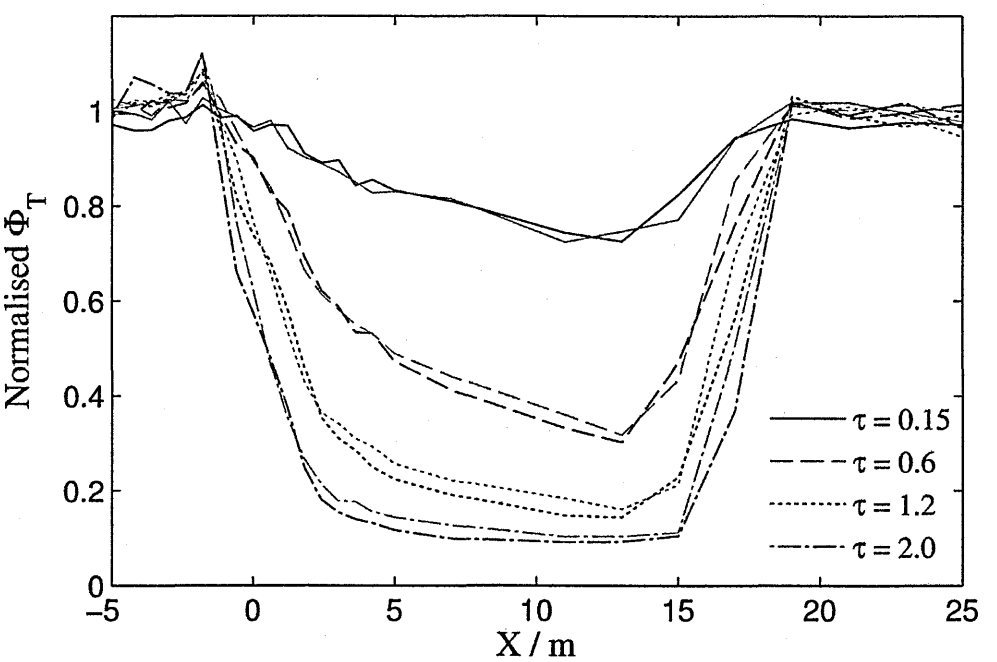

Figure 3-7: As fig.6, but showing the FS simulated transits.

3.3.2 Effect of dust distribution

To determine the effect of varying internal dust distributions on the transit signature, the observed Φ_S in the core and non–illuminated wall relative to the illuminated wall was plotted as a function of dust devil uniformity, defined as the ratio of the core dust concentration to the dust concentration present in the walls, N_{core} / N_{wall}. Figure 3-8 shows that for small N, Φ_S in the dust devil core is strongly dependent on the internal dust distribution. A dust devil with $\tau = 0.15$ and a core dust concentration 1/3 of the wall results in an increase in Φ_S of ~35 % in the core relative to the illuminated wall. As the dust devil becomes more uniform Φ_S in the core

increases, with almost twice the scattered light observed relative to the illuminated wall for the uniform case. At τ = 1.2 the dust concentration in the dust devil walls for Scenario 1 and 2 results in the optical free path of the photons being less than the width of the walls resulting in Scenarios 1 and 2 experiencing a decrease in Φ_S of ~10 and 2% respectively relative to the illuminated wall. Dust distributions with a higher degree of homogeneity (Scenario 3 and the uniform case) predict a 2% and 16% increase in Φ_S entering the PoM at the core than in the illuminated wall. This indicates that the different internal dust distributions will result in very different transit signatures, with Scenario 1 and 2 showing an increase in Φ_S in the illuminated wall over the core while the more uniform dust devils will display a lower Φ_S in the illuminated wall relative to the core. As the dust concentration increases, heterogeneities in the internal dust distribution become less important. At τ = 2.0, Scenario 1 and the uniform case predict ~40% and ~30% less scattered light in the core respectively. The scattered light in the non–illuminated wall relative to the illuminated wall showed little dependence on the internal dust distribution, with the relative Φ_S constant for all internal dust distributions considered.

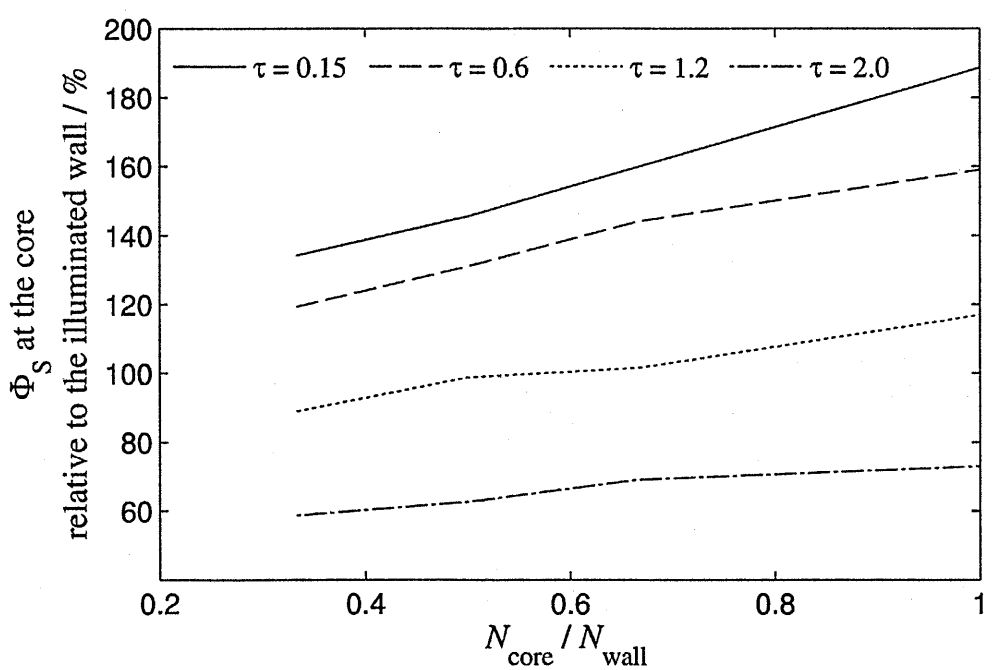

Figure 3-8: The observed Φ_S in the core relative to the illuminated wall as a function of the N_{core} / N_{wall}.

The FS simulations showed the relative Φ_T to be approximately constant for all τ cases. This indicates the internal dust distribution will have an almost negligible effect on the transit signature of a dust devil transit when measuring Φ_T. The primary parameter governing the transit signature shape is the total amount of dust along the line joining the source to the detector. From the Beer-Lambert law the direct irradiance is a function of τ only for a fixed θ_z. Therefore the manner in which the dust is distributed with the dust devil will have no impact on the direct component if τ is fixed and the resulting small variations in the FS transit signatures are due only to the scattered component. This correlates with the assumption that the direct component forms the majority of the total surface irradiance during 'clear sky' conditions.

3.3.3 *Effect of core size*

To investigate different internal structures the dust devil core radius (R_{core}) was varied using values of 1/4, 1/2 and 3/4 of the R_{dd} to determine the effect of different core and wall thickness on Φ_S. This corresponds to a core radius of 0.5 m, 1.0 m and 1.5 m respectively for a dust devil with an R_{dd} of 2 m. The dust distribution defined in Scenario 2 was applied to dust devils with τ = 0.6 and 1.2.

The NV transits, Figure 3-9, reveal that Φ_S is highly dependent on the vortex core size. Since the quantity of dust in the two regions is held constant as the core volume is increased, N in the wall is enhanced while the core sees a reduction in N. Reducing the core diameter has the opposite effect, increasing and decreasing the wall and core volume, hence lowering and enhancing the dust concentration in two regions respectively. Looking at the transit of a dust devil with a core radius of 1.5 m and τ = 1.2, the signature shows a significant departure compared to the R_{core} = 1.0 m case and more closely resembles a high τ dust devil with an R_{dd} and R_{core} of 1.0 m and 2.0 m respectively (Figure 3-6). This is because N in the wall of the two dust devils lead to a similar k_{ext} of 0.8 m^{-1} and 0.67 m^{-1}. At τ = 0.6 the increased dust concentration in the wall results in a broadening of the uniform Φ_S in the dust devil interior and the appearance of two peaks in Φ_S at the outer edge of the illuminated and non–illuminated

walls. For both N, the transit signature of a dust devil with a small central core will have the signature of a peak in Φ_S at the dust devil centre similar to the transit by a uniform dust devil.

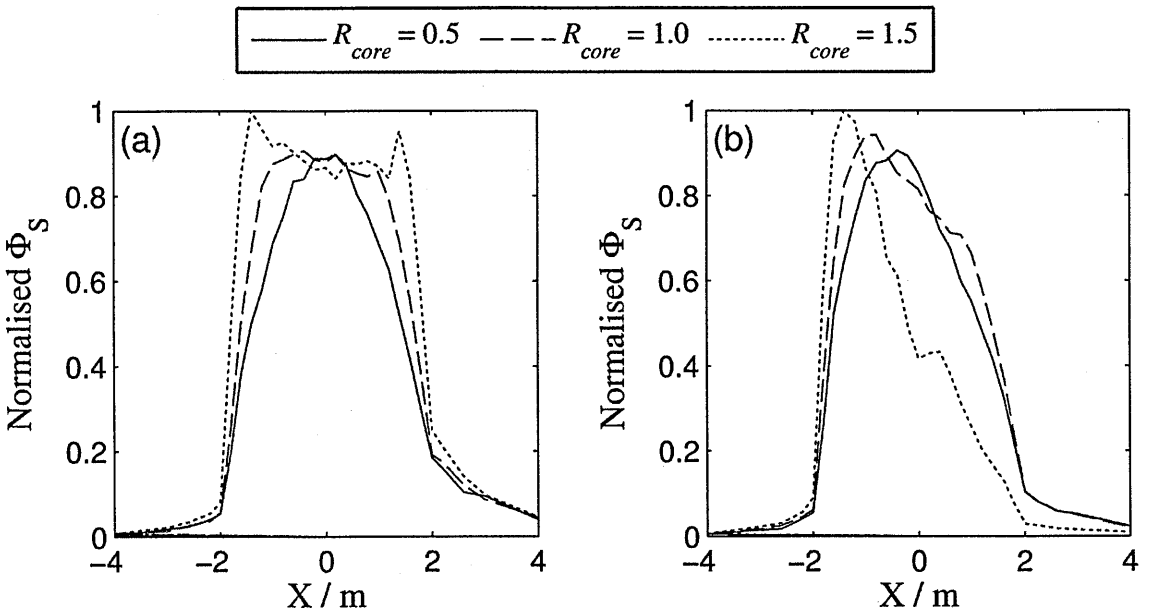

Figure 3-9: Transit signatures of dust devils with core radii of 0.5 m, 1.0 m and 1.5 m. The internal dust distribution from scenario 2 is used and the dust devils have a τ of (a) 0.6 and (b) 1.2.

The simulated transits show that Φ_S is strongly dependent on N in the vortex wall which is a function of τ, R_{dd}, R_{core} and also the internal dust distribution. Therefore, if both τ and the dust devil size are known, the transit signature will be able to give insight not only into the internal structure and dust distribution, but more importantly the dust concentration. For example, a large scattered component in the illuminated wall relative to the core is characteristic of a dust devil with large N in the vortex wall. This can be the result of a dust devil with a moderate dust loading and large internal core resulting in a small wall volume or by a vortex with a high dust loading and a small core but with the majority of the dust contained within the wall. If the scattered component is approximately uniform during the dust devil transit, this is an indication of small N throughout the vortex.

3.3.4 Effect of transit direction

The Φ_S and Φ_T over the NV and FS model surfaces, Figure 3-5, can be used to determine the transit signature for any dust devil bearing over the PoM by interpolating over this model surface. The bearing of the dust devil is defined here as the angle α_{dd} at which the PoM enters the vortex relative to the illuminated edge. A number of simulated dust devil transits were performed at different bearings to investigate the effect on Φ_S and Φ_T and the results are shown in Figure 3-10. All simulations in this section apply to a dust devil with R_{core} = 1 m and R_{dd} = 2 m with k_{ext} of 0.1 m^{-1} and 0.4 m^{-1} in the core and wall respectively. As illustrated for the NV case, the direction of travel over the PoM relative to the illuminated side can result in a significantly different transit signature, especially for large N in the dust devil wall. The signatures show Φ_S will be greatest if the PoM passes through the illuminated wall; therefore if the dust devil is moving away from the Sun (α_{dd} =180°) and the PoM enters from the non-illuminated side, the peak Φ_S will be observed in the trailing wall (*i.e.* after the decrease in pressure at the core). Alternatively if the dust devil is heading towards the Sun (α_{dd} = 0°) the leading edge wall will experience the greatest irradiance. As $\alpha_{dd} \rightarrow 90°$, Φ_S in the illuminated wall will decrease while Φ_S in the non-illuminated wall increases. At $\alpha_{dd} = 90°$, Φ_S is constant along the path through the core.

The FS model shows that the Φ_T transit signature is modified significantly by the bearing of the dust devil over the PoM. At large angles from the illuminated wall, the path length through the dust devil shadow decreases resulting in a reduction of the transit signature width. As a result, the location where Φ_T is smallest migrates towards the dust devil centre. As the bearing tends towards perpendicular, a noticeable change in the gradient is observed as the PoM approaches the core with Φ_T nearly constant until entering the trailing wall. A perpendicular transit of a non–uniform dust devil is characterised by the point of lowest Φ_T coinciding with the core–ward edge of the leading and trailing walls and an increase in Φ_T at the dust devil core. It should be noted that the symmetry of the perpendicular transit is an artefact of

the *X-Y* plane symmetry assumed in the model and such symmetry is unlikely to be measured in reality. The transit signature for dust devils with a bearing such that the PoM enters the non-illuminated side of the dust devil will be the reverse of the transits shown in Figure 3-10.

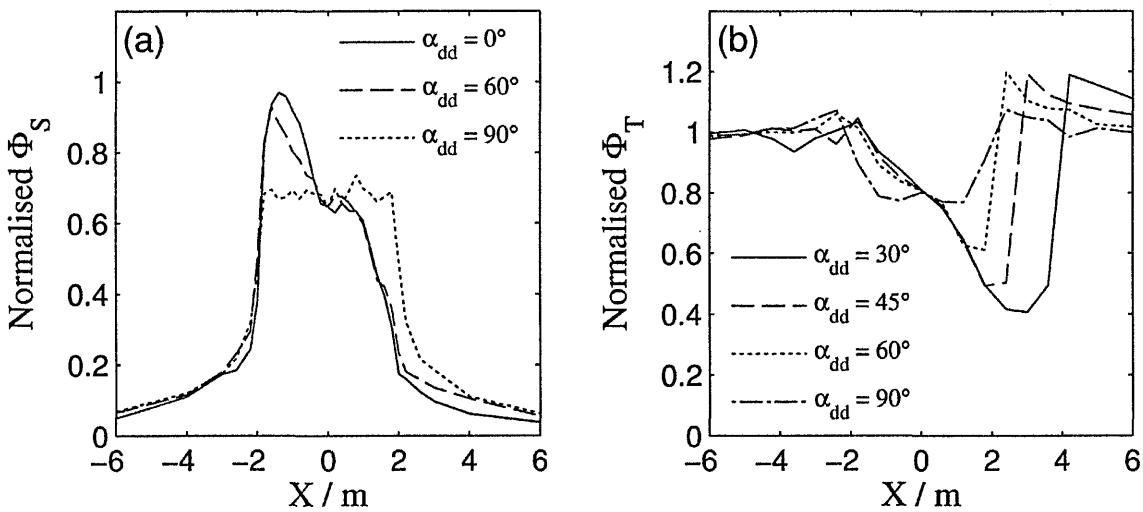

Figure 3-10: The variation in the dust devil transit signature for different trajectories over the PoM: (a) NV model (b) FS model.

3.3.5 *Effect of single scattering properties*

The optical properties of the dust particles entrained in the dust devil were varied to assess the sensitivity of the model to changes in the single scattering properties. Figure 3-11 shows a dust devil transit for both the NV and FS cases for changes in the g (with $\omega_0 = 0.95$ and the scattering phase function of the dust particle described by a Henyey-Greenstein phase function). A transit parallel and perpendicular to the *X*-axis is assumed for the NV and FS cases respectively. The FS case shows that Φ_T increases as $g \rightarrow 1$, whereas, an increase in Φ_S is observed for the NV case. The dependence on g can be explained by the scattering phase function; at high values of g the photons are scattered predominately at forward angles, therefore even though the photon has been scattered it will still be in the direct path to the PoM, and hence will be detected. As g decreases the probability of scattering away from the forward direction and out of the direct path increases; this results in fewer photons being detected. The reverse is true for the NV case where the photons must be scattered out of the direct path in order to be detected which has a lower probability of occurring at high g values. For the NV case, Figure 3-11a also reveals that

as g increases the measured scattered component in the non-illuminated side relative to the core increases. This is a result of more photons penetrating through to the non-illuminated side due to the higher probability of scattering at small angles. Similarly the opposite is true for the illuminated wall, where a decrease in Φ_S is observed for increased values of g.

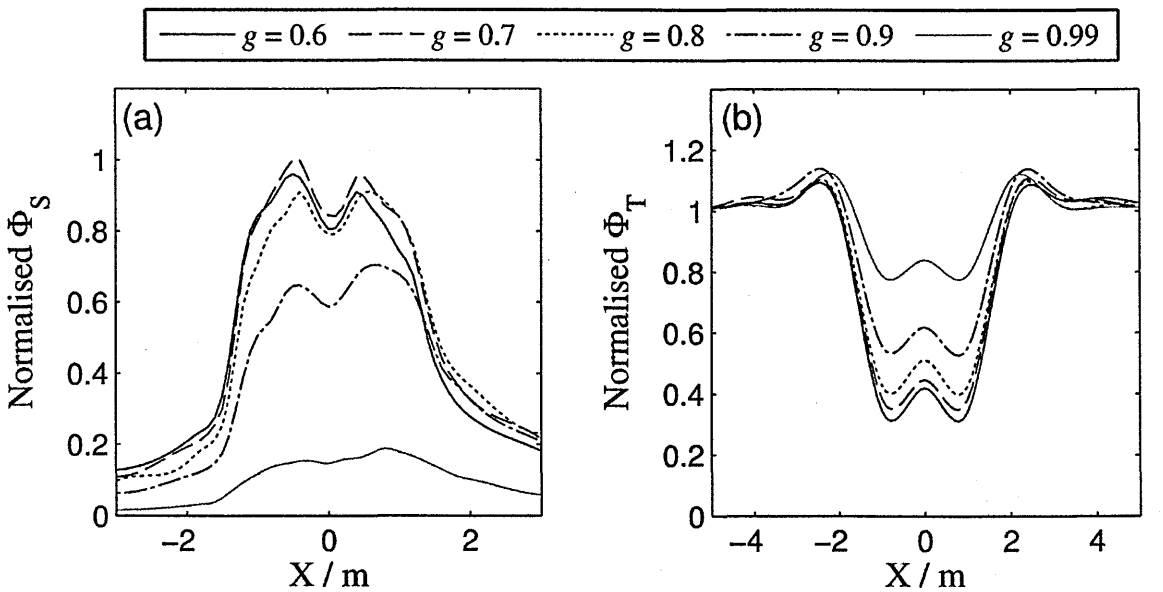

Figure 3-11: Transit of a dust devil moving along the X-axis for different values of g. ω_0 held constant at 0.95 (a) NV model, (b) FS model.

Unexpectedly, for the NV case, the maximum Φ_S does not correspond to the minimum value of g but occurs at $g = 0.73$. This can be explained by examining the effect increasing g has on the scattering phase function. For a solar elevation angle of 76.5° a photon needs to be scattered by an angle between approximately 5° and 30° in order to be detected given a field of view of 12.7°. The probability of scattering between these values decreases as $g \rightarrow 1$ as the favourable scattering angle approaches 0°. The maximum Φ_S occurs with $g = 0.73$, as it provides the photons the highest probability of scattering between 5° and 30°.

This indicates a bias effect associated with θ_z on the observed Φ_S for a given g value. At larger or smaller θ_z the angle through which the photons must be scattered in order to be detected will decrease and increase respectively. The implication is that as the Sun moves towards zenith the g value associated with the peak scattered component will increase as θ_z

decreases, since the angle through which the photons must be scattered in order to be detected approaches 0°. Conversely, as the Sun moves towards the horizon the g value will decrease accordingly. Figure 3-12 shows the number of photons detected for g values of 0.6, 0.7, 0.8, 0.9 and 0.98 for the NV case for different θ_z spanning 20 – 55°. As expected the largest scattered component correlates with the value of g that gives the photons the highest probability of scattering into the FoV. At $\theta_z = 40°$ the maximum scattered component is observed for dust particles with $g = 0.6$. As θ_z decreases, the g value associated with the highest scattered component correspondingly increases and at $\theta_z = 80°$ this correlates to $g = 0.98$. This leads to an important bias when interpreting data from potential observations and care is needed when attempting retrieval of the dust optical properties. The bias effect is not observed in the FS case as a result of the direct component forming the majority of the total illumination and reveals that the bias is limited to the scattered component.

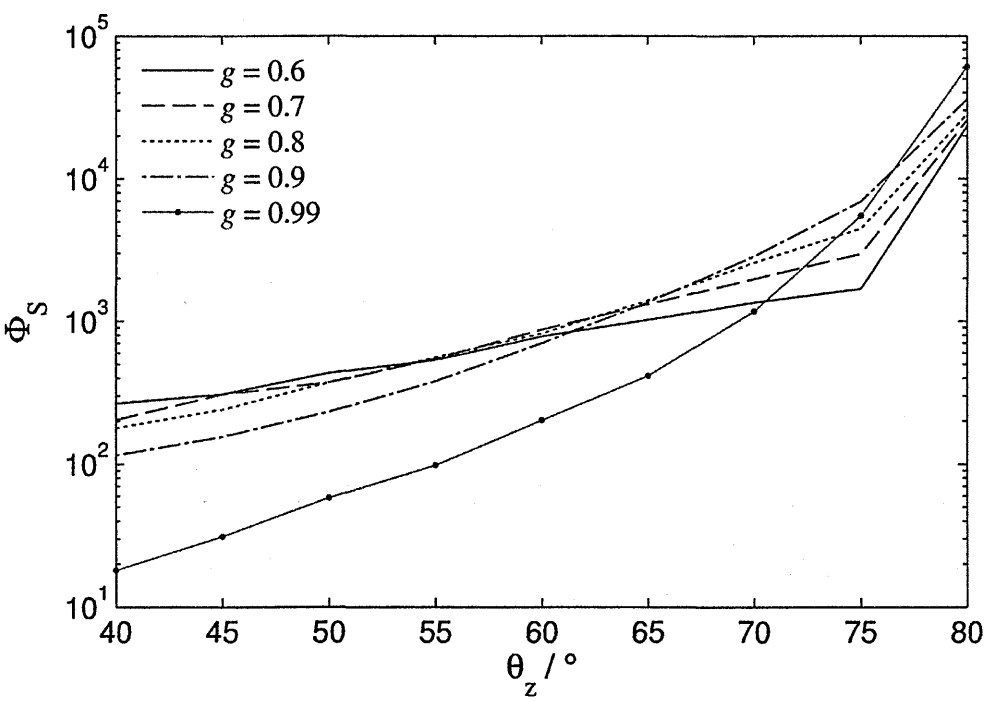

Figure 3-12: Number of scattered photons detected as a function of θ_z for dust components with different g.

The same transit was simulated for changes in ω_0, with g held constant at a value of 0.8 and the result is shown in Figure 3-13. Both the NV and FS simulations predict that smaller values of ω_0 result in lower Φ_T and Φ_S and correlates with a high attenuating dust component absorbing a larger portion of the incident light. At larger values of ω_0 the dust grains are less absorbing and more light is scattered, increasing the probability of detection, and correlates with a higher Φ_S and Φ_T.

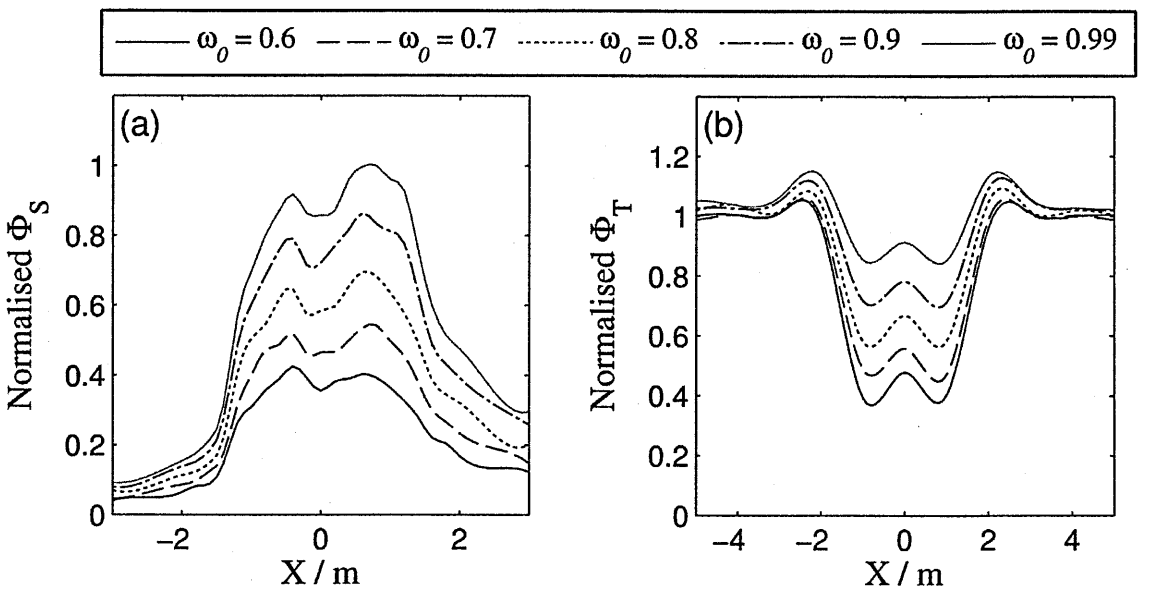

Figure 3-13: Transit of a dust devil moving along the X-axis for different ω_0 values with the asymmetry parameter held constant at 0.8: (a) NV model and (b) FS model.

3.4 Discussion of the MCLSM simulations

The most obvious difference between the FS and NV is the contrasting behaviour in the observed solar irradiance during the dust devil transit. In the NV case, assuming the Sun is not in the FoV, an overall increase in Φ_S is observed as a result of scattering. In the FS case, the Φ_T decreases during the transit since the loss of light from the direct component due to absorption and scattering by the dust particles is much larger than the gain from increased levels of scattering.

The NV simulations show that the measured scattered component inside a dust devil vortex is strongly dependent on the dust concentration distribution within the dust devil interior.

Importantly the dust concentration in the illuminated wall plays a significant role in determining the shape of the Φ_S transit signature, with large N being associated with a sharp increase in Φ_S as the PoM passes through the illuminated wall followed by significant decrease in Φ_S through the core and non-illuminated wall. When N is low enough to allow light to penetrate through to the core and non–illuminated wall, the dust concentration in these regions becomes more important. The implication of assuming a uniform dust distribution at low τ is an overestimation in the observed scattered component at the dust devil centre and an underestimation through both the illuminated and non-illuminated walls.

In the FS case, Φ_T transit signature shows a negligible dependence on the dust concentration and core size. This is because the direct component dominates the total illumination at the surface under 'clear sky' conditions.

The analysis into the variation in single scattering properties revealed that the value of the g that resulted in the largest Φ_S was dependent on θ_z, leading to a bias towards low g for high θ_z and $g \rightarrow 1$ for low θ_z. The same dependence was not observed when measuring Φ_T and implies that the θ_z bias is limited to the scattered component. This has important implications when attempting to retrieve the optical scattering properties as any attempt to determine g from narrow FoV observations will have to correct for this bias. Both Φ_S and Φ_T exhibit the same dependence on ω_0, with higher ω_0 corresponding to increased illumination.

The variation of light during a dust devil transit was investigated to determine whether the dust load, size and internal structure of the vortex could be estimated from a dust devil transit light signature. The implication of this work is that separate measurement of both the total *and* scattered light is crucial for characterising the distribution of dust within a dust devil by its transit signature. The total light observed provides information about the dust devil size and total amount of dust, while the scattered light gives details of the internal structure of the vortex. Variation in the dust particle single scattering properties were shown to modify significantly the amount of total and scattered light detected during the transit. These variations imply that the

transit signature of a dust devil passage will differ depending on the wavelength of observation and the properties of the suspended dust. Therefore by comparing the amount of scattered and total light observed during the transit at different wavelengths it is possible to determine single scattering properties of the dust.

Finally we conclude that *in situ* measurements of the optical signatures of transiting dust devils provide a powerful tool to characterise dust devils, including those on Mars, allowing for determination of their size, dust concentration, internal structure and dust distribution. Following the simulations presented here, the model could be validated by measuring terrestrial dust devil transits with visible spectrometers covering a spectral range of 300–800 nm. The nature of such measurements makes them an ideal technique to use on Mars, only requiring two upward viewing spectrometers of low complexity and mass. Measuring the wavelength dependent transit signatures of dust devils would provide a wealth of information on the characteristics of martian dust devils and the dust entrained within them.

Chapter Four: Spectral measurements of terrestrial dust devils

The Monte Carlo Light Scattering Model (MCLSM) discussed in the last chapter was applied to spectral measurements of terrestrial dust devils. The aim of the field work was to validate the MCLSM and whether dust devils could be characterised from their transit signature. The transit measurements also provided the opportunity to test whether the optical properties of the suspended dust particles could be retrieved from the attenuation of the solar spectrum during a dust devil transit.

The experiments were conducted in the Southern Nevada Desert (Eldorado Valley), in a closed playa basin outside Boulder City, U.S.A. The regional climate is arid and hot, with strong insolation and the conditions for dust devil formation occurring frequently. The basin itself is flat, hard and dry with regions of both fine and coarse material on the surface, making it ideal for vehicular activities, and covers an area of 13 km^2.

4.1 Experimental setup and execution

The instrumentation used for these experiments included a spectrometer, observing the ultraviolet and visible wavelength region (326–780 nm) and is referred to as (UV-VIS), pressure and temperature probes, a photodiode light sensor (Sun sensor) and a GPS receiver. The pressure, temperature and Sun sensor data form the 'PICO' dataset and are referred to as such from this point. The instrumentation had to be positioned in the path of the dust devils and, due to the unpredictable nature of dust devil formation, was required to be mobile. This was accomplished by setting up the instrumentation on the roof of a vehicle with the line of sight of the UV-VIS probe normal to the vehicle roof. The layout of the instrumentation used for these experiments is illustrated in Figure 4-1.

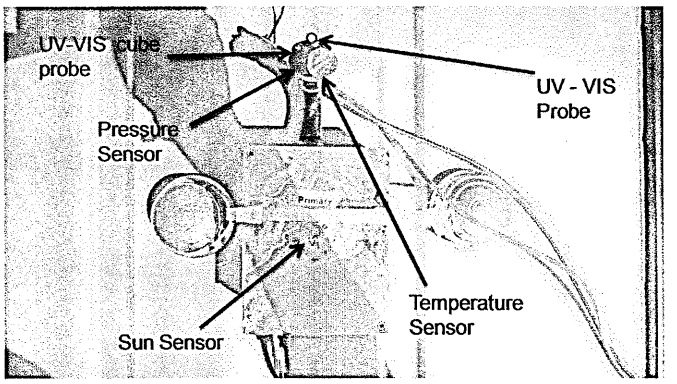

Figure 4-1: The experimental setup for the dust devil measurements.

The measurement process is illustrated in Figure 4-2. Two vehicles were used; the chase vehicle (with the instrumentation mounted on the roof) positioned itself in the path of the dust devil, while an orbital vehicle time-stamped and photographed the encounter to allow for visual referencing and comparison with the recorded data from the spectrometers. The GPS receiver recorded the time and position of each encounter. After each dust devil encounter, the chase vehicle remained stationary for an extended period of time to allow measurement of the incident (reference) spectrum once quiet conditions were restored. This was required for the retrieval of the dust single scattering properties.

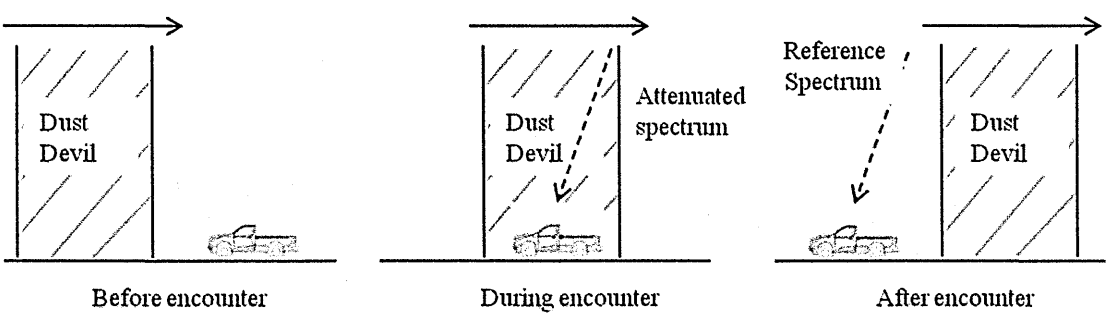

Figure 4-2: Illustration of the measurement process performed by the chase vehicle a) chase vehicle moves into the path of the dust devil b) the vehicle is stationary during the dust devil encounter c) the reference spectrum is obtained after the encounter.

The UV–VIS spectrometer used two different optical setups each with a different field of view (FoV). The first setup incorporated a diffuser attached to the end of the detector probe that allowed for measurement of the full sky irradiance (here on called FS, following the convention

in Chapter 3). The second optical setup was identical except the diffuser was removed, giving the UV-VIS spectrometer a narrower FoV (here on called NV, see Chapter 3). In the NV optical setup the optical fibre had a numerical aperture (dimensionless number that characterises the range of angles over which light can be detected) of 0.22. This resulted in the UV-VIS spectrometer having a FoV with a half angle of 12.7° projected from the probe aperture. Figure 4-3 illustrates the different fields of view for both optical setups and the angle, θ_d, defines the half angle of the UV-VIS FoV.

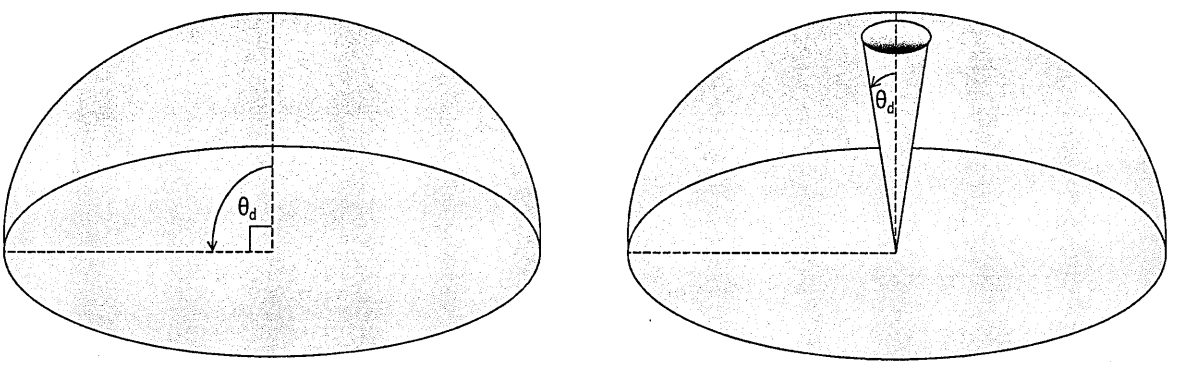

Figure 4-3: Diagrams showing the different viewing geometries for the two optical setups (a) full sky measurement and (b) narrow FoV observations.

The two optical setups allowed different components of the total surface irradiance to be measured. The FS setup measures both the diffuse 'scattered' component (light which reaches the detector that has undergone interactions with airborne dust particles) and the direct component (light which has not undergone interactions with the suspended dust). Reducing the detector FoV to a half angle of 12.7° prevented the detector from directly observing the solar disc in order to only measure the scattered component in the NV setup. It should be noted that the scattered component is defined as the amount of sunlight scattered from dust particles within the FoV of the NV setup and will be less than the total diffuse component measured by the FS setup.

4.2 Dust devil measurements

In total 78 encounters with dust devil vortices were recorded during the experimental campaign between the 20th and 25th of June 2009. The size of the vortices varied significantly, with diameters ranging from just a few metres to as large as twenty metres, and vortex heights varying from tens of metres to many hundreds of metres. Only a small proportion of the dust devil encounters were selected from each optical setup for further analysis. These are from June 21st (FS) and 23rd (NV) as both days had ideal atmospheric conditions: clear skies, low ambient wind speeds and strong insolation. On June 23rd only dust devils which occurred before 11 am and after 2 pm were considered. This was because between these times the solar elevation was such that part of the solar disc was directly in the FoV of the NV probe, resulting in saturation of the spectrometer. Simultaneous measurement of the total and scattering irradiance could not be achieved due to lack of available equipment. Another unexpected effect that restricted the number of dust devils available for analysis was interference from dust lifted by the chase vehicle. In the majority of the encounters this masked the dust devil transit. These criteria for the NV setup limited our analysis to one dust devil encounter for retrieval of its internal characteristics (dust distribution and core radius). The FS setup had fewer constraints and the dust optical properties for five dust devils were retrieved. The dust devils with the FS setup are label E1–E5 and the NV encounter is denoted by E6. Figure 4-4 illustrates the location of all the dust devil encounters on the 21st and 23rd which are shown in blue and red respectively.

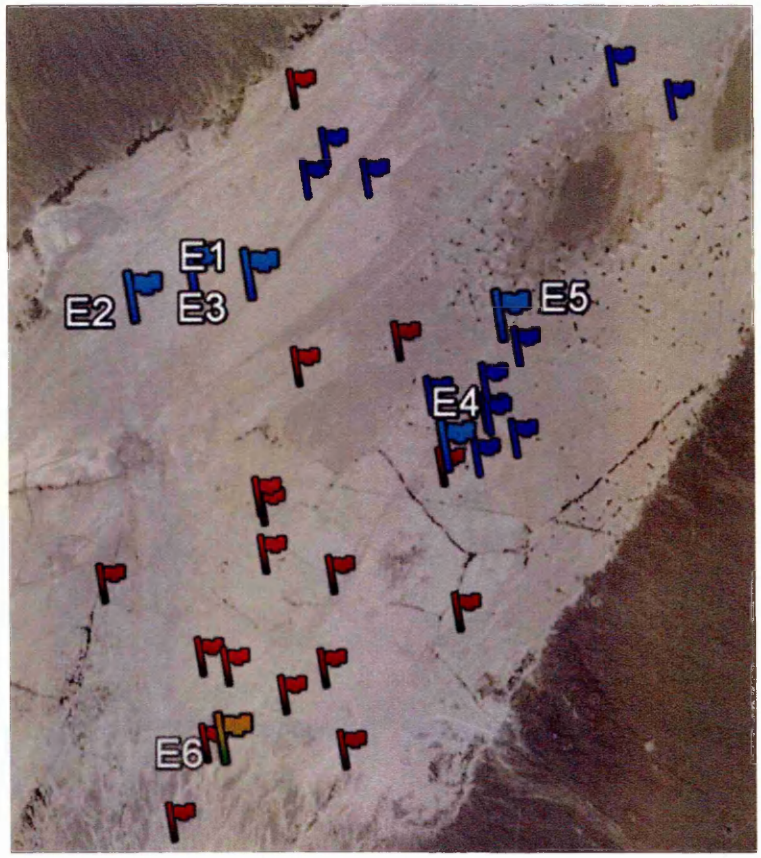

Figure 4-4: Location of the dust devil encounters considered for further analysis. The blue flags mark encounters on the 21st and the red flags for the 23rd. The light blue (21st) and orange (23rd) flags mark the dust devils analysed during this study.

4.2.1 Data reduction

Dust devil encounters are characterised in the dataset by a drop in pressure, a correlated increase in temperature and, following the results of Chapter 3, a decrease or increase in observed irradiance for the FS and NV setups respectively. The apparent transmission (T_a) describes the ratio of the reference irradiance to the irradiance measured during the transit. Since the measured irradiance during the dust devil encounter will contain scattered light, T_a is used to differentiate it from the true transmission. Figure 4-5 shows an example of a full dataset from the PICO and UV-VIS spectrometer for a given encounter, with T_a, from the UV-VIS, calculated at 386 nm. The dust devil transit corresponds to the reduction in T_a between 15 and 16 minutes. The motion of the chase vehicle, as it positioned itself in the path of the dust devil, caused 'noise' in the recorded data, with the spectrometer and pressure sensor being the most

affected. The similarity between the motion variations and a dust devil encounter highlights the importance of accurately time-stamping each encounter and carefully correlating between drops in pressure and variations in the observed irradiance.

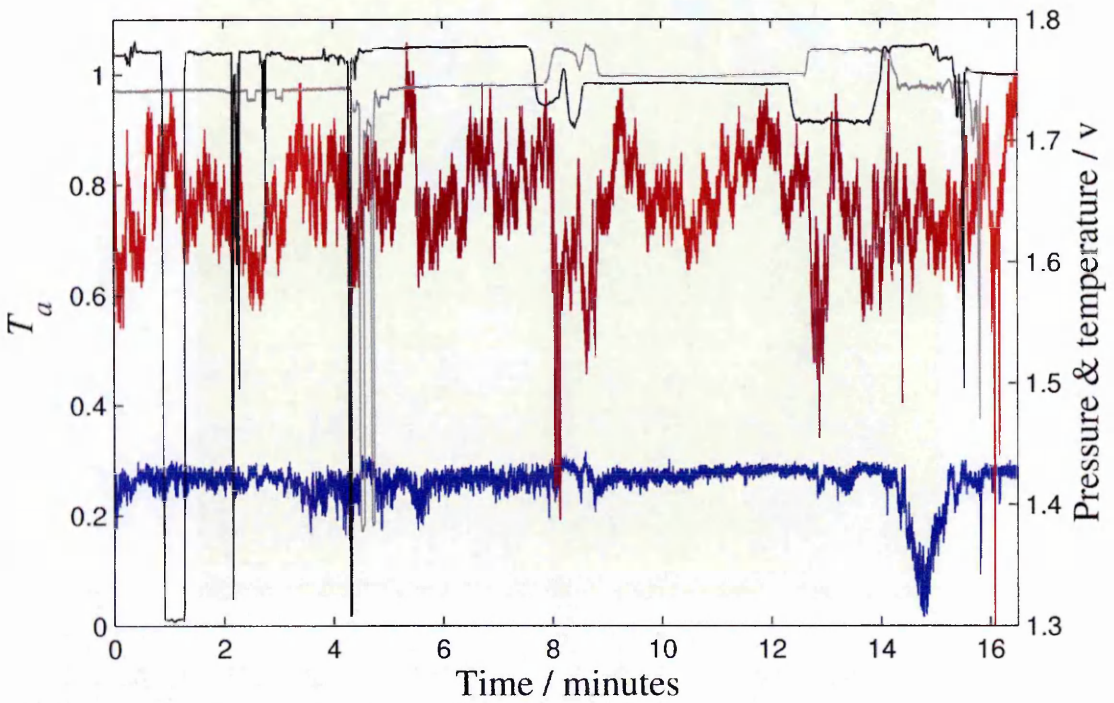

Figure 4-5: An example of a typical dataset obtained for a dust devil encounter. Careful time-stamping and correlation between the different sensors was necessary in order to extract the portion associated with the transit. The graph displays the UV-VIS (black lines) and the PICO datasets, Sun sensor (grey line), pressure (blue line) and temperature (red line).

The dust devil transits were identified by using the recorded time on the GPS and correlating the UV-VIS output with the PICO dataset. Unfortunately the UV-VIS did not record the measurement start time and the recorded end time of the measurement was the file creation time, which could be tens of seconds after the final measurement, resulting in an offset between the UV-VIS and PICO datasets. This was corrected for by applying a correction factor (T_ε) to the file creation time (T_{end}) using:

$$T_{sc} = \left(T_{\text{end}} - \frac{T_\varepsilon}{3600} \right) - \left(sc_{\text{end}} - sc \right) T_{\text{integration}} \tag{4.1}$$

Where *sc* and sc_{end} are the current and end scan number respectively, T_{sc} is the equivalent time for scan number sc, and $T_{integration}$ is the integration time of the spectrometer. The correction factor was varied until the UV-VIS and Sun sensor data were aligned. A number of additional checks were performed to identify the dust devil transit. The first method looked for differences in response between the Sun sensor and the UV-VIS (FS setup only). At T = 13.15 minutes, in Figure 4-5, the Sun sensor exhibits a drop in response but the UV-VIS has an unexpected increase in measured irradiance. This is a result of the different FoV between the UV-VIS and Sun sensor which resulted in the same response when the vehicle is stationary, and both are looking directly up but diverged as the angle of the vehicle changed. The final method of data reduction was to look directly at the irradiance spectrum produced by the UV-VIS spectrometer and identify the attenuation of light by the dust (discussed in Section 4-3). Figure 4-6 shows the reduced data for the dust devil encounter shown in Figure 4-5. Good correlation is observed between the increase in temperature and subsequent decrease in pressure and transmission.

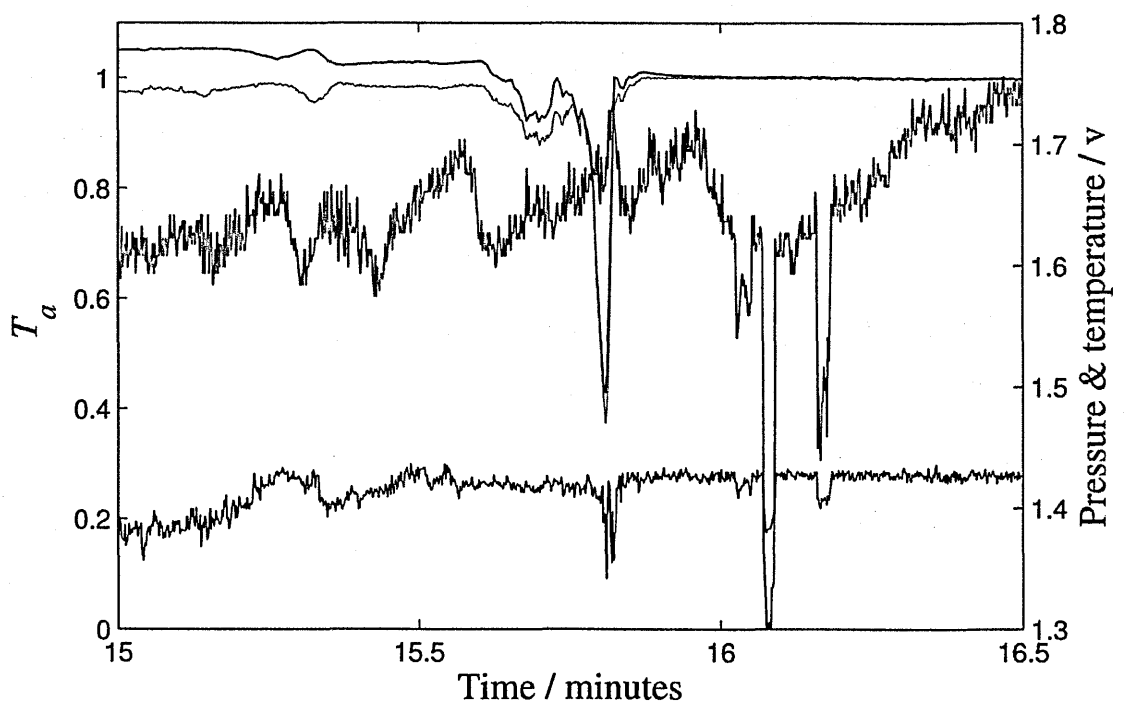

Figure 4-6: An example of the reduced data for a dust devil encounter. The graphs displays the UV-VIS (black lines) and the PICO data sets, Sun sensor (grey line), pressure (blue line) and temperature (red line).

The correlation between the PICO and the UV-VIS measurements for the dust devil encounters analysed, using the FS setup, are shown below in Figure 4-7, with T_a calculated at 386 nm. Good agreement between the Sun sensor and the UV-VIS measurements is seen for all encounters considered. Note, the point of lowest signal does not always correspond to the passing of the dust devil interior. E1–E3 all show the lowest detected signal occurring before the pressure decrease and temperature increase, *i.e.* before entering the dust devil core. From the results of Chapter 3, this indicates that the UV-VIS passes through the dust devil shadow prior to entering the interior, and the point of lowest illumination occurs when the length of the dust column is at maximum. The pressure profiles for encounters E1–E3 all show a distinct similarity, with a decrease observed upon entering the vortex, followed by an increase which subsequently decreases again before increasing back to ambient conditions. The increase in pressure is suggestive of downward flow of cooler air in the dust devil core, which was reported by Sinclair (1973), however no correlated temperature decrease is observed. This could be due to the temperature sensor being insensitive to these small variations in temperature.

As expected the temperature increases as the dust devil passes over the sensor. The highest temperature is experienced through the trailing wall and is a result of it being on the Sun-facing side. The similarity of the transit profiles for the different encounters is no coincidence and is an artefact of the orientation of the lake bed and the wind direction. As illustrated in Figure 4-4, the wind direction on the 21st was SW to NE and, given the position of the Sun in the sky, the probability of encountering a dust devil travelling towards the Sun was very small and limited to early morning.

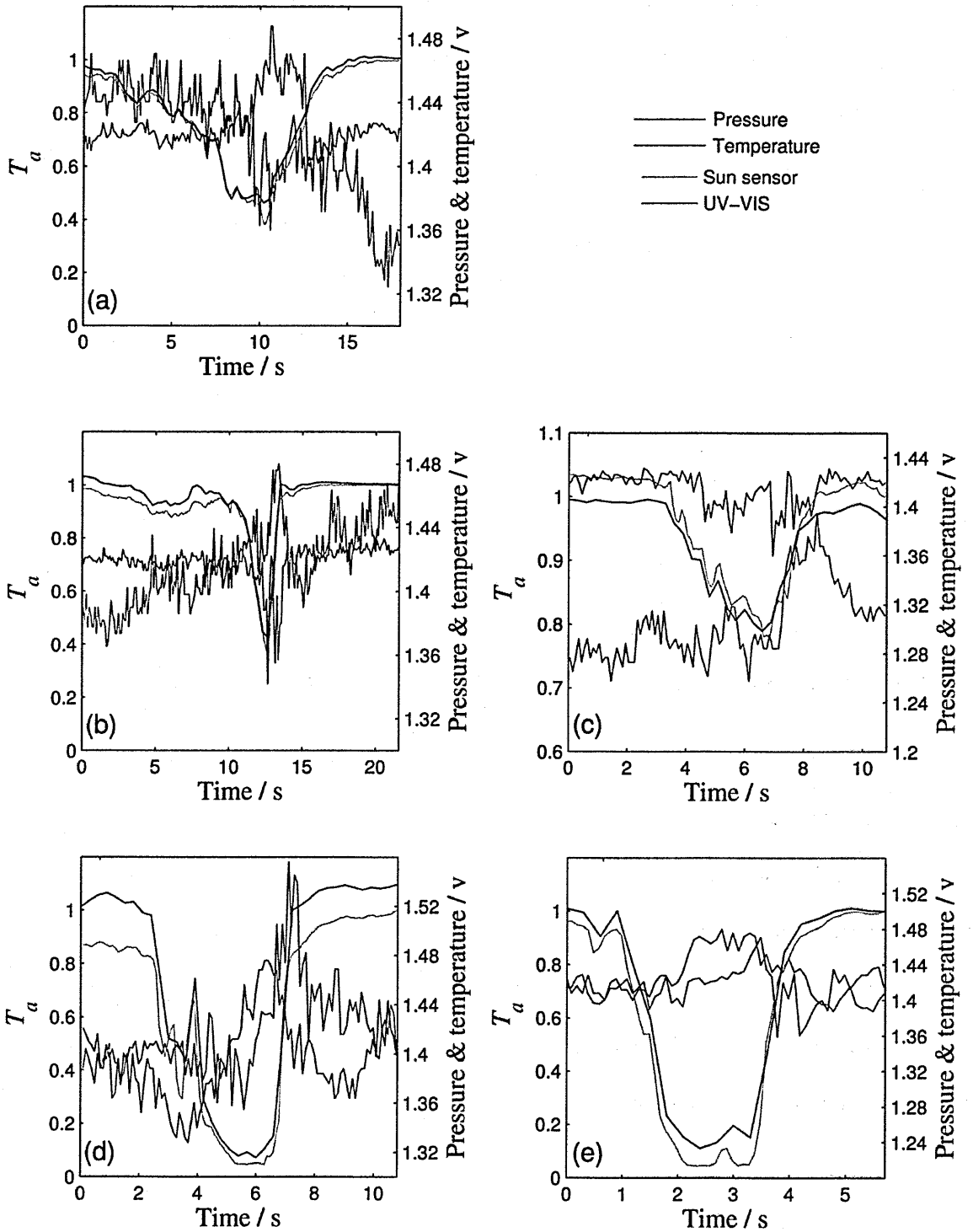

Figure 4-7: Correlation of the UV-VIS and PICO datasets for encounters: (a) E1, (b) E2, (c) E3, (d) E4 and (e) E5, which used the FS optical setup. The Sun sensor and UV-VIS measurements have been normalised to the reference signal to allow a direction comparison.

As shown in Chapter 3, the NV setup experiences an increase in irradiance during the dust devil encounter. When a dust devil transits over the UV-VIS, sunlight that would not normally be observed is scattered by the suspended dust into the UV-VIS probe, increasing the measured signal. This meant direct correlation with the Sun sensor response could not be achieved for encounter E6. However, further analysis of the PICO and UV-VIS datasets, Figure 4-8, reveals a correlation between features as illustrated by the arrows. The value of T_ϵ in Eq. (4.1) was varied until good agreement between these features was obtained. Upon close inspection, the features align well; the peak signal in the UV-VIS dataset correlates with the minimum in the Sun senor data. There is a small reduction in scattered light in the UV-VIS dataset at approximately 10 s and this correlates well with the expected pressure drop at the dust devil centre. The decrease in the scattered component at the dust devil centre agrees with the model predictions discussed in Chapter 3 and suggests a reduced dust concentration at the core of the dust devil.

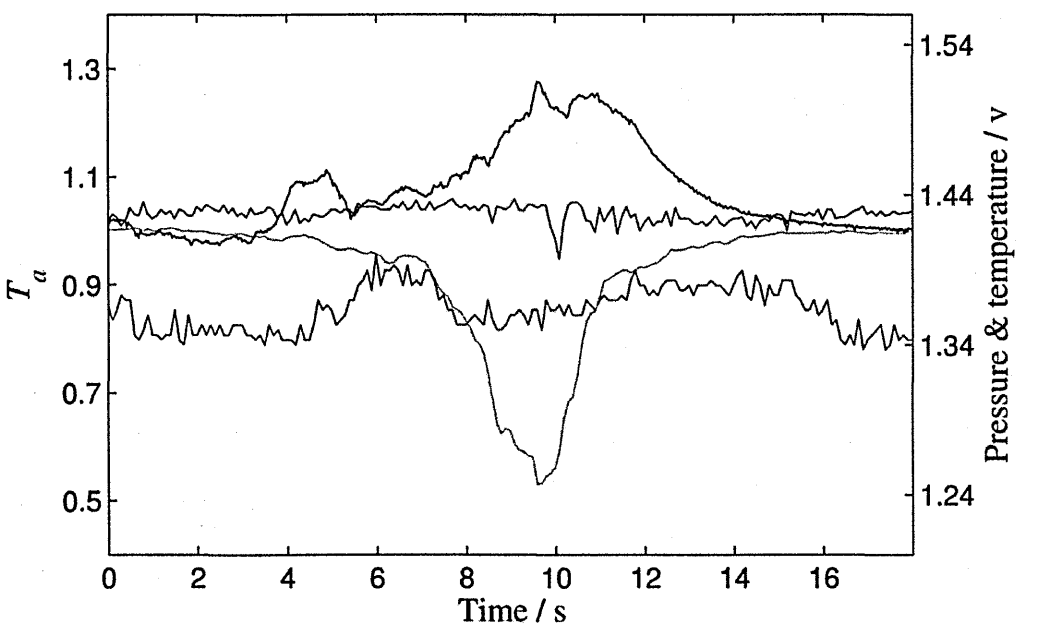

Figure 4-8: Comparison of T_a measured by the UV-VIS using the NV setup with the PCIO dataset for encounter E6.

4.2.2 Estimation of dust devil parameters

As illustrated in Chapter 3, the signature of a transiting dust devil depends on a number of variables: the dust devil's direction of travel relative to the Sun (α_{dd}), the solar zenith angle (θ_z) and azimuth angles (ϕ_{az}), the radius of the dust devil (R_{dd}) and the dust devil height (Z_{dd}). While θ_z and ϕ_{az} are essentially fixed for a given encounter, constraints must be applied to the other parameters.

The direction of travel for each dust devil was estimated using video footage, visual references taken during the transits and the pointing direction of the chase vehicle relative to the Sun. Loading the GPS co-ordinates recorded from the chase vehicle into Google Earth™ allowed the location of each encounter to be mapped and the pointing direction of the vehicle relative to North to be determined. The National Oceanic and Atmospheric Administration NOAA solar calculator[2] was used to calculate ϕ_{az} at the time of the encounter using the latitude and longitude recorded by the GPS. The solar data was imported and overlaid onto the encounter location map providing a reference between the vehicle pointing direction and ϕ_{az}. The visual references were then correlated with the maps to determine the dust devil travel direction. An estimation of the dust devil tangential velocity was achieved using the approximate diameter calculated from the static images and the time taken for the dust devil to transit across the chase vehicle. Transit time was determined from the recorded encounter video.

The physical dimensions of the dust devils were estimated using images which contained the chase vehicle near each vortex. Knowing the length, width and height of the chase vehicle to be approximately 5.5, 2.0 and 1.9 m respectively it was used as a size reference to place limits on the dust devil dimensions as Figure 4-9 illustrates.

[2] http://www.esrl.noaa.gov/gmd/grad/solcalc/

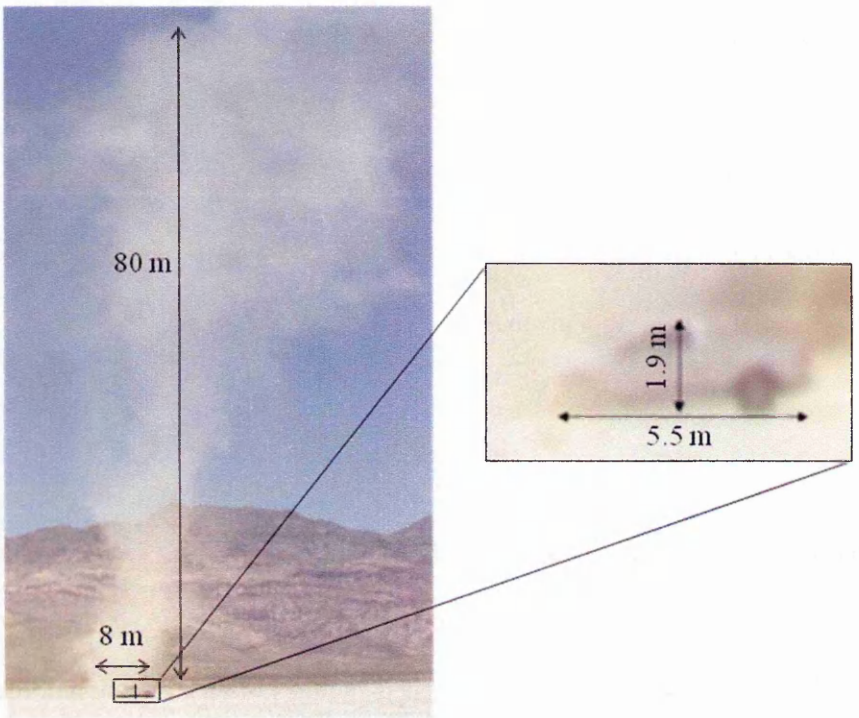

Figure 4-9: Illustration of how the dust devil dimensions were approximated for each encounter.

The horizontal velocity of the dust devils caused a tilt in their structure, in the direction of the ambient wind, and cannot currently be accounted for in the MCLSM. The angle of tilt causes the path length of the incident light through the vortex to vary with position inside the dust devil, as illustrated in Figure 4-10 for encounter E2, where I_{ref} is the direction of the incident light, l_{core} is the path length of light observed at the vortex centre and l_{lw} is the path length of light observed in the leading wall of the vortex. As Figure 4-10 shows, the tilt of the vortex leads to the condition of $l_{core} \leq l_{lw}$, resulting in an underestimation of the amount of dust in column through l_{lw} if a dust devil height of 9.7 m is used.

To assess the effect of the dust devil height (Z_{dd}) two simulations were performed: One with a dust devil height of 12 m and the other with a height of 38 m. In both cases the dust devil radius was assumed to be 4 m and the dust optical depth (τ_d) was held constant between the two scenarios (*i.e.* increasing the path length through the dust decreases the dust concentration such that the measured τ is constant). A highly scattering dust component was chosen as, shown in Chapter 3, the scattered component is strongly dependent on the dust concentration and thus,

more sensitive to uncertainties in the dust devil height. Therefore the dust was given an ω_0 and g of 0.95 and 0.7 respectively. Figure 4-11 shows T_a at the dust devil core as a function of τ and reveals that the dust devil with Z_{dd} = 12 m experiences a higher transmission at all τ. This higher transmission is the result of detecting a higher scattered component compared to the taller dust devil, which in turn is a consequence of a higher dust concentration in the shorter vortex. The higher dust concentration increases the probability of scattering back into the path of the detector's line of sight, whereas the lower dust concentration for Z_{dd} = 38 m reduces the probability of scattering back into the path due to lower photon-dust interactions. This is a consequence of assuming vertical homogeneity within the model, where an increase in the path length through the dust requires a reduction in the dust concentration such that τ is constant. Therefore a cautious approach is used, with the dust devil height taken to be the vertical extent of the high dust loading in the lower portion of the dust devil vortex as illustrated in Figure 4-10b.

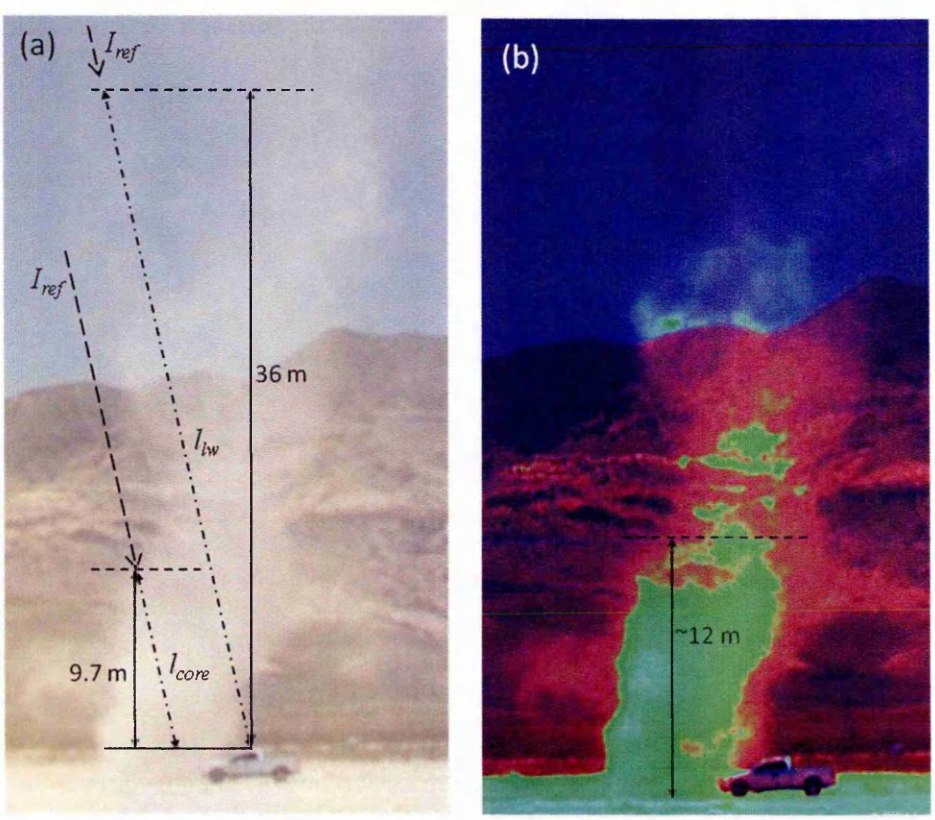

Figure 4-10: (a) Uncertainty in the dust devil attitude during a dust devil encounter, (b) enhanced image showing the vertical extent of the vortex with the highest dust loading confined to an altitude of 12 m above the surface

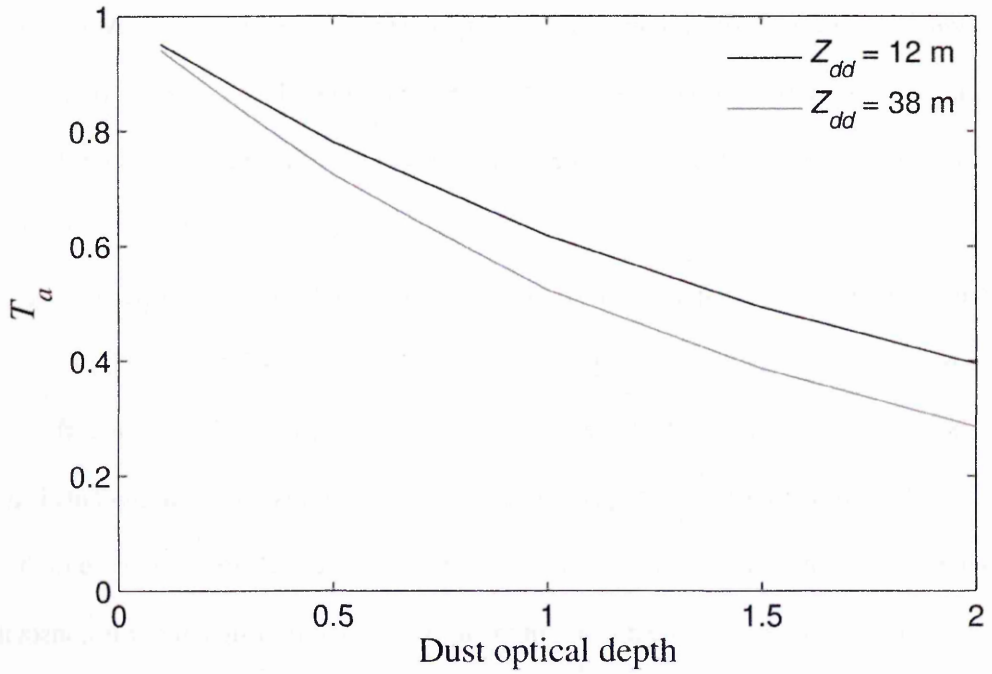

Figure 4-11: The apparent transmission at the core of a 4m dust devil with an height of 12 m and 38 m.

Encounters E4 and E5 involved the same dust devil and provides an excellent opportunity to determine the accuracy of the estimates for the dust devil velocity and dimensions. By measuring two transits the bearing dust devil along the surface and its velocity could be calculated more accurately than for a single transit. T_a at 450 nm as a function of time is shown in Figure 4-12a. A wavelength of 450 nm was used as less scattered light is detected at shorter wavelengths however, due to the high dust abundance, the measured total irradiance at wavelengths <450 nm was of the same order as the instrument noise. The time-series reveals four significant reductions in T_a and corresponds to the dust devil transits E4 and E5, and passage of the chase vehicle through the dust devil shadow, Shadow (1) and Shadow (2). Figure 4-12b shows the measured transmission spectrum during the E4 and E5 transits and passage through Shadow (1) and Shadow (2). The transmission spectra, for the dust devil transits, show greater extinction at shorter wavelengths in comparison to the transmission through Shadow (2); here an increase in irradiance is observed. The increase at blue wavelengths through the dust devil shadow is a result of direct component being sufficiently reduced such that the diffuse component from the clear sky forms a larger fraction of the total irradiance. Light scattered by

air molecules is described by Rayleigh scattering and is proportional to λ^{-4}; blue light scatters at larger angles, leading to the diffuse component being higher at shorter wavelengths. Shadow (1) exhibits similar spectral extinction as the dust devil transits and is a result of the chase vehicle passing through the peripheral dust haze lofted by the dust devil.

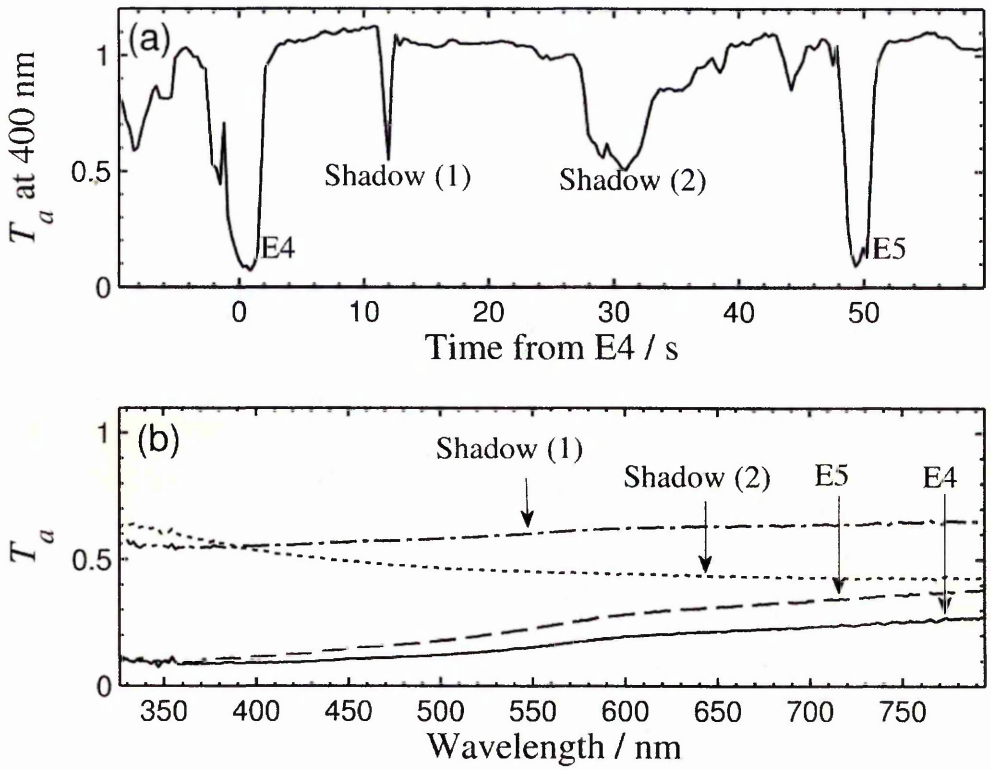

Figure 4-12: (a) The apparent transmission spectrum measured during the dust devil transits E4 and E5 and through the dust devil shadow. (b) T_a at 450nm as a function time.

The geometry of encounter E4 and E5 is shown in Figure 4-13a, which shows the location and distance between the two transits, the direction of the incoming solar radiation, the position of the chase vehicle approximately thirty seconds after E4 (T_{30}) and an estimation of the size of the dust devil shadow. The path taken by the chase vehicle is denoted by the white line. The velocity of the dust devil was calculated by measuring the distance between E4 and E5 in Google Earth (315.7 m) and taking the time between the two transits from the UV-VIS data set (49.2 s). This gave an average velocity of 6.4 ms^{-1}, consistent with the transit velocity estimated from the image and video references of 6.5 ms^{-1} for E5. A lower velocity of approximately 5.8

ms^{-1} was determined for E4 which suggests that the surface speed of the dust devil increased between the two encounters.

Assuming that the dust devil travelled in a straight line, the bearing across the playa (β_{dd}) is given by the angle of the line joining the two encounter positions relative to North. This was found to be approximately 23.0°. Given ϕ_{az} = 268°, the path taken by the spectrometer through the dust devil (α_{dd}) was calculated to be 115° relative to the illuminated dust devil wall. The different angles are illustrated in Figure 4-13b.

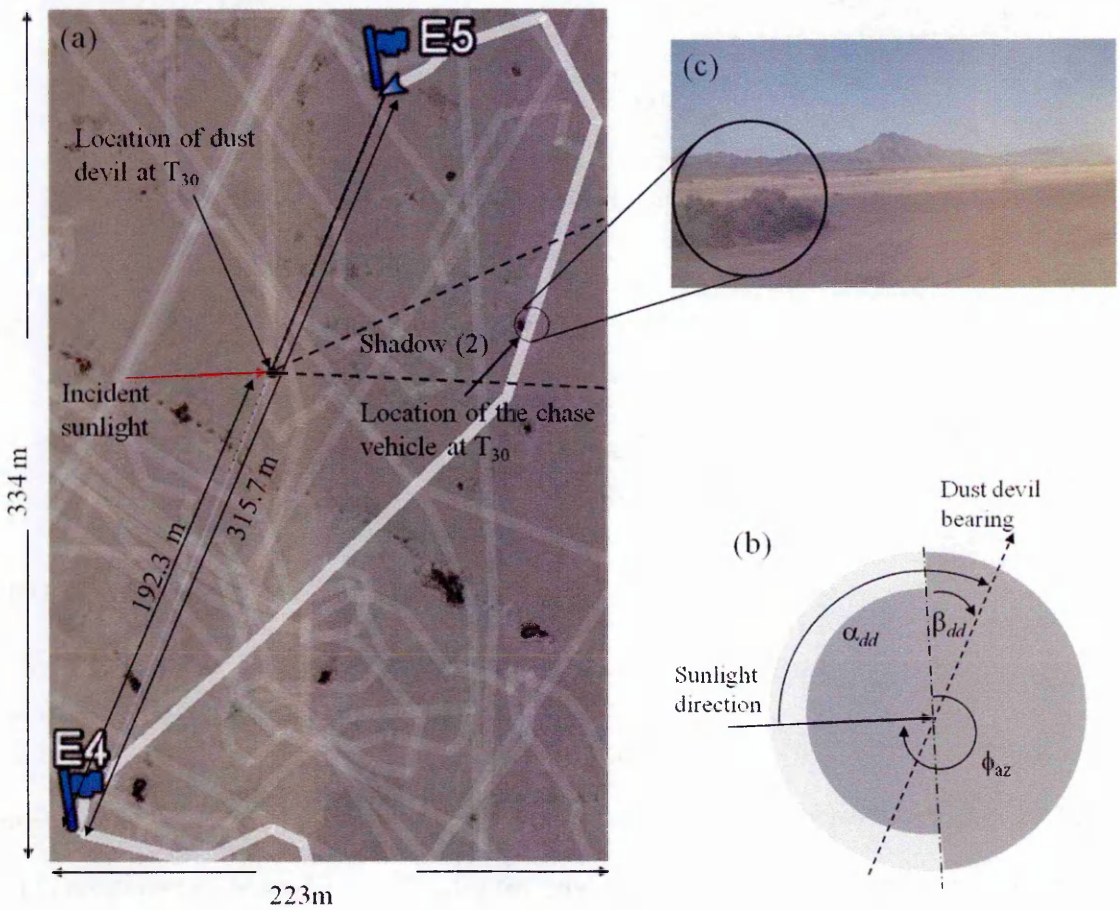

Figure 4-13: Encounter correlation for E4 and E5. (a) schematic of the surface geometry for E4 and E5, (b) determination of the dust devil bearing, (c) image from the chase vehicle at T_{30} showing correlation with the predicted location of the dust devil shadow at T_{30}.

The accuracy of the above determinations can be uniquely tested for this encounter. The UV-VIS dataset displays a decrease in T_a at T_{30}, Shadow (2), consistent with the image shown in Figure 4-13c. The image is taken from the encounter video at T_{30} and shows the chase vehicle passing through the shadow of the dust devil. The location of the dust devil at T_{30} was calculated using the estimated average velocity of the dust devil. Furthermore, knowing the direction of the incident solar radiation, the solar elevation, and the dimensions of the dust devil, the surface footprint and direction of the dust devil shadow could be estimated. It is assumed that the dust devil dimensions remained constant between the E4 and E5 transit. The height of the dust devil was limited to the top of the central vortex, estimated to be 330 m. Therefore, with a solar elevation angle of 43°, the shadow footprint would extend approximately 354 m along the ground. As shown in Figure 4-13a, the shadow will cross the path taken by the chase vehicle and shows good correlation with the encounter video, Figure 4-13c.

The velocity, radius and height of the dust devils considered in this analysis are shown in Table 4-1. Also shown is the apparent optical depth (τ_a) for each encounter and is calculated from the Beer-Lambert law using the reference irradiance and the irradiance measured during the encounter. Note that τ_a differs from τ since the addition of scattered light, in the total irradiance measurement, during the dust devil transit will cause the calculated τ to be lower than the actual value and therefore serves as a lower limit.

Encounter	Dust devil radius / m	Dust devil height / m	surface velocity / ms^{-1}	Bearing relative to illminated wall / °	τ_a at 450 nm
E1	10.0	15	5 – 7.0	253	0.75
E2	4.0	12	5 – 7.5	230	0.57
E3	5.0	50	-	210	0.18 – 0.21
E4	9.0	50	5.5 – 7.5	115	2.30 – 2.71
E5	9.0	50	6.4 – 7.5	115	1.63 – 2.00
E6	1.5	15	-	31	0.9

Table 4-1: Estimated dust devil parameters from the visual references and UV-VIS data.

4.3 Possible sources of error and uncertainties

The following sections discuss possible sources of error and uncertainty encountered during the experimental campaign.

4.3.1 Presence of a dust haze

The image in Figure 4-14 reveals the presence of a dust haze that extended from tens of metres to greater than hundreds of metres around the dust devil vortices, and may be evidence of a persistent dust haze present in the experimental area.

The impact of this dust haze was difficult to assess due to its spatial heterogeneity and the variability in dust concentration. The initial attempts to fit the transit signatures included this dust haze by adding an additional concentric ring of dust around the dust devil vortex that had a lower k_{ext} than the dust devil, but higher than a clear atmosphere. However, the symmetric nature of the MCLSM resulted in a dust haze that was too uniform, and while changes in the dust concentration could be modelled in the *X*-*Y* plane, the inability to model vertical changes to the dust abundance resulted in erroneous transit signatures outside of the vortex. It was decided therefore to fit only the part of the transit signature that corresponded to the interior of the dust devil, where the impact of the dust haze could be considered negligible.

Figure 4-14: Enhanced colour image showing the dust haze that was present during the first two days of the experiments.

4.3.2 Uncertainty in dust devil dimensions and non-uniformity

Dust devils are continually evolving systems with their dust distribution and concentration altering significantly over very short timescales. Even within the time frame of a transit, over the instruments, the dust distribution and concentration can potentially vary considerably. Figure 4-15 shows images taken before, during and after the transit of a dust devil measured on the 21st June. The upper image has been processed by changing the image brightness, contrast and colour temperature and, while the brightness is not strictly related to the dust particle concentration, it may provide insight into the dust devil structure. The lower image is the unprocessed image, to provide a direct comparison. The unaltered image appears to show the dust devil to be stable throughout the encounter with variations in the dust loading difficult to distinguish. The processed images suggest a possible heterogeneous structure, with the highest dust concentration occurring around the vortex and relatively close to the surface. The images show that during the encounter the primary dust devil spawned a 'little brother'. This occurrence was also reported by Sinclair (1973), who observed a similar process of primary vortices forming a new secondary vortex.

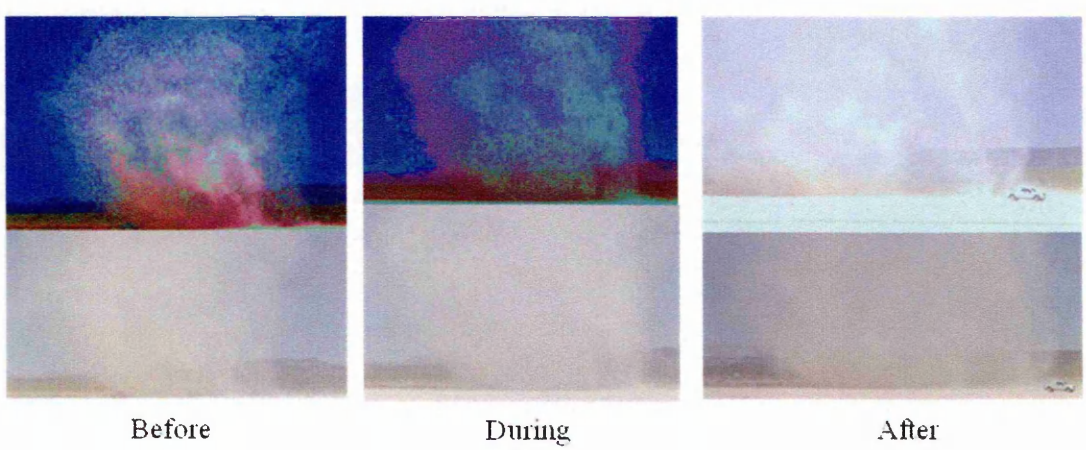

Figure 4-15: Enhanced images taken during a dust devil transit illustrating the evolution of the dust devil structure over short time scales.

Another source of error comes from the use of 2-D images to determine the vortex size. Even with the enhanced images it was difficult to determine any depth. Dust which appears to

be part of the main vortex may actually be in front or behind the perceived vortex vector in the image.

4.3.3 *Interference from the chase vehicle*

Another important artefact in the measurements is the effect the chase vehicle had on the transiting dust devil. It was observed from videos taken of the dust devil transits that the structure and dust loading of small dust devils, with low dust concentrations and diameters comparable to the dimensions of the chase vehicle, changed significantly upon encountering the chase vehicle. In some cases the encounter with the vehicle proved fatal, resulting in the termination of the vortex, while others became more intense with increased dust loading. Others abruptly changed their direction of motion along the surface. It is suspected that this last case occurred in response to the pressure differential created by the vehicle as it approached the dust devil, a variable dependent on the time between the vehicle coming to rest and the transit. Not enough data was collected to determine any correlation between the effect on the dust devil to the position and orientation of the vehicle and wind direction. These parameters would play a significant role, as well as others which were not measured (*i.e.* the pressure differential generated by the chase vehicle) on the modification of the dust devil vortex as it encountered the chase vehicle. The effect of the chase vehicle on large dust devils, with diameters greater than the dimensions of the chase vehicle, or intense small vortices with high dust loading was considerably smaller and no obvious change to the dust devils were observed. This has implications for measuring dust devils on Mars where, depending and the size of the spacecraft, termination or modification of transiting vortices may occur.

4.4 Retrieval of the dust single scattering properties

As the dust devil transits over the spectrometer, the incident solar radiation will be attenuated by the suspended dust particles entrained within the vortex, modifying the solar spectrum observed at the surface. The measured reference and attenuated spectra for encounters E1–E5 are shown

in Figure 4-16. To remove the diurnal variation in illumination, and to allow direct comparison between the different dust devils and reference spectrum, the spectra have been normalised to the peak irradiance within the wavelength range of the spectrometer. The variation in the different reference spectra was negligible and therefore only one is shown.

The normalised spectra reveal that the attenuation caused by the dust is small at τ_a between 0.2–1.0 at 450 nm in encounters E1–E3, with only slight absorption seen at wavelengths shorter than 550 nm and increased scattering at longer wavelengths. At $\tau_a > 2.0$ the dust concentration is sufficient to cause a significant modification to the solar spectrum, with high absorption seen at wavelengths shorter than 550 nm and a significant increase in the observed light at wavelengths longer than 550 nm. The higher attenuation is due to the fact that, at $\tau_a > 2.0$, the majority of the detected light is from the scattered component (*i.e.* has undergone interaction with dust particles). This implies that the imaginary refractive index (n_i) of the dust particles is larger at shorter wavelengths, compared to longer wavelengths, to account for the observed absorption and scattering at wavelengths shorter and longer than 550 nm respectively.

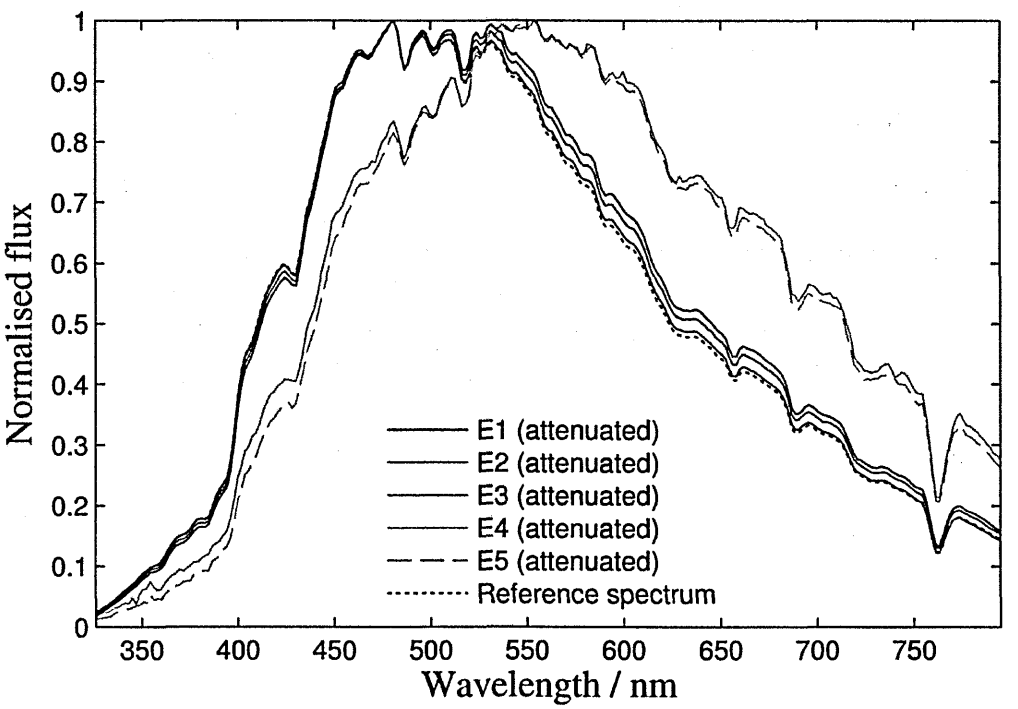

Figure 4-16: (a) The measured reference and attenuated solar spectrum normalised to the peak irradiance for each encounter considered for the retrieval.

The higher attenuation measured during encounters E4 and E5 may also be a result of the vortex intensity, size and wind speeds (as observed from video references) which greatly exceed those of the other encounters. Larger size and higher winds speeds enable greater quantities of larger dust particles to be lifted to higher altitudes. As discussed in Chapter 2, this will result in a greater fraction of light being absorbed by the dust particles. As discussed by Greeley *et al.* (2003) and Neakrase *et al.* (2006), the efficiency of a vortex to lift small particles is governed by the pressure drop (ΔP) at the vortex core. The observed ΔP for the different dust devil encounters were 4.3% (E1), 5.2% (E2), 3.9% (E3), 5.0% (E4), 4.8% (E5), and 2.4% (E6). This indicates that encounters E2, E4 and E5 will have larger quantities of finer and coarse particles relative to E1 and E3. The variation in ΔP between E1and E3 will also affect greatly the particle size distribution for these encounters. Therefore, it is suggested that the particle size distribution of dust suspended in the dust devils will vary considerably and likely unique for each vortex. Due to experimental constraints the particle size distributions could not be measured *in situ* at the time of the measurements and is the largest source of uncertainty in the retrieval of the dust optical properties.

4.4.1 Dust particle size distribution

With no prior knowledge of the particle size distribution, the effect of different distributions with various coarse and fine modes on the particle single scattering properties, ω_0, g and Q_{ext}, was investigated. The size distribution of terrestrial desert dust is generally bimodal in nature defined by a fine fraction ($r < 1.0$ μm) and a coarse fraction ($r > 1.0$ μm). Sinclair (1973) determined a median radius for the particle size to be 0.6 μm for a small size dust devil (< 3 m). However as discussed by Sinclair, there was insufficient sampling for particles below 5 μm during his measurements and suggests that an inflection in the measured size distribution towards smaller particles is likely, indicating a bimodal particle size distribution. Furthermore, Sinclair suggested that the size of the particles suspended by a dust devil will tend to be larger

than desert sand aerosols and more analogous to soil aerosols. The mean volume radius r_v and variance σ_v^2 are used to define the particle volume distribution from:

$$\frac{dV(r)}{d\ln r} = \sum_{i=1}^{2} \frac{V_i}{\sqrt{2\pi}\sigma_{v,i}} \exp\left[\frac{(\ln r - \ln r_{v,i})^2}{2\sigma_{v,i}^2}\right], \tag{4.2}$$

where V_i represents the particle volume concentration, r is the particle radius, $r_{v,i}$ is the median radius and $\sigma_{v,i}$ is the standard deviation which are calculated from:

$$\ln r_v = \frac{\int_{r_{min}}^{r_{max}} \ln r \frac{dV(r)}{d\ln r} d\ln r}{\int_{r_{min}}^{r_{max}} \frac{dV(r)}{d\ln r} d\ln r} \tag{4.3}$$

$$\sigma_v = \left[\frac{\int_{r_{min}}^{r_{max}} (\ln r - \ln r_v) \frac{dV(r)}{d\ln r} d\ln r}{\int_{r_{min}}^{r_{max}} \frac{dV(r)}{d\ln r} d\ln r}\right]^{1/2} \tag{4.4}$$

$$V = \int_{r_{min}}^{r_{max}} \frac{dV(r)}{d\ln r} d\ln r \tag{4.5}$$

The different size distributions considered are shown in Figure 4-17, for various coarse (r_{vc} = 1.2, 2.5 and 5.0 μm) and fine (r_{vf} = 0.15, 0.3 and 0.6 μm) median radii. The variance was held constant at $\sigma_v^2 = 2.0$, which is representative of terrestrial aerosols (Reid *et al.*, 2003).

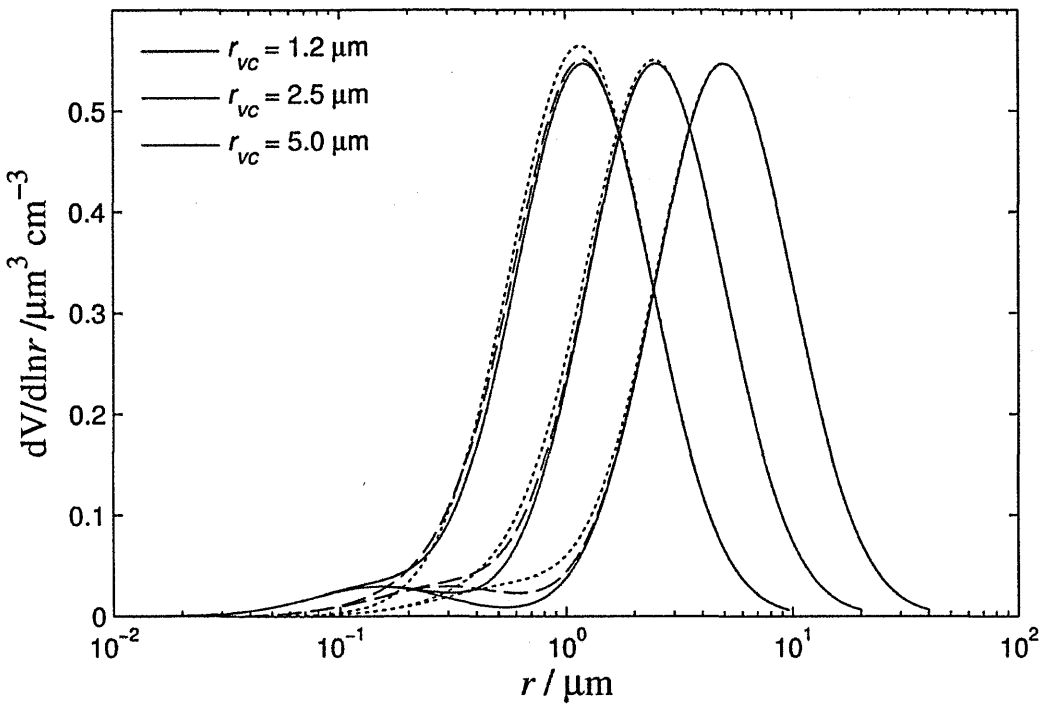

Figure 4-17: The volume size distribution as a function of particle radius for different model radii. The solid, dashed and dotted lines indicate a r_{vf} of 0.12, 0.3 and 0.6 µm respectively.

The refractive indices of the dust particles were taken by Dubovik *et al.* (2002) for Bahrain-Persian Gulf dust and the single scattering properties calculated using Mie theory; the results are shown in Figure 4-18. As expected from the discussion in Chapter 2, as the particle size of the coarse fraction increases, lower ω_0 and higher g values are predicted over the wavelength range. The effect of increasing r_{vf} results in a divergence in ω_0 and g at shorter wavelengths towards lower and higher values respectively. At longer wavelengths (> 550 nm) ω_0 and g are insensitive to changes in r_{vf} with a fine fraction volume of 5% of the total particle volume. However even at this low concentration of fine particles, Q_{ext} displays significant sensitivity to the particle size of the fine fraction, with the introduction of r_{vf} = 0.15 µm and 0.3 µm into the r_{vc} = 5.0 µm distribution resulting in a negative gradient. This implies that the measured τ will increase towards longer wavelengths for the particle volume size distributions considered, with the exception of r_{vf} = 0.15 µm and 0.3 µm and a r_{vc} of 5.0 µm. In these two cases a reduction in τ will be observed with increasing wavelength.

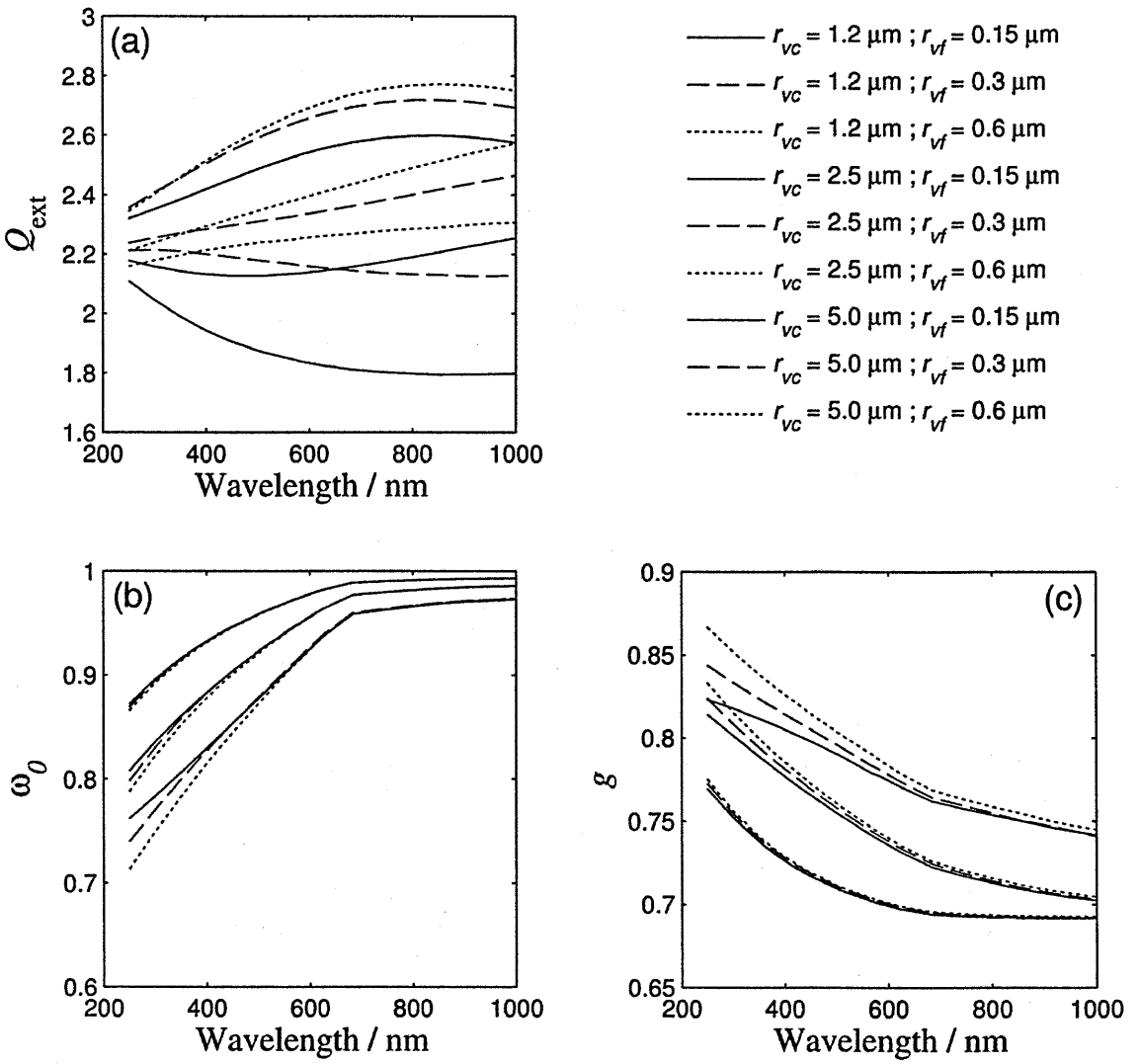

Figure 4-18: (a) Q_{ext} (b) ω_0 and (c) g as a function of wavelength for various particle size distributions.

To investigate the effects of increasing the abundance of the fine mode relative to the coarse mode, the fraction of the total volume occupied by the fine mode was increased from 0% to 20% for a particle volume distribution with r_{vc} = 2.5 µm and r_{vf} = 0.3 µm; the results are shown in Figure 4-19.

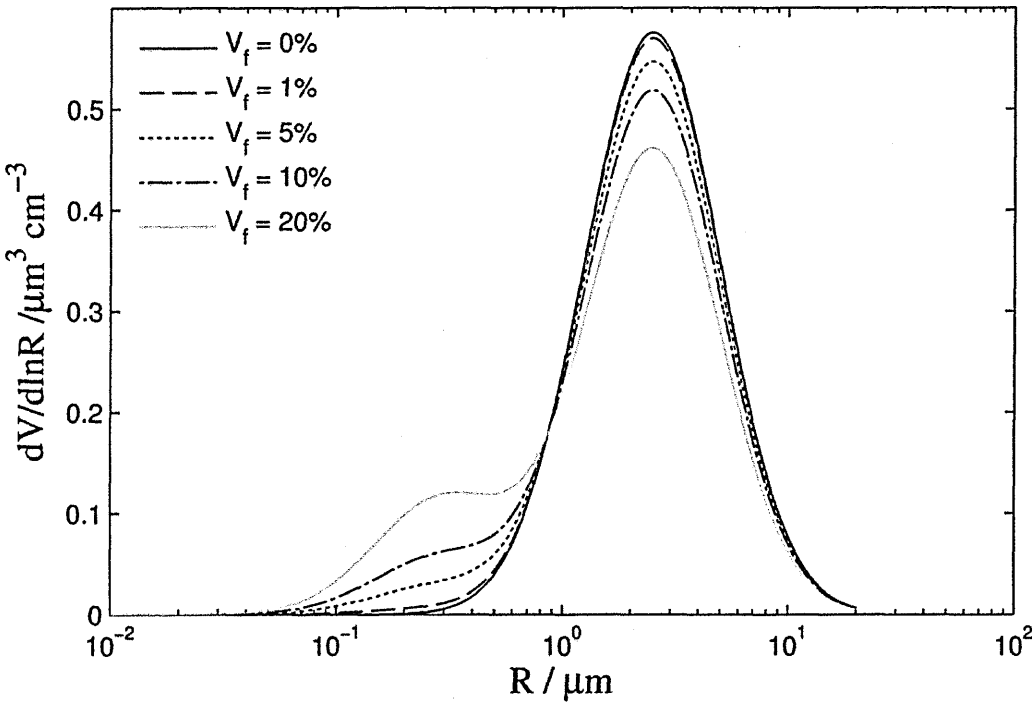

Figure 4-19: The effect on the size distribution as a result of increasing the volume occupied by the fine particles.

The change in Q_{ext}, ω_0 and g, as a result of increasing the volume occupied by the fine particle mode, is illustrated in Figure 4-20. It is observed that even small additions of fine particles can cause a noticeable difference in all single scattering parameters. Increasing the volume fraction of fine particles to 10% of the total volume leads to approximately half the amount of light at 400 nm being absorbed relative to the $V_f = 0\%$ case. The fine particles also result in increased backscattering, observed as a decrease in g over the wavelength range, while the gradient of Q_{ext} becomes negative with increasing V_f. This is important as the efficiency of a dust devil in lifting fine particles is governed by the ΔP at the core. From the calculated ΔP for E1-E5 each dust devil will suspend different amounts of fine particles. This implies that each dust devil will have its own unique set of Q_{ext}, ω_0 and g parameters since the volume fraction of coarse and fine particles will be different for each encounter.

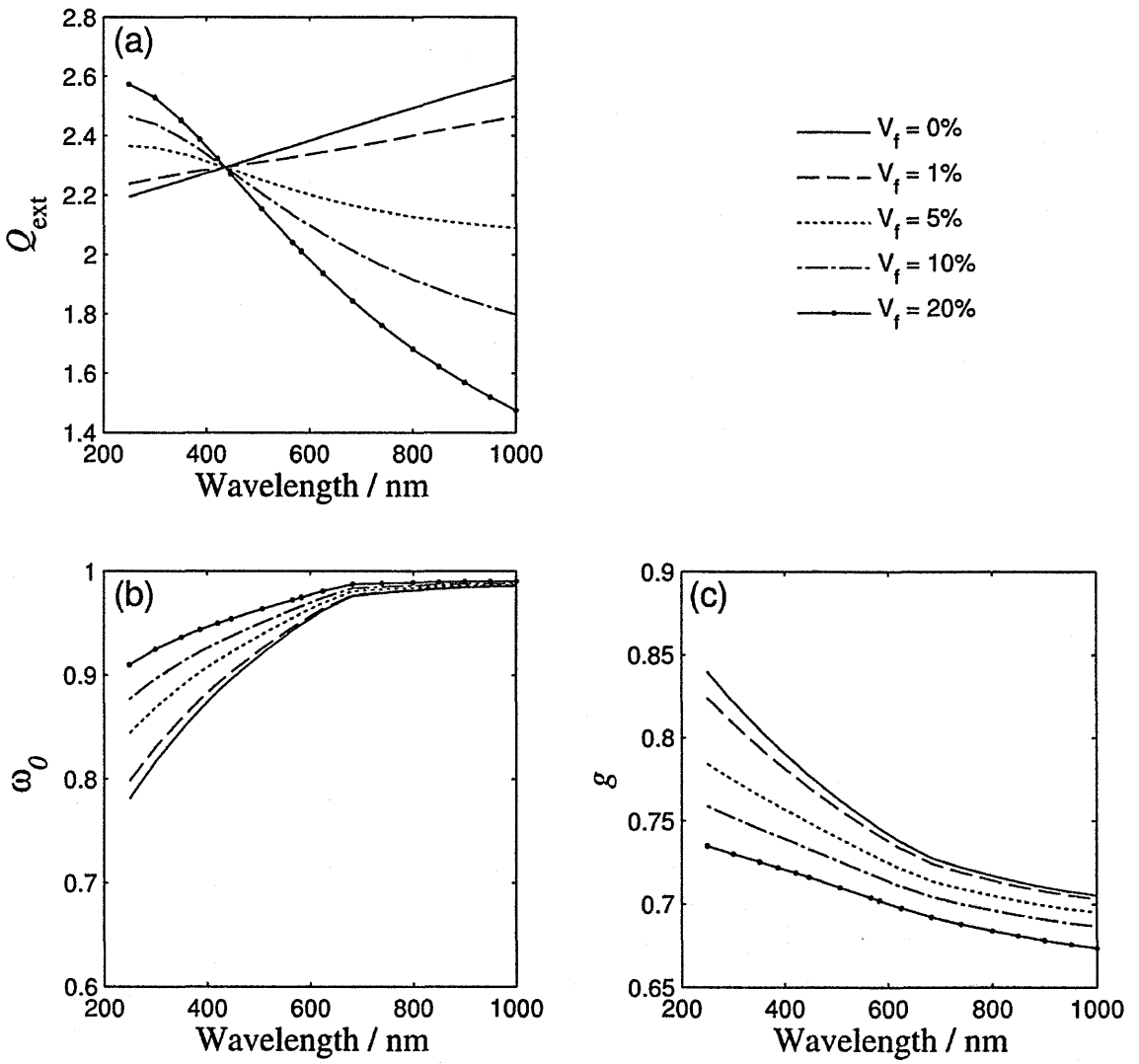

Figure 4-20: The effect of increasing the fraction of total volume occupied by the fine particle on (a) Q_{ext}, (b) ω_0 and (c) g.

Relatively small variations in the particle size can cause significant differences in Q_{ext}, ω_0 and g, greatly impacting the results of radiative transfer solutions. Another problem is the bimodal nature of the particle size distribution for desert dust which adds at least three additional parameters: r_{vc}, r_{vf} and the volume fraction of each mode that must be sought in order to retrieve accurate optical properties. This leads to a minimum of five interdependent parameters that must be varied until the model converges on the best solution, which is undesirable given the MCLSM computational limits in terms of run-time. Another source of uncertainty is the assumption that the particles are homogenous spheres and using Mie theory to calculate their single scattering properties. Therefore, to remove the assumption on particle

shape, and to reduce the number of dependent variables, the Henyey-Greenstein analytical phase function (Henyey and Greenstein, 1941) was used to approximate the particle scattering phase function and the parameters retrieved were ω_0, g and τ.

4.4.2 Retrieval method

The physical dimensions of the dust devils E1–E5, determined in Section 4.2.2, were used to create model dust devils for the MCLSM. The centre of the dust devil vortices were taken to be the point on the transit signature where ΔP was at maximum. As stated previously, τ_a provides a lower limit to the dust concentration. Therefore, to ensure adequate sampling of the dust concentration is achieved, τ was incrementally increased from τ_a to a value three times larger.

For each τ the MCLSM is executed sequentially for dust components of varying single scattering albedo and asymmetry values, with $0.6 < \omega_0 < 0.99$ and $0.6 < g < 0.99$. These limits on ω_0 and g are based on retrieved values for various desert aerosols (Kaufman, 1987, Dubovik *et al.*, 2000). The output of the simulations results in a matrix relating the number of photons detected to combinations of ω_0 and g values. The simulated reference signal is found by executing the MCLSM with the dust devil removed from the model volume. This is accomplished by setting k_{ext} to a very small number, such that, the optical free path of the photons is greater than the distance from their starting positions to the surface along their trajectory. Figure 4-21 shows T_a as a function of ω_0 and g for a given τ and reveals that no unique solution will exist, with the same transmission predicted for different combinations of ω_0, and g.

The implications of multiple solutions for different values of ω_0, g and τ are significant, resulting in erroneous retrieval of the dust particles single scattering properties. Therefore reasonable constraints had to be applied to the retrieval routine. One method is to restrict the potential values of ω_0 and g by using results from similar studies to define an upper and lower limit for each wavelength. However this method is essentially forcing the result to converge

within the defined limits of dust components which may have a different composition and particle size distribution to the measured particles. For this reason it was decided to base our constraints primarily on the observed attenuation during the dust devil transits.

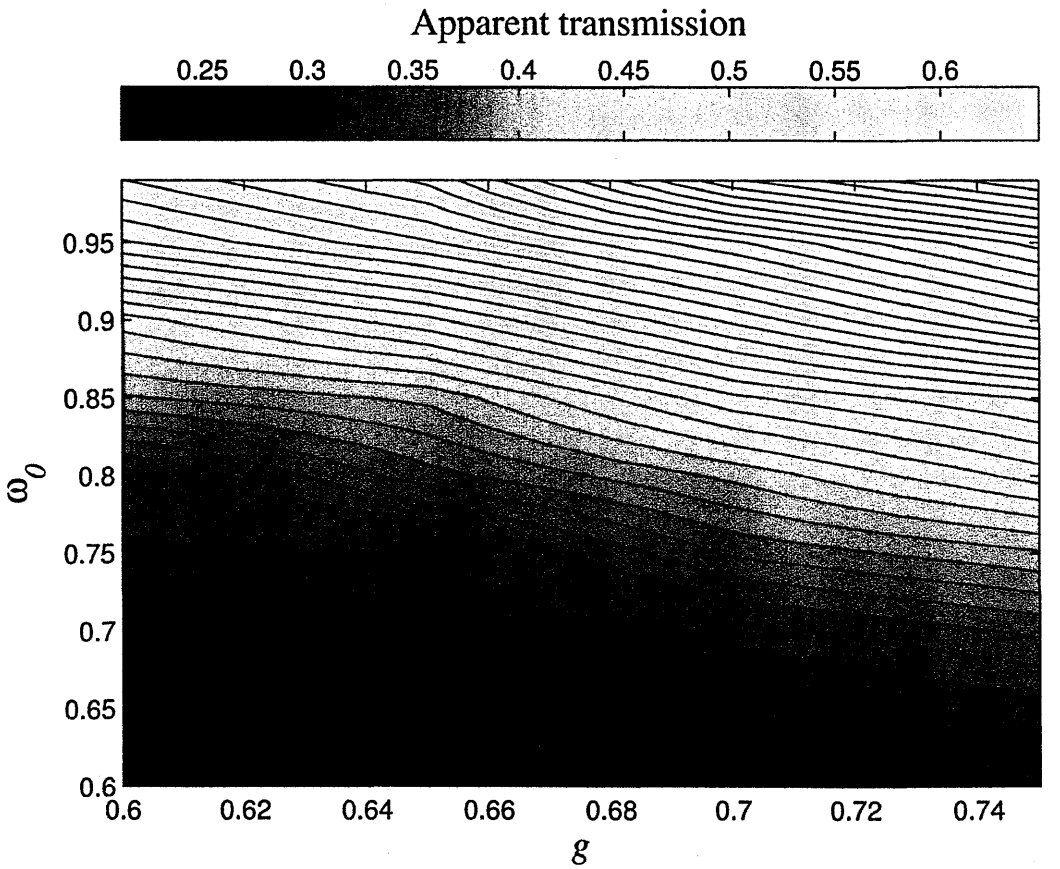

Figure 4-21: T_a as a function of ω_0 and g. No unique solution will be found since the same T_a is observed for different combinations of ω_0 and g. .

The transmission of light for each encounter is shown in Figure 4-22 and, with the exception of E4 and E5, is approximately constant above 600 nm. This indicates that the amount of scattered light received at these wavelengths is similar, hence an approximately constant ω_0 and g. Below 600 nm the transmission decreases, owing to higher absorption by the dust particles, leading to a decrease in ω_0 towards shorter wavelengths. Encounters E4 and E5 do not exhibit a constant transmission at wavelengths longer than 600 nm. Furthermore, the decrease in transmission at shorter wavelengths is enhanced in comparison to the other encounters. This is

consistent with the hypothesis that E4 and E5 contained larger particle sizes relative to E1–E3, resulting in higher absorption at all wavelengths.

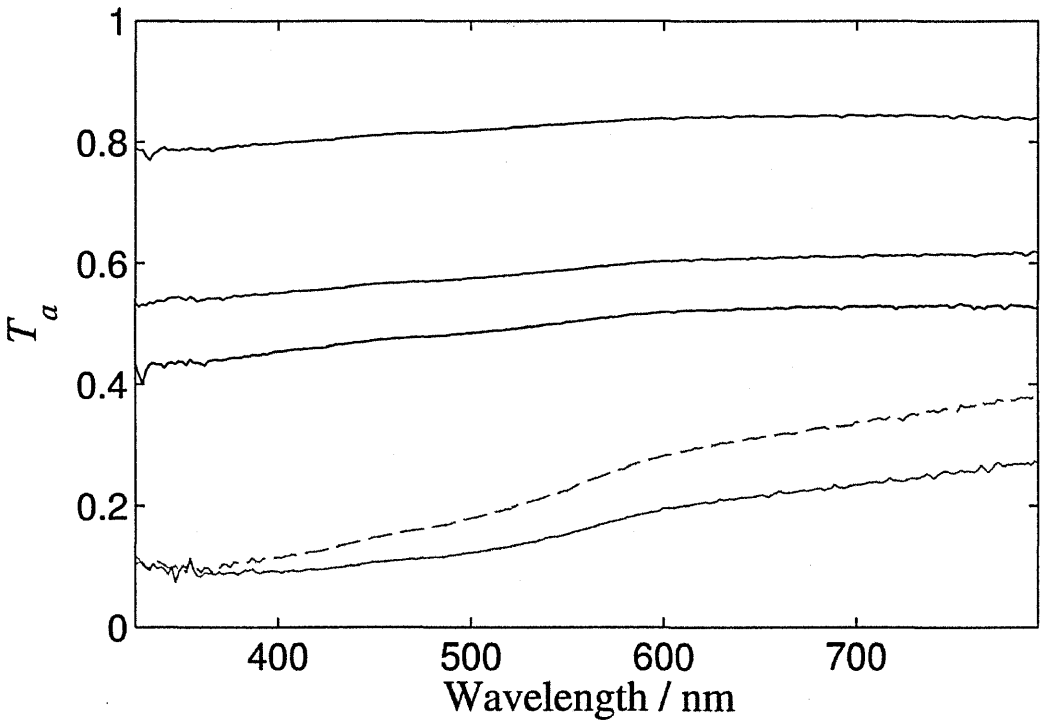

Figure 4-22: T_a as a function of wavelength for the different dust devil encounters.

From the transmission spectrum it can be deduced that ω_0 increases towards longer wavelengths. Therefore a constraint was applied to the retrieval routine such that $\omega_0(\lambda_1) \leq \omega_0(\lambda_2) \leq \omega_0(\lambda_3) ... \leq \omega_0(\lambda_n)$. At longer wavelengths (> 1000 nm) this condition is expected to break down, however as shown by Reid *et al.* (2003) the constraint is valid over the wavelength region of interest. After examination of g as a function of wavelength for different particle size distributions (Figure 4-18) it was assumed that g had to obey the constraint $g(\lambda_1) \geq g(\lambda_2) \geq g(\lambda_3) ... \geq g(\lambda_n)$. To further reduce the number of possible solutions a secondary constraint was applied, confining the possible values of ω_0 and g for the subsequent wavelength. The ω_0 and g wavelength dependence for the different size distributions (Figure 4-18 and Figure 4-19) show that variations in ω_0 and g greater than 0.05 do not occur over a wavelength increment of 50 nm, therefore it was assumed that:

$$\omega_0(\lambda_i) \geq \omega_0(\lambda_{i-1}) + 0.05 \tag{4.6}$$

$$g(\lambda_i) \leq g(\lambda_{i-1}) - 0.05 \tag{4.7}$$

Placing reasonable constraints on $\tau(\lambda)$ was more difficult as, depending on the quantity of fine particles, $\tau(\lambda)$ could either increase or decrease with wavelength. Therefore $\tau(\lambda)$ was chosen to obey the constraint, $\tau(\lambda_i) = \tau(\lambda_{i-1}) \pm 0.04 \times \tau(\lambda_{i-1})$, *i.e.* within 4% of $\tau(\lambda)$ for the preceding wavelength. The value of 4% corresponds to the mean difference in Q_{ext} between two adjacent wavelengths for the size distributions described in the previous section.

The retrieval process begins by finding the combinations of ω_0, g and τ for each wavelength that resulted in the modelled transmission to be within 1% of the measured transmission. All solutions for the shortest wavelength λ_1 are then cycled through sequentially and the ω_0, g and τ solutions obeying the above constraints for the next wavelength, λ_2, are filtered. One of these solutions for λ_2 is randomly chosen and the algorithm moves to the next wavelength where another solution conforming to applied constraints is randomly selected. The process stops once the longest wavelength λ_n is reached and the modelled transmission as a function of wavelength is compared to the measured transmission to produce a merit of fit value given by:

$$\chi^2 = \frac{1}{N_\lambda} \sum_{N_\lambda}^{i} \frac{\left(T_{dd}(0,\lambda_i) - T_m(0,\lambda_i)\right)^2}{T_{dd}(0,\lambda_i)^2} \tag{4.8}$$

where N_λ is the number of fitted wavelengths and $T_{dd}(0,\lambda)$ is the measured transmission, ($T_{dd}(t,\lambda)$), and $T_m(0,\lambda)$ is the modelled transmission ($T_m(t,\lambda)$) at the centre of the vortex ($t = 0$). If χ^2 is less than 10^{-4} (corresponding to a 1% error in transmission at each wavelength) then the solution is stored. The process repeats until all possible solutions are found or the maximum number of iterations (10^6) is reached (the algorithm was tested to ensure that all possible solutions were found, and with the above constraints, 10^6 iterations was sufficient). In total 10 wavelengths between 350 nm and 800 nm were selected for fitting. Ideally a larger number of wavelengths would have been fitted, however, adding additional wavelengths significantly

increased the computational time required for the retrieval process and therefore a compromise had to be reached.

4.4.3 Retrieval results

The applied constraints limited the number potential solutions, however as expected no unique solution was obtained for the different dust devil encounters. Therefore the retrieved $\omega_0(\lambda)$ and $g(\lambda)$ corresponding to the lowest χ^2 value and the standard deviation for each wavelength are shown in Figure 4-23. The retrieved $\omega_0(\lambda)$ for each dust devil indicates that the dust is more absorbing of light at wavelengths less than 550 nm and is more efficient at scattering light at wavelengths greater than 550 nm. These results are consistent with previously retrieved values of ω_0 for desert aerosols which range from 0.63 to 0.87 at 500 nm (Shettle and Fenn, 1976, WMO, 1983, Hess *et al.*, 1998) . The retrieved values for $\omega_0(\lambda)$ are lower in comparison to the results of Fouquart *et al.* (1987) who, using measurements from aircraft, determined ω_0 for the broadband solar spectrum to be 0.95 for Saharan dust. Furthermore, Dubovik *et al.* (2002) retrieved $\omega_0 > 0.9$ over the solar spectrum for desert aerosols at different locations on Earth agreeing with the results of Fouquart *et al.* (1987). The higher predicted absorption for Nevada desert sand particles (in the Eldorado valley) suggests that they either, have a different composition resulting in a higher imaginary refractive index (n_i) relative to the desert particles measured by Fouquart *et al.* (1987) and Dubovik *et al.* (2002) or the particles suspended within the dust devil are larger, leading to higher absorption of the incident solar radiation. The lower $\omega_0(\lambda)$ retrieved for encounters E1, E2, E4 and E5, compared to E3, correlates with the presence of larger particles suspended by these vortices, resulting in increased absorption of the incident light . This is consistent with the larger ΔP observed at the vortex centre, and the higher wind speeds observed for E1, E2, E4 and E5 relative to E3, making these dust devils more efficient at suspending larger particles.

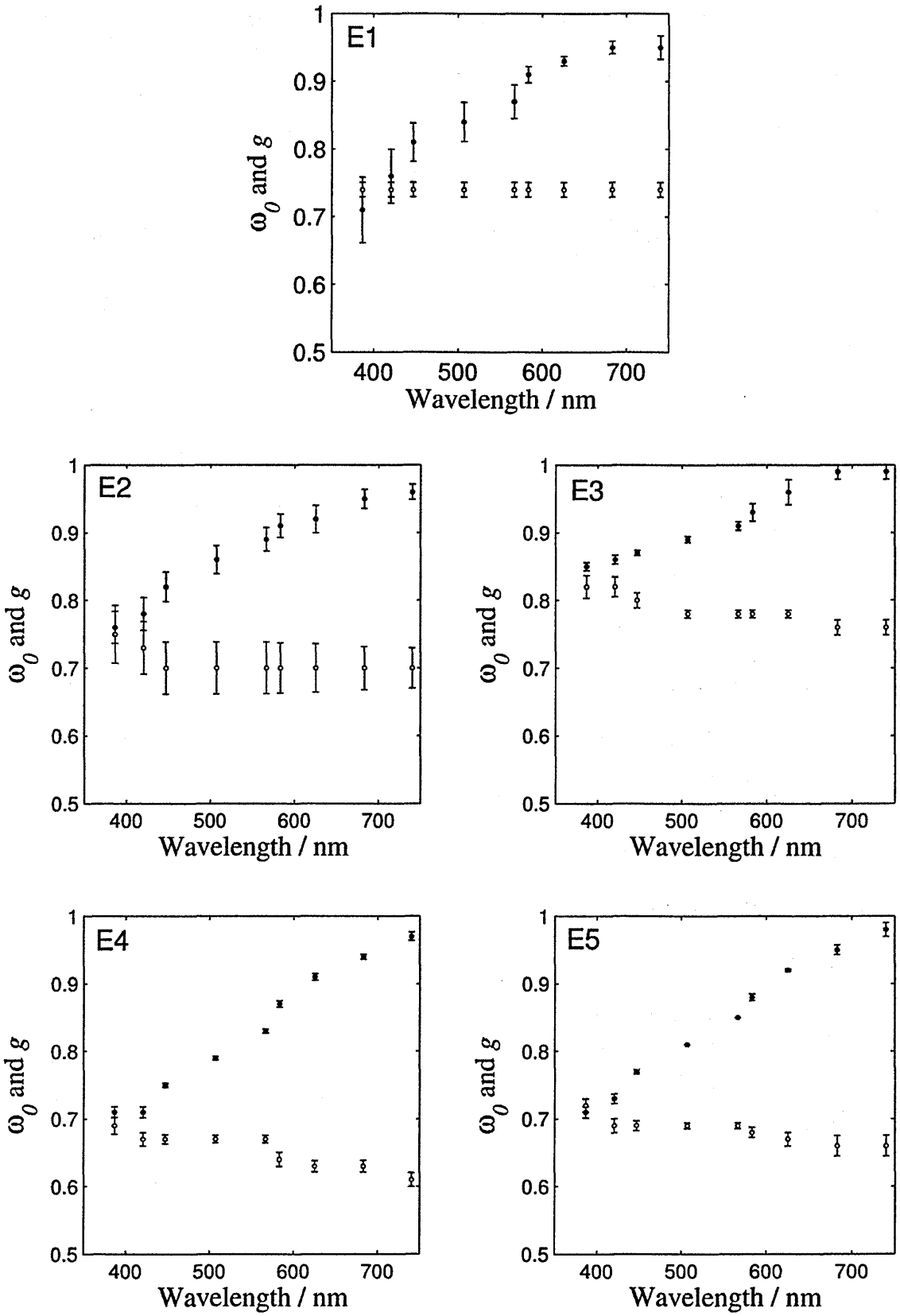

Figure 4-23: The retrieved $\omega_0(\lambda)$ and $g(\lambda)$ for encounters E1, E2, E3, E4 and E5. Closed circles represent ω_0 and open circles denote g.

A first order approximation of n_i for the suspended particles was performed. Sinclair (1974) determined a median particle radius of 0.6 μm for the particle number distribution in a small dust devil vortex. For the same dust devil, Sinclair (1974) also determined that the median particle radius for the mass distribution was 40.0 μm, with 70% of the mass contained within particles with a radius larger than 25.0 μm. Therefore, the particle volume size distribution was estimated using two log-normal distributions, Eq.(4.2), to describe the coarse and fine particle fractions. The median particle radius r_{vc} was held constant at a value of 40.0 μm (since volume is proportional to mass). The fraction of the total volume occupied by the coarse particles (V_c) and r_{vf} were varied until 70% of the mass was contained in particles with a radius greater than 25 μm and the median particle radius of the particle size distribution (r_m) was equal to 0.6 μm. The values of V_c and r_m that best matched the desired particle distribution was $V_c = 0.81$ and $r_{vf} = 1.21$ μm. The single scattering properties of the dust particles were calculated using Mie theory for different values of n_i for each of the wavelengths used to fit the $\omega_0(\lambda)$ profiles. The retrieved $\omega_0(\lambda)$ for E3 were then interpolated to find $n_i(\lambda)$. E3 was used as its physical size was the closest to the small vortex measured by Sinclair (1974). The particle volume distribution measured by Dubovik *et al.* (2002) for Bahrain-Persian Gulf desert aerosols was also used to estimate $n_i(\lambda)$, for the dust particles entrained in the dust devils, in order to determine the sensitivity of the retrieved $n_i(\lambda)$ on the particle size distribution. The retrieved $n_i(\lambda)$ for both distributions are shown in Figure 4-24 along with comparisons from other $n_i(\lambda)$ retrievals for desert aerosols. For the estimated particle size distribution using the values from Sinclair (1974), the retrieved $n_i(\lambda)$ for Nevada desert particles are consistent with the retrieved $n_i(\lambda)$ of Kaufman *et al.* (2001) and Dubovik *et al.* (2002) for desert aerosols in the Bahrain-Persian Gulf, Saudi Arabia and Cape Verde. The values presented in this study are slightly higher at wavelengths <450 nm in comparison to the Dubovik *et al.* (2002) values, however this could be due to natural variability in the particle composition. Applying a dust particle volume distribution more typical of dust aerosols (taken from Dubovik *et al.* (2002) for Bahrain-Persian Gulf dust), the retrieved $n_i(\lambda)$ are more consistent with the $n_i(\lambda)$ values from Patterson *et al.*

(1977) for sand particles in Tenerife, Sal Island, Sahara desert and Barbados. The higher $n_i(\lambda)$ values are due to a higher abundance of smaller particles in the assumed particle distribution, requiring n_i to increase in order to produce the same ω_0 as larger particles with a smaller n_i. Both retrieved $n_i(\lambda)$ values have larger errors at longer wavelengths; a result of progressively smaller variations in ω_0 for increasingly lower values of n_i, which the MCLSM is currently insensitive to.

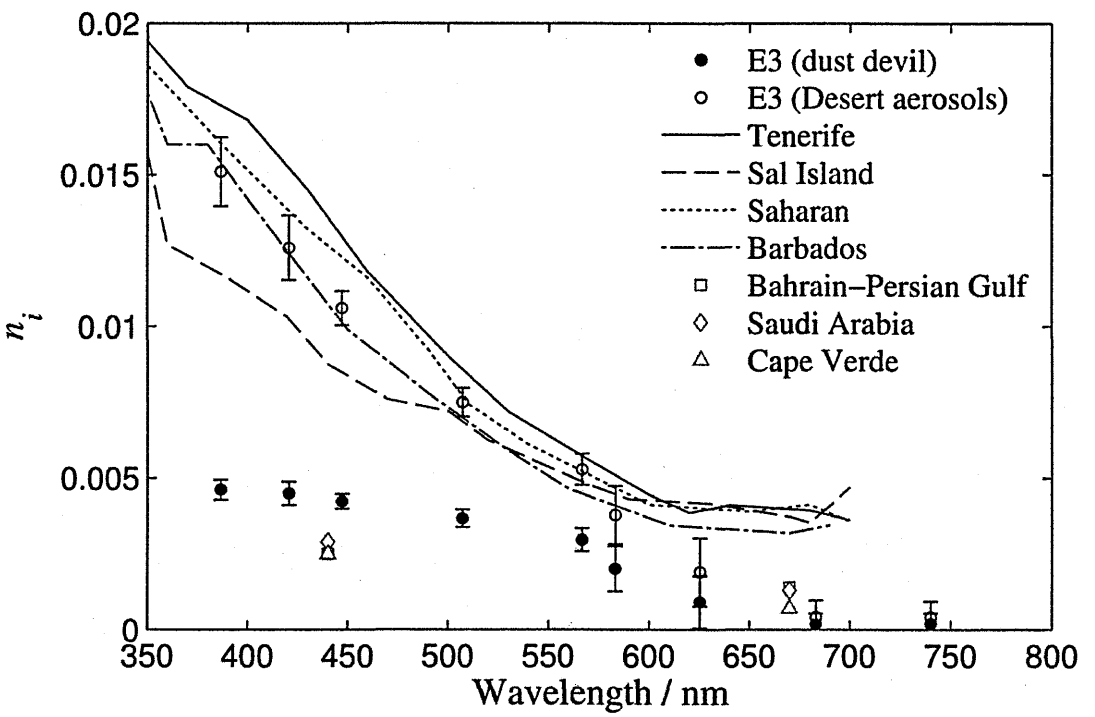

Figure 4-24: The retrieved refractive index as a function of wavelength for dust suspended in dust devil vortices in the Nevada desert. For comparison $n_i(\lambda)$ retrieved values by Patterson *et al.* (1977) for sand particles from Tenerife, Sal Island, Sahara desert and Barbados, and the retrieved $n_i(\lambda)$ for Bahrain-Persian Gulf , Saudi Arabia and Cape Verde from Dubovik *et al.* (2002) are shown.

As suggested by Sinclair (1974), the particle size distribution within dust devils will contain a greater quantity of larger particles and will be more analogous to soil particle distributions. Therefore it is concluded that the estimated particle size distribution using the values from Sinclair (1974) provides the best estimate for $n_i(\lambda)$ for Nevada desert aerosols.

4.5 Determination of the dust devil structure and vertical mass fluxes

As was shown in Chapter 3, fitting the dust devil transit signature can provide an estimation of the dust devil internal dust distribution and the dimensions of the dust column. The parameters in Table 4-1, the retrieved single scattering properties and τ for each dust devil were used to generate a model of transmission over the desert surface, as illustrated in Figure 4-25 for the two optical setups (NV and FS). A dust devil transit signature can be estimated by interpolating over the model surface.

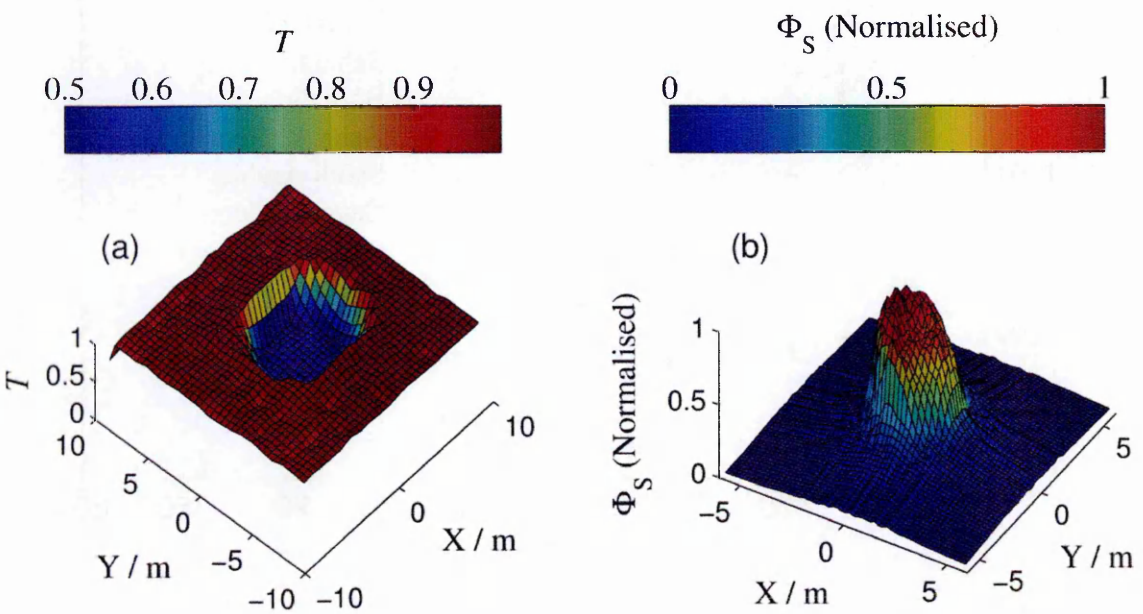

Figure 4-25: The transmission and normalised scattered light over the model surface for the two optical setups: (a) NV and (b) FS.

The dust devil encounters E1–E5 measured the total surface irradiance at the surface and, as shown in Chapter 3, this causes their transit signature to be insensitive to variations in the dust devil internal structure. This permits the assumption that the dust concentration within the dust devils is constant, *i.e.* no lower dust concentration within the core. To determine whether the MCLSM would produce accurate retrieval of the dust devil transit parameters, the bearing and velocity were iterated about the values given in Table 4-1and an additional parameter defining the offset from the dust devil centre was also iterated. The offset was left as

a free parameter between 0 and a maximum value equal to the dust devil outer radius. The transit signature corresponding to a given offset and bearing is found by interpolating over the modelled surface, while the velocity is used to convert the model spatial coordinates to time. The "goodness" of the fit is determined by modifying the merit value in Eq.(4.8) to:

$$\chi_t^2 = \frac{1}{N_t} \sum_{N_t}^{i} \frac{\left(T_{dd}(t_i,\lambda) - T_m(t_i,\lambda)\right)^2}{T_{dd}(t_i,\lambda)^2} \tag{4.9}$$

where $T_{dd}(t_i,\lambda)$ and $T_m(t_i,\lambda)$ are the measured and modelled transmissions during the dust devil transit respectively and N_t is the number of data points fitted in the encounter timeseries. As discussed in Section 4.3, the leading edges of the dust devil transit signatures are contaminated by dust lofted by the chase vehicle and peripheral dust around the vortex. These currently cannot be modelled, therefore only the portion of the transit signature associated with the dust devil interior is fitted.

Figure 4-26 shows the best model fit for the transits of the investigated encounters using the FS setup (E1–E5). The simulated transit signatures are consistent with the measured transit signatures, with the best fits observed for the large dust devils E4 and E5 which both had a high dust concentration. The MCLSM is less able to reproduce the transit profiles for vortices with low dust concentrations such as encounter E3. This is likely a result of complex heterogeneities in the dust distribution within the dust column, causing the observed τ to vary significantly during the encounter.

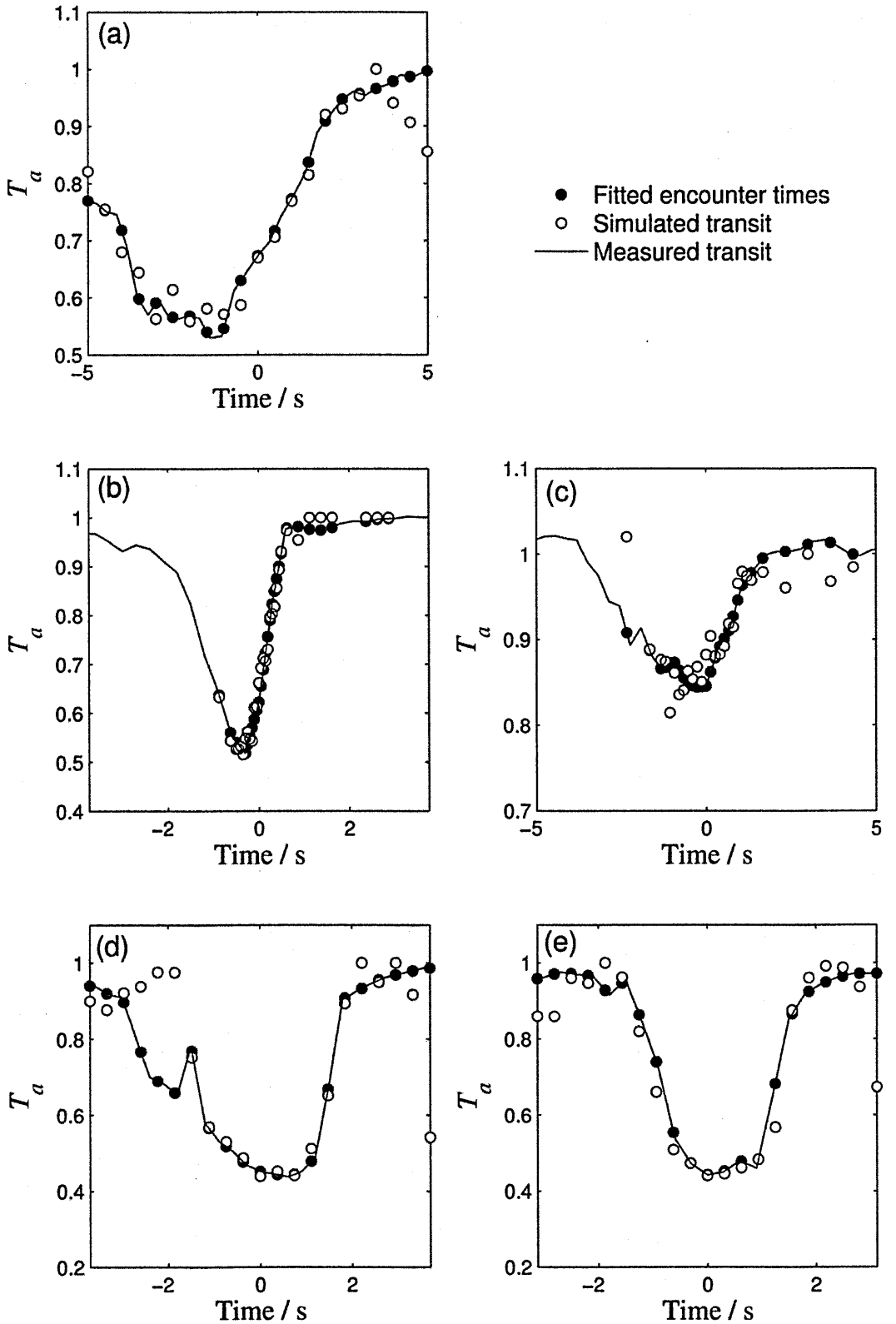

Figure 4-26: Model fits of the dust devil transit signatures for E1, E2, E3, E4 and E5.

The transit parameters corresponding to the best model fit for the transit signatures of E1–E5 are given in Table 4-2. The vortex surface velocities for encounters E2, E4 and E5 are in good agreement with the estimated values (Table 4-1). The fitted bearing shows a larger variation with good correlation observed for encounter E1 and lesser agreement for encounters E2, E4 and E5. The error in the bearing for encounter E2 is likely the result of the extreme intensity of this vortex. This resulted in rapid changes in the dust devils direction and velocity across the playa. The transit geometry for encounter E4 and E5 was close to perpendicular and the extreme physical dimensions and dust loading made the model transit profile relatively insensitive to small changes in the dust devil transit direction.

Encounter	**Surface velocity / m s^{-1}**	**Bearing relative to illminated wall / °**	**Offset in Y-axis from centre / m**
E1	4.0	252	1.4
E2	8.0	152	1.2
E3	3.0	256	1.0
E4	5.4	86	-0.2
E5	6.4	80	-0.6

Table 4-2: The best fit model parameters for encounter E4 and E5.

The fitted $n_i(\lambda)$ for encounter E3 provided an estimate for the extinction cross-section (C_{ext}) of the dust particles. Using C_{ext} and the retrieved $k_{ext}(\lambda)$ for the different encounters (from the fitted transmission spectrum) the total number of particles suspended in the vortex was estimated from the relationship $k_{ext} = C_{ext}N$, where N is the dust concentration. With the particle number density known, the particle volume density was determined by interpolating the volume size distribution and, assuming a dust particle density of 1600 kg m^{-3} for the desert sand, the total mass concentration was estimated. The vertical velocity was taken from Metzger *et al.* (2011) which had similar dust devil radii to those analysed in this study. Table 4-3 shows the retrieved k_{ext} at 386 nm, the calculated mass concentration, assumed vertical velocity and the vertical mass flux of material for E1–E5. The vertical mass flux provides a measure for the

amount of material injected into the atmosphere per unit time; thus knowing the life-time of the dust devil can permit estimation of the total mass of material injected into the atmosphere.

Encounter	k_{ext} at 386 nm / m^{-1}	Mass concentration / mg m^{-3}	Vertical velocity / m s^{-1}	Vertical mass flux / mg m^{-2} s^{-1}
E1	0.0	4.0	1.2	4.8
E2	0.1	12.4	1.6	19.8
E3	0.0	4.1	1.6	6.6
E4	0.4	40.3	2.3	92.8
E5	0.4	40.1	2.3	92.3

Table 4-3: The retrieved k_{ext} at 386 nm, mass concentration, assumed vertical velocities and the calculated vertical mass flux.

The determined mass concentrations and vertical mass fluxes are consistent with those measured by Metzger *et al.* (2011) for particulate matter (particle diameter between 0.1 μm and 10.0 μm). The attenuation of the solar spectrum at UV and visible wavelengths is highly sensitive to the abundance of the small particles, of comparable size to the wavelength of observation, with larger particles having less of an influence. This explains the agreement between the mass concentrations derived in this study and the particulate matter concentrations found by Metzger *et al.* (2011) . The large dust devil of E4 and E5 had an extremely high dust loading and lasted for several minutes. This is similar to the documented event '2005 EV_16-06-05/1543' by Metzger *et al.* (2011) , with both examples exhibiting similar dimensions and dust loading. The peak mass concentrations determined for E4 and E5 are in good agreement with the mass concentration derived for the '2005 EV_16-06-05/1543' event of 98 mg m^{-2} s^{-1}. Furthermore, using a Light Detection And Ranging (LIDAR) instrument, Rennó *et al.* (2004) estimated a peak dust loading within terrestrial dust devils to be 100 mg m^{-3}, consistent with peak mass concentration determined for E4 and E5.

In order to fit the transit signature for E6, observed using the NV setup, a number of assumptions had to be made. Firstly, τ was unknown since only the scattered component was measured, therefore the τ measured by the Sun senor was used as an estimate. Secondly, retrieval of the single scattering properties for E6 was unsuccessful since inadequate

information on the total irradiance meant the total amount of light incident on the dust particles was unknown. Attempts were made to retrieve the single scattering properties by fitting the normalised attenuated spectrum, however this lead to erroneous retrieval of the dust particle single scattering properties. Comparing the visual references and video for E6 with encounters E1–E5 and the ΔP at the core, it was determined that the best approximation would be to use the retrieved $\omega_0(\lambda)$ and $g(\lambda)$ from E3.

The scattered component is sensitive to the dust concentration within the vortex. Therefore, the scattered light at the surface was modelled for vortices with different core radii, and dust concentration within the surrounding dust column walls. Fitting the transit signature follows the same procedure applied to the FS cases, with the addition of three variables: the extinction coefficient in the dust devil core and wall, $k_{ext\text{-}c}$ and $k_{ext\text{-}w}$ and the core radius (R_{core}). Figure 4-27 shows the three fitted transits for E6 (E6a, E6b, E6c) that correspond to the lowest χ_t^2 values, with all simulated transits showing good agreement with the measured scattered light signature. All fits predicated a R_{core} of 0.5 m with a $k_{ext\text{-}c}$ equal to 0.05 m^{-1}, while $k_{ext\text{-}w}$ had values of 0.125 m^{-1}, 0.25 m^{-1} and 0.45 m^{-1} for E6a, E6b and E6c respectively. The lower dust concentration in the dust devil core is consistent with the reduction in scattered light measured by the UV-VIS spectrometer and the predictions in Chapter 3.The trailing edge of the simulated dust devil shows closer agreement to the observed transit signature than the leading edge of the dust devil. It is proposed that this is the result of two possible mechanisms: contamination of the transit signature by dust lifted by the chase vehicle, or different dust concentrations in the leading and trailing walls.

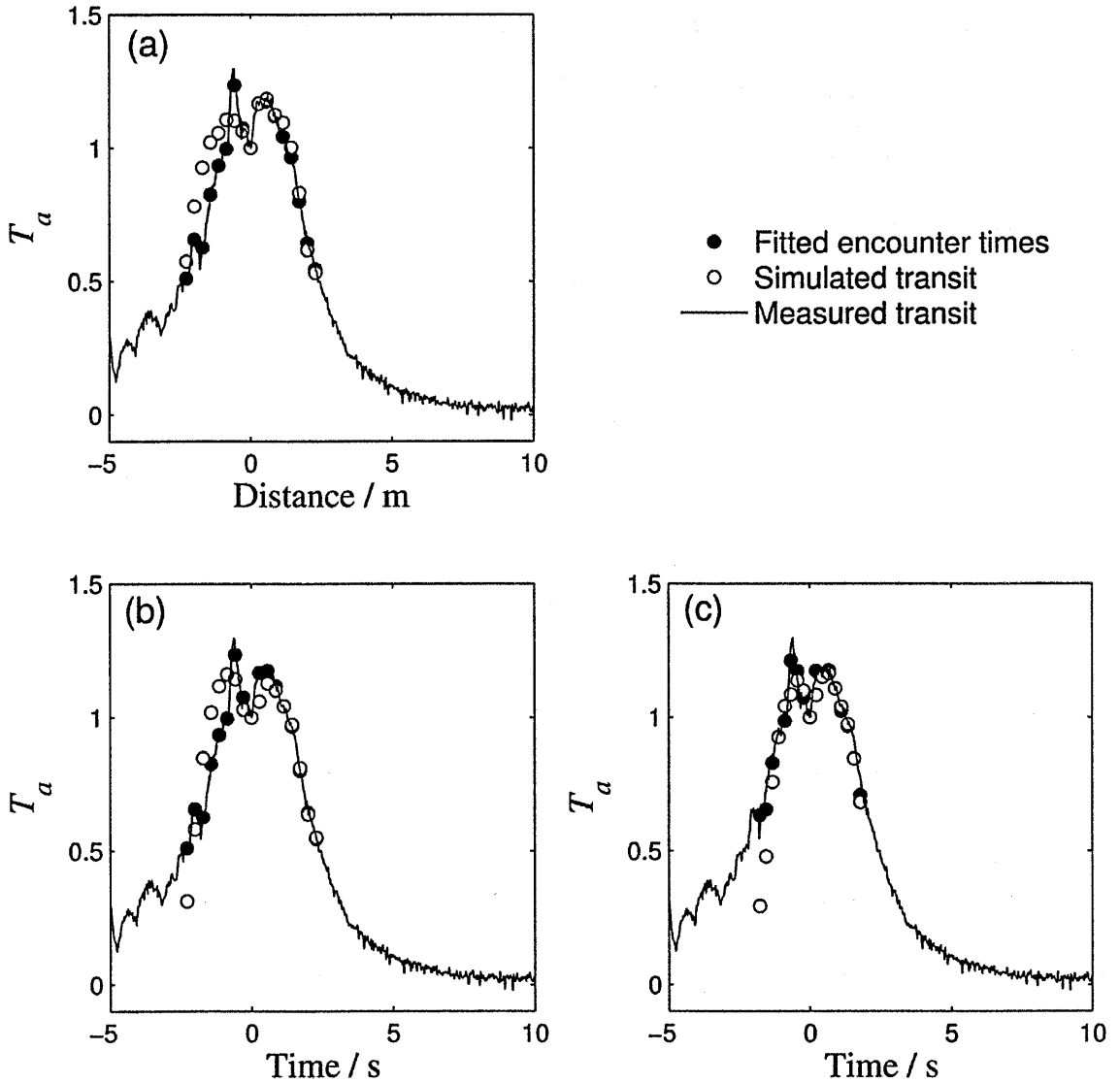

Figure 4-27: The best fit for different dust concentrations for E6.

The mass concentration was determined for the three simulated dust devils that best approximated the spectral signature of E6. The different $k_{ext\text{-}w}$ predicted in the dust devil wall resulted in mass concentrations of 13.5 mg m^{-3} for E6a, 48.7 mg m^{-3} in E6b and 22.6 mg m^{-3} for E6c.The mass concentration in the core of the vortices was determined to be 0.514 mg m^{-3}. Therefore the core contains significantly less dust than the surrounding walls; furthermore, vertical velocities in the core are generally small or even negative, *i.e.* downward flow (Sinclair, 1973), resulting in zero mass flux into the atmosphere. This highlights the importance of determining the dust distribution and vertical velocities within dust devils as these parameters will enable more accurate determination for the mass of particulate material injected into the

atmosphere. Absence of a total irradiance measurement during this encounter leads to an uncertainty in the mass concentration in the dust devil wall of up to 70%. This supports the requirement for simultaneous measurement of both the scattered and total light during a dust devil transit in order to obtain accurate mass concentrations.

4.6 Summary of results

The MCLSM has been successfully applied to dust devil vortices in the Eldorado Valley (Nevada). By simulating the transmission of light through dust devil vortices, an estimation of the dust particle single scattering properties and the imaginary refractive index of Nevada desert aerosols have been retrieved from spectral measurements during a dust devil transit. The retrieved single scattering properties were used successfully to determine the dust devil physical dimensions, internal distribution and core size for encounter E6 for which, the scattered light was measured. Finally, using the estimated $n_i(\lambda)$ to determine the particle extinction cross-section, the total mass and vertical mass flux was calculated. The results are consistent with a previous investigation of dust devils in the Eldorado Valley by Metzger *et al.* (2011). Uncertainty in the dust particle size distribution limits the accuracy of these results, however they serve as a good first order approximation, with the retrieved $n_i(\lambda)$ and calculated vertical mass fluxes consistent with similar studies into desert aerosols (Dubovik *et al.*, 2002) and terrestrial dust devils (Metzger *et al.*, 2011, Rennó *et al.*, 2004) respectively. Good correlation to these other studies validates the use of spectral measurements during dust devil transits as a technique for characterising terrestrial and martian dust devils, and the retrieval of the optical properties of the suspended dust particles.

Chapter Five: Effects of dust and ice aerosols on the downward irradiance at the martian surface

In this chapter the effect of dust and ice aerosols on the surface irradiance spectrum between 180–1100 nm is assessed over two Mars years using a radiative transfer model (RTM) of the martian atmosphere developed by Patel (2003) and Otter (2010). The attenuation of surface irradiance spectrum resulting from different aerosol species (airborne dust and ice particles of different size and composition) is explored and a method for differentiating between aerosols and retrieving of the ice particle size is discussed. Finally, the Monte Carlo Light Scatter Model (MCLSM), described in Chapter 3, was adapted to predict the optical signatures of martian dust devils.

5.1 Mars radiative transfer model

The martian RTM covers the wavelength region 180 – 1100 nm with a 1 nm resolution (Patel *et al.*, 2002, Patel, 2003, Patel *et al.*, 2004, Otter, 2010). The two stream delta-Eddington approximation (Joseph *et al.*, 1976) is used to simulate the interaction of the incident solar flux with the constituent components of the martian atmosphere. The output is an approximation of the downward surface irradiance at a local location on the planet surface (Otter, 2010). Two possible interactions can occur between the atmosphere and the incoming solar flux and are characterised as either scattering or absorption events. Absorption events will reduce the amount of light received at a particular wavelength at the surface, since absorbed radiation will tend to be re-emitted at wavelengths longer than that of the incident photon. Scattering events can either increase or decrease the light received depending on whether the photons are scattering into or out of the path of the incident solar flux. The total irradiance at the surface is the sum of the direct component and the diffuse component. The direct component describes radiation that has

passed through the atmosphere without interaction and the diffuse component is radiation that is scattered back into the path. An illustration of the direct and diffuse components is given in Figure 5-1.

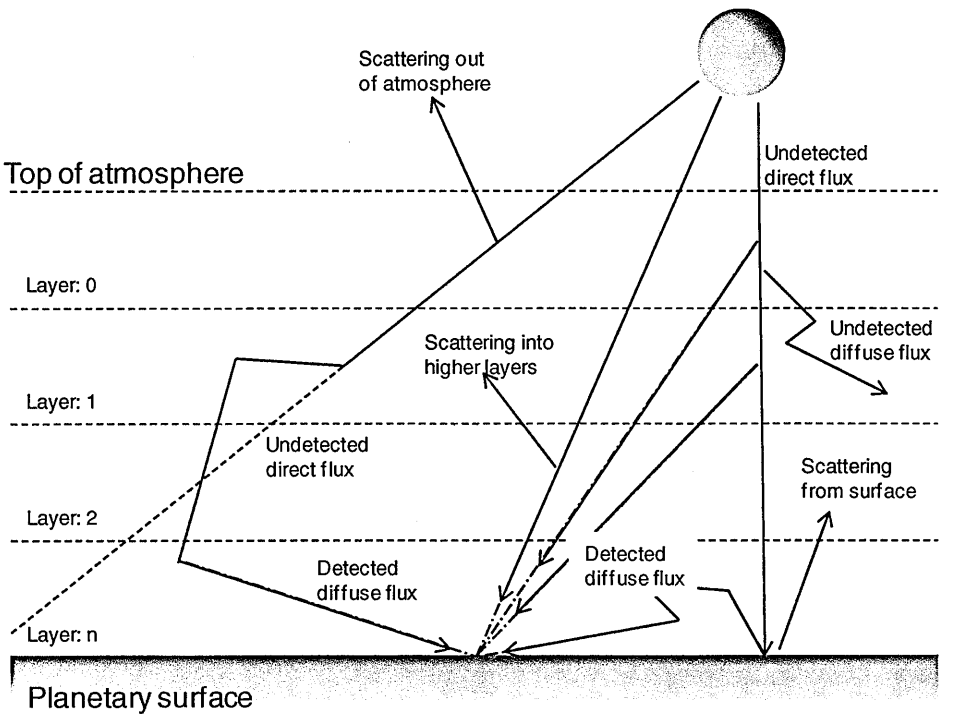

Figure 5-1: Illustration of how the incident light interacts with the layered atmosphere of the delta-Eddington approximation. Also shown are the interactions between the incident solar radiation and the planet's atmosphere resulting in the direct (blue lines) and diffuse (red lines) components, adapted from Otter (2010).

A simulated martian surface irradiance spectrum at local noon is illustrated in Figure 5-2 for a dust optical depth (τ) of 0.3, corresponding to the average opacity observed by the MER rover Spirit during northern summer (Lemmon, 2004). The presence of dust in the atmosphere increases the probability that incident solar radiation will be scattered and as a result the martian surface receives a relatively high diffuse component (~35% of the total observed irradiance).

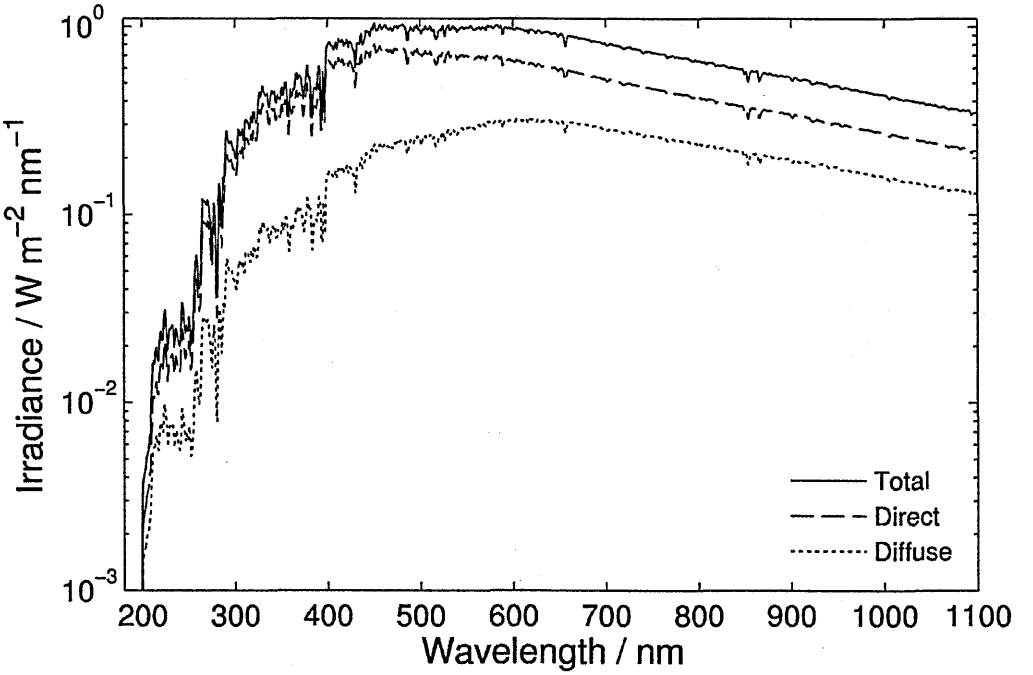

Figure 5-2: Simulated irradiance at the martian surface for an atmosphere with $\tau = 0.3$.

5.2 Effect of martian airborne dust on the downward irradiance at the surface

The following sections investigate the effect of airborne dust on the surface flux in the 180–1100 nm wavelength region for two Mars years, MY27 and MY28. The investigations use the atmospheric optical depths measured by Spirit during MY27 and MY28 which are shown in Figure 5-3 along with the atmospheric optical depths for MY29. The observed τ show a seasonal dependence, with low τ (0.2-0.4) observed during northern summer (aphelion) and higher τ (> 0.8) in southern summer (perihelion). A large increase τ is observed in MY28 compared with MY27 and MY29 between L_s = 270-330° and is associated with the presence of a large dust event.

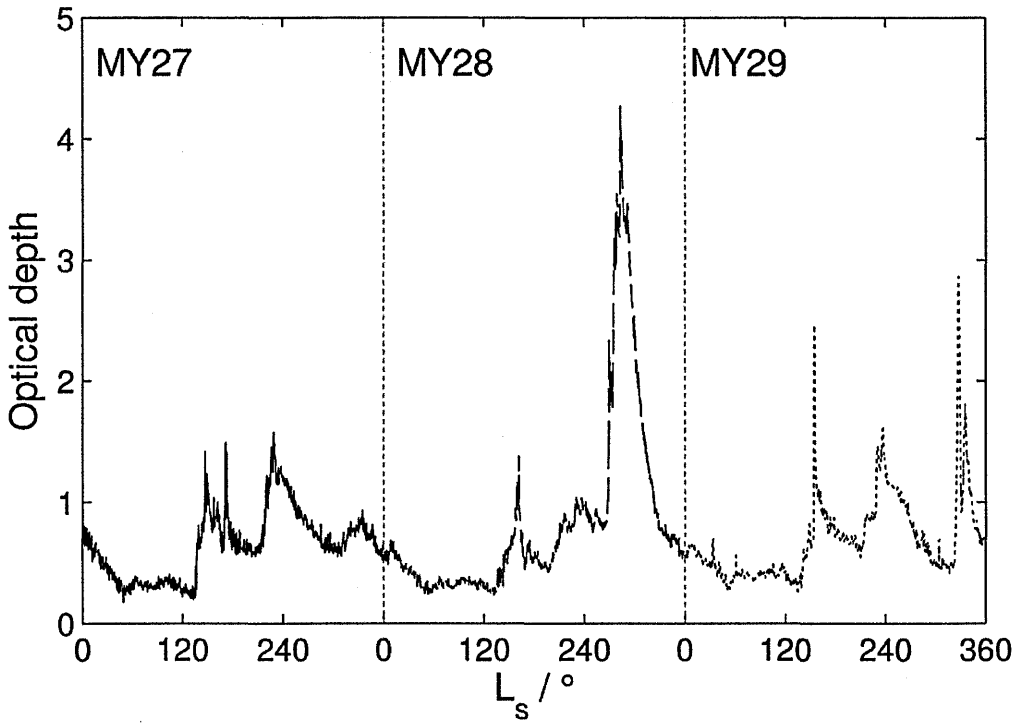

Figure 5-3: Optical depth measured by the Spirit rover during MY27, MY28 and MY29 (Lemmon, 2004).

Throughout this chapter, extensive use is made of the single scattering properties for martian dust retrieved by Ockert-Bell *et al.* (1997) and Wolff *et al.* (2009) and are referred to O97 and W09 from this point. A comparison between the two dust types is given in Section 5.2.2. Furthermore, unless stated otherwise, Table 5-1 shows the input parameters for the model. A latitude of 14.8° S was selected, as this coincides with the location of the Spirit rover.

Parameter	Value
Time of day	Local noon
Latitude	14.8° S
Solar Longitude (L_s)	121°
Dust Maximum Altitude	70 km
Conrath Parameter	0.007
Optical Depth (670 nm)	0.5

Table 5-1: Parameters used in the radiative transfer model.

5.2.1 Impact of dust on the downward surface irradiance

The simulated spectrum in Figure 5-2 is for low atmospheric dust content ($\tau = 0.3$). As Mars approaches perihelion, dust activity increases causing τ to exceed unity. The increased dust content of the atmosphere increases the amount of incident solar radiation scattered, leading to an increase in the diffuse component and a decrease in the direct component. Figure 5-4 shows direct, diffuse and total surface flux at local noon as a function of τ for W09 (black lines) and O97 (grey lines). As discussed by Otter (2010) the presence of dust in the martian atmosphere can, under certain conditions, cause the observed total surface irradiance to increase above the Top of the Atmosphere (ToA) value. This is a result of an increase in diffuse irradiance received at the surface as the dust opacity increases. During the analysis, Otter (2010) assumed the single scattering properties of O97 for the dust particles and found an increase over the ToA irradiance to be approximately 13% at $\tau = 1.2$. A larger increase of nearly 20% is observed at a higher opacity of 1.8 when substituting in W09. The point at which the total surface irradiance falls below the ToA value also varies as a result of the different dust single scattering properties and occurs at a τ of ~4.1 for W09 compared to ~2.7 reported in Otter (2010) for O97.

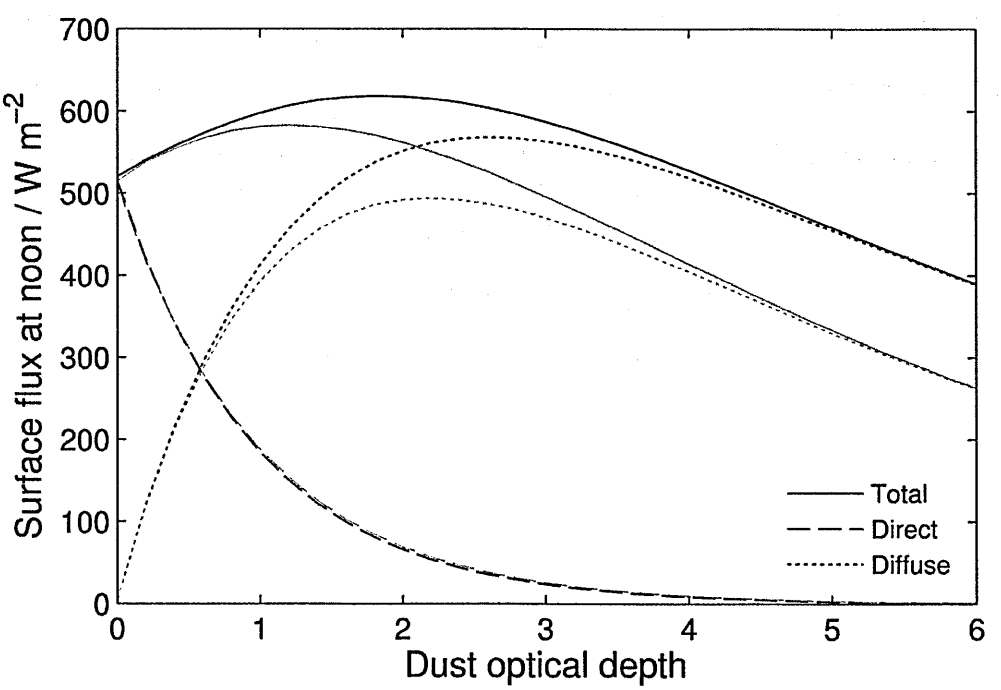

Figure 5-4: The surface flux at noon as a function of τ at the location of the Spirit rover. The solid line represents the total surface flux between 180–1100 nm. The back lines represent W09 and the grey lines denote O97 dust component.

The above analysis shows that variation in the dust particle single scattering properties has only a small impact on the surface flux at τ less than 0.58 (*i.e.* τ at which the diffuse and direct component contribute equally to the combined irradiance). At $\tau > 0.58$ the diffuse component forms a greater portion of the combined irradiance and as a result the surface irradiance becomes more sensitive to the scattering properties of the dust particles. The outcome is an almost 20% difference in total surface irradiance between W09 and O97.

Local noon corresponds to the time when the lowest airmass is encountered by the incident radiation. Earlier or later in the martian day the amount of atmosphere through which the incident radiation must travel increases, increasing the probability of scattering or absorption by dust particles. Figure 5-5 shows direct, diffuse and total surface flux as a function of τ for three hours before local noon. As was seen for the noon surface flux, the variation in the total surface flux resulting from two different dust components is small at low τ and only becomes significant once the diffuse component becomes the main contributor. However, unlike noon, the surface flux observed in the morning does not surpass the ToA value. This is because the increased path length through the atmosphere causes a greater portion of the incident radiation to be absorbed by the dust particles. Furthermore, lower solar zenith angles (θ_z) require the angle through which the incident radiation must be scattered in order to be detected to increase. The scattering phase function of the dust particles (see Chapter 2) indicates that less light is scattered at larger scattering angles, hence as θ_z decreases the diffuse component is reduced. Therefore the lower rate at which the diffuse component increases with increasing dust loading is insufficient to make up the loss in the total surface flux from the reduction in the direct component.

Figure 5-4 and Figure 5-5 illustrate that once the diffuse component becomes larger than the direct component, the surface irradiance becomes sensitive to changes in the dust particle single scattering properties. In the two cases considered a higher surface flux is observed for a W09 dust component than an O97 dust component.

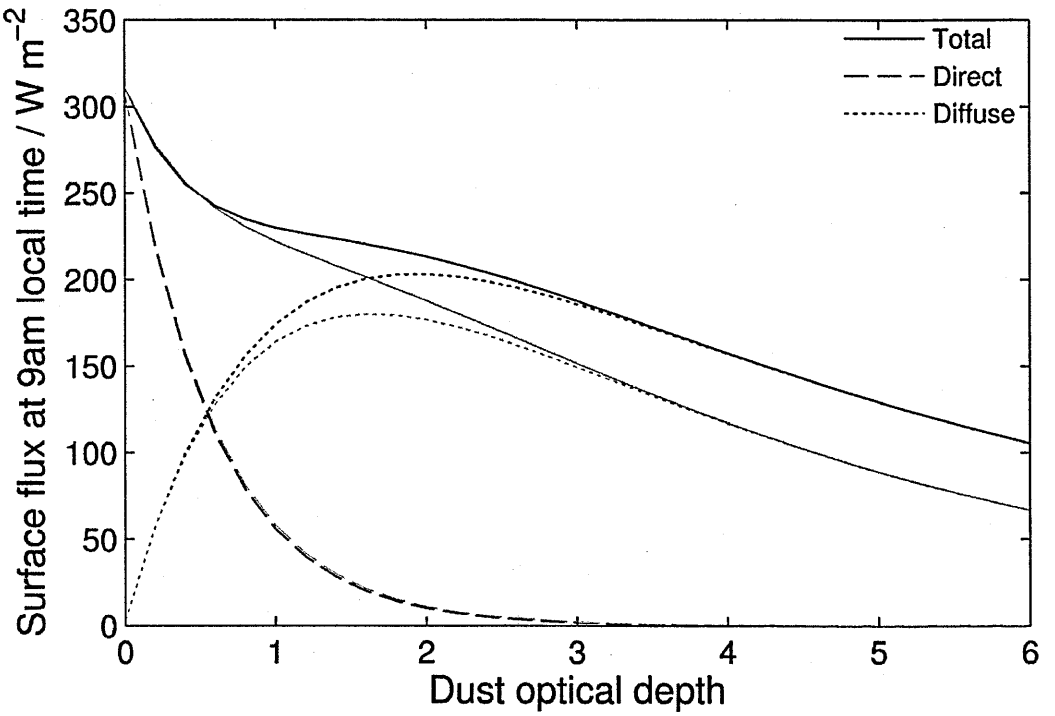

Figure 5-5: As figure 5-4 except for 9am local time.

The impact of dust on the surface flux, at noon, as a function of L_s is shown in Figure 5-6 for MY27 and MY28 with dust components described by O97 and W09. A reference scenario with no dust present in the atmosphere is also shown. During both MY27 and MY28 the dust has only a small effect on the total surface irradiance in northern summer, with a 5% difference relative to the dust free case. The dust has a greater impact on the surface flux during southern summer with an increase of 15% observed. The difference in the total surface irradiances between the W09 and O97 dust component are negligible under the low opacity conditions expected in northern summer. In the dustier southern summer, total surface irradiances are predicted to be 1–5% higher for a W09 dust haze relative to a dust haze composed of an O97 dust type. During the MY28 dust storm a W09 dust haze displays a total surface flux greater than 10% higher than the O97 dust haze.

The large dust storm between L_s = 265-320° is clearly evident and, for an O97 dust component, results in a noticeable decrease in total surface irradiance below the dust free case. At the point of peak τ (L_s = 283°) the total surface flux is reduced by 27% and 36%, relative to

MY27 and the dust free scenario. For W09 a decrease in surface irradiance is observed during the dust storm but this value is 11% higher than the dust free case.

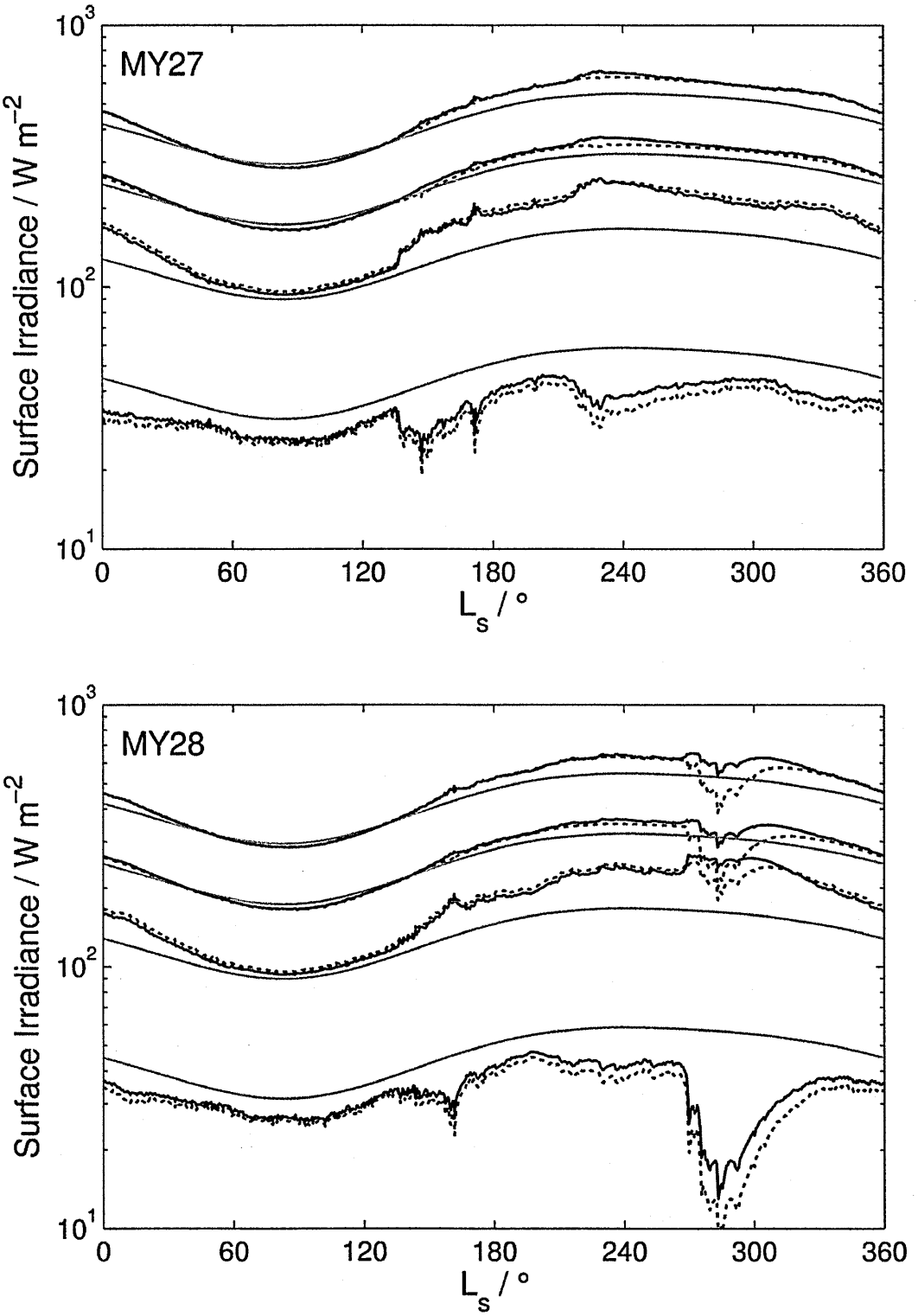

Figure 5-6: The total (black lines), visible (green lines), NIR (red lines) and UV (blues lines) noon surface flux as a function of L_s for MY27 and MY28. The solid and dashed lines denoted W09 and O97 single scattering properties respectively.

In northern summer the dust haze during MY27 and MY28 is stable around $\tau = 0.2–0.4$. At these the dust opacities the impact of dust on the surface flux is small. Under typical southern summer conditions the total surface flux can be expected to increase above the ToA value at noon. Large dust storms significantly reduce the surface flux but the large τ make the observed irradiance highly sensitive to the optical properties, and hence composition, of the dust component. The 28% change in the total surface flux between O97 and W09 during the MY28 dust storm implies that such events are invaluable for investigating potential heterogeneities in the background dust haze.

Separating the irradiance into different wavelength regions (UV, Visible, and NIR) provides insight into the portion of the UV-NIR spectrum most affected by the presence of dust. Relative to the dust free case, the highly absorbing nature of martian dust in the UV results in the observed UV irradiance being consistently ~15% and ~30% lower in northern and southern summer respectively. This will reduce the UV dose received at the martian surface. In northern summer the visible and NIR regions show less variability with ~5% less irradiance in the visible and ~8% increase in the NIR flux received at $L_s = 90°$ in comparison to the 'no dust' case. As the dust content in the atmosphere increases towards $L_s = 270°$, the visible and NIR irradiances show an increase of 10–15% and 30–50% above the dust free scenario respectively.

In the UV region, larger changes in the UV flux are predicted between the two dust components O97 and W09, especially during southern summer and through the MY28 dust storm peaking at approximately 35% (dust storm) and 10% (southern summer). In the expected nominal conditions less variance is seen between O97 and W09 in the visible and NIR compared to the UV, with < 1% observed at $L_s = 90°$ and ~3% at $L_s = 283°$ (MY27). At the time of the MY28 dust storm a considerable difference between O97 and W09 is observed in the visible and NIR regions, with the O97 dust experiencing a dramatic decrease in irradiance at both visible and NIR wavelengths. The W09 dust exhibits an increase in irradiance in both regions at the onset of the dust storm. As the dust content increases further, the visible irradiance sees a correlated decrease, however at the point of peak τ the O97 and W09

components show a difference in surface irradiance of ~30%. For W09, the NIR region displays a continuing increase in irradiance and at peak opacity W09 predicts 25% more NIR irradiance than O97. Note that during the MY28 dust storm the observed NIR irradiance is still 12% (O97) and 50% (W09) higher than the dust free atmosphere scenario.

Measuring the total surface flux provides only limited information about the scattering species in the atmosphere and little variation in the total surface flux was found between the two dust components O97 and W09 under nominal τ values. At $\tau > 3.0$, this difference becomes significant, but such values of τ are rare outside of large dust events. Therefore taking nominal conditions, the impact of varying the dust single scattering properties on the total surface irradiance at the Spirit Rover location is small.

As the atmospheric dust loading increases the total surface flux increases above the top of the atmosphere value and indicates that more solar energy is deposited into the atmosphere than would be present for a dust-free atmosphere. This will affect the atmospheric heating rate, which feeds back into the atmosphere circulation and dust lifting. Dividing solar spectrum into ultraviolet (UV,190-400 nm), visible (401-750 nm) and near infrared (NIR, 751-1100 nm), bands reveals that the increase in surface flux is due to the higher irradiances at the visible and NIR wavelengths as the dust content increases. This is a result of martian dust being more efficient at scattering light at these wavelengths. This highlights the importance of accurate retrieval of the dust particle optical properties in the visible and NIR, as these will determine the amount of additional solar radiation that reaches the lower atmosphere and surface and, in turn, this will affect the atmospheric state.

5.2.2 *Effect of Q_{ext}, ω_0, and g on the irradiance spectrum*

In Chapter 2, the single scattering properties of martian aeolian dust were reviewed. As discussed, the differences in the retrieved extinction efficiency (Q_{ext}), single scattering albedo (ω_0) and asymmetry parameter (g) could be the result of many factors, namely the assumptions used in describing the dust particle characteristics (*i.e.* spherical or non-spherical). However, the

differences in the retrieved optical properties could be the result of spatial heterogeneity in the background dust component. To gain insight into the sensitivity of the surface irradiance spectrum to variations in the retrieved single scattering properties, the values retrieved by Pollack *et al.* (1995), Ockert-Bell *et al.* (1997) and Wolff *et al.* (2009) were entered into the radiative transfer model. The values of Q_{ext}, ω_0 and g were determined for the model wavelength range through spline interpolation and a comparison is shown in Figure 5-7. Also shown are the single scattering properties produced by Mie theory for randomly-orientated spheres, with the refractive indices taken from Ockert-Bell *et al.* (1997) and Wolff *et al.* (2009).

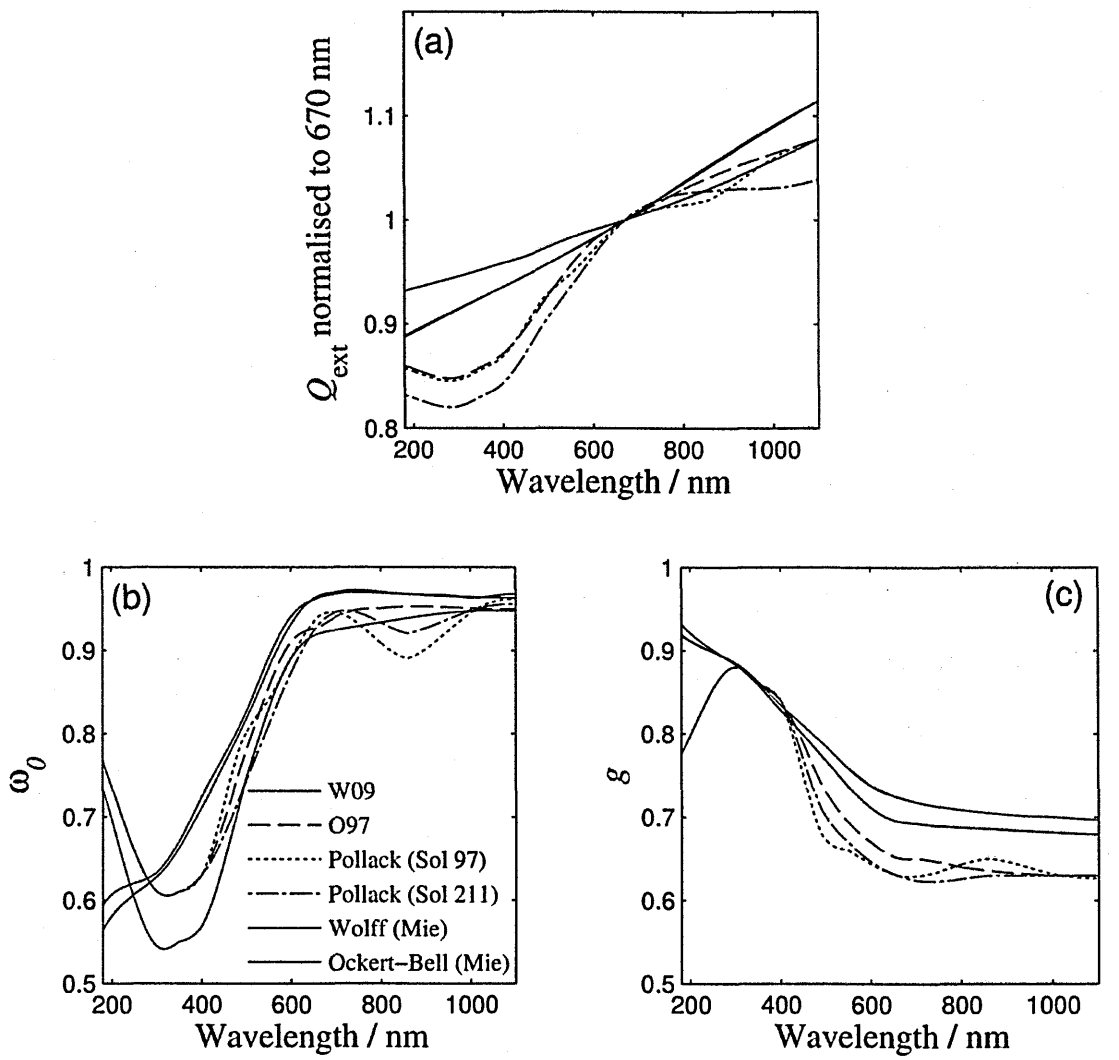

Figure 5-7: Comparison of the single scattering properties derived for martian aeolian dust including that produced by Mie theory for spherical particles.

A size distribution with $r_{eff} = 1.6$ μm and $v_{eff} = 0.4$ for the first and second moment is assumed (Wolff *et al.*, 2009). The most obvious contrast is in the single scattering properties calculated by Mie theory compared to the retrieved values. Mie theory predicts the particles will absorb more of the incident radiation at all wavelengths and that the scattering will be more anisotropic. A full comparison of the single scattering properties was given in Chapter 2.

The surface irradiance spectrum resulting from the different dust single scattering properties is shown in Figure 5-8a. The resolution of the model has been reduced to 10 nm to allow for better distinction between the dust components. Noticeable differences in the irradiance spectrum are observed as a result of varying dust single scattering properties. The spherical particle approximation for O97 (grey dashed line) shows between 10% and 15% less irradiance over the majority of the spectrum and highlights how poor an approximation the spherical particle assumption is for modelling martian aeolian dust. The spherical approximation for W09 shows closer agreement but still predicts ~5% less irradiance than a W09 dust component. Figure 5-8b shows the ratio of the surface irradiance produced by the different aerosols relative to the spectrum produced by O97. With the exception of the O97 spherical particle case, the variation in surface irradiance for the majority of the spectrum is ±5%. Larger differences (>10%) are observed at 400 and 850 nm but the most significant is the almost 15% decrease in irradiance produced by W09 in the UV (< 300 nm). These differences are associated with variations in Q_{ext}, ω_0 and g of 6.8%, 12% and 7.8% at wavelengths less than 280 nm and 6.3%, 8.7% and 0.6% change in the 315 – 400 nm wavelength region. This variance in the UV irradiance at the surface resulting from two different dust types forms the discussion of the next section.

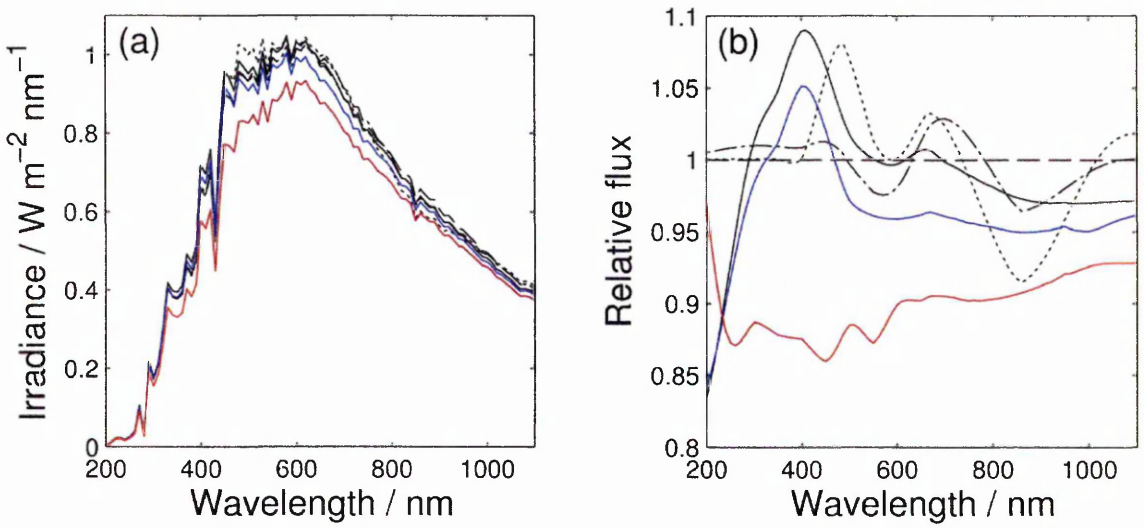

Figure 5-8: a) Surface irradiance spectrum for different dust components b) the irradiance ratio between the different dust components to O97. The dust components have the single scattering properties of W09 (Black line), O97 (dashed line), Pollack *et al.* (1995), sol 97 (dotted line) and Pollack *et al.* (1995), sol 211 (dash dot line). The blue and red lines show the Mie result for the refractive indices retrieved by Wolff *et al.* (2009) and Ockert-Bell *et al.* (1997).

5.2.3 UV radiation at the surface of Mars for different dust properties

The UV flux at the surface of Mars from 180–400 nm forms only a small part of the solar flux (< 5 % of the solar constant) but the impact of this UV radiation on potential life is significant. Short-wave UVC (190–280 nm) is very damaging to DNA and a full study into the UV environment at the martian surface is given by (Patel *et al.*, 2002, Patel *et al.*, 2004). The recent retrieval of ω_0 by Wolff *et al.* (2010) at 258 nm and 320 nm has revealed that the dust maybe more absorbing in the 200–300 nm wavelength region and less absorbing in the 300–400 nm region than was suggested by Ockert-Bell *et al.* (1997). The O97 dataset for the optical properties of martian dust is widely used as it comprises the most complete dataset as a function of wavelength. O97 was previously used to calculate the UV flux at the surface of Mars and to determine the total UV dose (J m^{-2}) during a single sol and the Beagle 2 mission life-time (Patel *et al.*, 2004, Patel *et al.*, 2002). The purpose of this study is to determine if a W09 dust component produces a significant difference in UV flux at the surface of Mars compared to O97 dust component. The difference in UV dose is quantified across both a single sol and an average mission life-time. The total dose as a function of τ for both W09 and O97 dust aerosols is also investigated

The total UV flux at noon across a latitude strip from the north pole (90°) to the south pole (-90°) as a function of L_s is shown in Figure 5-9a and Figure 5-9b, for aW09 and O97 dust component respectively. The latitude and L_s values are binned at a resolution of 2° and the TES (Thermal Emission Spectrometer) average year scenario included in the Mars radiative transfer model is used to determine the seasonal and latitudinal dependence on τ. The two dust scenarios are very similar and follow the same distribution as described by Patel (2003), but differences as a result of the different dust single scattering properties can be seen. This is especially true at L_s = 180–330°, when UV flux and dust opacity are at a maximum. Figure 5-9c shows the difference in UV flux between the dust scenarios with the maximum difference of approximately 4% observed around L_s = 250° correlating with the seasonal variation in τ. The variation in the calculated UV flux at noon results from an average difference of 6.5, 3.5 and 3.8% in Q_{ext}, ω_0 and g respectively in the 190 – 400 nm region between the two dust components.

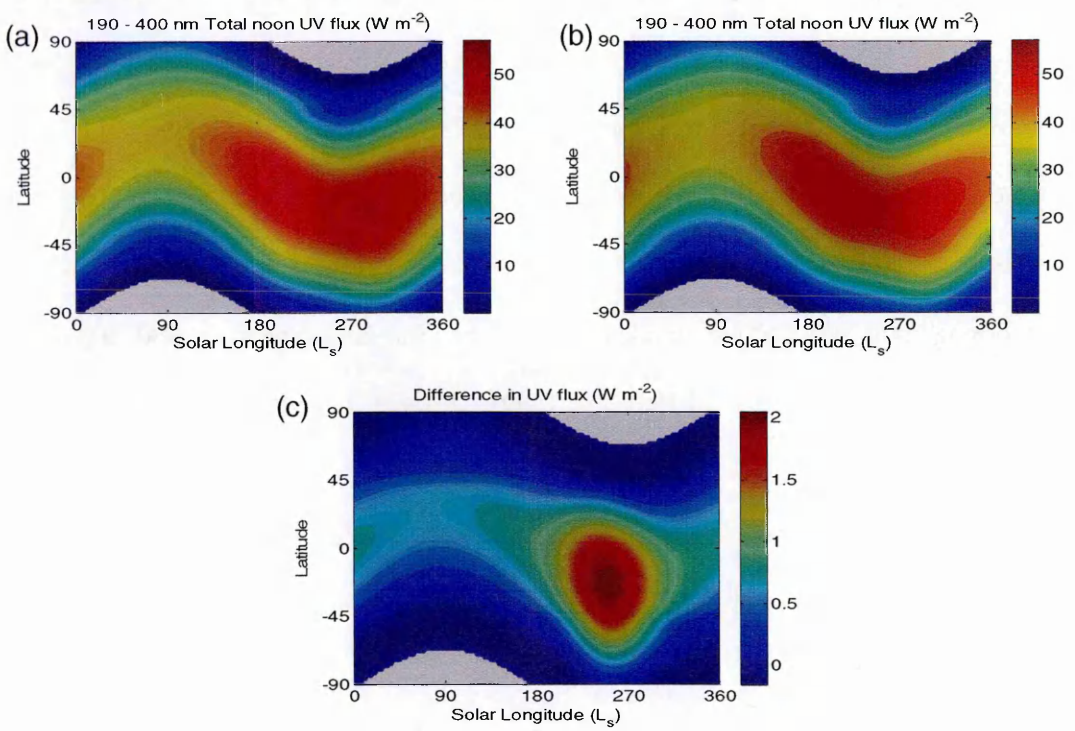

Figure 5-9: The latitudinal and seasonal variation of local noon UV flux for, (a) W09 and (b) O97 dust components. (c) shows the difference between the noon UV flux with the positive values indicating that a W09 dust component results in a higher UV flux.

The latitudinal and seasonal analysis shows that between 190–400 nm an approximate 4% difference in ω_0 and g and ~6% difference in Q_{ext} can affect the amount of UV radiation absorbed and scattered and will impact the total UV dose received at the surface. Figure 5-10 shows the total daily UV dose at the surface of Mars for O97 and W09 as a function of τ. Perihelion was selected for this study as it receives higher UV irradiance as a result of the eccentric Mars orbit and experiences greater dust activity at the time. At τ greater than unity, a 2.5% larger UV dose is received with a W09 dust haze relative to O97 dust haze. Negligible difference in UV dose is observed at τ lower than unity.

Figure 5-10b shows that at low τ the direct component is the main contributor to the total UV dose received at the surface. This indicates that the daily UV dose is only weakly dependent on the diffuse component, hence on ω_0 and g, and more strongly coupled to Q_{ext}. The difference in Q_{ext} results in W09 having a 7.7% higher τ compared to O97 at UV wavelengths, explaining the higher UV dose received for O97 at low dust opacities. The higher ω_0 values of W09 result in a larger diffuse component compared to O97 which is more absorbing. As the diffuse component becomes comparable with the direct component the larger diffuse component of W09 is sufficient to make the total UV dose exceed that received for the O97 dust component.

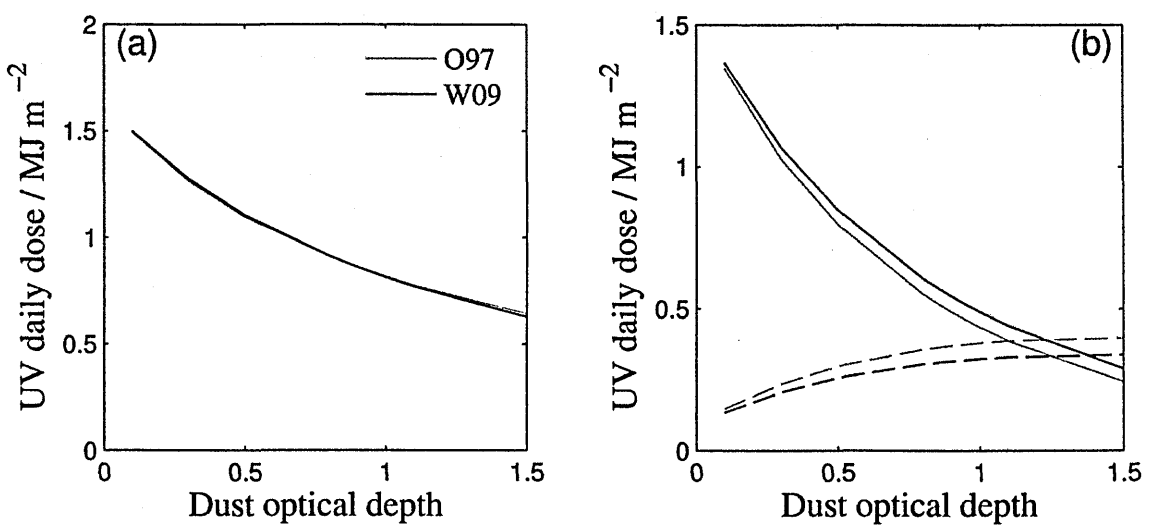

Figure 5-10: a) Total UV daily dose as a function of τ for O97 and W09. b) The UV daily from the received from the direct component (solid lines) and diffuse component (dashed lines).

From τ measured by Spirit (Figure 5-3), Figure 5-10 implies that a negligible difference in UV daily dose during northern summer (where τ is consistently below ~ 0.9) will be observed between the two dust components W09 and O97. During the dustier southern summer, a larger UV dose (> 2.5%) would be received for a dust component with the single scattering properties of W09 compared to O97.

The total dose received during two different martian years for both dust types was simulated to provide an insight into the differences in total UV dose between a year with no dust storm and one with a significant dust event. The UV spectrum was divided into in constituent parts; UVC (190–280 nm), UVB (280–315 nm) and UVA (315–400nm). The daily UVC dose for both years for the two dust types is plotted in Figure 5-11. Between L_s = 50–130°, when τ is consistently between 0.2 and 0.4, there is a difference of approximately 5–7% in the daily UVC dose between the two dust types, with a greater UVC dose received for a O97 component. From L_s = 150–330°, up to 10–15% more UVC radiation is received for O97 compared to W09. Greater than 40% difference is found during the dust storm in MY28 at L_s = 250° which exhibited τ values exceeding 4.0. The difference is the result of ω_0 for O97 being ~12% higher than that of W09 averaged over the 190–280 nm wavelength range. Less UVC radiation is absorbed and more is scattered by the dust. This leads to the O97 case having a higher diffuse component than the W09 case, increasing the UVC flux incident at the surface. The single scattering albedo is not the only contributing factor however; the wavelength dependence of Q_{ext} results in W09 dust component having a 7.7% higher τ between 190–280 nm leading to a lower direct component.

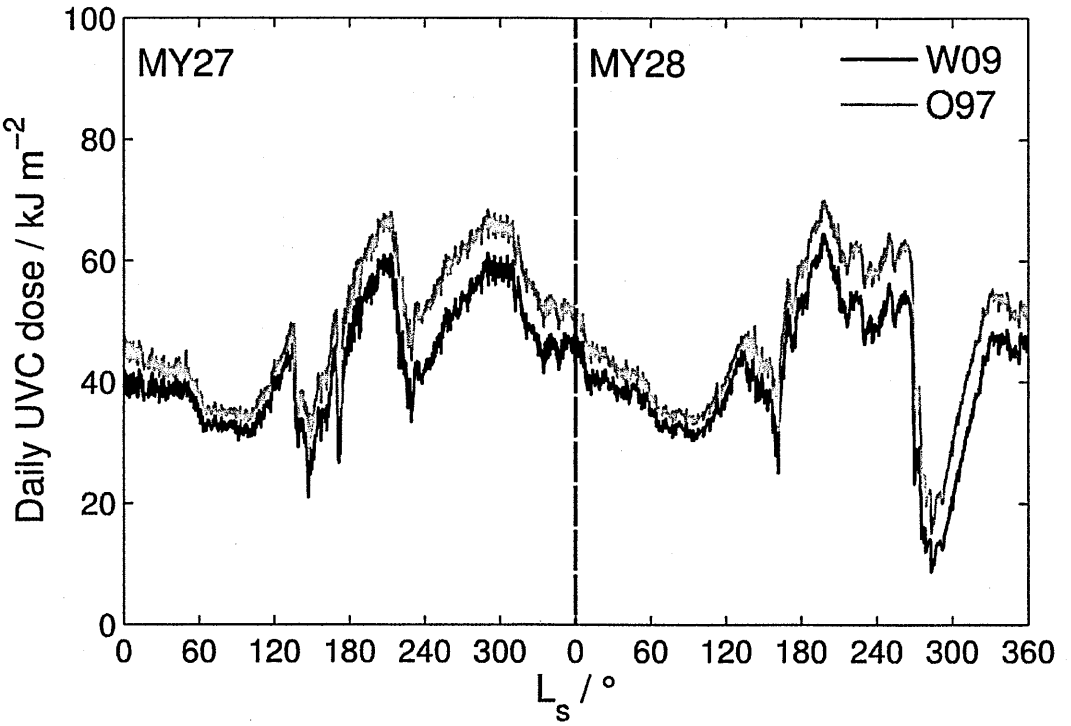

Figure 5-11: Difference in UVC dose as a function of L_s for O97 and W09 during MY27 and MY28.

The total daily dose of UVB and UVA radiation is shown in Figure 5-13 and Figure 5-13 respectively. During northern summer the difference in daily UVB and UVA dose between O97 and W09 is small (1–3%). With the approach of southern summer the difference in dose increases, with a maximum difference of approximately 10% (UVB) and -20% (UVA) observed during the large dust storm in MY28 (the negative indicates the UVA dose is greater for W09 compared to O97). The UVB band shows the smallest difference between the two dust components and is correlated with the region where ω_0 is similar for W09 and O97 with an average difference of just 2.5%. This results in a comparable diffuse component, making the region more dependent on Q_{ext} in determining which dust background receives the larger UVB dose. In the UVA wavelength region, the W09 dusts component experiences a larger diffuse component since its ω_0 values are 8.5% higher compared to the O97 case. At $\tau < 0.48$ the diffuse irradiance is insufficient to increase the UVA dose received above that of the O97 dust background. At higher τ however, the W09 diffuse irradiance is sufficient to cause the total UVA dose received at the surface to be greater than that of the O97 case.

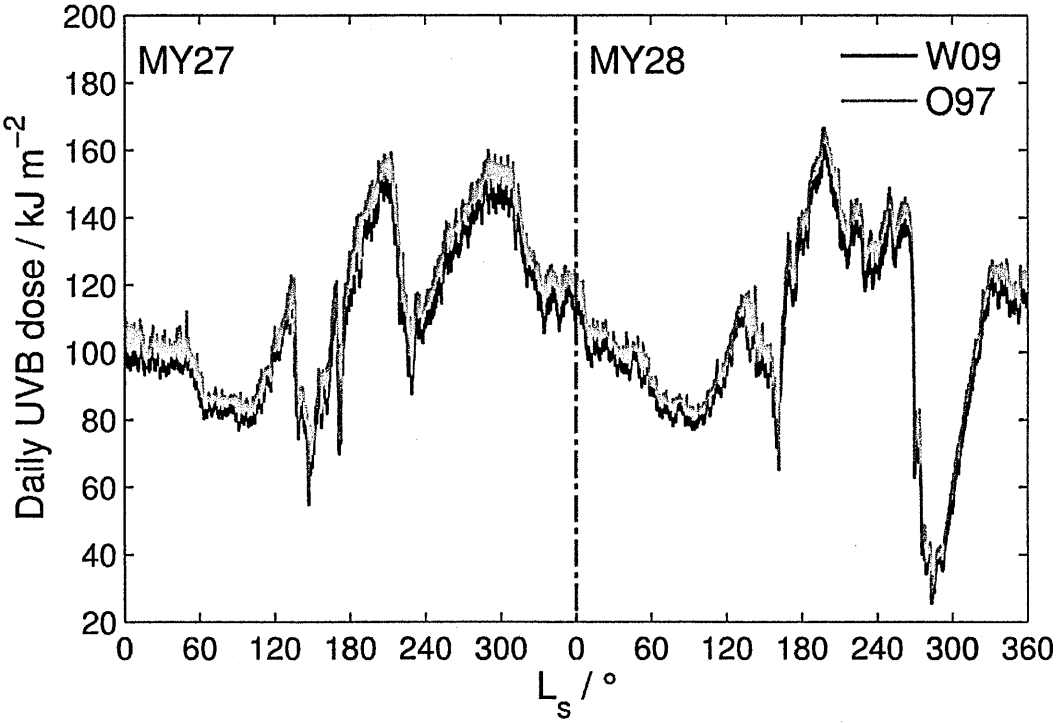

Figure 5-12: Same as figure 5-11 except for UVB.

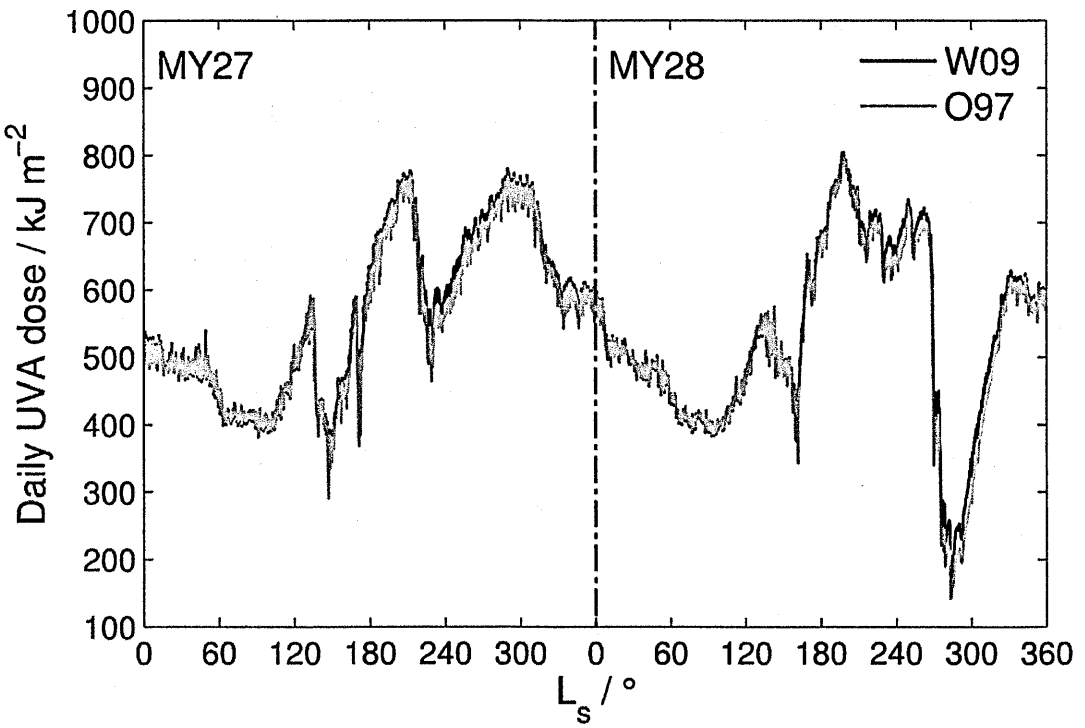

Figure 5-13: Same as figure 5-11 except for UVA.

The total cumulative UV dose for each year in the different UV regions is summarised in Table 5-2. The greatest discrepancy in cumulative dose is observed in the UVC region which shows a difference of approximately 12% between the two dust types and is well correlated to an average difference of 12 % in the single scattering albedo values. The other regions show similar cumulative UV doses with differences of 4% and 1% for UVB and UVA respectively. Interestingly, the UVA cumulative dose is comparable for both dust types, a result of the incident UVA being higher for an O97 dust background at τ lower than 0.48 and higher for a W09 background at larger τ. The net effect is a small difference to the cumulative UVA dose during the martian year.

Mars Year	Wavlength Band	UV Dose / MJ m^{-2}	
		W09	O97
MY27	UVC	28.52	32.13
	UVB	72.11	75.13
	UVA	367.99	364.55
MY28	UVC	26.86	30.44
	UVB	68.09	70.95
	UVA	349.18	344.55

Table 5-2: Summary of the cumulative UVC, UVB and UVA dose for the two different dust components O97 and W09 during MY27 and MY28.

Comparing MY27 and MY28, the presence of a planet-encircling dust storm reduces the cumulative UV dose by approximately 6% in all UV regions for both dust types. This indicates that while large dust events of different dust types can cause large variation on the daily dose (>20 % in UVC and UVA), the impact on the cumulative dose throughout a martian year is significantly smaller.

UV exposure has to be taken into consideration for human missions to Mars, where the time on the surface would be approximately one Mars year for a long-stay mission. If the assumption is made that landing occurs at $L_s = 0°$ this gives a total cumulative UV dose of 468.62 MJ m^{-2} (444.13 MJ m^{-2}) for W09 and 471.81 MJ m^{-2} (445.94 MJ m^{-2}) for O97 if MY27 (MY28) τ conditions are present. Therefore an average 3.5% difference in the assumed optical properties of the dust in the wavelength range 190–400 nm will result in a slight under or over

estimation of the total UV dose received at the surface during the mission. More importantly, the higher energy UVC radiation will see a 12% difference depending on the optical properties of the dust, with large variations in the daily dose observed for both UVC and UVA dependent on the amount of dust present in the martian atmosphere.

Furthermore, under martian UV conditions, Kerney and Schuerger (2011) observed positive growth of *Bacillus subtilis* in analogue martian soil after direct contact with a rover wheel; a scenario similar to the planned landing for the Curiosity rover. During the time of the Curiosity landing Mars will be at approximately L_s = 150° with dust opacities between ~1.0 (MY27) and ~0.5 (MY28) likely to be present. If conditions are similar to MY27 then a O97 dust component will result in a UVC daily dose ~15% higher than a W09 dust component, leading to fewer *B. subtilis* endospores surviving at the surface. More importantly the lower UVC dose observed for a WO9 dust component will increase the survivability and viability of *B. subtilis* endospores under martian UV conditions.

5.2.4 Dust-dependent UV dose: Implications for astrobiology

UVC radiation has been shown to be the primary factor that determines short-term survivability and viability of microorganisms under simulated martian UV conditions (Schuerger *et al.*, 2003, 2006). Schuerger *et al.* (2003) determined that the effective lethal dose (LD) rate of UVC + UVB (200 to 315 nm) for 99.9% (LD_{99}) and 100% (LD_{100}) was 0.39 kJm^{-2} and 11.9 kJm^{-2} for *Bacillus subtilis* endospores.

To assess the different influence of O97 and W09 on the survivability of *B. subtilis*, a similar method to that used by Schuerger *et al.* (2003) was applied. Using the Mars radiative transfer model, the total noon instantaneous UVC+UVB flux at the martian surface for various τ was determined. This improves upon the work of Schuerger *et al.* (2003) since they only take it account the direct component that reaches the surface when calculating the noon irradiances. To estimate the time required to accumulate LD, the noon surface flux was converted to dose rate per minute (kJ m^{-2} min^{-1}) and then dividing LD_{99} by this value for each τ. Three different

latitudes were considered for the analysis, 14.8°S, 4.5°S and 68.0°N corresponding to the landing sites of Spirit, Curiosity and Phoenix and the results are shown in Tables 5.3- 5.5. Each table gives the total noon UVC+UVB surface flux and the time taken to reach LD_{99} for O97 and W09. Two seasons are shown, northern summer (L_s = 90°) and southern summer (L_s = 270°). Note the high latitude of the Phoenix lander location exposes it to the polar night, hence during the northern winter no solar radiation reaches the lander.

	L_s 90°				L_s 270°			
	UVC+UVB flux / W m^{-2}		Time to LD_{99} / Minutes		UVC+UVB flux / W m^{-2}		Time to LD_{99} / Minutes	
Optical depth	O97	W09	O97	W09	O97	W09	O97	W09
0.0	6.91	6.91	0.94	0.94	12.85	12.85	0.52	0.52
0.1	6.72	6.71	0.97	0.97	12.77	12.79	0.51	0.51
0.3	5.85	5.82	1.11	1.12	11.66	11.68	0.56	0.56
0.7	4.48	4.46	1.45	1.46	9.67	9.72	0.67	0.67
1.4	2.98	3.01	2.18	2.16	7.13	7.24	0.91	0.90
2.5	1.75	1.80	3.71	3.60	4.59	4.72	1.42	1.38
3.5	1.13	1.17	5.75	5.55	3.14	3.24	2.07	2.01

Table 5-3: Time required to accumulate the lethal (LD_{99}) UVC+UVB doses for dust components O97 and W09 at the Spirit rover location.

	L_s 90°				L_s 270°			
	UVC+UVB Flux / W m^{-2}		Time to LD_{99} / Minutes		UVC+UVB Flux / W m^{-2}		Time to LD_{99} / Minutes	
Optical depth	O97	W09	O97	W09	O97	W09	O97	W09
0.0	7.83	7.83	0.83	0.83	12.00	12.00	0.54	0.54
0.1	7.78	7.78	0.84	0.84	12.05	12.07	0.54	0.54
0.3	6.94	6.94	0.94	0.94	10.91	10.92	0.60	0.60
0.7	5.55	5.55	1.17	1.17	8.92	8.95	0.73	0.73
1.4	3.89	3.94	1.67	1.65	6.44	6.53	1.01	1.00
2.5	2.39	2.46	2.72	2.64	4.07	4.19	1.60	1.55
3.5	1.59	1.64	4.09	3.96	2.75	2.84	2.36	2.29

Table 5-4: Time required to accumulate the lethal (LD_{99}) UVC+UVB doses for dust components O97 and W09 at the Curiosity landing site.

Optical depth	L_s 90° UVC+UVB flux / W m^{-2}		L_s 90° Time to LD_{99} / Minutes		L_s 270° UVC+UVB flux / W m^{-2}		L_s 270° Time to LD_{99} / Minutes	
	O97	W09	O97	W09	O97	W09	O97	W09
0.0	6.62	6.62	0.98	0.98				
0.1	6.38	6.37	1.02	1.02	-	-	-	-
0.3	5.51	5.47	1.18	1.19	-	-	-	-
0.7	4.16	4.13	1.56	1.58	-	-	-	-
1.4	2.72	2.74	2.39	2.38	-	-	-	-
2.5	1.57	1.62	4.14	4.01	-	-	-	-
3.5	1.01	1.04	6.47	6.24	-	-	-	-

Table 5-5: Time required to accumulate the lethal (LD_{99}) UVC+UVB doses for dust components O97 and W09 at the Phoenix lander.

The time taken to reach LD_{99} for *B. subtilis* endospores ranges from 0.84 minutes ($\tau = 0.1$) at the Curiosity landing site, to greater than 6.0 minutes ($\tau = 3.5$) at Phoenix. The ~40% higher incident solar radiation received at the martian surface during southern summer results in a proportional decreases in the time taken to reach LD_{99}. Under low τ the survival time at the Spirit and Curiosity locations is approximately 30 seconds, at τ typical of a planet-encircling dust storm (> 3.0) the time increases to approximately 2 minutes. Comparing the results to the seasonal variation in τ (Figure 5-3) the expected dust opacities during northern summer range from 0.1-0.3, giving a typical survival time of *B. subtilis* endospores of approximately 1 minute at all locations considered. During southern summer τ ranges between 0.7 and 1.4, leading to a survival time between ~0.7 and 1.0 minute at the Spirit and Curiosity locations. Under optimum conditions the reproductive time of *B. subtilis* is 15 minutes. Given that the survival time for this microbe during a typical annual seasonal cycle is ~ 1 minute, this suggests that any contaminated surface exposed to the total UVC + UVB surface flux will be sterilised.

Negligible difference ($\leq$ 1 s) in the time to taken reach LD_{99} for the different dust components is observed at τ below 1.4. Even at the high dust opacities seen during a planet-encircling dust storm, the change in time is negligible (~5 s). This indicates that the variation in

the dust single scattering properties between O97 and W09 will have little impact on the survival of *B. subtilis* endospores exposed to the total UVC+UVB surface flux.

The difference in time taken to reach LD_{99} between W09 and O97 dust components is only of the order of seconds if *B. subtilis* endospores are exposed to the total UVC + UVB flux. However microorganism could be present on all spacecraft surfaces including those obscured from the direct component, thus will only be exposed to the diffuse component. This will lower the instantaneous UVC+UVB dose rate leading to an increase in the time taken to reach LD_{99}. Applying the methods above, it is assumed the *B. subtilis* endospores are only exposed to the diffuse irradiance. The Curiosity landing location and the location of Phoenix are compared for this analysis and the result for 100% of the diffuse irradiance is shown in Table 5-6 for O97 and W09 at $L_s = 90°$.

	L_s 90° - Curiosity				L_s 90° - Phoenix			
	UVC+UVB flux / W m^{-2}		Time to LD_{99} / Minutes		UVC+UVB flux (W m^{-2})		Time to LD_{99} / Minutes	
Optical depth	O97	W09	O97	W09	O97	W09	O97	W09
0.1	1.02	1.09	6.38	5.95	0.81	0.87	8.00	7.47
0.3	1.38	1.54	4.71	4.23	1.08	1.20	6.02	5.40
0.7	1.78	2.04	3.66	3.19	1.36	1.55	4.78	4.18

Table 5-6: Time required to accumulate LD_{99} for *B. subtilis* endospores exposed to 100% of the diffuse irradiance for dust components O97 and W09 at the Curiosity and Phoenix locations.

Even exposed to only the diffuse component the time taken to reach LD_{99} is still in the order of minutes indicating that microorganisms will be sterilised even from areas shielded from direct light. In order for *B. Subtilis* to survive, the UVC+UVB dose rate per minute needs to be less than 26 J m^{-2} min^{-1}. Therefore, assuming a τ of 0.3, the contaminated surface must shield the *B. subtilis* from 70% (Curiosity) and 60% (Phoenix) of the incident diffuse irradiance. It should be noted that this does not take into account reflections and scattering form the surface and other

spacecraft surface which will increase the diffuse component, hence further reducing the survival time.

5.2.5 *Differentiating between different dust species*

In Section 5.2.1 it was shown that variations in the total surface irradiance due to dust components W09 and O97 were small. The total surface flux provides no information to determine whether the dust background is homogenous or heterogeneous in terms of dust composition. Measuring the UV-NIR spectrum allows direct comparison of the irradiance at two wavelengths. Furthermore we can compare the wavelengths in regions which have significantly different single scattering properties. The retrieved single scattering properties of martian dust (Figure 5-7) indicate that the dust is highly absorbing at short wavelengths (< 500 nm) and efficient at scattering at longer wavelengths. It is also important to note that by taking the ratio of the irradiance at two wavelengths, the seasonal variation in irradiance is removed. Therefore, the ratio of the combined irradiance (direct + diffuse) at 388 nm to 750 nm, hereafter denoted $\Re_I$, was calculated for W09 and O97 for MY27 and MY28 and is shown as a function of L_s in Figure 5-14. Note that 388 nm was selected since, as mentioned by Otter (2010), it coincides with a minimum in O_3 absorption (the main absorbing component after dust between 200-1100 nm), thus any change in the spectrum will be a result of the dust only. Similarly, 750 nm was selected as it sits in between two weak H_2O absorption bands. The difference between W09 and O97 is clearly seen in $\Re_I$, with W09 showing a larger ratio of 7% during northern summer when the opacity ranges from 0.2-0.5, approximately 15% between L_s = 180°–350° and > 30% during the MY28 dust storm.

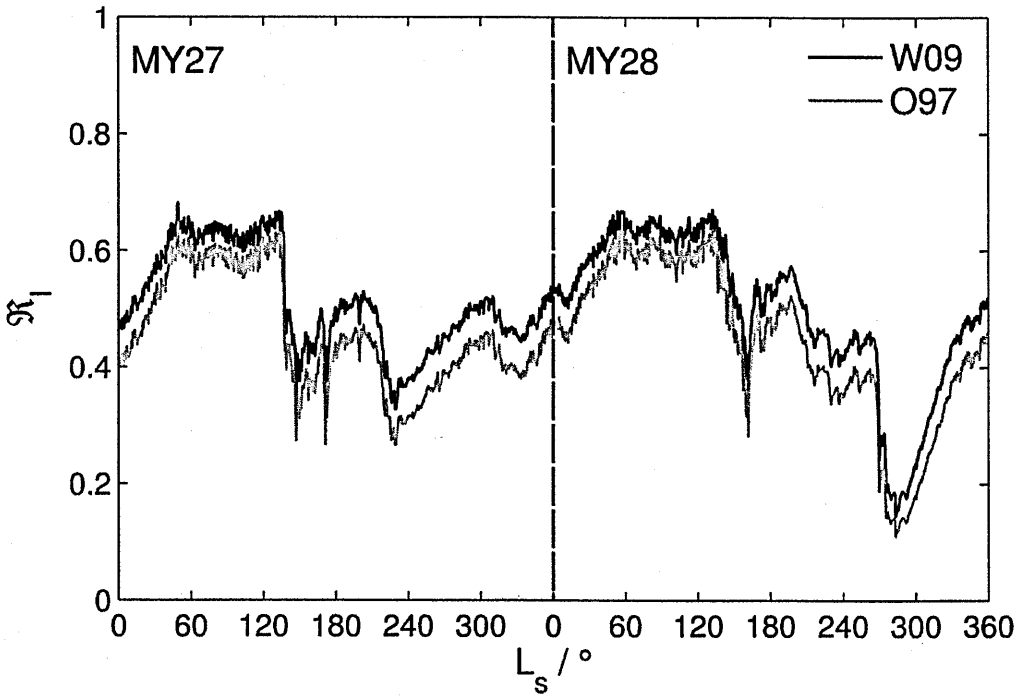

Figure 5-14: $\Re_I$ as a function of L_s for O97 (grey line) and W09 (black line) during MY27 and MY28.

Figure 5-14 shows differences between two dust backgrounds but *in situ* measurements of the surface irradiance spectrum will provide only one profile for $\Re_I$. This single profile could be produced by either a homogenous or heterogeneous dust particle composition. Figure 5-15 shows a hypothetical variation in $\Re_I$ as a function of L_s, resulting from such a varying background dust component. An O97 dust background is assumed over the majority of the hypothetical MY27 and MY28. At given times of the year (correlating with increases in opacity) the dust background is changed to have the single scattering properties of W09. The composite $\Re_I$ signature, Figure 5-15, tells us very little about the background dust component. It indicates that the irradiance at 750 nm is higher than at 388 nm, but this fact provides no insight into the heterogeneity of the dust background.

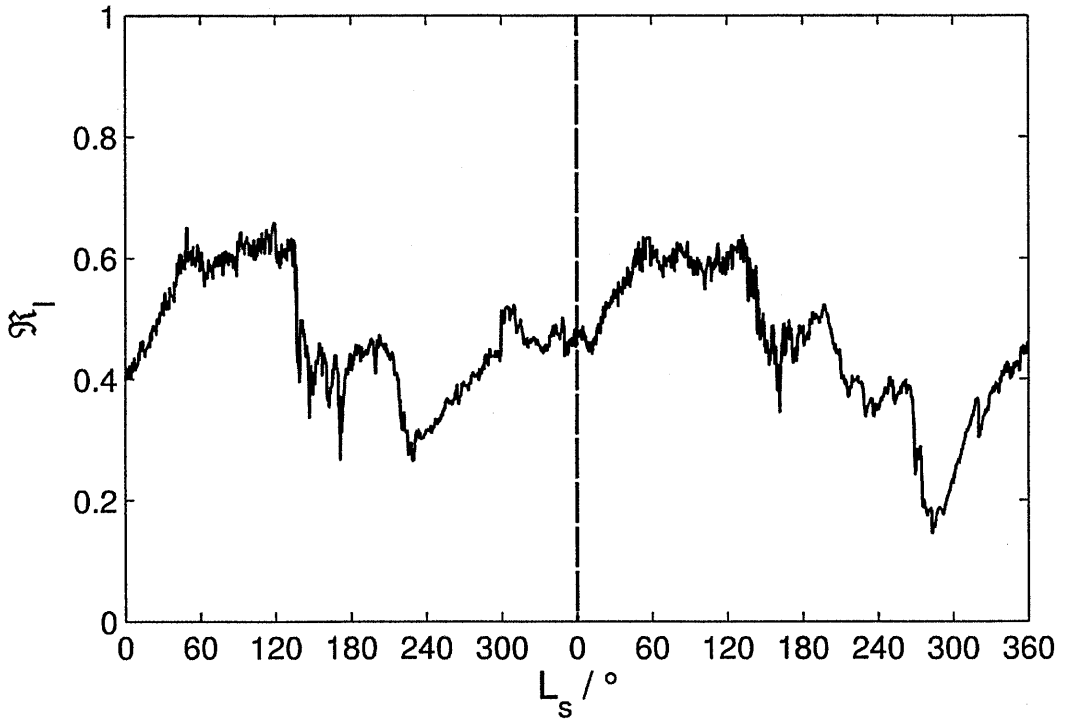

Figure 5-15: $\Re_I$ as a function of L_s for the hypothetical MY27 and MY28 scenario. O97 forms the background dust component. W09 is added during increases in τ, simulating a change in the atmospheric dust component.

One method of differentiating between potential dust components is to plot $\Re_I$ as a function of τ as illustrated in Figure 5-16 for W09, O97, and the hypothetical composite background. W09 and O97 show different gradient curves with increasing dust opacity and superimposed on these are the $\Re_I$ values associated with the composite dust background. This indicates that the hypothetical dust background was not constant during the simulated MY27 and MY28. Furthermore, it is possible to determine on which sol this change occurred by matching the measured τ to the date of observation and the relevant spectrum retrieved for analysis. Seasonal variation in $\Re_I$ is observed for a given τ, however the variation is negligible compared to the variation caused by differences in the single scattering properties between W09 and O97.

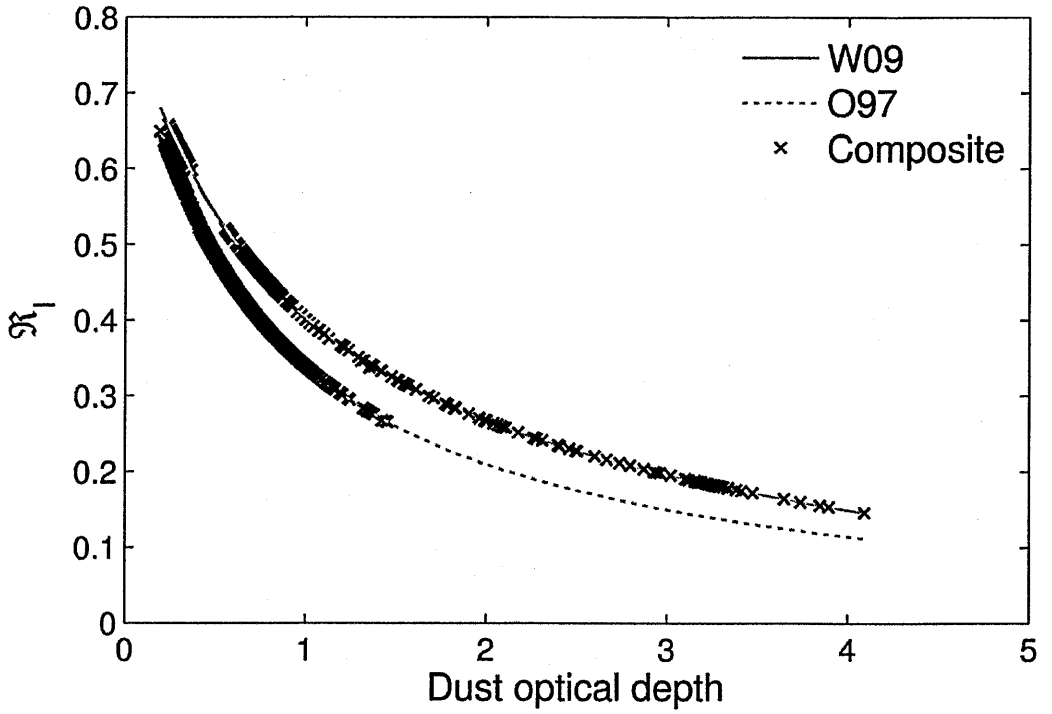

Figure 5-16: $\Re_I$ as a function of τ for MY27 and MY28. Dust components of W09 (grey line) and O97 (grey dashed line) are shown. Also shown is a composite scenario which is explained in the text.

While the ratio of the combined irradiance at 388 nm to 750 nm can distinguish between different dust components, at dust opacities representative of northern summer, the ratio profiles converge. This is expected since below $\tau = 0.58$ the direct component contributes more to the combined irradiance, and hence the spectrum becomes less sensitive to changes in the scattered diffuse component. Unfortunately the information regarding the scattering nature of the dust particles is contained in the diffuse component. If we make the assumption that only the diffuse component is measured (either by observation or by subtracting the direct component from the combined irradiance) then a better comparison can be made: the diffuse irradiance at 388 nm relative to that at 750 nm, $\Re_D$, Figure 5-17. In comparison to $\Re_I$, $\Re_D$ shows greater sensitivity to variation in the dust component at optical depths expected to be present in the martian atmosphere during most of the year (0.2–0.8). A smaller change in $\Re_D$ between O97 and W09 is observed at extreme opacities (>3.0), however the difference is still greater compared to that seen in $\Re_I$.

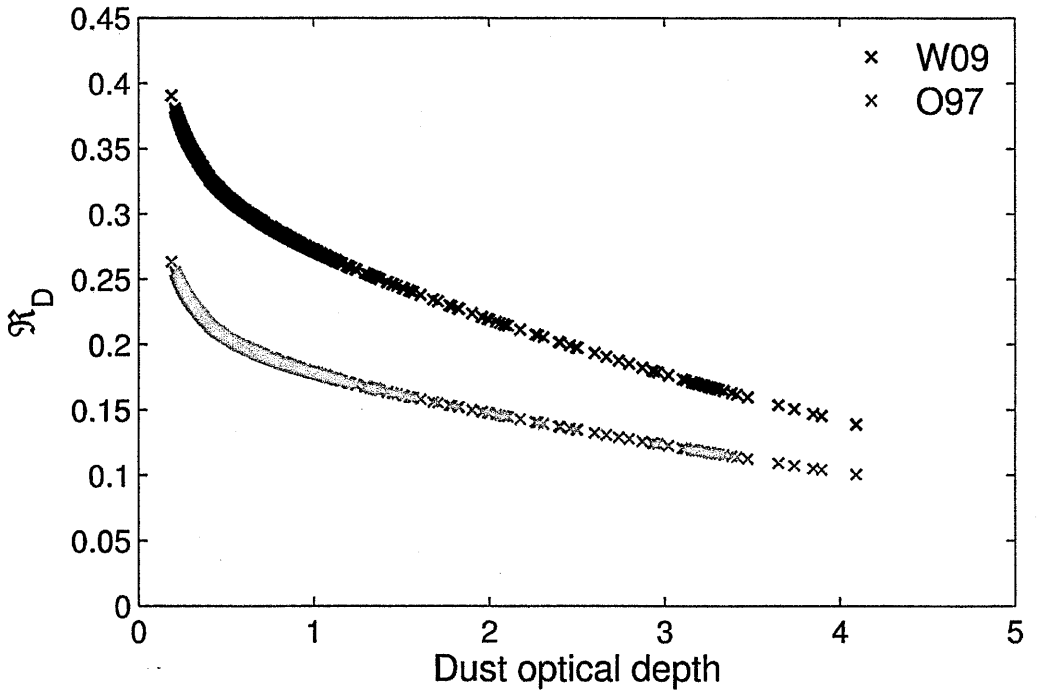

Figure 5-17: As Figure 5-16 but for $\Re_D$ for W09 and O97.

It should be noted that this is an idealised case and in reality $\Re_I$ and $\Re_D$ will likely have values between the two curves shown in Figure 5-16 and Figure 5-17 as a result of mixing of the two components. However any change in $\Re_D$ and $\Re_I$, at a given τ, is still indicative of a change to the background dust component and can be used to investigate the variability in the dust species forming the background dust haze.

This analysis shows that *in situ* measurement of the combined irradiance spectrum and its components provides a powerful tool for distinguishing variation in the dust background over seasonal and diurnal time-scales. Such measurements would allow insight into the fundamental question on the variability in the composition of the suspended dust. The study also emphasises the importance in measuring not only the combined surface irradiance, but also simultaneous measurement of either the direct or diffuse components.

5.3 Transits of martian dust devils

The previous section was concerned with the impact of dust on large spatial and temporal scales. However, small local scale dust phenomena occur frequently on the surface of Mars such as dust devils (Chapter 2). In this section the MCRT is applied to martian dust devils to determine their transit signature (light curve as a function of time).

Dust devils observed in Gusev crater by the Spirit rover were analysed extensively by Greeley *et al.* (2006) and Greeley *et al.* (2010) and provide statistics on dust devil size and dust content over the dust devil season in Mars Year MY27-MY29. Their results show significant variation in dust devil size with diameters of about 2 m to more than 250 m and with vertical heights ranging from less than 10 m to greater than 300 m. The dust concentration within the dust devils was also observed to vary considerably ranging between 2.1×10^{-9} kg m^{-3} and as high as 4.6×10^{-4} kg m^{-3}. The mean dust devil diameter measured by Greeley *et al.* (2010) was 19, 24 and 39 m in MY27, MY28 and MY29 respectively. Ideally the mean diameter, over the three years, of 27 m would have been used but to model a dust devil of this size resulted in a significant increase in the simulation runtime. Therefore a dust devil with a diameter of 20 m was selected to simulate the transit of a martian dust devil over a spectrometer and corresponds to the maximum dust devil size allowed within the constraints of the model. The vertical extent of the model dust devil was taken to be 50 m as this dust devil height was commonly observed by Spirit in Gusev crater (Greeley *et al.*, 2006). The optical depth of the dust devil (τ_{dd}) was given values of, 0.01, 0.14 and 2.64, corresponding to the minimum, mean and maximum dust devil opacity measured by Greeley *et al.* (2006). For the size of our model dust devil this gave dust concentrations of 7.0×10^{-7}, 9.8×10^{-6} and 1.9×10^{-4} kg m^{-3}, well within the range reported by (Greeley *et al.*, 2010).

In Chapter 4 it was shown that on a clear sky day on the Earth the direct component dominates the total measured signal with the diffuse component being orders of magnitude smaller and to first order approximation can be assumed negligible when simulating dust devil

transits. As shown in Section 5.1, the high dust content of the martian atmosphere results in a diffuse component of comparable magnitude or larger than the direct component and thus cannot be assumed negligible. To estimate the direct and diffuse fractions of the total irradiance τ measured by Spirit was used, Figure 5-3.

The Mars radiative transfer model was used to estimate the direct and diffuse irradiance received at the surface for three different dust background optical depths (τ_{bg}): 0.41, 0.81 and 1.57 and correspond to the minimum, mean and maximum τ of the Spirit dataset over all three dust devil seasons. Note our maximum τ_{bg} does not correlate with the peak τ in Figure 5-3 because, from inspection of statistical data produced by Greeley *et al.* (2010), during this time no dust devils were observed. Furthermore, the increased opacity around sol 1700 and sol 2000 also showed suppressed dust devil activity. This results from the fact that under high atmospheric dust loadings, dust devil formation is dampened.

The dust background was assumed to have the single scattering properties of W09. The wavelength dependence of the optical properties of martian dust will result in the fractional contribution of the direct and diffuse component towards the total irradiance to be different for largely separated wavelengths. Figure 5-18 shows the fraction of the combined signal contributed by the direct and diffuse components for the irradiance at 388 nm (blue lines) and 750 nm (red lines). For 388 nm, the direct component forms 75% of the total irradiance for τ_{bg} = 0.41 and 60% at τ_{bg} = 0.81. At 750 nm, the larger diffuse component results in the direct component forming only 55% and 32% of the total irradiance at τ_{bg} = 0.41 and 0.81 respectively. For the maximum τ_{bg} (1.57) simulated, the diffuse components dominates at both wavelengths with the direct component contributing 34% and 12% to the combined irradiance at 388 nm and 750 nm respectively. Note at τ_{bg} = 0 Rayleigh scattering becomes important and leads to the diffuse component at 388 nm not tending to zero as $\tau_{bg} \rightarrow 0$.

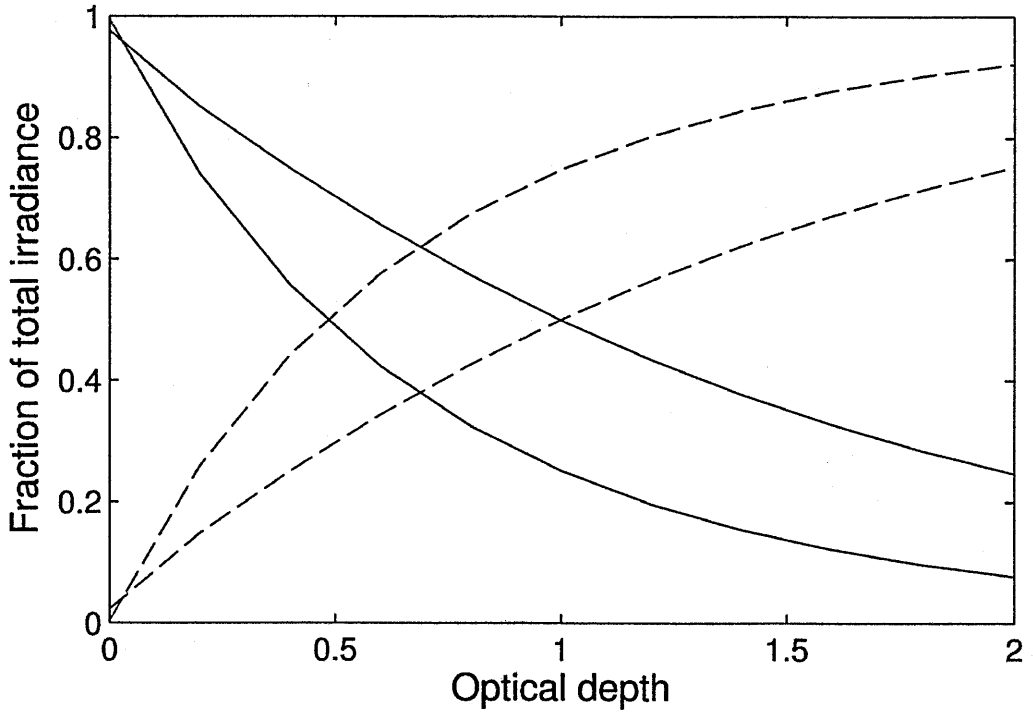

Figure 5-18: The relative contributions to the total surface irradiance from the direct (solid lines) and diffuse (dashed lines) components. The blue lines denote a wavelength of 388 nm and the red lines represent a wavelength of 750 nm.

The incident diffuse light cannot be assumed a point source and will be incident at all angles. This will modify the optical signature of a transiting dust devil from the 'clear sky' simulations performed for terrestrial dust devils in Chapter 4, with the alteration dependent on τ and composition of the dust background.

5.3.1 Modelling the diffuse component

The MCLSM was adapted for the martian atmosphere and simulates the transmission of light through the lowest 50 m of the atmosphere and it is assumed that the direct and diffuse irradiance 50 m above the surface is equal to the surface irradiance calculated by the radiative transfer model. The MCLSM, described in Chapter 3, for terrestrial dust devils made the assumption of a negligible diffuse component resulting from the 'clear sky' and that the total irradiance was dominated by the direct component from the Sun. The Mars MCLSM differs from the terrestrial MCLSM in that both the direct and diffuse components of the total

irradiance had to be simulated in order to predict accurate optical signatures of transiting martian dust devils. The direct component is modelled separately from the diffuse component and follows the procedure described in Chapter 3 for terrestrial dust devils. To help differentiate the photons comprising the direct and diffuse components, photons forming the diffuse component are called 'diffuse photons' and the photons forming the direct component are called 'direct photons'. The diffuse photons were given a random position on the surface and a random trajectory. The point of intersection with the model boundary was calculated and taken to be the initial position of the diffuse photons. The trajectories are then reversed and used as the initial travelling direction of the photon. This method allows photons travelling at all angles over the hemisphere and always ensures sufficient photons are detected by assuming all photons impact the model surface. The initial photon zenith angle (θ_{pz}) is determined from a probability distribution which weights the random θ_{pz} depending on τ_{bg}. The weighting is required because diffuse photons with high θ_{pz} travel a greater distance through the atmosphere before they reach the surface and therefore have a higher probability of being absorbed or scattered out of the path to the detector. Assuming that the dust is the dominant scattering and absorbing component in the martian atmosphere for visible wavelength, the light received for any particular θ_{pz} angle will be diminished by a factor $\exp\left(-\tau_{\mathrm{L}} L/\cos\theta_{pz}\right)$, where τ_{L} is the optical depth per unit length and L is the path length from 2 km to 50 m. Therefore if N_{p} is the number of diffuse photons entering the model volume, then the number of photons for a given θ_{pz} angle is $N_{\mathrm{p}} \exp\left(-\tau_{\mathrm{L}} L/\cos\theta_{pz}\right)$, resulting in fewer photons with large θ_{pz} being incident relative to photons with a small θ_{pz}. The θ_{pz} probability distribution for the three τ_{bg} scenarios is shown in Figure 5-19. For low τ_{bg} there is a high probability of diffuse photons having an incident θ_{pz} between 0 and 70° before exponentially decreasing at high θ_{pz}. The probability of photons having high incident θ_{pz} quickly decreases as τ_{bg} increases with the high τ_{bg} scenario showing the photons being 20 % less likely of having an incident θ_{pz} of 50°. The initial azimuth angle of the photons is found by producing a uniform random number between 0 and 2π.

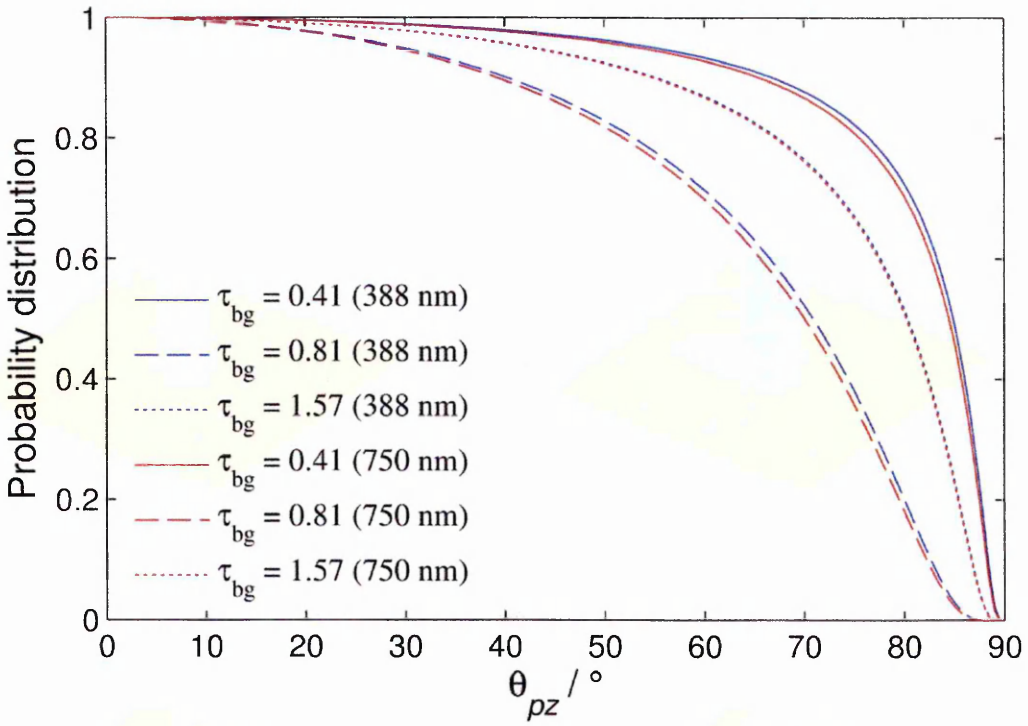

Figure 5-19: The θ_{pz} probability distribution for photons incident on the model surface.

The position of the direct and diffuse photons after 1-5 scattering events for dust devils with $\tau_{dd} = 2.64$ and $\tau_{dd} = 0.01$ at two wavelengths 388 nm and 750 nm is illustrated Figure 5-20. The background dust haze was assumed to have a columnar optical depth of 1.57. For dust devils with low dust content, the simulations predict a low contrast between the background dust haze and the dust devil, with no definition of the dust devil observed at red wavelengths (750 nm). As expected, for high background atmospheric dust loadings visually detecting low opacity dust devils will be extremely difficult and will tend to blend with the dust haze. At blue and UV wavelengths, low opacity dust devils are more distinguishable but still suffer a reduced definition from the background haze. Of note is the absence of a vortex shadow for dust devils with low dust content on the model martian surface. This occurs because the diffuse component from the dust background haze is larger than the amount removed from the direct component by the dust devil. Dust devils with a high dust concentration are easily seen over the background haze at both wavelengths. The reduction in the direct component is sufficient that the addition of the background diffuse component is unable to make up the loss and therefore a vortex shadow is observed.

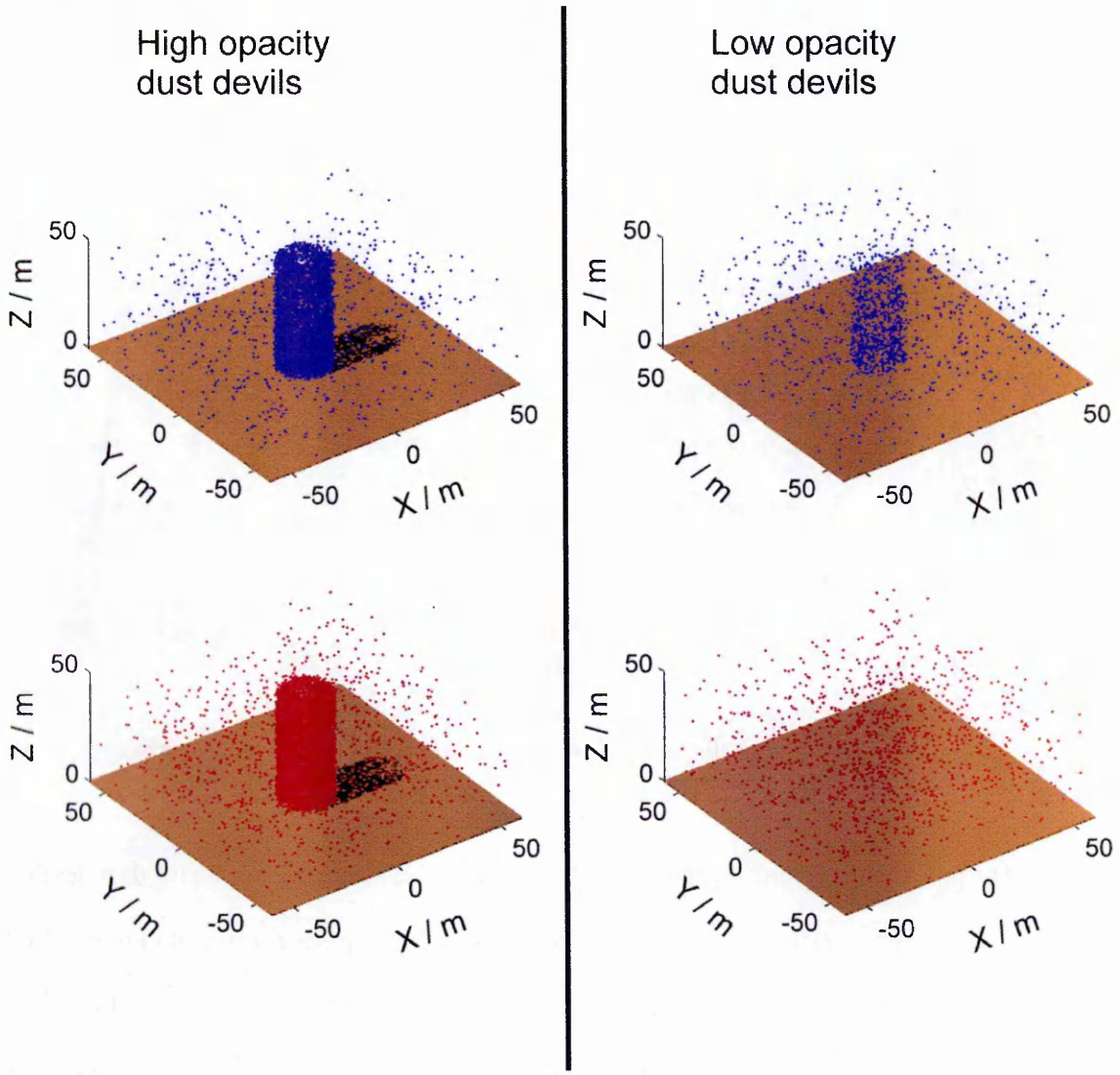

Figure 5-20: Direct and diffuse photon positions after 1-5 scattering events for a high dust background component and low and high opacity dust devils. Blue denotes a wavelength of 388 nm and red represents a wavelength of 750 nm. The incident solar radiation is plane parallel along the axis.

The simulations correlate well with images of dust devils captured by IMP which revealed a low contrast at red wavelengths between dust devil vortices and the background dust haze (Metzger *et al.*, 1999b). At 388 nm the dust devil is more easily distinguished from the background haze agreeing with the analysis performed by Metzger *et al.* (1999b), who used the 450 nm filter on IMP to resolve the vortices.

5.3.2 Transit signatures of martian dust devils

The background diffuse component replaces the fraction of light lost from the direct component and will result in the modification of the optical signature of the transiting dust devils from the clear sky simulations performed for terrestrial dust devils (Chapter 3). The transit of the three different dust devils for low (0.41), mean (0.81) and high (1.57) value of τ_{bg} are shown in Figure 5-21 for a θ_Z of 52.2° and 75.6° respectively (local time of two hours before noon and one hour after noon). The results indicate that transits by dust devils with low dust loading at small θ_Z will be difficult to distinguish from the background irradiance with an observed transmission greater than 0.9. Of particular note is the lack of distinction of the transiting dust devil with uniform illumination observed through the vortex and shadow. For a low atmospheric dust loading (τ_{bg} = 0.41), the predicted transit signature for a vortex with τ_{dd} = 0.14 closely resembles the expected transit signatures for terrestrial dust devils (Chapter 3), with the point of lowest illumination seen after the passage of the vortex core. The effect of the diffuse component on the transit profile is observed as a more gradual increase in irradiance back to ambient, whereas on the Earth we see a significantly steeper gradient as the irradiance increases back to ambient values. High opacity dust devils produce a pronounced reduction in irradiance through the vortex and are characterised by a sharp increase in irradiance of approximately 10%, followed by a more gradual increase before sharply increasing to ambient upon exiting the dust devil shadow. The first increase coincides with the detector exiting the non-illuminated wall and measuring the ambient diffuse irradiance. The more gradual increase for around 15 seconds is a result of the vortex taking up a smaller fraction of the FoV as it moves away from the Point of Measurement (PoM), thus increasing the amount of sky observable. Finally, as the PoM moves outside the dust devil shadow the irradiance quickly returns to ambient levels. Of particular note, the point of lowest transmission is within the dust devil interior, within the non-illuminated wall, and not the dust devil shadow as would be the case on Earth (Chapter 3).

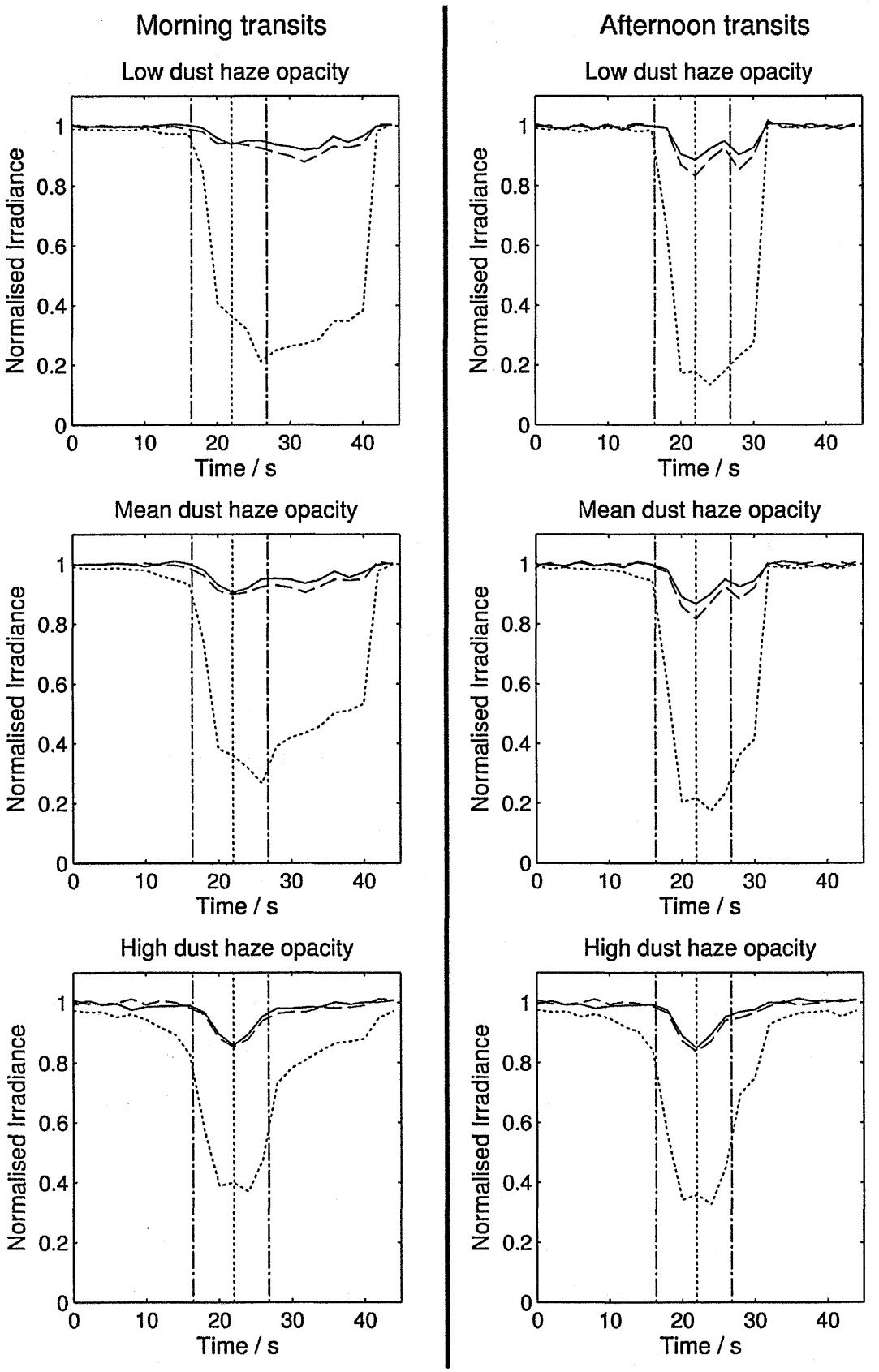

Figure 5-21: The spectral signature at 388 nm during a transit of a martian dust devil of low(solid lines), mean(dashed) and high(dotted) dust content. Three different dust haze opacities were considered, 0.41, 0.81 and 1.57 (see text). Two different times are also considered, 10:00 and 13:00. The dust devil interior and centre are denoted by the dotted and dash-dot lines.

As expected, small θ_z results in a significantly shorter transit profile, correlating with a reduction in the length of the dust devil shadow. Small θ_z increase the path length through the dust column, therefore the irradiance received during an afternoon transit is less than observed during the morning transits. Most importantly the point of lowest transmission is observed inside the dust devil interior for all vortex dust loadings.

For mean and high τ_{bg}, the portion of the transit profile associated with the dust devil interior becomes well defined for both morning and afternoon transits and the point of lowest illumination is observed close to or at the core. A shadow is still observed at mean τ_{bg}, resulting in a gradual increase towards ambient illumination, with the low and mean opacity dust devils showing no discernible change upon exiting the non-illuminated wall. The rapid increase in irradiance observed for high opacity dust devils upon exiting the non-illuminated wall becomes more pronounced with an increase in irradiance of 25 % and 35 % for morning and afternoon transits respectively. At high τ_{bg} no discernible shadow is observed and the transit profiles are symmetrical about the dust devil centre for both morning and afternoon transit.

This result is advantageous; in Chapter 4 it was seen that one of the most challenging aspects of characterising dust devils from their transit signature was determination of the position of the dust devil interior in the signature time-series. On Mars the high diffuse component acts to distinguish the dust devil interior making it more easily identifiable in the transit profile. As observed for a mean τ_{bg}, the point of lowest transmission occurs within the dust devil interior and for dust devils vortices with low and mean dust loadings, correlates with the centre of the dust devil core.

The transit signatures at 750 nm are shown in Figure 5-22 and, for a dust devil with mean and high dust content, are similar to that seen for 388 nm. Comparing the low τ_{dd} dust devil, at all τ_{bg} simulated, the presence of a shadow (created by the direct component) is not observed in the transit signature.

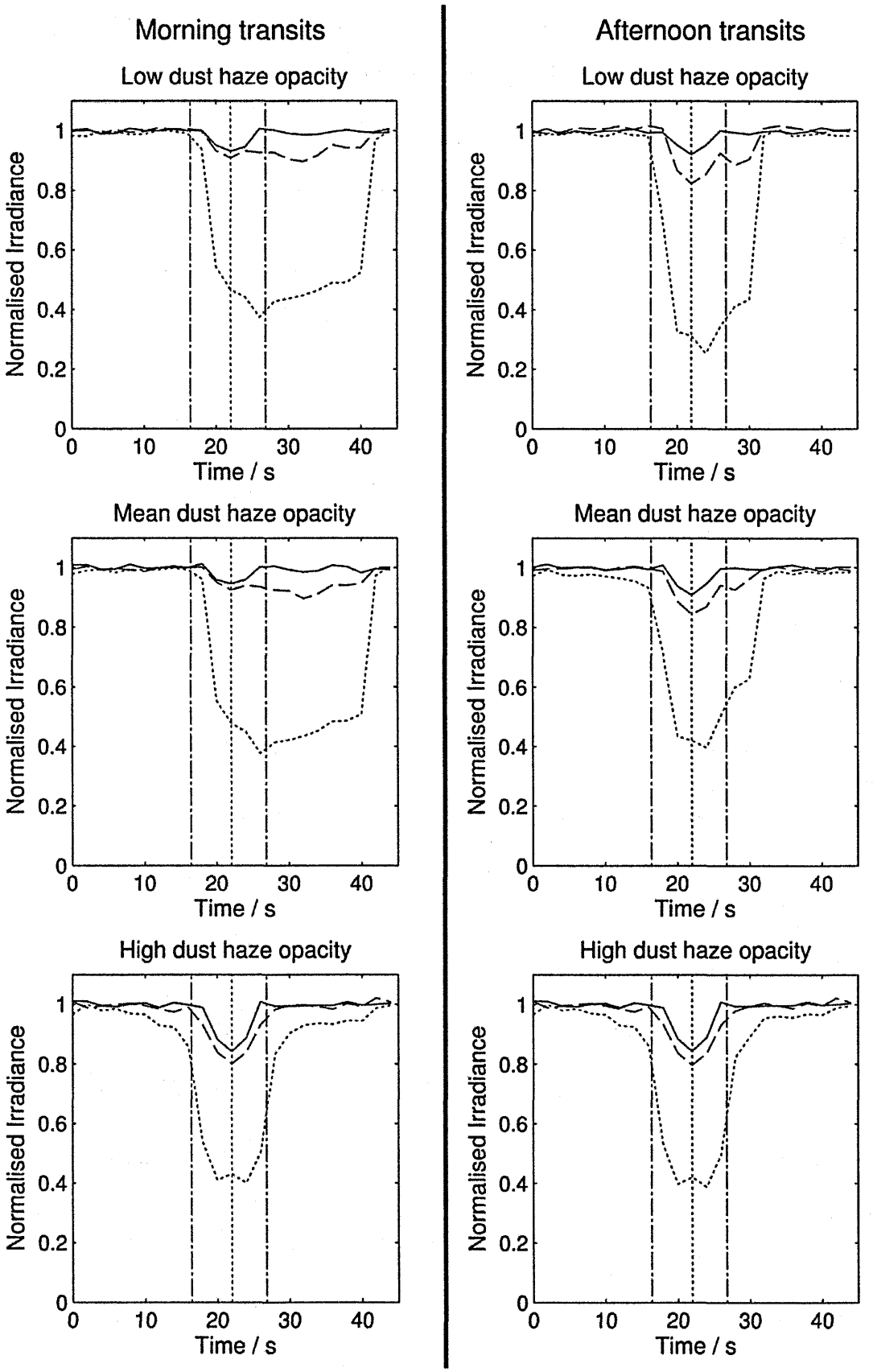

Figure 5-22: As figure 6-21, but at a wavelength of 750 nm.

The absence of a discernible shadow at 750 nm makes the portion of the transit signature associated with the dust devil interior more distinguishable in comparison to 388 nm. The enhanced definition of the dust devil at 750 nm is the opposite experienced when directly imaging dust devils on Mars (as illustrated in Figure 5-20 and correlated by images of dust devils taken by IMP).

The high diffuse irradiance observed at the martian surface result, the portion of the transit signature corresponding to the dust devil interior is more easily distinguished when compared to terrestrial transit signatures (Chapter 3&4). In contrast to directly imaging dust devils, the simulations imply that detecting a transit of a dust devil with low dust content under low and nominal τ_{bg} is best accomplished at red wavelengths where the higher diffuse component reduces the vortex shadow, providing better definition of the dust devil interior within the transit signature.

5.3.3 Single scattering properties for the entrained dust

One the main questions regarding martian dust devils is whether the dust entrained within vortex is the same as the background dust component. While not always present, observational evidence has shown the presence of dust "skirts" around martian dust devils, indicating that larger particles can be lofted into the lowest few metres of the atmosphere (Sinclair, 1973, Greeley *et al.*, 1992). The larger dust grain size will modify the single scattering properties relative to the background dust haze resulting in different attenuation of the solar spectrum.

To investigate the change in attenuation, the background dust haze was assumed to have refractive indices equal to those retrieved by Wolff *et al.* (2009) and a particle size distribution described by a power law with r_{eff} = 1.6 μm and v_{eff}= 0.4 (Wolff *et al.*, 2009). Four different cases were considered. The first assumes the dust entrained within the dust devil is identical to the background haze (D1). The second and third cases were assumed to have the same composition as the background haze (*i.e.* same refractive indices) but the effective radius of the size distribution was increased to 2.5 μm (D2) and 5.0 μm (D3) respectively. A dust devil with

the optical properties of O97 was also simulated (D4), to determine whether changes in the dust composition would be observed. The velocity of the dust devil across the surface was assumed to be 2.5 ms^{-1}. To simplify the analysis the dust concentration is assumed constant through the vortex, *i.e.* no dust free core.

The transit signatures for the different cases, relative to case D1 is shown in Figure 5-23 as a function of time. Similar variations are observed at 388 nm with all dust components showing a 1-2% difference. Within the dust devil interior D1 experiences a higher irradiance at 388 nm compared to the other cases correlated to a higher ω_0. Greater variation in the spectral signature is observed at 750 nm, with D4 displaying lower irradiances through the dust devil transit. D2 and D3 see an increase in irradiance over the D1 case, peaking in the non-illuminated wall of the dust devil at ~1% for D2 and ~2% for D3.

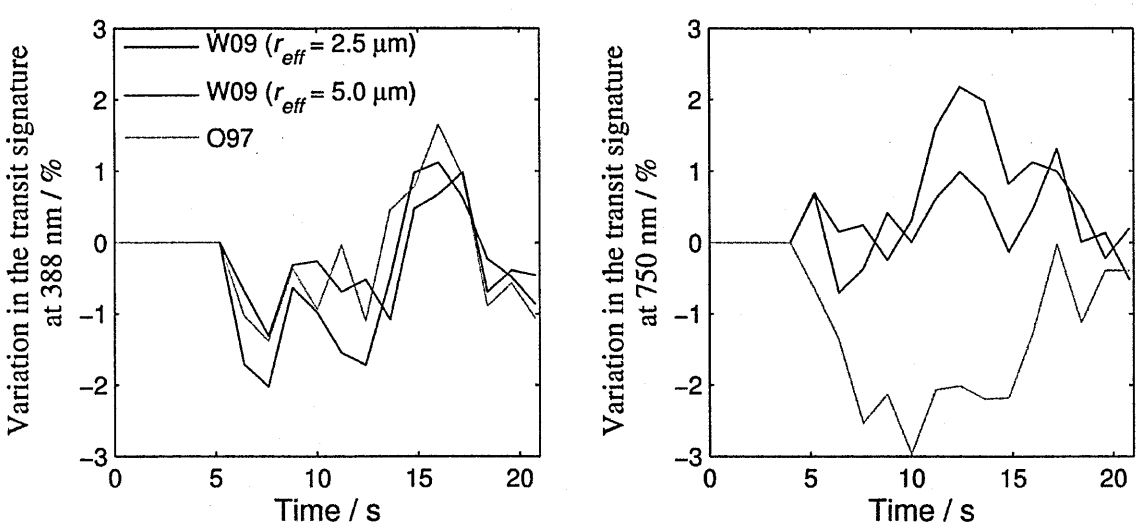

Figure 5-23: The variation in the transit signatures at 388 nm and 750 nm of dust devils with different dust components entrained within the vortex. W09 with r_{eff} = 2.5 (blue line), W09 with r_{eff} = 5.0 (red) and O97 (grey).

While the variations in the transit signatures are small (<5%) they will result in a difference in $\Re_I$ and $\Re_D$. Applying the technique used to differentiate between different dust backgrounds, $\Re_I$ and $\Re_D$ are shown as a function of the apparent optical depth (τ_a) at 670 nm in Figure 5-24. τ_a is the increase in τ over the background value prior to the dust devil transit and is calculated

from $\tau_a = -\ln\left(I_a(670)/I_{dd}(670)\right)$ where $I_a(670)$ is the ambient irradiance at 670 nm and $I_{dd}(670)$ is the irradiance at 670 nm during the transit of the dust devil. Also shown is $\Re_I$ and $\Re_D$ for an equivalent increase in τ_{bg}. Comparing the dust devil transits, there is sufficient variation between $\Re_I$ and $\Re_D$ to distinguish between the different dust components. Therefore by measuring the transit signature of transiting dust devils and comparing their $\Re_I$ and $\Re_D$ values as a function of τ_a it can be determined whether the entrained dust differs between different vortices.

Comparing $\Re_I$ and $\Re_D$ of the dust devils to equivalent increases in τ_{bg}, significantly different $\Re_I$ and $\Re_D$ values are observed for equivalent τ. As was discussed in Chapter 3 the scattered component during a dust devil transit is highly sensitive to the dust concentration. The higher dust concentration increases the probability of photon-particle interaction leading to a higher chance the photon will be absorbed by the particle. Thus for the dust devil opacities considered here, the measured diffuse component during the dust devil transit is lower than the equivalent increase in the dust background leading to different $\Re_I$ and $\Re_D$.

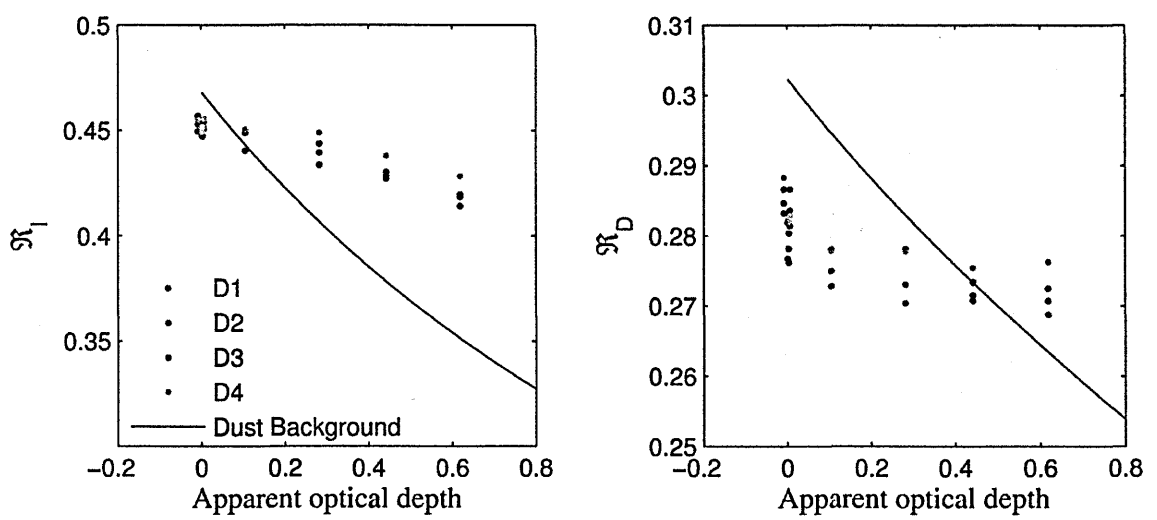

Figure 5-24: $\Re_I$ and $\Re_D$ as a function of the τ_a for dust devils with different dust components of D1 (black), D2 (blue), D3 (red), and D4 (grey). $\Re_I$ and $\Re_D$ for an equivalent increase in τ_{bg} is denoted by the sold black line.

It was discovered in Chapter 3 for terrestrial dust devils that the direct component was insensitive to the dust concentration. Therefore to remove the dependence on the dust concentration, the ratio of the direct irradiances at 388 nm and 750 nm ($\Re_{Dir}$) was plotted as a function of τ_a and is shown in Figure 5-25 for the different dust components. The $\Re_{Dir}$ dependence on τ is equivalent for a dust devil transit and an increase in the dust background. Case D4, which suspended dust particles with the composition of O97, results in a significantly higher $\Re_{Dir}$ and is easily distinguished from the dust background. For dust particles with the same composition and only slightly larger in size (D2), large differences are observed at low τ (< 0.3). With increasing τ it becomes apparent that the gradient of $\Re_{Dir}$ for D2 is steeper than that of D1 indicating a change in the dust component. At low τ, $\Re_{Dir}$ is lower for larger particles (D3) relative to D1. The gradient of $\Re_{Dir}$ for the D3 case is less steep than both D1 and D2 resulting in lower $\Re_{Dir}$ values at higher τ. While variations in $\Re_{Dir}$ can identify changes to the suspended dust component it is important to sample τ sufficiently so that the gradient of $\Re_{Dir}$ can be determined; this provides another measure for identifying changes in the dust component.

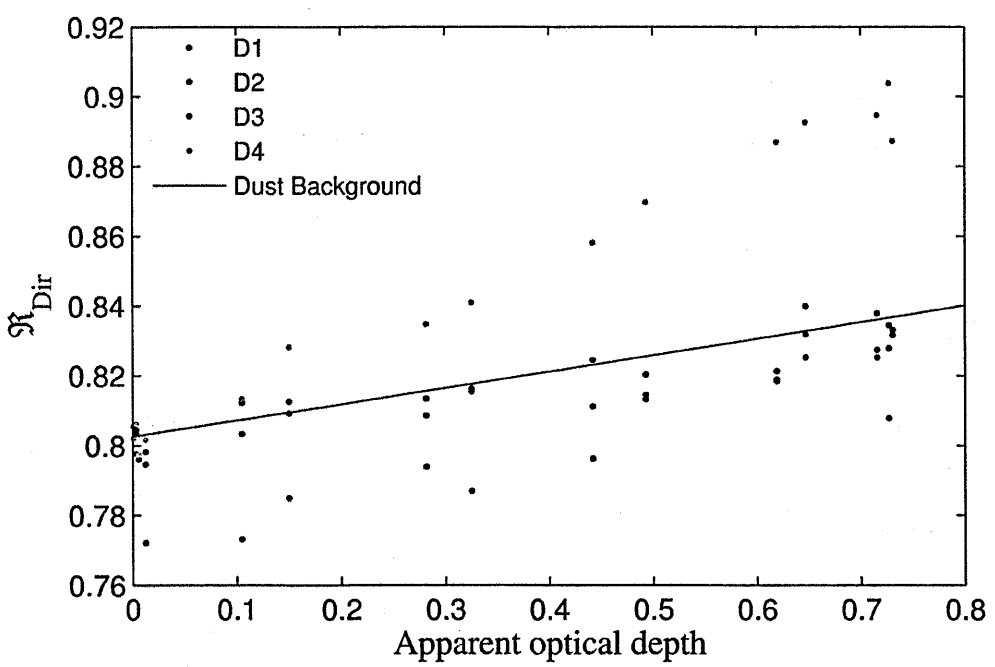

Figure 5-25: $\Re_{Dir}$ as a function of the τ_a for dust devils with different dust components of D1 (black dots), D2 (blue dots), D3 (red dots), and D4 (grey dots). $\Re_{Dir}$ for an equivalent increase in τ_{bg} is denoted by the sold black line.

Similar to differentiating between different dust background components, $\Re_I$ and $\Re_D$ can be used to compare transits of different dust devils to determine whether the dust suspended within the vortices differs. However as shown in case D1, the sensitivity of the diffuse component to the dust concentration results in $\Re_I$ and $\Re_D$ having different values when compared to an equivalent increase in the dust background even if identical dust is entrained in the dust devil. $\Re_{Dir}$ enables comparisons between the dust background and the dust suspended in dust devil vortices. By sampling the τ sufficiently, the gradient of $\Re_{Dir}$ provides another measure for identifying changes to the dust component. It should be noted that measuring the direct component is extremely difficult and advocates the need for simultaneous measurements of the total and diffuse surface irradiance, from which the direct component can be determined.

5.4 The effect of water-ice clouds on the downward irradiance at the surface

As discussed in Chapter 1, the atmospheric temperature can fall below the condensation point of water, resulting in the formation of H_2O condensate clouds at altitudes between 8 km and 30 km and also the formation of near surface fogs during the martian night. One of the main applications for a visible spectrometer on the surface of Mars is discerning between airborne dust and ice particles and the retrieval of the ice particles characteristics.

5.4.1 Attenuation of the irradiance spectrum

The attenuation of the irradiance spectrum for different ice particle sizes was investigated and compared to the attenuation by the suspend dust. Figure 5-26 shows the variation in attenuation of the irradiance spectrum resulting from the passage of a water-ice cloud with an optical depth (τ_{cld}) of 0.3, relative to an equivalent increase in the dust haze, with the single scattering properties of W09 assumed. The ambient background dust haze had an optical depth of 0.3, leading to an overall atmospheric optical depth of 0.6 during the cloud event. From the two types of cloud observed by Clancy *et al.* (2003), the ice particle size distribution was assumed to

have a r_{eff} of 1.0 μm and 2.0 μm for type 1 clouds, and 3.0 μm and 4.0 μm for type 2 clouds. It is acknowledged that the retrieval by Clancy *et al.* (2003) invokes non-spherical particles. However, for this analysis more accurate particle shapes proved to computationally intensive and, therefore, spheres were used as an approximation. Immediately obvious is the distinct increase in irradiances at wavelengths shorter than 500 nm for both cloud types. This is because ice particles have an ω_0 extremely close to unity, leading to the majority of the incident light being scattered, increasing the diffuse irradiance. At longer wavelengths (>500 nm) both the dust and the ice particles exhibit a high diffuse component. However, the presence of ice particles in the martian atmosphere leads to a reduced irradiance at these longer wavelengths. This is a result of a higher fraction of the scattered light being reflected back into space.

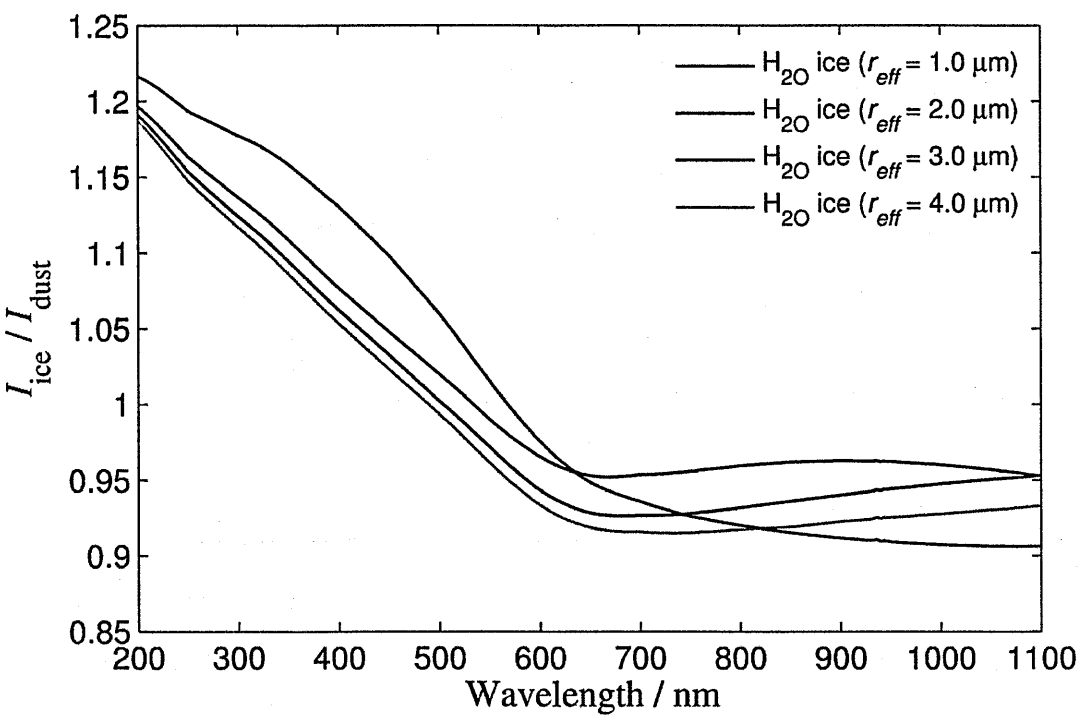

Figure 5-26: The variation in the surface irradiance spectrum during the passage of a H_2O ice cloud relative to an equivalent increase in τ_{bg}.

Measuring the attenuation of the irradiance spectrum at wavelengths shorter than 500 nm allows the determination of whether a water-ice cloud is present. However, from the attenuated spectrum it is difficult to determine the size of the ice particles within the cloud, τ_{cld} and τ_{bg}. It is important to know the dust loading since different quantities of dust and ice

aerosols, and variation the ice particle shape, can lead to equivalent attenuation of the irradiance spectrum. Hence accurate retrieval of the atmospheric dust content is required if the ice particle abundance and size is to be retrieved.

5.4.2 Retrieval of water- ice aerosol characteristics

The attenuation of the irradiance spectrum enables distinction between dust and ice aerosols. However, the retrieval of τ_{bg} and ice aerosol size is problematic, given that there is no unique solution for the observed attenuation. The technique applied to distinguish between different dust components in the background haze (Section 5.2.5) and within dust devils (Section 5.3) can be applied to water-ice particles. Figure 5-27 shows $\Re_I$ as a function of atmospheric optical depth. If the increase in τ is due to the passage of a water-ice cloud, the irradiance at both 388 nm and 750 nm wavelengths increases. This leads to a decrease in the $\Re_I$ gradient, with the new gradient dependent on the ice particle size. However, if the increase in τ is a result of increased dust loading then $\Re_I$ has a distinctly steeper gradient, in comparison to ice particles, since the irradiance at 388 nm and 750 nm decrease and increase respectively. Furthermore, by extrapolating back to zero τ_{cld}, τ where the ice $\Re_I$ lines intersect with the dust $\Re_I$ line provides an estimation of τ_{bg}.

This scenario is an idealised case where τ_{bg} was assumed to be constant. However, over long time-scales, the dust loading will increase and decrease depending on current atmospheric state. To assess the effect of a varying dust haze with time, τ measured by the Opportunity rover (Lemmon, 2008) was used to estimate realistic values for τ_{bg} and τ_{cld} during martian northern summer. To estimate τ_{bg}, the lowest τ values between L_s = 40–120° (as measured by Opportunity) were selected, and interpolated over L_s. The interpolated τ_{bg} was then subtracted from the Opportunity data with the residuals taken to be τ_{cld}. The dust and ice optical depths are illustrated in Figure 5-28.

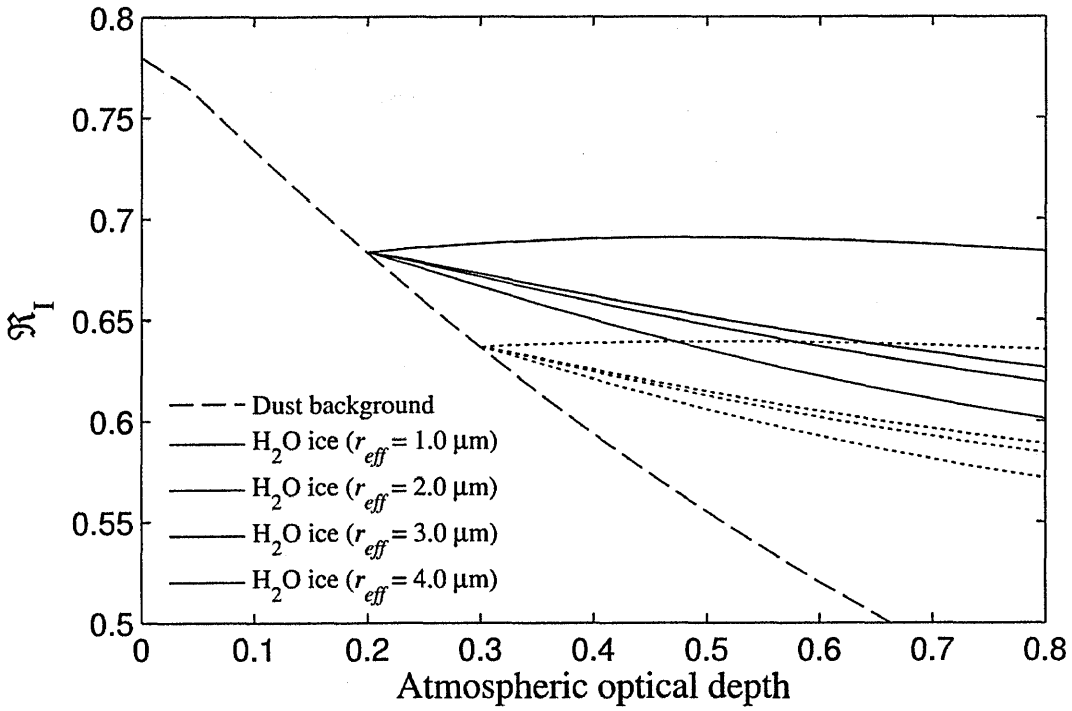

Figure 5-27: $\Re_I$ as a function of the atmospheric optical depth. The solid and dotted lines represent the passage of an ice cloud with a τ_{bg} of 0.2 and 0.3 respectively.

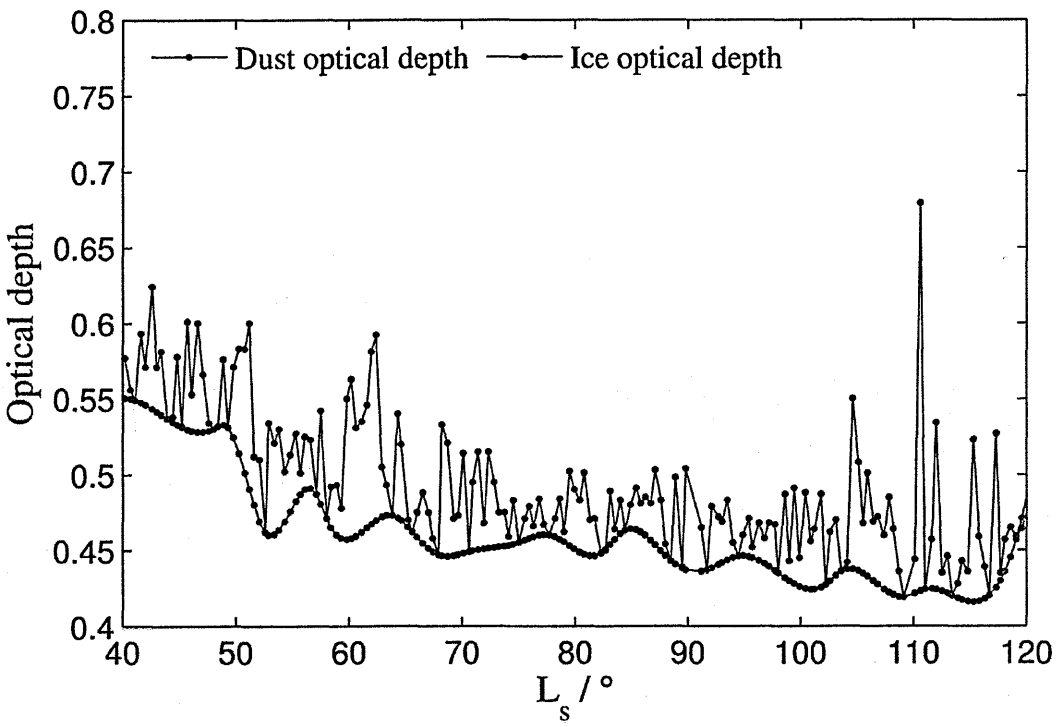

Figure 5-28: Dust and ice optical depth as a function of L_s.

The irradiance at noon was calculated using the Mars Radiative Transfer Model and the $\Re_I$ profiles for the different cloud types as a function of atmospheric optical depth for a varying τ_{bg} are shown in Figure 5-29a. Over long time-scales, the inclusion of a varying dust haze results in less defined $\Re_I$ profiles between the different ice particle sizes, and no unique intersection with the $\Re_I$ line for dust. Figure 5-29b shows $\Re_I$ for two cloud events over shorter time-scales, from $L_s = 56°$ to $L_s = 65°$ and $L_s = 105°$ to $L_s = 115°$. Clear distinction between the ice particles with $r_{eff} = 1.0$ μm and 3.0 μm is observed and the point of intersection with the $\Re_I$ for dust occurs for the two cloud events at a τ_{bg} of 0.47 and 0.42 respectively. This correlates with the simulated τ_{bg} (Figure 5-28).

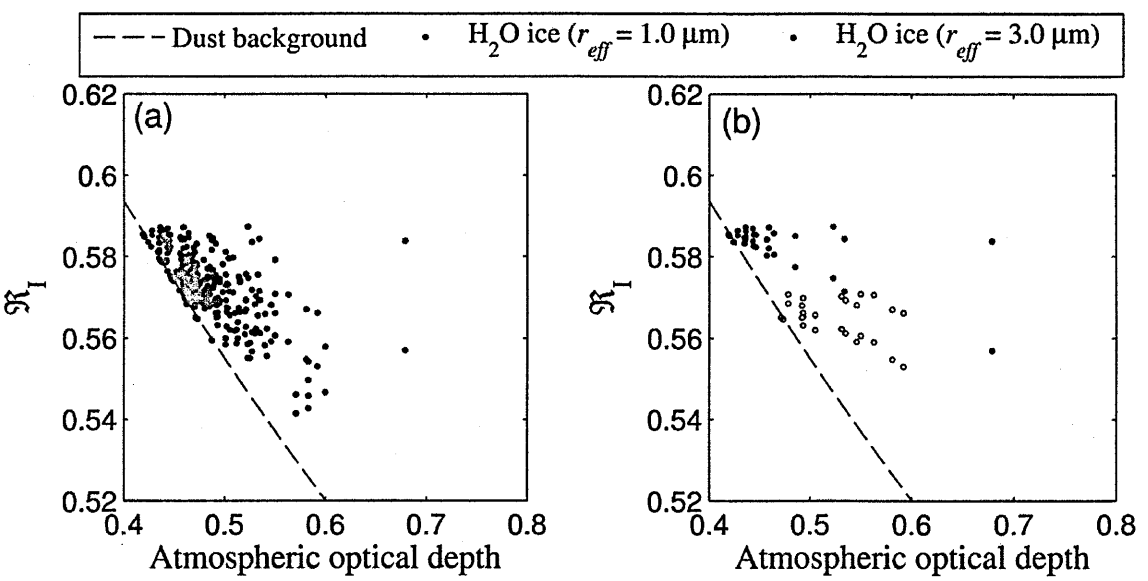

Figure 5-29: $\Re_I$ as a function of atmospheric optical depth for a varying τ_{bg} from (a) $L_s = 40°$ to $L_s = 120°$ and (b) from $L_s = 56°$ to $L_s = 65°$ (filled circles) and $L_s = 105°$ to $L_s = 115°$ (clear circles).

These simulations have shown that measuring $\Re_I$ over seasonal time-scales in order to differentiate between ice particle sizes breaks down. Variations in τ_{bg} complicate the estimation of both the dust background and ice abundance over long time-scales, since varying the abundance of both aerosols can lead to the same $\Re_I$ values. However, as shown, this analysis method for differentiating between ice particle sizes can be applied over time-scales where the dust background can be assumed to vary only slightly.

The highly efficient scattering by ice aerosols leads to a redistribution of the solar energy deposited into the martian atmosphere. The size and shape of the ice particles dictates how much of the incident radiation is scattered towards the surface and how much is scattered back to space. The more EM radiation that is scattered back to space the lower the energy deposited in the atmosphere. This affects the atmospheric heating rate and thus the atmospheric circulations and the coupled feedbacks with the dust aerosols. Hence methods for retrieving the ice particle shape and size are highly important if their radiative impact on the Mars climate system is to be fully understood.

Chapter Six: Wind tunnel measurements of suspended dust

The European Mars Simulation Wind Tunnel Facility (MSWTF) at the University of Aarhus was used to conduct experiments to measure the wavelength dependent attenuation of light by different dust aerosol samples in suspension under simulated martian atmospheric conditions. Using the Monte Carlo Light Scattering Model (MCLSM), the optical properties of the dust samples were to be retrieved. Unfortunately the experiments were too ambitious and the MCLSM could not simulate the irradiance spectra to sufficient accuracy in order to retrieve the optical properties of the dust samples. Experiments were performed to simulate the scenario at the martian surface of the passage of a dust cloud composed of dust particles with a different composition to the ubiquitous background dust haze.

6.1 The Mars Simulation Wind Tunnel Facility and experimental setup

The aim of the experiments were to validate the retrieval technique applied to dust particles entrained by terrestrial dust devils and to demonstrate the retrieval of dust aerosol optical properties in dusty environments with a high scattered irradiance (analogous to conditions on Mars).

The MSWTF is a re-circulating wind tunnel, with a volume of 50 m^3, and dust injection system to allow suspended particulates (aerosols) in the airflow. The wind tunnel is capable of producing pressures, temperatures and wind speeds analogous to martian ambient conditions. The chamber employs a unique LED-based optical illumination system allowing variable illumination levels over the visible wavelength region (Merrison *et al.*, 2009).

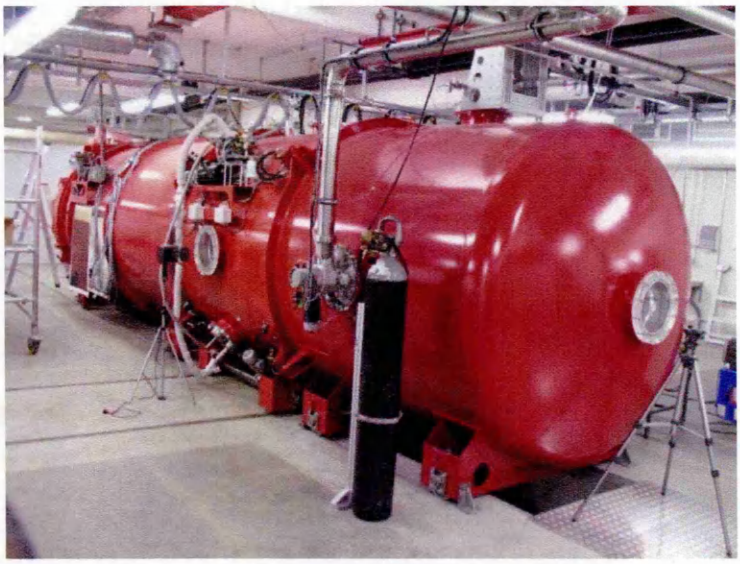

Figure 6-1: Image of the Mars Simulation Wind Tunnel Facility.

6.1.1 Spectroscopic instrumentation

Two irradiance spectrometers, measuring the ultraviolet and visible wavelength region, were used in the experiments. The two spectrometers were set up to look across the MSWTF at the light sources with a path length of approximately 217 cm through a quartz window as illustrated in Figure 6-2.

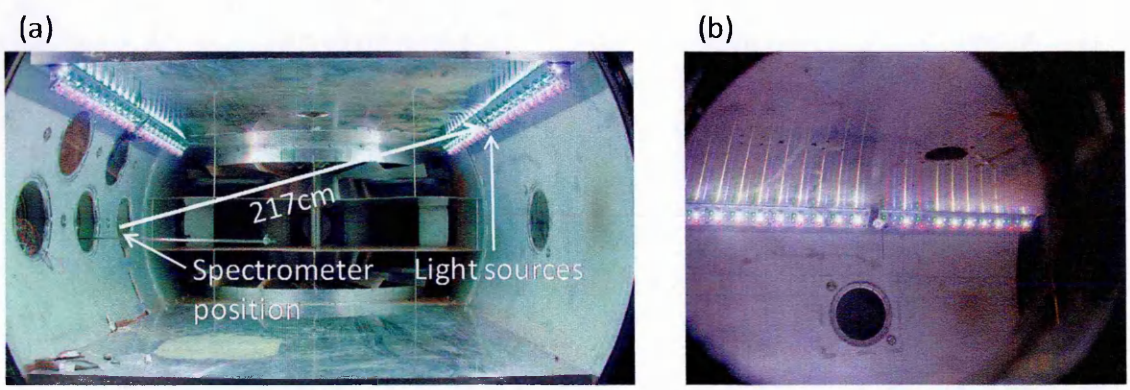

Figure 6-2: (a) experimental setup showing the MSWTF and the positions of the spectrometers and light sources and (b) the approximate chamber volume observed by the UV-VIS spectrometer.

The attenuation data was taken solely from the primary spectrometer (designated UV-VIS). The spectra recorded by the UV-VIS were calibrated using the Avantes AvaLight-HAL CAL light source. The spectra produced by the secondary spectrometer (designated validation spectrometer) were cross-calibrated against the UV-VIS spectrometer. Figure 6-3 shows the irradiance spectrum measured by the UV-VIS spectrometer compared with the spectrum measured by the validation spectrometer for the halogen bulb and LED arrays. Both spectrometers produce very similar spectra for both types of light sources with the largest differences seen at wavelengths > 600 nm with a variation of approximately 1% and 2% observed for the halogen and LED spectra respectively. The Avantes AvaLight-HAL CAL light source had a calibration uncertainty of 2.5% between 380 nm and 1100 nm and a light source output uncertainty of 9.5% placing the difference between the two detector responses well within the error of the calibration. A greater difference between the irradiance spectra is seen at wavelengths below 400 nm with a difference of 10% being observed. The calibration and calibration light source output uncertainty at wavelengths <380 nm is 5% and 12% respectively which could account for the increased error in irradiance.

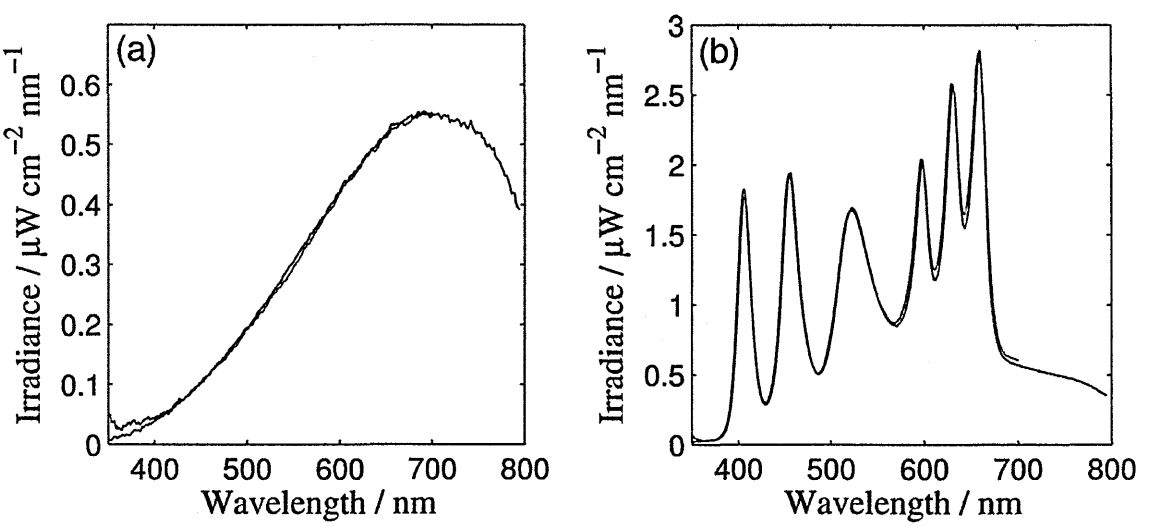

Figure 6-3:The measured the irradiance spectrum by the UV-VIS spectrometer (black line) and the validation spectrometer (red line) produced by (a) the halogen bulb and (b) the LED arrays.

6.1.2 Light sources

Two light sources were used, a 50 W halogen bulb with a beam angle of 10°, which produced a broadband spectrum over the 320–800 nm wavelength region, and an array of Light Emitting Diodes (LEDs). The LED arrays consisted of multiple colours; UV, blue, green, amber, red, dark red and white, with spectral peaks at 405, 465, 525, 590, 627, 660 and 465/540 nm respectively. The halogen bulb was mounted inside the chamber alongside the LED arrays so that the spectrometer viewing probes did not have to be altered and a constant path length of 2.17 m could be maintained when switching between the different light sources. The irradiance spectrum for the halogen and LED array is shown in Figure 6-4.

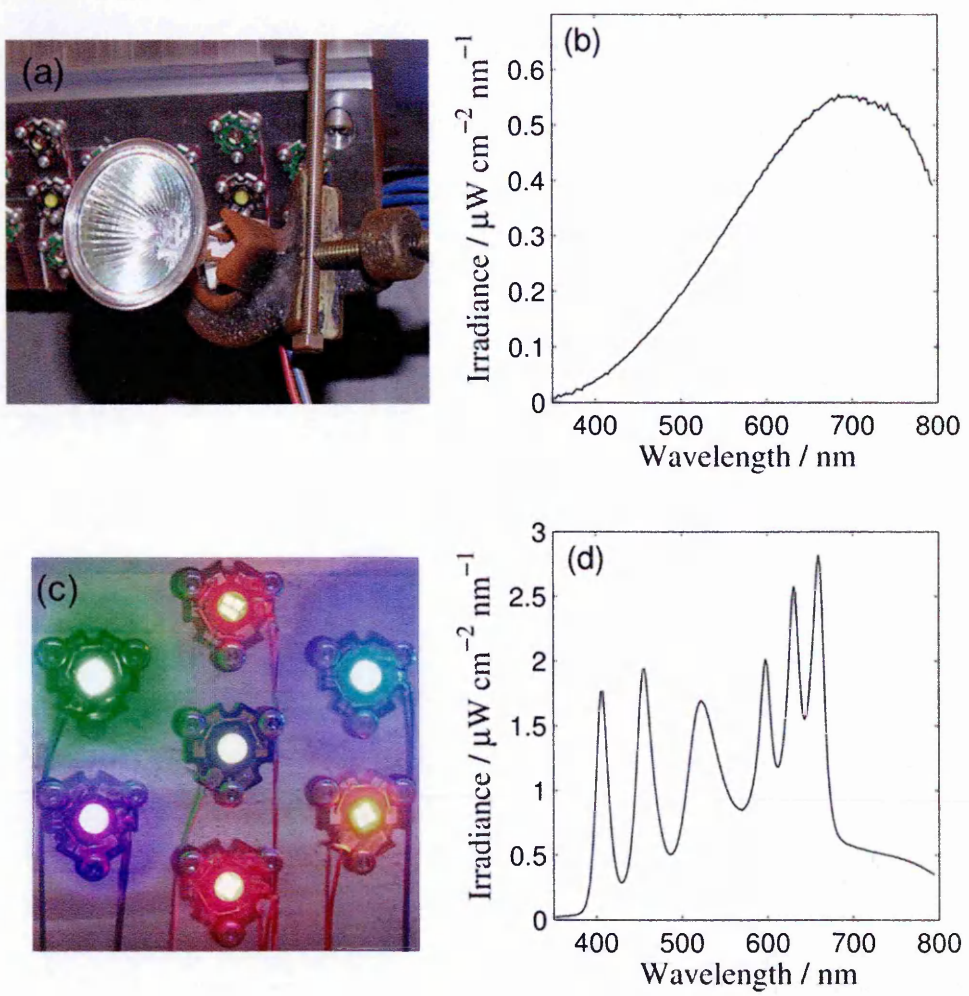

Figure 6-4: (a) Image of the halogen bulb used in the experiments. (b) The measured irradiance spectrum of the halogen bulb. (c) Layout of one of the LED arrays. There were 20 identical arrays along each side of the MSWTF. (d) An example of the irradiance spectrum produced by the LED arrays.

6.1.3 Determination of LED radiant flux

The measured reference irradiance spectrum (I_{ref}) is the irradiance received at the spectrometer location as a result of the twenty LED arrays and/or the halogen bulb facing the spectrometer, with no dust present in the chamber. The twenty LEDs on the same side of the chamber as the spectrometers will also provide some contribution to the reference spectrum due to reflections from the opposite wall, as will higher order reflections. Quantifying the contribution as a result of all reflections is beyond the scope of this work and is thus included within the calculated radiant flux of the LED arrays. This assumption results in the calculated 'output' of the individual LEDs being larger than their "true" values. The error induced as a result of this assumption will be small, since the dominant component observed by the spectrometer is the direct component from the twenty facing LED arrays and the halogen bulb.

To determine the radiant flux of the LED arrays the contribution towards the observed reference spectrum from all twenty had to be calculated from I_{ref}. The distance from each LED array to the detector was measured and the output angular dependence of the individual LEDs was determined from the manufacturer datasheet. Figure 6-5 illustrates the contribution to I_{ref} from each LED array. $R_{dn,1\text{-}20}$ is the reduction in radiant flux as a result of the line of sight being off the plane normal to the LEDs. $R_{s,1\text{-}20}$ is the distance from the LED arrays to the point of observation and P_0 is the radiant flux unit solid angle.

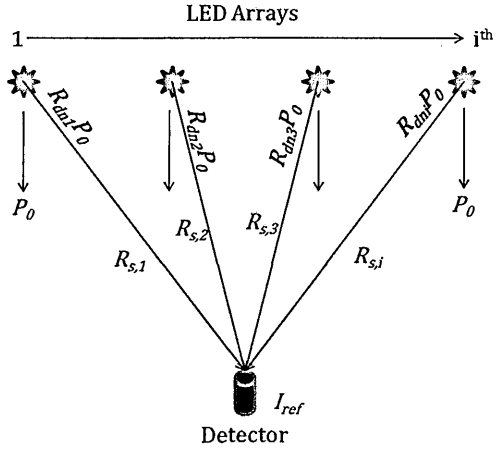

Figure 6-5 Determination of the output power of the individual LED arrays.

The measured irradiance, I_{ref}, is thus given by:

$$I_{ref} = \frac{P_0 R_{dn,1}}{R_{s,1}^2} + \frac{P_0 R_{dn,2}}{R_{s,2}^2} + \frac{P_0 R_{dn,3}}{R_{s,3}^2} + \ldots + \frac{P_0 R_{dn,i}}{R_{s,i}^2} \tag{6.1}$$

Hence, rearranging for P_0, the radiant flux of the LED arrays per unit solid angle is given by:

$$P_0 = I_{ref} \left(\sum_{i=1}^{20} \frac{R_{dn,i}}{R_i^2} \right)^{-1} \tag{6.2}$$

Figure 6-6 shows the angular dependence of the output intensity for the different LEDs in single array. Of note are the UV and blue LEDs which have a much broader angular distribution compared to the longer wavelength LEDs. For small displacement angles (with the exception of the dark red LED) the angular distribution of the relative intensity is similar for all LEDs. However at larger angular displacements, 45°, there is an approximate difference of 60% between the red LED output intensity compared with the UV and blue LED.

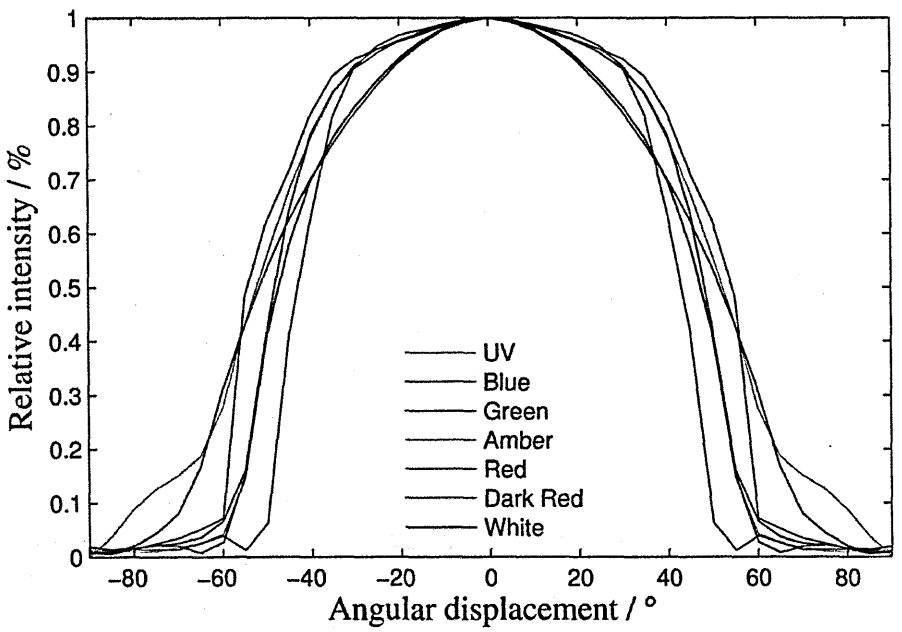

Figure 6-6: Relative intensity as a function of angular displacement for the individual wavelengths.

To determine the significance of the angular dependence on the output radiant flux for the different LEDs, the irradiance within the MSWTF was modelled by dividing the chamber into a discrete number of volume elements (discrete volume model). The irradiance received at

each node was calculated using the determined LED radiant power from Eq.(6.2) and knowing the distance from the volume elements to each of the LED arrays. A slice through the modelled MSWTF is given in Figure 6-7 showing the irradiance in the *X*-*Z* plane at different locations along the *Y*-axis of the chamber from the blue and red LEDs in a single array. It shows that volume elements at large angular displacements, from the normal to the LED surface, receive more irradiance from the blue LEDs than the red LEDs. However, the number of LED arrays present reduces the effect of this angular dependence, since the majority of the light incident on any volume element is from the array with the smallest angular displacement to the volume element.

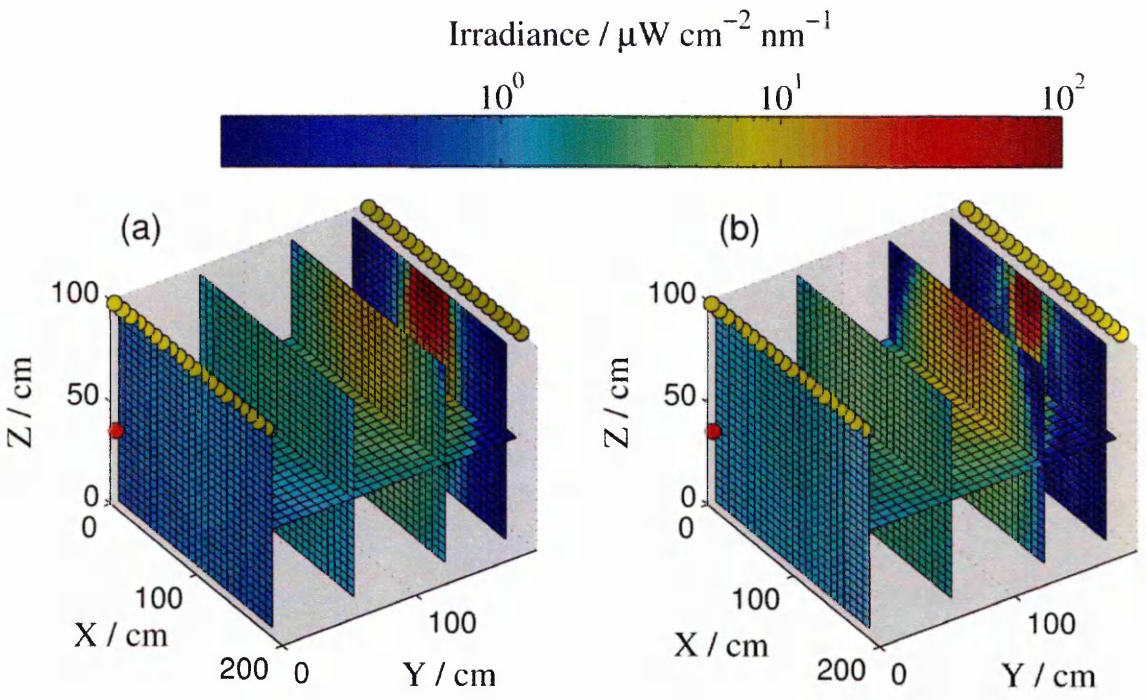

Figure 6-7: Slices through the modelled chamber showing the irradiance at each node from a single (a) blue and (b) red LED highlighting the differences in angular displacement. The yellow circles mark the location of the LED arrays and the red dot denotes the location of the UV-VIS probe.

Another factor that reduces the importance of the LED angular displacement is the field of view (FoV) of the detector. The volume elements that are most sensitive to the radiant power angular dependence are near the limits of the chamber volume (*i.e.* near the chamber edge walls and floor) which are not visible to the detector. The need to take into account the angular displacement of the LED output would therefore seem superfluous, but since the deep-red LED

shows an almost 10% difference in output at smaller displacement (~30°), the angular displacements of all the individual LEDs are considered in the model for completeness.

6.1.4 Dust samples

A number of materials with different optical properties were chosen to be suspended within the MSWTF environment. The materials are in three categories:

- mineral and iron oxide samples;
  - quartz, hematite and magnetite,
- clay samples;
  - kaolinite and montmorillonite
- martian dust simulants;
  - Salten Skov 1 (Nørnberg *et al.*, 2009) and Mars JSC-1 (Allen *et al.*, 1998).

Hematite and Mars JSC-1 have absorption spectra analogous to martian dust aerosols, being highly absorbing of light at short wavelengths (<500 nm) and efficient at scattering longer wavelength light (>500 nm) (Sokolik and Toon, 1999, Allen *et al.*, 1998). Kaolinite and quartz have very low imaginary refractive indices and thus are not representative of martian dust (Egan and Hilgeman, 1979). However, they have a single scattering albedo (ω_0) of ~1 over the spectral range 350–750 nm and as such will demonstrate similar spectral absorption to water-ice particles over these wavelengths. It should be noted that the shapes of quartz and kaolinite particles do not accurately represent those for water-ice particles, and therefore the amount of scattered light will be significantly different. However, they did provide a means of assessing the retrieval of aerosol optical properties in a highly scattering environment. The particle volume size distribution (normalised such that the integral over all particle sizes is unity) is shown in Figure 6-8 for each of the samples. The graph shows that each sample has a broad distribution of particles.

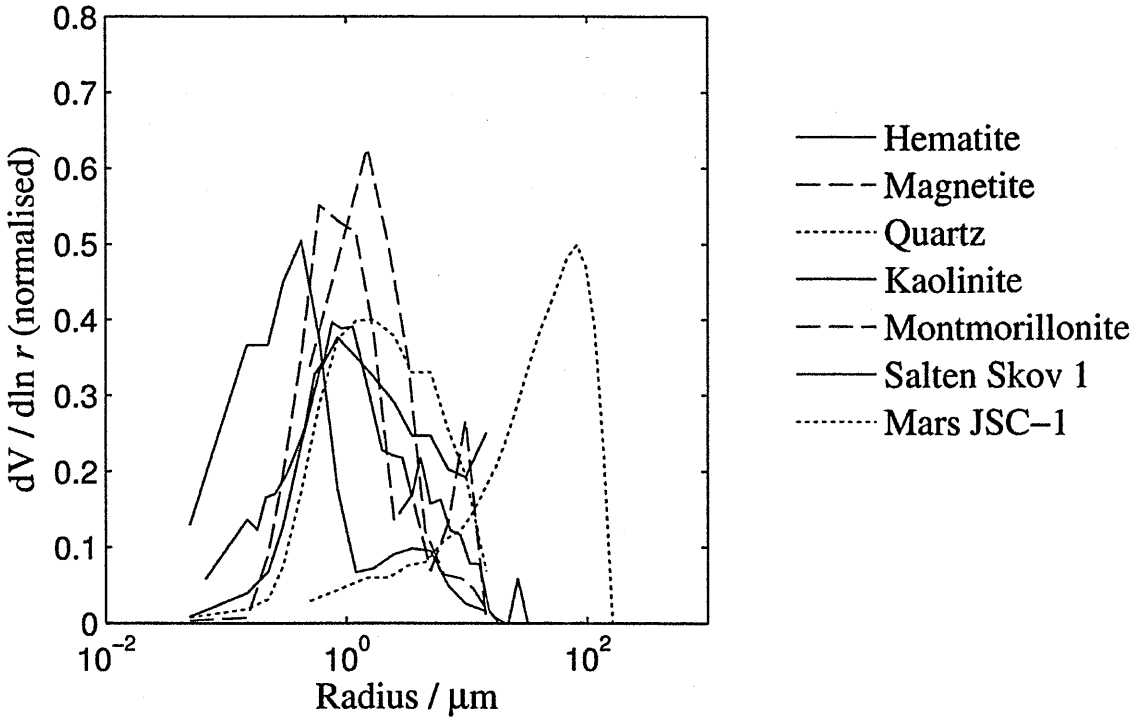

Figure 6-8: The particle size distributions of the various dust samples.

The hematite sample displays a bimodal distribution with a fine fraction peak below 1.0 μm and a coarse particle fraction, with a peak showing at a radius of approximately 3.5 μm. Using Eq (4.2) the particle size distribution for hematite was approximated using two log-normal distributions to describe the fine and coarse particle mode. Therefore the fraction of the volume in the fine and coarse modes was varied along with the median volume radii for the fine fraction (r_{vf}) and coarse fraction (r_{vc}). The approximated particle size distribution of the hematite sample is shown in Figure 6-9. Good correlation is observed over all particle sizes for log-normal distributions where $r_{vf} = 0.37$ μm, $r_{vc} = 4.0$ μm and with 90% of the sample mass constrained to a particle size of below 2.5 μm. The calculated effective radius (r_{eff}) of the hematite distribution was 0.35 μm, which is approximately an order of magnitude smaller than the effective particle size expected in the martian atmosphere.

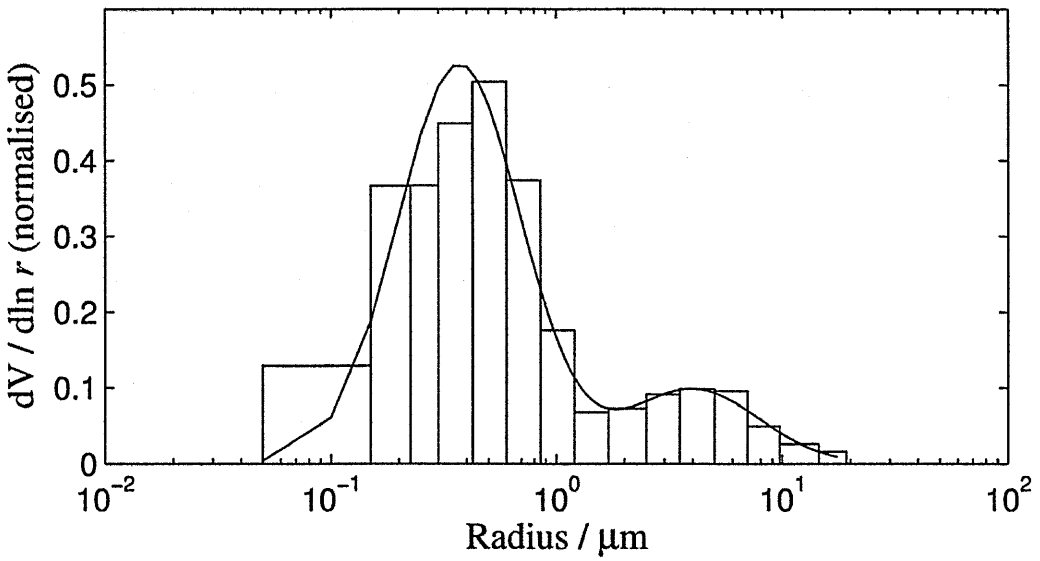

Figure 6-9: The approximated size distribution for the hematite dust sample using two log-normal distributions.

The other dust sample used, with known optical properties optically similar to martian dust, was Mars JSC-1. However Mars JSC-1 had a high abundance of large particles (> 100.0 μm), which were two to three orders of magnitude higher than those expected for Mars. Furthermore, these larger particles were expected to settle out of the MSWTF environment significantly faster than the smaller particles in the sample. This resulted in an uncertainty in the actual particle size distribution for Mars JSC-1 at the time of measurement. Therefore, the hematite sample was used as a validation for the optical property retrieval as the particle size distribution at the time of measurement was expected to remain closer to the measured size distribution of the sample prior to injection.

6.1.5 Effect of dust particle shape

The composition and dust particle size of the samples varied significantly, which will have an effect on the particle shape within each sample. Figure 6-10 shows SEM images of JSC-1, quartz and hematite. The SEM images of the dust samples show the individual particle shapes vary significantly from nearly spherical through to cylindrical. As discussed in Chapter 2, this will affect greatly the single scattering properties of the suspended aerosols. The individual

particles of the hematite samples were extremely small (< 1 μm) and tended to form large spheroidal aggregates as shown in Figure 6-10c. However, the large aggregates were expected to disperse due to the force of the pressurised injection system of the MSWTF, leaving only the smaller non-spherical aggregates in suspension in the MSWTF environment.

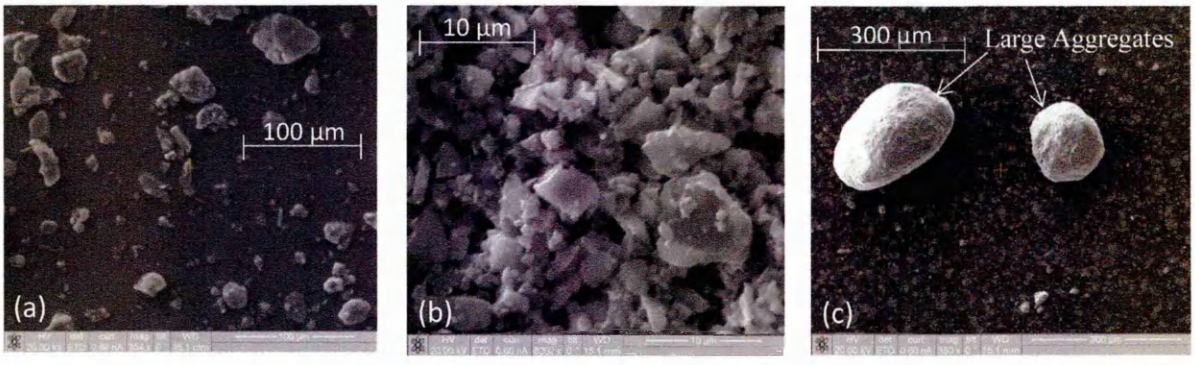

Figure 6-10: SEM images of (a) Mars JSC-1, (b) quartz and (c) hematite.

To assess the sensitivity of the measured spectrum to the particle shape, the scattered irradiance from each volume element, in the discrete volume model, to the detector was calculated as illustrated in Figure 6-11, where $I_{(S,N)}$ is the incident irradiance on the volume element and $I_{(N,F)}$ is the irradiance per unit solid angle scattered towards the spectrometer.

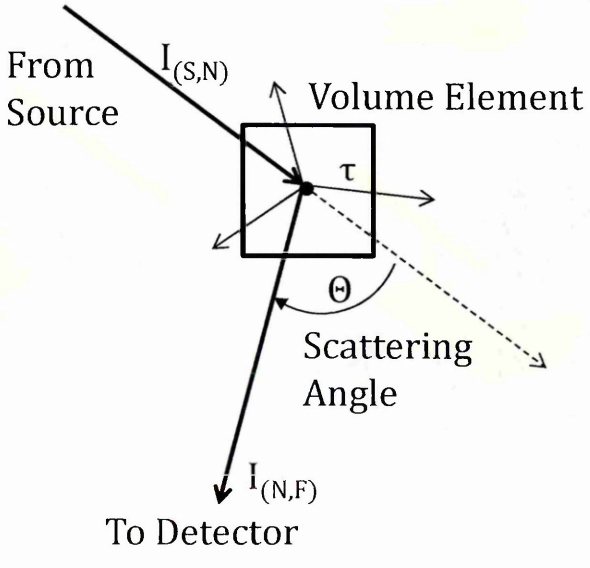

Figure 6-11: The scattering process that takes place at each node in the model.

Assuming single scattering, the required scattering angle for each volume element in order for the scattered light to be detected by the UV-VIS spectrometer was calculated. The average scattering angles for each volume element is shown in Figure 6-12. The average scattering angle from all the facing LED arrays is less than 50° for the majority of the chamber volume seen by the UV-VIS spectrometer. Pollack and Cuzzi (1980) showed that the particle phase function is relatively insensitive to the particle shape at scattering angles < 20°, moderately dependent between 20° and 60° and highly sensitive at angles > 60°. This implies that light from the twenty facing LED arrays that undergoes scattering by the suspended dust particles will be relatively insensitive to the particle shape and more strongly dependent on the particle size distribution and composition. For the LED arrays on the same side of the chamber as the UV-VIS probe (back wall LEDs) the scattering angles are large (> 70°) and are within the region were the particle shape has a strong effect on the scattering phase function. This suggests that the use of Mie theory will overestimate the amount of light scattered by these LEDs towards the UV-VIS spectrometer due to the characteristic high backscattering lobe of Mie solutions.

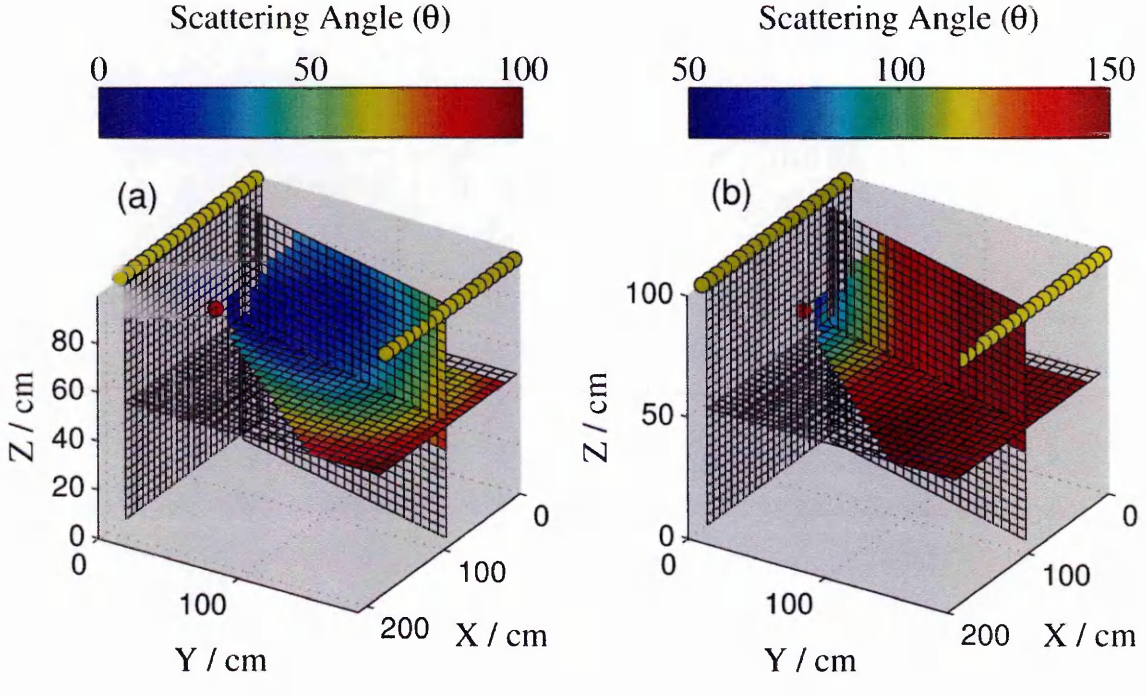

Figure 6-12: Scattering angles for (a) the facing LED arrays and (b) back wall LED arrays. The sources (yellow dots) and fibre (red dot) are shown in the plot for prospective.

To quantify the relevance of this error, the amount of light scattered at 525 nm (corresponding to the centre of the measured LED spectrum and to the peak wavelength of the green LED) by each discrete volume was determined for a simulated dust component with the composition and particle size distribution of the kaolinite sample. Kaolinite particles were assumed as their low imaginary refractive index results in the majority of the light being scattered, and it is this scattered component that is being quantified. Figure 6-13 shows the scattered light from each volume element towards the UV-VIS spectrometer. In comparison to the facing LED arrays the amount of scattered light from the back wall LEDs is two orders of magnitude lower at the observation point of the UV-VIS probe, however the remainder of the chamber volume experiences scattered irradiances < 3 orders of magnitude smaller. As a result of the significantly smaller contribution to the scattered irradiance from the back wall LEDs the particle shape is assumed to have negligible effect on the outcome of the retrieval.

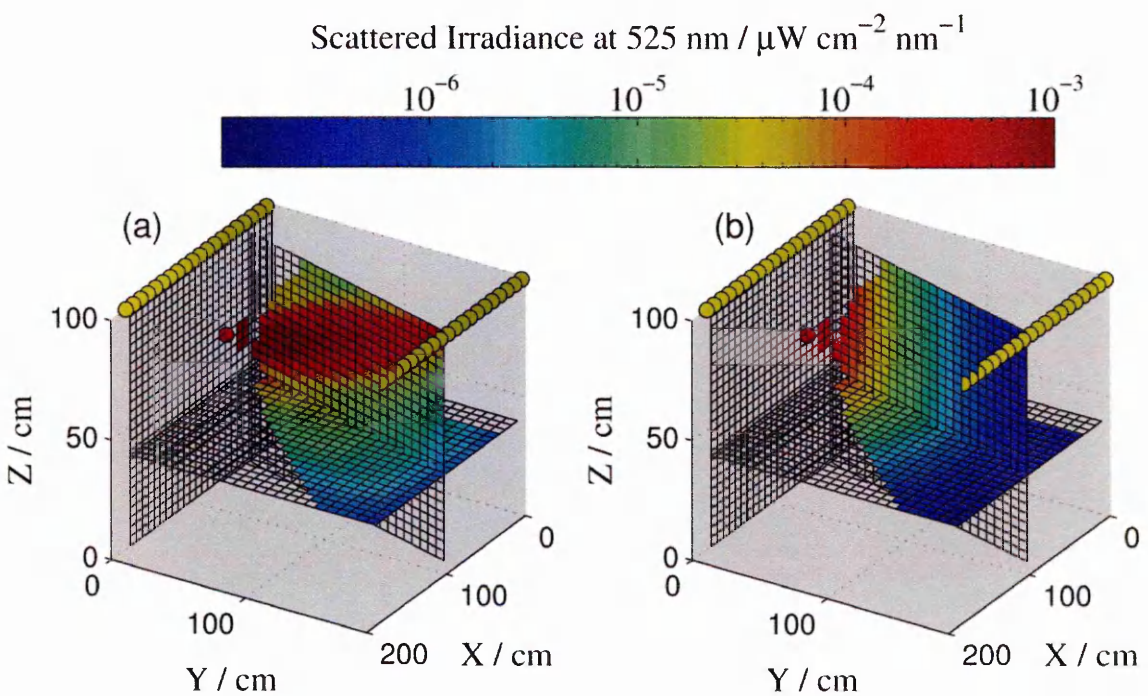

Figure 6-13: Scattering irradiances for (a) the facing LED arrays and (b) back wall LED arrays. The sources (yellow dots) and fibre (red dot) are shown in the plot for prospective.

6.2 Experimental procedure

Eleven measurements were made of suspended dust. The experiments were conducted in three sets corresponding to the three separate days. Table 6-1 lists the measurement number, the material suspended, the mass of material injected and the light source used for each measurement.

Measurement	Sample	Mass / g	Light Source
M1	Salten-Skov 1	34.39*	Halogen
M2	Salten-Skov 1	68.78*	Halogen
M3	Salten-Skov 1	34.39*	LED
M4	Salten-Skov 1	68.78*	LED
M5	kaolinite	17.22	Halogen / LED
M6	magnetite	90.16	Halogen / LED
M7	hematite	52.05	Halogen / LED
M8	hematite / magnetite	43.71 / 62.29	Halogen / LED
M9	quartz	17.74	LED
M10	hematite	20.72	LED
M11	hematite / Mars JSC - 1	35.69 / 35.03	LED

* Calculated by taking the average of 3 filled vials and multiplying by the number of injections

Table 6-1: List of the experiments carried out, showing total mass of each sample and the light source used.

The experimental procedure begins with recording the dark spectrum, required for the calibration of the UV-VIS spectrometer. The reference spectrum (*i.e.* light source on with no dust present) was then measured, after which the acquisition of 'experiment' spectra was initiated. After approximately five seconds the dust sample was injected into the MSWTF. Once the dust has become uniformly distributed in the MSWTF airflow the attenuated spectrum was measured. The experimental procedure is illustrated in Figure 6-14.

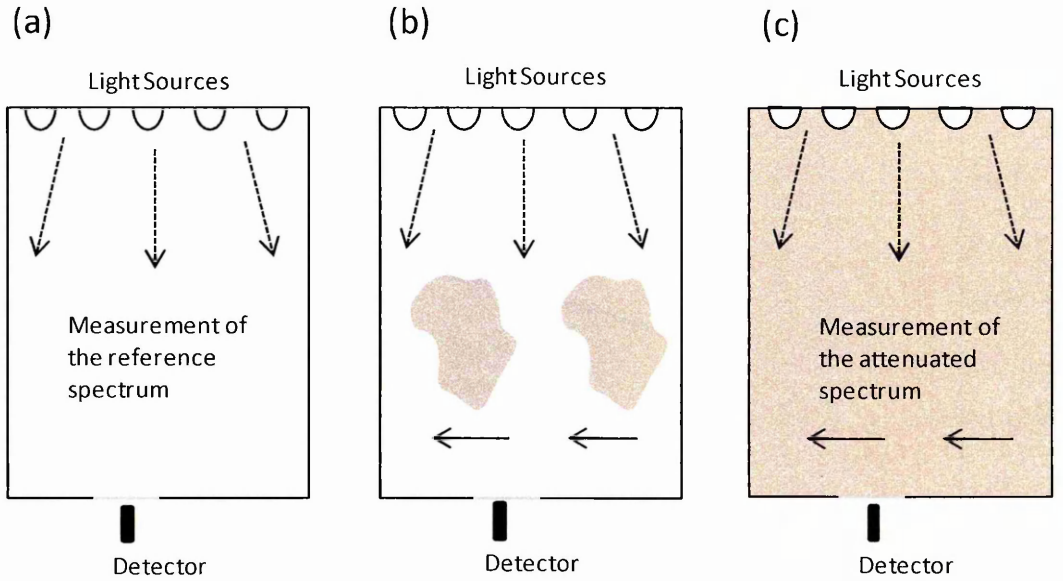

Figure 6-14: The experimental procedure for the experiments. (a) Light source reference spectrum taken in dust free environment. (b) Dust sample is injected into the wind tunnel resulting in the passage of dust clouds. (c) Once the dust is uniformly distributed within the chamber an attenuated spectrum is taken.

Figure 6-15 shows the transmission as a function of time for measurement M2 with the other experiments showing similar behaviour. For each measurement the reference spectrum was taken as the average over the first twenty scans prior to the injections of the dust samples (represented by the black line in Figure 6-15). The four injections of the dust sample are clearly seen and cause a significant reduction in the observed transmission followed by a sharp increase as "thick" dust clouds pass between the light source and the detector (denoted by the red line in Figure 6-15). After the last injection oscillations in the measured irradiance were observed but these dampen quickly as the dust becomes well mixed and uniform. The data for attenuated spectra measurements were taken from the uniform region (denoted by the blue line in Figure 6-15), which was taken to be 70 s after the oscillations from the injections subsided. The average over twenty scans was taken to further remove any possible heterogeneity in the distribution of the dust within the chamber that might still have been present.

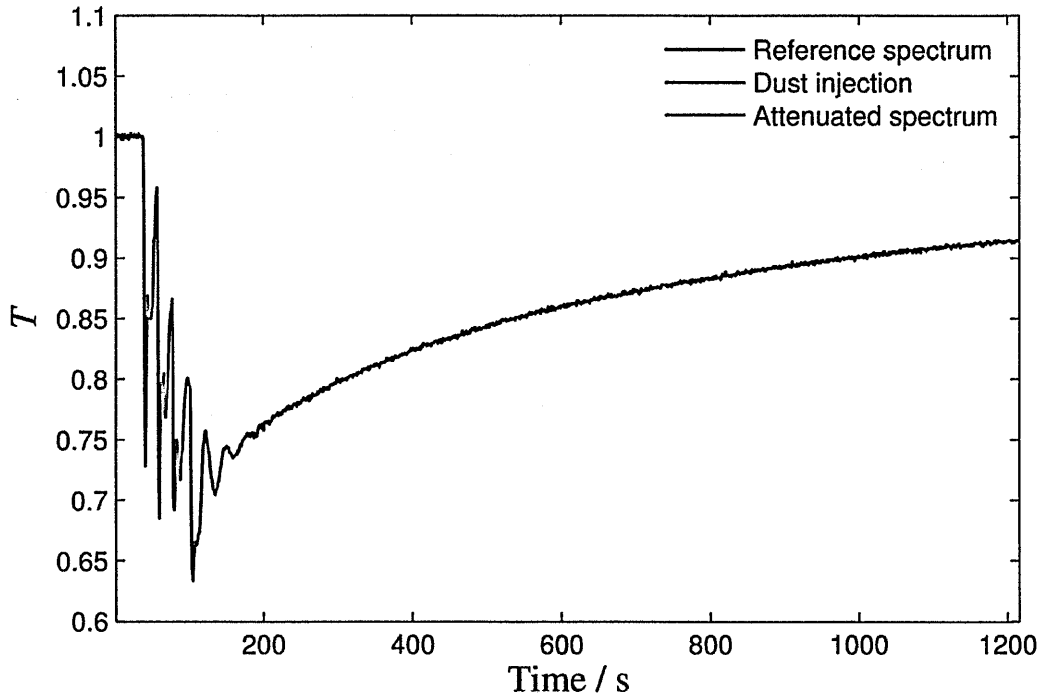

Figure 6-15: Transmission as a function of time for experiment M2 showing the different stages of the experiment and the locations where the reference and attenuated spectra are measured.

The measured spectra were grouped into three separate τ values (measured at 400 nm) equal to 0.09 (quartz, hematite and kaolinite), 0.15 (Mars JSC -1, kaolinite and Salten Skov) and 0.6 (magnetite and hematite). This allowed direct comparisons between the measured transmission spectra for the different dust samples. The retrieval of the dust optical properties was performed at six wavelengths, corresponding to the peak wavelengths of the LED array. The transmission spectra for the different cases considered are shown in Figure 6-16. The transmission spectrum produced by kaolinite and quartz are similar, with approximately constant transmission at all wavelengths. This is expected since kaolinite and quartz particles have extremely low n_i over the wavelength range measured, leading to negligible absorption of the incident light. Magnetite particles displayed strong absorption at all wavelengths while hematite, JSC-1 and Salten Skov 1 dust particles exhibited high absorption at wavelengths less than 550 nm and were efficient at scattering at longer wavelengths. This contrast in behaviour at different wavelengths is illustrated in Figure 6-16c where the transmission of magnetite and hematite is shown. At short wavelengths (<550 nm) both magnetite and hematite particles show

strong absorption, resulting in near identical transmission at these wavelengths. At longer wavelengths magnetite continues to show strong absorption, however hematite displays a significant increase in transmission as a result of increased scattering which is detected by the UV-VIS.

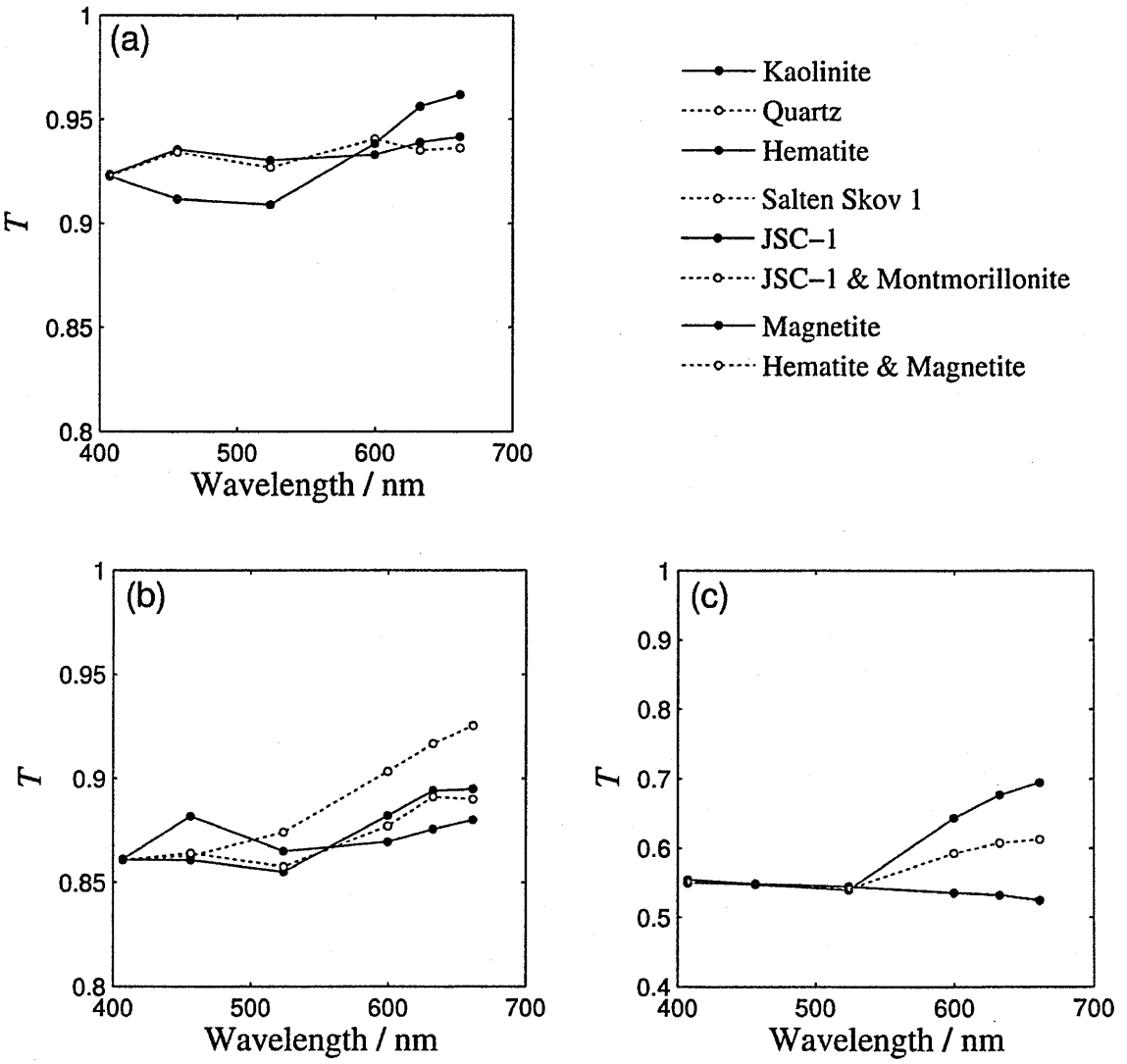

Figure 6-16: The measured transmission for different dust samples for τ of (a) 0.09, (b) 0.15 and (c) 0.5.

6.2.1 Detection of the scattered light component

Both light sources were used in separate experiments involving Salten Skov 1 and, therefore, provided an opportunity to compare the measured spectrum and retrieved optical properties from the two different light sources. This provides a "ground truth" to the derived optical

properties as they should be equal regardless of the light source used. The transmission spectra for Salten Skov 1 at different τ (0.09, 0.15, 0.3) for the halogen and LED light sources are shown in Figure 6-17. By comparing the transmission spectra of Salten Skov 1 for the different light sources, information on the scattering properties of the dust can be gained. The measured transmission spectra for both light sources are consistent for low τ (0.09), with slight variations observed at wavelengths longer than 600 nm. As τ increases to 0.15 a departure is observed between the measured transmission spectra at longer wavelengths > 500 nm, with the LED experiment measuring a greater irradiance. The narrower beam of the halogen light source illuminates a smaller volume of the MSWTF and hence, a smaller proportion of the dust particles are illuminated. This led to the measured halogen spectrum being less affected by increased scattering due to increases in dust abundance within the MSWTF. At $\tau = 0.3$ the transmission spectra using the LED arrays displays a ~9% increase in transmission over the equivalent for the halogen bulb.

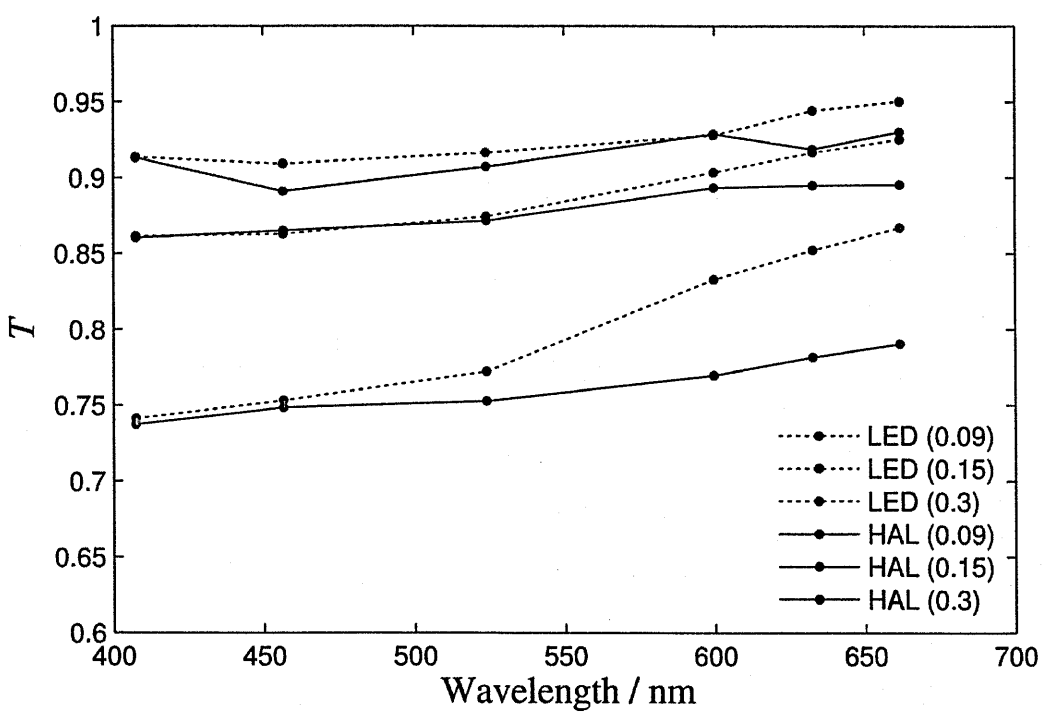

Figure 6-17: Transmission values for the Salten Skov 1 dust sample for τ of 0.09, 0.15, and 0.3 for the different light sources.

Another example that emphasizes the effect of scattering is experiment M9, where large dust opacities were achieved for hematite particles (>0.5). Figure 6-18 shows the measured irradiance spectrum for hematite dust for τ 0.05, 0.2, 0.4 and 0.55. The spectra have been normalised to 1 at 405 nm to enable comparison of the attenuation. If scattering were negligible then the normalised spectra should be equal for all τ (providing the particle size and composition remain constant) however, as illustrated, there is a correlated increase in irradiance at wavelengths greater than 525 nm as the dust abundance increases. This is because hematite particles are efficient at scattering light at wavelengths longer than 525 nm (Sokolik and Toon, 1999) and as the number of particles increases, the probability of the light being scattered into the UV-VIS probe increases. This leads to an increase in the measured irradiance.

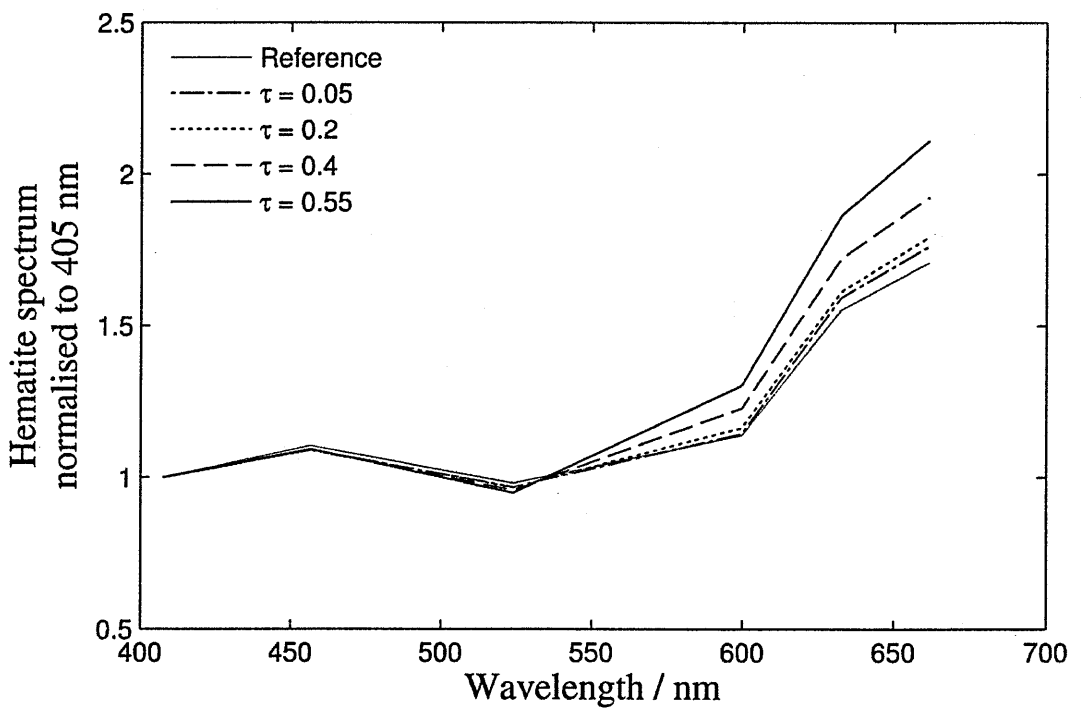

Figure 6-18: Attenuated irradiance spectrum for experiment M9 (hematite) at different τ. The spectra are normalised to 1 at 405 nm.

The occurrence of a significant scattered component in the measured irradiances artificially increases the observed transmission (as was seen in Chapter 4 for dust devil transits). This higher transmission will lead to an underestimation of τ and hence, the dust abundance. More importantly, the scattered component must be simulated in order to retrieve accurate

optical properties for the dust particles. To model the scattering of light within the chamber the MCLSM was adapted with the modifications described in the next section.

6.3 Adaptations to the Monte Carlo Light Scattering Model

The MCLSM was adapted to simulate the scattering and absorption of light scattered by a uniform suspension of dust particles inside the MSWTF. The most significant modification from that used for dust devil modelling (Chapter 3 & 4), was to the boundary conditions that describe the photon trajectory after interaction with the wind tunnel internal walls. Another change was the initial position of the photons, which was at the location of the 40 LEDs or at the location of the halogen lamp. The different viewing geometry of the spectrometer probe, compared to the dust devil experiments, also required modification of the photon detection condition.

6.3.1 Photon initial position and trajectory

The photons injected into the wind tunnel are divided equally between the 40 LED arrays with their initial locations equal to the positions of the LEDs. The injection trajectory of the photons is described by two angles: the photon zenith angle, which is determined from the LED intensity distributions (Figure 6-6) using the rejection method (Whitney, 2011) and the photon azimuth angle, which is a random angle between 0 and 2π. Figure 6-19 illustrates the injection of 10^5 photons into the modelled MSWTF and the initial trajectories of the photons are shown.

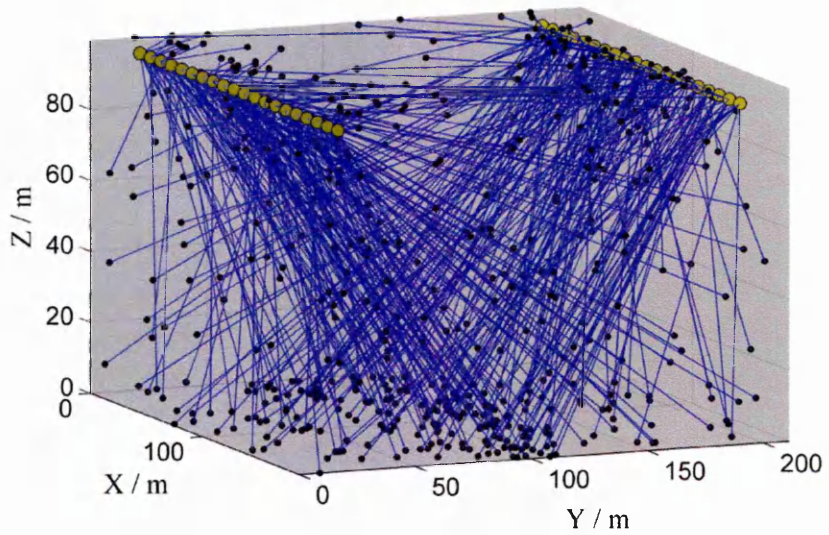

Figure 6-19: The initial trajectory of the photons entering the modelled MSWTF.

6.3.2 Boundary conditions

The MSWTF interior, ceiling and floor (Figure 6-2) are metallic creating a significant amount of reflected light. The walls of the chamber were less reflective due to the rough metal finish leading to more isotropic scattering. The floor was reflective but the settling of the dust led to the surface having the scattering properties of the suspended dust.

Therefore the ceiling was given a high single scattering albedo ($\omega_0 = 0.99$), with the photons intercepting the ceiling assumed to be reflected at the angle of incidence. The scattering from the walls was assumed to be isotropic and less than that from the ceiling ($\omega_0 = 0.8$). Determining an appropriate boundary condition for the floor was more problematic as a result of dust settling. The dominant dust type, on the floor surface, was Salten Skov but without knowledge of the single scattering properties, or the scattering phase function, the photons scattered from the surface could not be modelled. The reflective surface of the floor also complicated the scattering problem. A portion of the photons incident on the floor surface passed through the settled dust particles without interacting and were reflected from the metal surface. Therefore a cautious approach was used, which assumed isotropic scattering from the floor surface and, based on the colour characteristics of Salten Skov, ω_0 was given a wavelength

dependent value with higher absorption at blue wavelengths and higher scattering at red wavelengths.

6.3.3 Photon detection

The UV-VIS spectrometer was positioned outside the modelled MSWTF correlating with the experimental setup. The quartz window restricted the spectrometer FoVresulting in only a portion of the chamber volume being observed. The approximate FoV is shown in Figure 6-20 which illustrates the detection location of the scattered light (blue lines). As shown all twenty facing LEDs were visible to the UV-VIS probe, with the direct component (red lines) being detected from all twenty LED arrays.

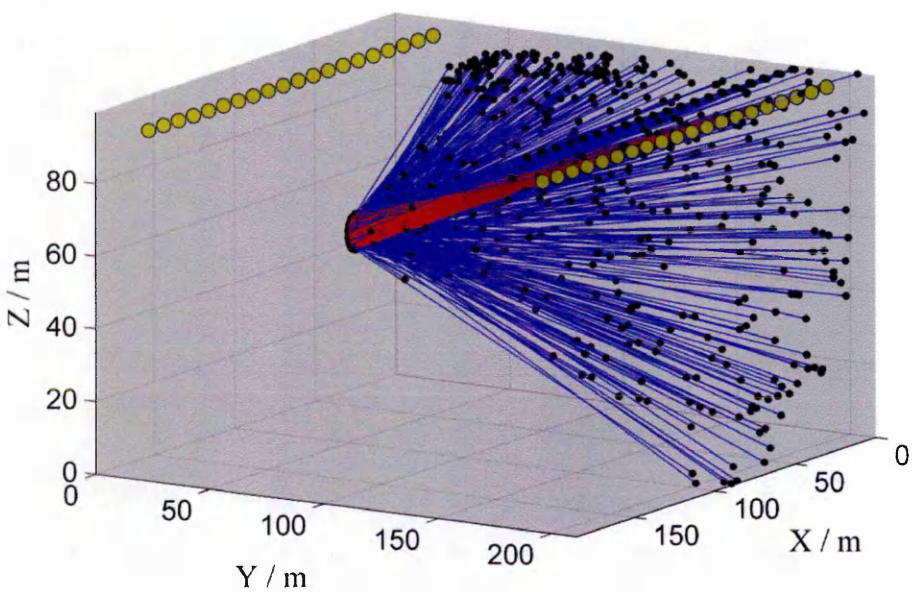

Figure 6-20: Illustration of the direct and scattered photons detected in the modelled MSWTF.

6.4 Discussion on the retrieval of optical properties

The experiments performed were too ambitious, resulting in the MCLSM being unable to retrieve accurately the optical properties of the suspended dust particles. The reflective surfaces

of the MSWTF boundaries led to an uncertainty in the simulated irradiance spectrum of greater than 15% at all wavelengths.

The radiated power of the LED arrays for each wavelength was determined from the method outline in Section 6.2.2 and knowing the number of photons injected the measured reference and attenuated spectra were simulated. A comparison of the measured and simulated reference and attenuated irradiance spectra is shown in Figure 6-21 for hematite particles using the complex refractive indices from Sokolik and Toon (1999). An average over 10 model simulations is shown along with the standard deviation of the predicted irradiances. The modelled spectrum is qualitatively consistent with the measured spectrum. However, the high scattering environment of the MSWTF resulted in large variations in the number of photons detected by the MCLSM and led to variations in the irradiances spectra of greater than 10%.

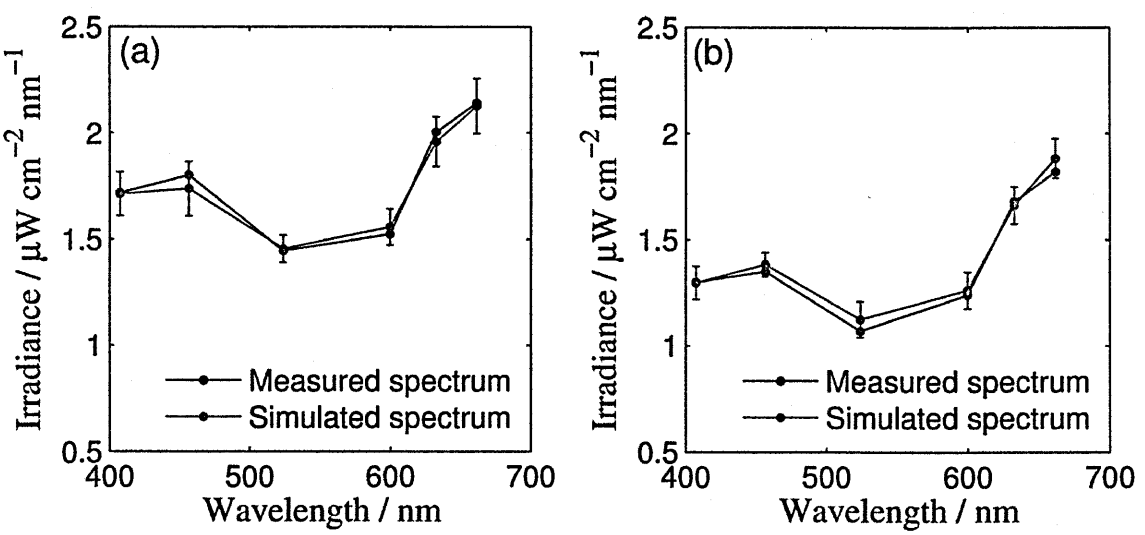

Figure 6-21: The measured and model spectrum for experiment M10. (a) shows the reference spectrum and (b) shows the attenuated spectrum.

The large variations in the simulated irradiance spectrum masked the attenuation resulting from variation in the particle n_i. A decrease in the hematite n_i of 20% from the Sokolik and Toon (1999) values, led to a change in ω_0 of 0.01 at 405 nm and 0.03 at 660 nm and would result in a decrease in measured irradiances of 1–3%. This is an order of magnitude smaller than the modelled uncertainty and led to ambiguous retrieval of the dust optical properties.

The error in the modelled irradiances could be improved by increasing the number of simulations over which the average is taken. However, the model runtime increases by the same factor *i.e.* averaging over hundred simulations instead of ten, increases the model runtime by ten times. This is the limiting factor, currently averaging over 10 simulations led to a simulation duration of 300 minutes per wavelength for twelve n_i values, leading to an overall runtime of 1800 minutes. Increasing the averaging, results in unrealistic simulation times, especially if other parameters such as, particle size and τ, have to be varied.

The experiments could be improved by reducing the amount of scattered light entering the detector from the chamber boundaries. This could be accomplished by using only a single light source, such the halogen bulb. This would limit the amount of reflected light in the chamber in comparison to the LED arrays resulting in less variation in the simulated irradiances. Blackening the chamber walls would also have the same effect, resulting in absorption of the incident light on the chamber boundaries as opposed to scattering. The most important change, however, would be to confine FoV of the spectrometer, such that the volume of the wind tunnel observed would be a narrow corridor linking the UV-VIS probe to the light source. This would prevent light reflected off the boundaries being detected, resulting in the light detected being more sensitive to scattering from the dust particles.

6.5 Differentiating between two dust samples

Two experiments were performed to simulate the scenario at the martian surface of the passage of a dust cloud composed of dust particles with a different composition to the ubiquitous background dust haze. The purpose of these experiments was to validate the method outlined in Chapter 5 for differentiating between two dust components in the martian atmosphere. The experimental procedure involved injecting the first dust sample into the chamber; after a uniform dust distribution was achieved (*i.e.* a ubiquitous background 'haze'), the second dust sample was injected to simulate the passage of a local dust cloud containing particles of different composition. For Experiment One, hematite was injected initially into the chamber

followed by magnetite; in Experiment Two, JSC-1 was injected prior to montmorillonite. Due to dust settling, the abundance of hematite in the chamber continually decreased with time. Therefore to approximate a constant dust background haze, τ and $\Re_I$ (ratio of irradiances at two widely spaced wavelengths) were calculated over the injection period of the secondary dust component which was 37 s for Experiment One and 25 s for Experiment Two. The transmission as a function of time for these two experiments is show in Figure 6-22.

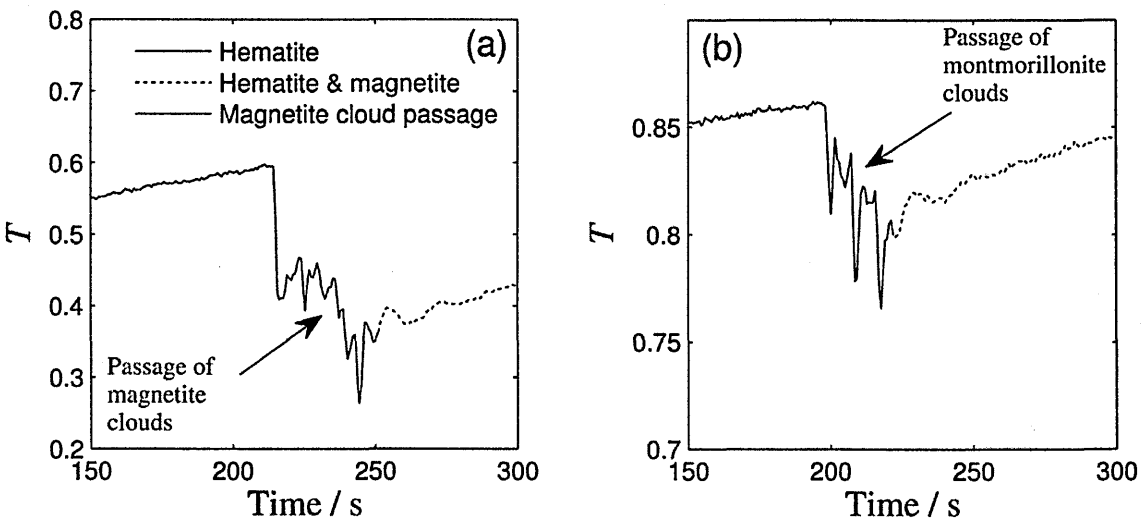

Figure 6-22: The time-series showing the simulated passage of a dust cloud containing particles of different composition super imposed on a ubiquitous background dust haze. (a) Experiment One, a background of hematite and cloud a magnetite and (b) Experiment Two, a cloud containing montmorillonite particles and a background of Mars JSC-1.

The LED arrays were used for these experiments, therefore $\Re_I$ at 388 nm and 750 nm could not be measured (which would have made it consistent with Chapter 5) as this was outside of the LED spectral range. However, the actual wavelengths used to calculate $\Re_I$ can differ provided that there is a change in the dust optical properties between the two wavelengths. The two wavelengths used in this analysis were 405 nm and 660 nm which corresponded to the peaks of the blue and dark red LEDs respectively. Figure 6-23 shows $\Re_I$ as a function of τ for the two experiments performed. As the dust cloud passed the UV-VIS a departure was observed in the $\Re_I$ signature correlating well with the simulations in Chapter 5. A linear fit was applied to the background and cloud $\Re_I$ signatures and extrapolating back to $\tau = 0$ for the dust clouds, τ for

the background hazes was determined to be 0.58 and 0.15 for Experiment One and Experiment Two respectively. The retrieved τ for the background dust for Experiment Two correlates well with the measured τ of 0.15, while the τ measured for Experiment One was lower at 0.52. The error in Experiment one could be the result of using a linear fit to approximate the magnetite cloud $\Re_I$ signature. Another explanation could be the result of additional residual hematite particles being injected along with the magnetite samples, increasing the hematite abundance in the chamber. The injection mechanism on the MSWTF used a pressurised system to evacuate the container holding the dust sample. However the entire sample did not always successfully evacuate, and while cleaning was performed, removing all the remaining particles could not be achieved.

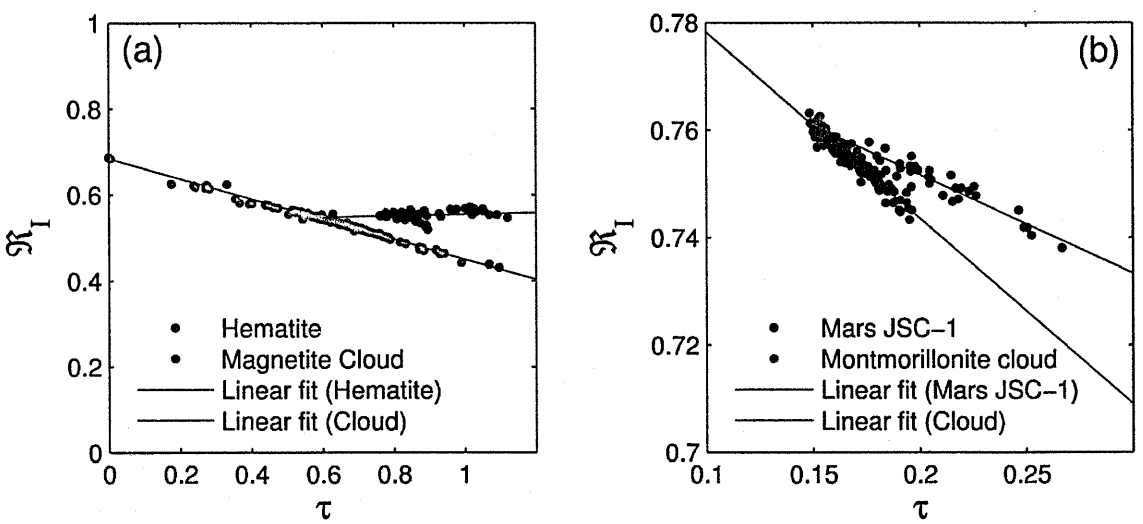

Figure 6-23: $\Re_I$ as a function of τ within the MSWTF for the two cloud simulations (a) hematite with a cloud of magnetite and (b) Mars JSC-1 with the passage of a montmorillonite cloud.

Magnetite and montmorillonite have extremely different optical properties, as indicated by their transmission spectrum (Figure 6-16). Magnetite shows strong absorption within the 350–800 nm wavelength range, while in contrast montmorillonite predominantly scatters light within this wavelength region. However, both the magnetite and montmorillonite clouds cause an increase in $\Re_I$. This is a result of the magnetite particles absorbing the longer wavelength light that would be scattered by the hematite particles. At shorter wavelengths both particles show strong absorptions. This leads to the irradiance at 405 nm being relatively unchanged and

a lower irradiance at 660 nm, resulting in an increase in $\Re_I$. Similarly, both Mars JSC-1 and montmorillonite are efficient at scattering light with wavelengths > 520 nm. However Mars JSC-1 exhibits stronger absorption at shorter wavelengths. Therefore, the introduction of montmorillonite results in higher scattered irradiance at 405 nm but only small variation in the irradiance at 660 nm, hence $\Re_I$ will increase.

This is an important feature of $\Re_I$ as dust components of significantly different composition can result in similar $\Re_I$ values making retrieval of the optical properties of the particles contained in the cloud difficult. However, it is proposed that measuring $\Re_I$ provides a powerful tool for quickly and efficiently distinguishing events that cause a change in the composition of an ubiquitous dust haze (*i.e.* a dust cloud containing particles of a different composition). Such an identified event can then undergo a subsequent full spectral analysis.

The experiments simulating the passage of a dust cloud, containing particles of different composition to a ubiquitous dust background, have shown that plotting $\Re_I$ as a function of τ is a valid technique for distinguishing between aerosols of different composition and correlates well with the simulations performed in Chapter 5. Furthermore, by producing linear fits to the $\Re_I$ signature, τ for the background haze has been determined for both experiments and are consistent with the measured values. This provides a validation for using $\Re_I$ as a means of discerning compositional changes to the ubiquitous dust haze on Mars.

6.6 Summary

The high scattering environment in the MSWTF, resulting from the metallic boundaries, caused large uncertainties in the simulated irradiance spectra. This led to ambiguous retrieval of the dust optical properties. The primary factor governing the model accuracy is the number of photons injected into the model, currently limited to 10^7 due to available computing resources. Therefore to increase the model accuracy the simulations had to be sequentially repeated, to represent additional photons, resulting in a linear increase in model runtime. In order to produce

irradiance spectra with an uncertainty of ~15%, averaging was required over 10 simulations with each simulation performing 50 model executions of 10^7 photons. As indicated by discussion in Section 6.4, this led to unrealistic simulation runtimes. Therefore, other methods were applied in order to increase artificially the number of photons detected or to reduce the scattered component from the chamber walls.

The simplest method was to limit the number of scattering events processed per model execution. This reduced the number of scattering events from the chamber boundaries, improving the simulation runtime. This had negligible effect on the model output however, since the largest contributor to the scattered irradiance is from the first scattering events, with higher order scattering events contributing significantly less to the total scattered irradiance.

The modelled chamber boundary conditions were varied, *i.e.* increasing the absorption from the ceiling, walls, and floor. However increasing the absorption or assuming no scattering from the chamber walls led to an underestimation in the observed irradiance and, therefore, the scattered light from the boundaries could not be assumed to be negligible.

Another method, which could not be fully explored due to computing limitations, was to arrange the LEDs to point directly at the detection area, such that the majority of the photons injected would have an initial trajectory towards the detector. A correction factor to the photon weights would then be applied based on the angle of the photon trajectory to the true pointing direction of the LED array. The photon weight would then be calculated by interpolating over the LED intensity distributions (Figure 6-6. This limits the number of photons that interact with the chamber boundaries and increases the number of photons that form the direct component and interacted with dust particles along the spectrometer line of sight, which (from Figure 6-13) contributes to the majority of the scattered light from the dust. The correction factor ensures that the relative contribution from the direct irradiance, dust scattered irradiance and boundary scattered irradiance remains unchanged. Unfortunately tracking the photon weightings required the creation of an additional array, which extended the computing requirement of the MCLSM

beyond available limits. Therefore, (contrary to the original aim) the number of photons injected had to be reduced, lowering the overall photon density in the model. More analyses are required to fully explore this avenue but it is currently the best option (unless the programming language is changed to one that can handle increase array sizes) for improving the accuracy of the MCLSM for the MSWTF environment.

Chapter Seven: Discussion and further work

The remit of this thesis was to investigate the following research questions as outlined in Section 1.1.

1) What are the critical factors required for successful retrieval of the optical properties of dust particles in suspension around dust devil vortices?
2) What can we determine from spectral measurements of dust devil vortices in order to determine the internal characteristics and the mass concentration?
3) What are the differences between martian and terrestrial dust devil transit signatures and what are the implications?
4) How do compositional changes to the dust background component of the martian atmosphere affect observations of dust devils and is there a method for differentiating between different dust and ice aerosol components?

Here, each research question is explored individually and conclusions based on the results presented in this thesis are discussed.

7.1 Retrieval of the dust optical properties of dust devil vortices

In order to retrieve the optical properties of dust particles in suspension around terrestrial dust devil vortices, a Monte Carlo Light Scattering Model (MCLSM) was developed, capable of simulating the transmission of light through a dusty environment. The MCLSM traces the path taken by photons through the model volume and calculates the interaction between the photons and dust particles (*i.e.* absorption or scattering) by sampling probability distributions. The Monte Carlo method was applied as the high dust concentrations observed in dust devils led to the requirement that multiple scattering of light by the dust must be taken into account, with the single scattering assumption leading to an underestimation in the scattered light.

The retrieved $\omega_0(\lambda)$ values indicate a highly scattering dust component ($\omega_0 > 0.95$) at wavelengths greater than 625 nm. A decrease in ω_0 towards shorter wavelengths was observed, resulting in of higher absorption. These results are consistent with previous studies of desert dust aerosols generally displaying greater absorption towards blue wavelengths relative to longer wavelengths (Kaufman, 1987, Dubovik *et al.*, 2000, Kaufman *et al.*, 2001). The retrieved $\omega_0(\lambda)$ values for the dust entrained in the dust devils are lower than those predicted for suspended desert dust aerosols and are indicative of either larger particles being lifted by the vortices or a higher imaginary refractive index for Nevada desert sand in the Eldorado Valley.

A first-order approximation for the imaginary refractive index $n_i(\lambda)$ of Nevada desert aerosols was presented for two assumed particle size distributions, that of dust devils and terrestrial desert aerosols. The former was based on measurements of terrestrial dust devils by Sinclair (1974) and contains a large fraction of large particles ($r > 10.0$ μm) while the latter uses the particle volume distribution measured by Dubovik *et al.* (2002) for Bahrain-Persian Gulf desert aerosols which contains fewer large particles. $n_i(\lambda)$ values for the two size distributions were significantly different, with the retrieval resulting in desert aerosols exhibiting $n_i(\lambda)$ an order of magnitude higher than those retrieved for using the size distribution of Sinclair (1974).

This is significant as the two sets of $n_i(\lambda)$ values will result in the dust particles displaying contrasting behaviour once in suspension in the atmosphere. For the particle size distribution measured by Sinclair (1974), the low ω_0 values are a result of large particles being present. However, these large particles quickly fall back to the surface and it is the fine fraction that remains suspended in the atmosphere. The removal of the large particle fraction will lead to an increase in ω_0 to >0.9 over the 380–750 nm wavelength range, as less incident light is absorbed by the smaller particles, resulting in less direct solar heating of the surrounding atmosphere. In contrast, assuming smaller particles which are typical of desert aerosols requires n_i to increase to achieve the same absorption observed for the larger particles. Thus once suspended in the atmosphere they will absorb more light in comparison to the remaining fine fraction of the

Sinclair (1974) size distribution and will actively warm the atmosphere. Erroneous assumptions for the size of the dust particles entrained in dust devils vortices can therefore lead to contrasting implications of their radiative effect on atmospheric heating. This highlights the importance of *in situ* measurement of the dust particle size distribution if accurate retrieval of the dust particle optical properties are to be obtained from spectral measurements of dust devil vortices. As discussed by Sinclair (1974), the particle size distribution within dust devils will contain a greater quantity of larger particles and will be more analogous to soil particle distributions. Therefore, it is concluded that the estimated particle size distribution using the values from Sinclair (1974) provides the best estimate for $n_i(\lambda)$ for Nevada desert aerosols. This in turn suggests that the fine particle fraction injected into the atmosphere by the dust devils in the Nevada desert will result in less heating of the surrounding atmosphere compared to Saharan desert aerosols measured by Patterson *et al.* (1977).

Analyses of desert dust particles in suspension around dust devil vortices in the Nevada desert has shown that the required parameters critical for the successful retrieval of the dust optical properties are: the physical dimensions of the vortex; the spatial distribution of the dust; the dust optical depth; the particle size distribution. These parameters are required to model the transmission of light through the vortex in order to reproduce spectra which have been attenuated by the dust particles. The largest uncertainty in the retrieval of $n_i(\lambda)$ is the lack of knowledge of the particle size distribution of the entrained dust particles. Any subsequent dust devil field studies must incorporate *in situ* measurement of the particle size distribution for each encounter. This would allow validation of the retrieved $n_i(\lambda)$ presented in this study and provide more accurate measurement of the total mass of particulate material lifted into the atmospheric boundary layer.

An investigation into the dependence of the amount of scattered light on the dust particle single scattering properties revealed that the estimate for the asymmetry parameter (g) that resulted in the largest scattered irradiance (Φ_S) during a dust devil transit, was dependent on the solar zenith angle (θ_z). This led to a bias towards low g (~0.6) for high θ_z and $g \rightarrow 1$ for low θ_z.

The same dependence was not observed when measuring the total irradiance (Φ_T) which indicates that the θ_z bias is limited to the scattered component. This has important implications when attempting to retrieve the optical scattering properties from measurements of scattered light, as any attempt to determine an estimate for g from narrow field of view (FoV) observations would need to correct for this bias. This is significant as a higher value of g will result in an increase in scattered light in the non-illuminated side of the vortex. Therefore if a lower value of g is assumed for the dust particles, the dust concentration must be reduced to compensate for the lower irradiance that will be observed. This could lead to an underestimation of the mass of dust entrained in the vortex and hence the total mass of material injected into the atmosphere.

7.2 Predicted and measured transit signatures of terrestrial dust devils

The MCLSM was applied to both modelled and terrestrial dust devils to simulate the optical signature during a dust devil transit. The aim was to determine whether the dust devil parameters required for the retrieval of the dust optical properties (physical dimensions, vortex centre, spatial distribution of dust, dust optical depth and the particle size distribution) could be obtained from their transit signatures.

7.2.1 MCSLM predictions

This work has shown that the optical signature of a transiting dust devil is highly dependent on the method of observation, with the narrow field of view (NV, assuming the Sun is not in the FoV) and full sky (FS) simulations showing contrasting transit signatures.

In the FS case, Φ_T decreases during the transit since the loss of light from the direct component, as a result of absorption and scattering by the dust particles, is much larger than the gain from increased diffuse scattering. Predictions of Φ_T transit signatures revealed a negligible

dependence on the dust concentration and core size. This is due to the dominance of the direct component in the total irradiance at the surface under 'clear sky' conditions and therefore, Φ_T is dependent upon the total extinction along the line of sight to the Sun.

In the NV case, the incident solar flux interacts with the dust column of the dust devil vortex resulting in light, which would otherwise be undetected, being scattered into the point of measurement (PoM). This causes the observed light to increase during a dust devil transit. The NV simulations have shown that Φ_S inside a dust devil vortex is strongly dependent on the dust distribution within the dust devil interior. The Φ_S dependence on the dust concentration manifests itself in the transit signature as a reduction in Φ_S in the region of lower dust concentration and an increase in Φ_S through regions of higher dust concentration. Investigations of terrestrial dust devils have revealed central cores that are relatively free of dust particles (Sinclair, 1974). The NV simulations have shown that this dust free core becomes clearly defined in the Φ_S transit signature as a reduction in Φ_S, enclosed by regions of increased Φ_S as the PoM passes through the vortex. Therefore, by measuring the Φ_S signature of a transiting dust devil, the vortex core dimensions can be quantified, providing a more accurate determination of the dust column volume. Furthermore, measurement of both Φ_T and Φ_S allows determination of the direct component, from which the dust optical depth can be calculated. Therefore, if the dust particle size distribution and optical properties are known, estimation of the total mass concentration and the total mass of dust particulates injected into the atmosphere can be determined. This will result in varying levels of direct solar heating of the atmosphere, dependent on the optical properties of the dust.

7.2.2 Transit signature of terrestrial dust devils

Optical measurements of terrestrial dust devils in the Eldorado Valley, Nevada, were used to validate the predictions of dust devil transit signatures from the MCLSM. The total and scattered irradiances measured during the transit of terrestrial dust devils are consistent with the

predictions of the MCLSM: the total irradiance experiences a reduction, while the scattered component exhibits an increase during the transits.

Good correlation between the measured and modelled transit signatures was achieved, further validating the retrieved single scattering properties. The transit signatures for Φ_S also displayed good agreement with the MCLSM for the portion of the transit signature associated with the dust devil interior. As the UV-VIS spectrometer passed through the dust devil core a drop in irradiance was observed, which is also seen in the MCLSM for the case of a dust devil with a reduced dust concentration in the core. The higher degree of non-uniformity in the dust concentration surrounding natural dust devil vortices resulted in a departure from the transit signatures predicted by the MCLSM for the scattered light outside of the vortex. A more gradual increase in irradiance prior to entering the dust devil vortex, resulting from peripheral dust lifted by the vortex, was often observed in the field experiments. This increase in scattered light occurred many tens of seconds before the transit, providing further evidence for large peripheral dust hazes that extend tens of metres to greater than hundreds of metres around dust devil vortices.

The mass concentrations and vertical mass fluxes calculated for the dust devils analysed in this work are consistent with those measured by Metzger *et al* (2011) for particulate matter (particle radius between 0.05 μm and 5.0 μm). This suggests that spectral measurements of dust devils at visible wavelengths are highly sensitive to the fine particle fraction entrained in dust devil vortices. This correlates well with the known fact that the attenuation of visible light occurs more efficiently for particles of comparable size to the wavelength of observation, with larger particles having less of an effect. The sensitivity of the spectral measurements to the fine fraction is one of the key outcomes of this work, as it is the fine particle fraction that remains suspended in the atmosphere once the dust devil has subsided. These aerosols can modify the radiative properties of the atmosphere depending on the quantity injected, potentially affecting local and regional-scale atmospheric dynamics. It is therefore important to retrieve accurately the mass concentration of the fine particle mode in dust devil vortices.

The implication of this work is that separate measurement of both the total *and* the scattered light is crucial for determining the internal characteristics of a dust devil from its transit signature in order to estimate the parameters required to retrieve accurately the dust single scattering properties. Measurements of just one of these aspects could result in ambiguous interpretation. The total irradiance provides information about the dust devil size and the total amount of dust in the dust column, while the scattered component gives insight into how the dust is distributed within the interior of the vortex. As was seen for encounter E6 (Chapter 4), the lack of information regarding the total irradiance resulted in 30% uncertainty in the mass concentration contained with the dust devil wall. Furthermore, the optical properties were retrieved from the measured total irradiance, with the vortices assumed to be homogenous dust columns. Knowledge of the scattered component during these encounters would have allowed determination of the dust spatial distribution, leading to an estimation of k_{ext} both within the walls and the vortex core. In addition, the combined total and scattered irradiances would also have allowed calculation of the direct light component, which allows determination of the 'true' dust optical depth. This would have led to more accurate retrieval of the dust optical properties.

7.3 Transit signatures of martian dust devils

The MCLSM was used to determine the transit signatures of martian dust devils at 388 nm and 750 nm. At these wavelengths the dust particles show contrasting spectral behaviour, being mainly absorbing at 388 nm and scattering at 750 nm.

One of main uncertainties encountered for characterising terrestrial dust devils from their transit signatures was from the interference from the dust devil shadow, masking the point of entry (or exit depending on the dust devil trajectory) into the dust devil interior. This led to an uncertainty in the calculated outer diameter of the dust devil. The higher background diffuse irradiance, resulting from scattering by background suspended dust, results in a modification of the transit signature for martian dust devils in comparison to terrestrial dust devils. This work

has shown that the high diffuse irradiance observed at the martian surface diminishes the uncertainty due to the effect of the vortex shadow. As a result, the portion of the transit signature corresponding to the dust devil interior is more easily distinguished when compared to terrestrial transit signatures. This indicates that spectral measurements of martian dust devils enable a more accurate determination of the outer diameter and internal volume in of the vortex in comparison to terrestrial measurements, and will provide a comparatively better estimate for the mass of material injected into the atmosphere.

In contrast to directly imaging dust devils, the simulations imply that detecting the transit of a dust devil with a low dust content under low and nominal dust haze optical depths is optimal at wavelengths between 600–750 nm, where the higher diffuse component reduces the vortex shadow, thus providing better definition of the dust devil interior within the transit signature. Future Mars missions aimed at investigating the martian surface environment, should therefore include an instrument capable of measuring the solar spectrum between 600–750 nm in order to characterise martian dust devils. These measurements allow a more accurate determination of the total mass of particulate material injected into the martian climate system by dust devils, improving the accuracy of Global Climate Models (GCMs) through correlation with the *in situ* measurements.

The dust component suspended by the simulated martian dust devils was varied to determine what effect the injection of larger particles would have on the transit signature and whether any discernible difference could be observed between different particle size distributions. It was shown that the transit signature is highly dependent on the particle size distribution, especially at longer wavelengths, where the scattered light observed during the transit is strongly dependent on g. Determination of the size distribution of particles entrained in martian dust devils is important as larger particles absorb more of the incident solar radiation. Therefore, if during the passage of a dust devil larger particles are lofted into the atmosphere, a localised increase in the atmospheric heating rate will be experienced relative to the nominal heating rate due to the increased absorption of solar radiation by the larger particles.

In situ measurement of the particle size distribution within dust devil vortices on Mars is significantly more challenging. However, optical measurements will provide greater detail on the internal dust distribution and core size and, coupled with simultaneous measurement of pressure, temperature and wind speed in the vortex, will enable refinement of dust lofting modelling, which can be used to constrain the particle sizes that are likely to be lifted.

7.4 Effects of martian dust and ice aerosols on the surface irradiance spectrum

The effect of martian dust aerosols on the surface irradiance was explored using an adapted Mars radiative transfer model, RTM, (Patel, 2003, Otter, 2010) and measurements of dust optical depths made by the Spirit rover for two Mars years, MY27 and MY28. These two years were used as MY27 is representative of a typical annual dust cycle and MY28 illustrates an annual dust cycle with the occurrence of a large dust event during southern summer.

A comparison was performed between two dust components. One scenario was assumed to have the single scattering properties of Wolff *et al.* (2009), designated 'W09', and the other scenario used the single scattering properties retrieved by Ockert-Bell *et al.* (1997), denoted 'O97'. During a large dust event, the small variations in the single scattering properties have been shown to have a significant effect on the surface irradiance. The results suggest that ~30% more solar radiation will reach the lower atmosphere and surface for a W09 dust component, whereas, an O97 dust component will see a lower total irradiance This indicates that the amount of solar energy encountered at the surface and absorbed by the atmosphere will be significantly different between the two dust types during large-scale dust events. The higher scattering of W09 dust will lead to more solar radiation reaching the lower atmosphere and thus, the lower atmosphere will experience increased heating relative to an O97 dust component. The more absorbing O97 dust will lead to increased heating at higher altitudes and less heating at lower levels in the atmosphere. The heating of the atmosphere at high altitudes, away from the surface, results in a more statically-stable atmosphere (Andrews, 2000). This leads to fewer

small scale instabilities, such as gravity waves and convective motions, while large scale baroclinic instabilities tend towards larger spatial scales. This typically results in a reduction in the near-surface wind stress, reducing the amount of dust lofted into the atmosphere. This mechanism is believed to be responsible for controlling the decay of global dust events (Newman *et al.*, 2002), therefore a O97 dust component would lead to a more rapid decay compared to a W09 dust component for the same quantity of dust in the atmosphere.

The heating rate of the martian atmosphere is influenced strongly by the absorption of visible light, since the majority of the incident solar energy is contained in the visible region of the incident solar spectrum. Currently martian GCMs apply a scaling factor of between 1.5 and 2.5 to the dust optical depth measured in the infrared (9–15 μm) to approximate the dust optical depth at visible wavelengths (Forget *et al.*, 1999). However, the measured optical depth at IR wavelengths does not have a direct relation to the atmospheric heating resulting from the absorption of visible light. Therefore knowledge of the dust spectrum at visible wavelengths is vital for accurate predictions of atmospheric heating rates. The scaling of dust optical depth from the infrared to the visible is a key parameter of GCMs as it controls the local radiative balance. However, the value of the scaling factor is uncertain, and more accurate determination of this value is required to determine if modelled heating rates are consistent with the observed dust opacity. This highlights the importance of measuring the dust optical depth, and of accurate retrieval of dust optical properties at visible wavelengths, for which an irradiance spectrometer would be ideally suited.

The daily UV dose received during MY27 and MY28 was determined for the two dust components, W09 and O97. The UVC (190–280 nm) dose received during a large dust event was shown to be highly dependent on the dust single scattering properties, with a >20% higher UVC dose received when implementing the single scattering properties of W09 compared to O97. Integrating over MY27 and MY28 revealed that the presence of a planet-encircling dust event in MY28 reduced the cumulative UV dose by approximately 6% in all UV regions for both dust types. This indicates that while variations in the atmospheric dust content and single

scattering properties can affect significantly the daily UV dose, the cumulative effect during an annual cycle is small.

An investigation into the survival of *Bacillus subtilis* endospores in the martian UV environment concluded that, with a dust optical depth of 0.3 (typical of northern summer), the contaminated surface environment must shield the *B. subtilis* cells from 70% (Curiosity landing site) and 60% (Phoenix landing site) of the incident diffuse irradiance. This implies that, even if the microorganisms are protected from the direct solar irradiance, the high diffuse irradiance experienced at the martian surface is sufficient to sterilise partially shielded surfaces. More work is required to fully assess the survivability of microorganisms in sheltered locations on the surface of Mars, however the MCSLM can be adapted to simulate the UV irradiance on the underside and sheltered surfaces of martian landers and rovers. This will allow a more accurate determination of the UV dose received by microbes in such locations, and whether microbes may be able to survive the martian UV environment.

The presence of ice particles, in the form of condensate clouds, results in increased scattering at all wavelengths considered here. Reduced levels of irradiance are observed at wavelengths longer than 550 nm as a result of a higher fraction of the scattered light being reflected back into space. At shorter wavelengths the incident light is scattered rather than absorbed, resulting in an increase in surface irradiance. This makes distinguishing the passage of water-ice clouds relatively simple: the change in the irradiance spectrum at wavelengths less than 500 nm can be analysed. However, ice aerosols formed of pure water-ice crystals have high ω_0 values (of ~1) indicating that the majority of the incident solar radiation is scattered. With the majority of the solar radiation scattered by ice aerosols, their radiative impact is highly sensitive to how they scatter the radiation (*i.e.* their scattering phase function), which is dependent on the crystal shape and size. Retrieval of the ice aerosols size and shape is therefore crucial, as this will determine how much solar radiation is scattered back to space and how much is scattered toward the surface.

7.5 Differentiating between different dust compositions and ice particle size

A method was developed to distinguish changes in the composition of the dust that forms the background haze from spectral irradiance measurements. The ratio of the total irradiance at 380 nm and 750 nm is defined as $\Re_I$ and similarly the ratio of the diffuse irradiance at 380 nm and 750 nm is defined as $\Re_D$. The gradient of $\Re_I$ and $\Re_D$ as a function of the observed dust optical depth over short and long time-scales has been shown to provide a good indication on whether the attenuation of the solar spectrum by the dust has changed. While an ideal case is presented, any change in $\Re_I$ or $\Re_D$ at a given optical depth is still indicative of a change to the background dust component, and can be used to investigate the variability of the background dust haze. The analysis has shown that *in situ* measurement of the total irradiance spectrum, and the direct and diffuse components, provides a powerful tool for distinguishing variation in the dust background over seasonal and diurnal time-scales. Such measurements would allow insight into the fundamental questions concerning the variability in the composition of the suspended dust, which will impact the atmospheric state by altering atmospheric heating. This study emphasises the importance in measuring not only the combined surface irradiance, but also simultaneous separate measurement of either the direct or diffuse component.

These ratios can also be used to compare transits of different dust devils to determine whether the dust suspended within the vortices differs. However, due to the sensitivity of the diffuse component to the dust concentration, it is more appropriate to use the ratio of the direct irradiance at 388 nm and 750 nm ($\Re_{Dir}$) if comparing between the dust background and the dust suspended in a dust devil vortex. Furthermore, by sampling the optical depth sufficiently, it is concluded that the gradient of $\Re_{Dir}$ provides another measure for identifying changes to the dust component. Measurement of the direct component is extremely difficult and advocates the need for simultaneous measurements of the total and diffuse surface irradiance, from which the direct component can be determined.

It has been shown that measurements of water-ice clouds over short time-scales (such that the background dust optical depth can be assumed constant) can utilise $\Re_I$, with the gradient of $\Re_I$ as a function of optical depth providing an estimation of the ice particle size. By extrapolating to zero ice optical depth, the dust optical depth of the background haze can be estimated. It is important to know how much dust is present as this will influence the amount of atmospheric heating, which the condensation level is dependent upon. Furthermore, in order to retrieve an accurate estimate for the particle size, the dust content of the atmosphere must be known in order to remove its radiative effects.

The experiments at the Mars Simulation Wind Tunnel Facility simulating the passage of a dust cloud, containing particles of different composition to a ubiquitous dust background, have shown that plotting $\Re_I$ as a function of optical depth is a valid technique for distinguishing between aerosols of different composition and correlates well with the simulations performed in Chapter 5 for Mars. Furthermore, by producing linear fits to the $\Re_I$ signature, the background haze optical depths has been determined for both experiments and are consistent with the measured values.

7.6 Further work

The dust distribution entrained by the modelled dust devils is currently limited to symmetrical heterogeneities about the dust devil interior which are uniform in the vertical. While the purely vertical assumption is adequate for fitting the portion of the transit signature associated with the dust devil interior, and retrieval of the dust optical properties, more accurate modelling of dust devil transit signatures would require the capability to simulate dust devils that are tilted by the ambient boundary layer winds. Adapting the MCLSM to allow the dust concentration to vary in three dimensions solves this problem, *i.e.* by enabling asymmetric heterogeneities to be introduced into the model. However, this would require transferral of the current model to a more efficient programming language that is better equipped to deal with the large memory requirements of such Monte Carlo simulations, and as such is a task for future work.

Additional field studies of terrestrial dust devils are required to further refine retrieval of the optical properties of the dust in suspension around dust devils and to assess fully the characterisation of their internal structure from their transit signatures. Future field measurements will utilise simultaneous observations of the total and scattered irradiances, and also measurement of the particle size distribution within the vortex. The transit trajectory can be constrained by driving directly towards the dust devil, opposite to its ambient motion. This allows the vehicle's path to be mapped, with the bearing of the vehicle relative to north being exactly 180° to that of the dust devil. Marking the scan number and offset from the dust devil centre would provide a validation of the fitted transit signatures and more accurate determination of the vortex velocity.

The simulations of martian water-ice clouds assume complete cloud cover over the measurement area, whereas images from the Spirit and Opportunity rovers and Phoenix lander have shown that the cloud cover can be patchy. The effect of patchy cloud cover on the irradiance spectrum could be analysed by adapting the MCLSM to simulate the radiative transfer. Furthermore, the MCLSM could be applied to obtained optical and spectral signatures of morning fogs. Predicting the effect on the atmospheric optical depth as the water-ice shells of the composite fog particles sublime could be correlated to actual measurements from the martian surface.

7.7 Final remarks

In situ measurements of the optical signatures of transiting dust devils provide a powerful tool to characterise dust devils, both on Earth and Mars, allowing determination of the vortex size, dust concentration, internal dust distribution and the optical properties of the dust in suspension around the vortex. The nature of such measurements makes this an ideal technique for use on Mars, only requiring two upward viewing spectrometers (observing the UV-NIR wavelength region) of low complexity and mass. Ideally the entire UV-NIR wavelength band would be measured at high resolution, however considering the results of this thesis a minimum of three

wavelengths would be required, namely 388, 670 and 750 nm. The optical depth measured at 670 nm would allow correlation between predicted atmospheric heating rates from GCMs and the actual dust abundance in the martian atmosphere. Furthermore it would enable refinement of the dust optical depth visible-IR scaling factor employed in current Mars GCMs. Observing the irradiance at 750 nm would allow characterisation of dust devil vortices that transit over the spectrometer, providing enhanced definition in the transit signature between the vortex shadow and interior compared to shorter wavelengths. Measuring the irradiance at 388 nm and 750 nm, would allow the ratios $\Re_I$, $\Re_D$ and $\Re_{Dir}$ to be calculated. The $\Re_I$ ratio can also be applied to ice aerosols, enabling retrieval of the ice particle size within water-ice clouds and determination of the optical depth of the dust background. These ratios allow variations in the dust composition and size, within a dust devil vortex and the background haze, to be inferred. This would permit measurement of the spatial and temporal variability of the composition of martian aeolian dust.

References

Allen, C. C., Jager, K. M., Morris, R. V., Lindstrom, D. J., Lindstrom, M. M. and Lockwood, J. P. (1998) 'JSC MARS-1: A Martian Soil Simulant', *Space 98,* pp 469-476.

Alpert, P., Kaufman, Y. J., Shay-El, Y., Tanre, D., Da Silva, A., Schubert, S. and Joseph, J. H. (1998) 'Quantification of dust-forced heating of the lower troposphere', *Nature,* Vol 395, No 6700, pp 367-370.

Andrews, D. G. (2000) *An introduction to atmospheric physics*, Cambridge, Cambridge University Press.

Bagnold, R. A. (1941) *The Physics of Blown Sand and Desert Dunes*, London, Methuen.

Balme, M. and Greeley, R. (2006) 'Dust devils on Earth and Mars', *Reviews of Geophysics,* Vol 44, No 3, pp RG3003.

Balme, M. R., Pathare, A., Metzger, S. M., Towner, M. C., Lewis, S. R., Spiga, A., Fenton, L., Renno, N., Elliot, H., Saca, F., Michaels, T., Russell, P. and Verdasca, J. (2012) 'Field measurements of horizontal forward motion velocities of terrestrial dust devils: Towards a proxy for ambient winds on Mars and Earth', *Icarus,* Vol 221, No 2, pp 632-645.

Balme, M. R., Whelley, P. L. and Greeley, R. (2003) 'Mars: dust devil track survey in Argyre Planitia and Hellas Basin', *Journal of Geophysical Research,* Vol 108, No E8, pp 5086.

Battan, L. J. (1958) 'Energy of a Dust Devil', *Journal of Atmospheric Sciences,* Vol 15, pp 235-236.

Bell, J. M., Bougher, S. W. and Murphy, J. R. (2007) 'Vertical dust mixing and the interannual variations in the Mars thermosphere', *Journal of Geophysical Research,* Vol 112, No E12, pp E12002.

Bohren, C. F. and Huffman, D. R. (1983) *Absorption and Scattering of Light by Small Particles*, John Wiley and & Sons Inc.

Boyce, P. (1973) 'Remote sensing photometric studies of Mars in 1971', *Icarus,* Vol 18, No 1, pp 134-141.

Bryant, H. C. and Cox, A. J. (1966) 'Mie theory and the glory', *Journal of the Optical Society of America,* Vol 56, No 11, pp 1529-1532.

Cantor, B., Malin, M. and Edgett, K. S. (2002) 'Multiyear Mars Orbiter Camera (MOC) observations of repeated Martian weather phenomena during the northern summer season', *Journal of Geophysical Research,* Vol 107, pp 5014.

Cantor, B. A. (2007) 'MOC observations of the 2001 Mars planet-encircling dust storm', *Icarus,* Vol 186, No 1, pp 60-96.

Cantor, B. A., James, P. B., Caplinger, M. and Wolff, M. J. (2001) 'Martian dust storms: 1999 Mars Orbiter Camera observations', *Journal of Geophysical Research,* Vol 106, No E10, pp 23653-23687.

Cantor, B. A., Kanak, K. M. and Edgett, K. S. (2006) 'Mars Orbiter Camera observations of Martian dust devils and their tracks (September 1997 to January 2006) and evaluation of theoretical vortex models', *Journal of Geophysical Research,* Vol 111, No E12, pp E12002.

Capen, C. F. and Martin, L. J. (1971) 'The developing stages of the Martian yellow storm of 1971', *Lowell Observatory Bulletin,* Vol 7, pp 211-216.

Cashwell, E. D. and Everett, C. J. (1959) *A practical manual on the Monte Carlo method for random walk problems*, Pergamon Press.

Chassefière, E., Blamont, J. E., Krasnopolsky, V. A., Korablev, O. I., Atreya, S. K. and West, R. A. (1992) 'Vertical structure and size distributions of Martian aerosols from solar occultation measurements', *Icarus,* Vol 97, No 1, pp 46-69.

Clancy, R. T., Grossman, A. W., Wolff, M. J., James, P. B., Rudy, D. J., Billawala, Y. N., Sandor, B. J., Lee, S. W. and Muhleman, D. O. (1996) 'Water vapor saturation at low altitudes around Mars aphelion: A key to Mars climate?', *Icarus,* Vol 122, No 1, pp 36-62.

Clancy, R. T. and Lee, S. W. (1991) 'A new look at dust and clouds in the Mars atmosphere: Analysis of Emission-Phase-Function sequences from global Viking IRTM observations', *Icarus,* Vol 93, pp 135-158.

Clancy, R. T., Lee, S. W., Gladstone, G. R., McMillan, W. W. and Rousch, T. (1995) 'A new model for Mars atmospheric dust based upon analysis of ultraviolet through infrared observations from Mariner 9, Viking, and PHOBOS', *Journal of Geophysical Research,* Vol 100, No E3, pp 5251-5263.

Clancy, R. T., Sandor, B. J., Wolff, M. J., Christensen, P. R., Smith, M. D., Pearl, J. C., Conrath, B. J. and Wilson, R. J. (2000) 'An intercomparison of ground-based millimeter, MGS TES, and Viking atmospheric temperature measurements- Seasonal and interannual variability of temperatures and dust loading in the global Mars atmosphere', *Journal of Geophysical Research,* Vol 105, No E4, pp 9553.

Clancy, R. T., Wolff, M. J. and Christensen, P. R. (2003) 'Mars aerosol studies with the MGS TES emission phase function observations: Optical depths, particle sizes, and ice cloud types versus latitude and solar longitude', *Journal of Geophysical Research,* Vol 108, No E9, pp 5098.

Clancy, R. T., Wolff, M. J. and James, P. B. (1999) 'Minimal aerosol loading and global increases in atmospheric ozone during the 1996-1997 Martian northern spring season', *Icarus,* Vol 138, No 1, pp 49-63.

Cockell, C. S., Catling, D. C., Davis, W. L., Snook, K., Kepner, R. L., Lee, P. and McKay, C. P. (2000) 'The ultraviolet environment of Mars: biological implications past, present, and future', *Icarus,* Vol 146, No 2, pp 343-359.

Colburn, D., Pollack, J. and Haberle, R. (1989) 'Diurnal variations in optical depth at Mars', *Icarus,* Vol 79, No 1, pp 159-189.

Conrath, B., Curran, R., Hanel, R., Kunde, V., Maguire, W., Pearl, J., Pirraglia, J., Welker, J. and Burke, T. (1973) 'Atmospheric and surface properties of Mars obtained by infrared spectroscopy on Mariner 9', *Journal of Geophysical Research,* Vol 78, No 20, pp 4267-4278.

Conrath, B. J. (1975) 'Thermal structure of the Martian atmosphere during the dissipation of the dust storm of 1971', *Icarus,* Vol 24, No 1, pp 36-46.

Curran, R. J., Conrath, B. J., Hanel, R. A., Kunde, V. G. and Pearl, J. C. (1973) 'Mars: Mariner 9 spectroscopic evidence for H2O ice clouds', *Science,* Vol 182, No 4110, pp 381-383.

Cushing, G. E., Titus, T. N. and Christensen, P. R. (2005) 'THEMIS VIS and IR observations of a high-altitude Martian dust devil', *Geophysical Research Letters,* Vol 32, No 23, pp L23202.

Debye, P. (1909) 'Der Lichtdruck auf Kugeln von Beliebigem Material', *Annalen der Physik,* Vol 335, No 11, pp 57-136.

Deepak, A. and Gerber, H. E. (1983) *Report of WMO (CAS)/Radiation Commission of IAMAP Meeting of Experts on Aerosols and Their Climatic Effects,(Williamsburg, Virginia, USA, 28-30 March, 1983),*

DeVoe, H. (1964) 'Optical properties of molecular aggregates. I. Classical model of electronic absorption and refraction', *The Journal of Chemical Physics,* Vol 41, No 2, pp 393.

DeVoe, H. (1965) 'Optical properties of molecular aggregates. II. Classical theory of the refraction, absorption, and optical activity of solutions and crystals', *The Journal of Chemical Physics,* Vol 43, No 9, pp 3199.

Draine, B. T. and Flatau, P. J. (1994) 'Discrete-dipole approximation for scattering calculations', *Journal of the Optical Society of America,* Vol 11, No 4, pp 1491-1499.

Drake, N. B., Tamppari, L. K., Baker, R. D., Cantor, B. A. and Hale, A. S. (2006) 'Dust devil tracks and wind streaks in the North Polar Region of Mars: A study of the 2007 Phoenix Mars Lander Sites', *Geophysical Research Letters,* Vol 33, pp L19S02.

Dubovik, O., Holben, B., Eck, T. F., Smirnov, A., Kaufman, Y. J., King, M. D., TanrÃ©, D. and Slutsker, I. (2002) 'Variability of absorption and optical properties of key aerosol types observed in worldwide locations', *Journal of the Atmospheric Sciences,* Vol 59, No 3, pp 590-608.

Dubovik, O., Smirnov, A., Holben, B. N., King, M. D., Kaufman, Y. J., Eck, T. F. and Slutsker, I. (2000) 'Accuracy assessments of aerosol optical properties retrieved from AERONET sun and sky-radiance measurements', *Journal of Geophysical Research,* Vol 105, No D8, pp 9791-9806.

Edgett, K. S. and Malin, M. C. (2000) 'New views of Mars eolian activity, materials, and surface properties: Three vignettes from the Mars Global Surveyor Mars Orbiter Camera', *Journal of Geophysical Research,* Vol 105, No E1, pp 1623-1650.

Egan, W. G. and Hilgeman, T. W. (1979) *Optical properties of inhomogeneous materials*, San Diego, Calif., Academic.

Ellehoj, M. D., Gunnlaugsson, H. P., Taylor, P. A., KahanpÃ¤Ã¤, H., Bean, K. M., Cantor, B. A., Gheynani, B. T., Drube, L., Fisher, D. and Harri, A. M. (2010) 'Convective vortices and dust devils at the Phoenix Mars mission landing site', *Journal of Geophysical Research,* Vol 115, pp E00E16.

Ferri, F., Smith, P. H., Lemmon, M. and Rennó, N. O. (2003) 'Dust devils as observed by Mars Pathfinder', *Journal of Geophysical Research,* Vol 108, No 7, pp 1–7.

Fisher, J. A., Richardson, M. I., Newman, C. E., Szwast, M. A., Graf, C., Basu, S., Ewald, S. P., Toigo, A. D. and Wilson, R. J. (2005) 'A survey of Martian dust devil activity using Mars Global Surveyor Mars Orbiter Camera images', *Journal of Geophysical Research,* Vol 110, No E3, pp E03004.

Forget, F., Hourdin, F., Fournier, R., Hourdin, C., Talagrand, O., Collins, M., Lewis, S. R., Read, P. L. and Huot, J. P. (1999) 'Improved general circulation models of the Martian atmosphere from the surface to above 80 km', *Journal of Geophysical Research,* Vol 104, No E10, pp 24.

Formisano, V., Atreya, S., Encrenaz, T., Ignatiev, N. and Giuranna, M. (2004) 'Detection of methane in the atmosphere of Mars', *Science,* Vol 306, No 5702, pp 1758-1761.

Fouquart, Y., Bonnel, B., Brogniez, G., Buriez, J. C., Smith, L., Morcrette, J. J. and Cerf, A. (1987) 'Observations of Saharan aerosols: Results of ECLATS field experiment. Part II: Broadband radiative characteristics of the aerosols and vertical radiative flux divergence', *Journal of Applied Meteorology,* Vol 26, pp 38-52.

Galeev, A. A. (1996) 'Russian Program of Planetary Missions', *Acta Astronautica,* Vol 39, No 1-4, pp 9-14.

Gierasch, P. and Goody, R. (1968) 'A study of the thermal and dynamical structure of the Martian lower atmosphere(Scaling of equations of motion in lower Martian atmosphere)', *Planetary and Space Science,* Vol 16, No 5, pp 615-646.

Gierasch, P. J. and Goody, R. M. (1972) 'The effect of dust on the temperature of the Martian atmosphere', *Journal of the Atmospheric Sciences,* Vol 29, No 2, pp 400-402.

Goguen, J. D., Clancy, R. T., Wolff, M. J. and James, P. B. (2003) 'UV optical properties of aerosol dust from HST STIS spectra of Mars during the 2001 dust storm', *Bulletin of the American Astronomical Society,* Vol 35, pp 914.

Golombek, M. P. (1997) 'The Mars Pathfinder Mission', *Journal of Geophysical Research,* Vol 102, No E2, pp 3953-3965.

Greeley, R., Balme, M. R., Iversen, J. D., Metzger, S., Mickelson, R., Phoreman, J. and White, B. (2003) 'Martian dust devils: Laboratory simulations of particle threshold', *Journal of Geophysical Research,* Vol 108, No E5, pp 5041.

Greeley, R., Lancaster, N., Lee, S. and Thomas, P. (1992) 'Martian aeolian processes, sediments, and features'. *Mars*, Tucson, The University of Arizona Press.

Greeley, R., Waller, D. A., Cabrol, N. A., Landis, G. A., Lemmon, M. T., Neakrase, L. D. V., Hoffer, M. P., Thompson, S. D. and Whelley, P. L. (2010) 'Gusev Crater, Mars: Observations of three dust devil seasons', *Journal of Geophysical Research,* Vol 115, pp E00F02.

Greeley, R., Whelley, P. L., Arvidson, R. E., Cabrol, N. A., Foley, D. J., Franklin, B. J., Geissler, P. G., Golombek, M. P., Kuzmin, R. O. and Landis, G. A. (2006) 'Active dust devils in Gusev crater, Mars: observations from the Mars exploration rover spirit', *Journal of Geophysical Research,* Vol 111, No E12, pp E12S09.

Grotzinger, J. P., Crisp, J., Vasavada, A. R., Anderson, R. C., Baker, C. J., Barry, R., Blake, D. F., Conrad, P., Edgett, K. S. and Ferdowski, B. (2012) 'Mars Science Laboratory mission and science investigation', *Space Science Reviews,* Vol 170, pp 1-52.

Haberle, R. M., Joshi, M. M., Murphy, J. R., Barnes, J. R., Schofield, J. T., Wilson, G., Lopez-Valverde, M., Hollingsworth, J. L., Bridger, A. F. C. and Schaeffer, J. (1999) 'General circulation model simulations of the Mars Pathfinder atmospheric structure

investigation/meteorology data', *Journal of Geophysical Research,* Vol 104, No E4, pp 8957–8974.

Haberle, R. M., Leovy, C. B. and Pollack, J. B. (1982) 'Some effects of global dust storms on the atmospheric circulation of Mars', *Icarus,* Vol 50, No 2-3, pp 322-367.

Haberle, R. M., Pollack, J. B., Barnes, J. R., Zurek, R. W., Leovy, C. B., Murphy, J. R., Lee, H. and Schaeffer, J. (1993) 'Mars atmospheric dynamics as simulated by the NASA Ames general circulation model 1. The zonal-mean circulation', *Journal of Geophysical Research,* Vol 98, No E2, pp 3093-3123.

Hansen, J. E. and Travis, L. D. (1974) 'Light Scattering in Planetary Atmospheres', *Space Science Reviews,* Vol 16, No 4, pp 527-610.

Hapke, B. (1981) 'Bidirectional reflectance spectroscopy,1-Theory (of planetary surfaces)', *Journal of Geophysical Research,* Vol 86, pp 3039-3054.

Harvey, B. (1996) *The new Russian space programme: from competition to collaboration,* Chichester, Wiley.

Henyey, L. G. and Greenstein, J. L. (1941) 'Diffuse radiation in the galaxy', *The Astrophysical Journal,* Vol 93, pp 70-83.

Hess, M., Koepke, P. and Schult, I. (1998) 'Optical properties of aerosols and clouds: The software package OPAC', *Bulletin of the American Meteorological Society,* Vol 79, No 5, pp 831-844.

Hess, S. L., Henry, R. M., Leovy, C. B., Ryan, J. A. and Tillman, J. E. (1977) 'Meteorological results from the surface of Mars: Viking 1 and 2', *Journal of Geophysical Research,* Vol 82, pp 4559.

Ives, R. L. (1947) 'Behavior of dust devils', *Bulletin of the American Astronomical Society,* Vol 28, pp 168-174.

Jakosky, B. M. and Farmer, C. B. (1982) 'The seasonal and global behavior of water vapor in the Mars atmosphere: Complete global results of the Viking atmospheric water detector experiment', *Journal of Geophysical Research,* Vol 87, No B4, pp 2999-3019.

Jaquin, F., Gierasch, P. and Kahn, R. (1986) 'The vertical structure of limb hazes in the Martian atmosphere', *Icarus,* Vol 68, No 3, pp 442-461.

Joseph, J. H., Wiscombe, W. J. and Weinman, J. A. (1976) 'The delta-Eddington approximation for radiative flux transfer', *Journal of the Atmospheric Sciences,* Vol 33, No 12, pp 2452-2459.

Kaimal, J. C. and Businger, J. A. (1970) 'Case studies of a convective plume and a dust devil', *Journal of Applied Meteorology,* Vol 9, pp 612-620.

Kaufman, Y. J. (1987) 'Satellite sensing of aerosol absorption', *Journal of Geophysical Research,* Vol 92, No D4, pp 4307-4317.

Kaufman, Y. J., Tanré, D., Dubovik, O., Karnieli, A. and Remer, L. A. (2001) 'Absorption of sunlight by dust as inferred from satellite and ground-based remote sensing', *Geophysical Research Letters,* Vol 28, No 8, pp 1479-1482.

Kerney, K. R. and Schuerger, A. C. (2011) 'Survival of Bacillus subtilis Endospores on Ultraviolet-Irradiated Rover Wheels and Mars Regolith under Simulated Martian Conditions', *Astrobiology,* Vol 11, No 5, pp 477-485.

Klein, H. P., Horowitz, N. H. and Biemann, K. (1992) 'The search for extant life on Mars'. *Mars*, The University of Arizona Press Tucson.

Lemmon, M. (2004) *MER Mars Pancam Atmospheric Opacity RDR V1.0, NASA Planetary Data System, MER1/MER2-M-PANCAM-5-ATMOS-OPACITY-V1.0*

Lemmon, M. (2008) *PHX Mars SSI Atmospheric Opacity RDR V1.0, NASA Planetary Data System, PHX-M-SSI-5-ATMOS- OPACITY-V1.0*

Lemmon, M. T., Wolff, M. J., Smith, M. D., Clancy, R. T., Banfield, D., Landis, G. A., Ghosh, A., Smith, P. H., Spanovich, N. and Whitney, B. (2004) 'Atmospheric imaging results from the Mars Exploration Rovers: spirit and opportunity', *Science,* Vol 306, No 5702, pp 1753-1756.

Leovy, C. and Mintz, Y. (1969) 'Numerical simulation of the atmospheric circulation and climate of Mars', *Journal of the Atmospheric Sciences,* Vol 26, No 6, pp 1167-1190.

Leovy, C. B. (1985) 'The general circulation of Mars: Models and observations', *Advances in geophysics,* Vol 28, pp 327-346.

Liu, J., Richardson, M. I. and Wilson, R. J. (2003) 'An assessment of the global, seasonal, and interannual spacecraft record of Martian climate in the thermal infrared', *Journal of Geophysical Research,* Vol 108, No E8, pp 5089.

Lorenz, L. V. (1890) 'Upon the light reflected and refracted by a transparent sphere', *Vidensk. Selsk. Shrifter,* Vol 6, pp 1-62.

Lowell, P. (1906) *Mars and its Canals*, The Macmillan company; London: Macmillan & co., ltd.

Määtänen, A., Fouchet, T., Forni, O., Forget, F., Savijärvi, H., Gondet, B., Melchiorri, R., Langevin, Y., Formisano, V. and Giuranna, M. (2009) 'A study of the properties of a local dust storm with Mars Express OMEGA and PFS data', *Icarus,* Vol 201, No 2, pp 504-516.

Markiewicz, W. J., Sablotny, R. M., Keller, H. U., Thomas, N., Titov, D. and Smith, P. H. (1999) 'Optical properties of the Martian aerosols as derived from Imager for Mars Pathfinder midday sky brightness data', *Journal of Geophysical Research,* Vol 104, No E4, pp 9009-9017.

Mateshvili, N., Fussen, D., Vanhellemont, F., Bingen, C., Dodion, J., Montmessin, F., Perrier, S. and Bertaux, J. L. (2007) 'Detection of Martian dust clouds by SPICAM UV nadir measurements during the October 2005 regional dust storm', *Advances in Space Research,* Vol 40, No 6, pp 869-880.

McCleese, D. J., Heavens, N. G., Schofield, J. T., Abdou, W. A., Bandfield, J. L., Calcutt, S. B., Irwin, P. G. J., Kass, D. M., Kleinböhl, A. and Lewis, S. R. (2010) 'The Structure and Dynamics of the Martian Lower and Middle Atmosphere as Observed by the Mars Climate Sounder: 1. Seasonal variations in zonal mean temperature, dust and water ice aerosols', *Journal of Geophysical Research-Planets,* Vol 115, No E12, pp E12016.

Merrison, J., Holstein-Rathlou, C., Gunnlaugsson, H. and Nornberg, P. (2009) 'A European Mars Simulation Wind Tunnel Facility', *European Planetary Science Congress 2009,* pp. 76.

Metzger, S. M. (1999a) *Dust devils as Aeolian Transport Mechanisms in Southern Nevada and the Mars Pathfinder Landing Site,* University of Nevada.

Metzger, S. M., Balme, M. R., Towner, M. C., Bos, B. J., Ringrose, T. J. and Patel, M. R. (2011) 'In-Situ Measurements of Particle Load and Transport in Dust Devils', *Icarus,* Vol 214, No 2, pp 766-772.

Metzger, S. M., Carr, J. R., Johnson, J. R., Parker, T. J. and Lemmon, M. T. (1999) 'Dust devil vortices seen by the Mars Pathfinder camera', *Geophysical Research Letters,* Vol 26, No 18, pp 2781-2784.

Metzger, S. M., Carr, J. R., Johnson, J. R., Parker, T. J. and Lemmon, M. T. (1999b) 'Dust devil vortices seen by the Mars Pathfinder camera', *Geophysical Research Letters,* Vol 26, No 18, pp 2781-2784.

Mie, G. (1908) 'A contribution to the optics of turbid media, especially colloidal metallic suspensions', pp. 377-445.

Mishchenko, M. I. (2009) 'Gustav Mie and the fundamental concept of electromagnetic scattering by particles: A perspective', *Journal of Quantitative Spectroscopy and Radiative Transfer,* Vol 110, No 14-16, pp 1210-1222.

Mishchenko, M. I., Hovenier, J. W. and Travis, L. D. (2000) *Light scattering by nonspherical particles : theory, measurements, and applications* San Diego, Academic Press.

Mumma, M. J., Villanueva, G. L., Novak, R. E., Hewagama, T., Bonev, B. P., DiSanti, M. A., Mandell, A. M. and Smith, M. D. (2009) 'Strong release of methane on Mars in northern summer 2003', *Science,* Vol 323, No 5917, pp 1041-1045.

Neakrase, L. D. V. and Greeley, R. (2010a) 'Dust devil sediment flux on Earth and Mars: Laboratory simulations', *Icarus,* Vol 206, No 1, pp 306-318.

Neakrase, L. D. V. and Greeley, R. (2010b) 'Dust devils in the laboratory: Effect of surface roughness on vortex dynamics', *Journal of Geophysical Research,* Vol 115, No E5, pp E05003.

Neakrase, L. D. V., Greeley, R., Iversen, J. D., Balme, M. R. and Eddlemon, E. E. (2006) 'Dust flux within dust devils: Preliminary laboratory simulations', *Geophysical Research Letters,* Vol 33, No 19, pp L19S09.

Newman, C. E., Lewis, S. R., Read, P. L. and Forget, F. (2002) 'Modeling the Martian dust cycle, 1. Representations of dust transport processes', *Journal of Geophysical Research,* Vol 107, No E12, pp 5123.

Nier, A. O., Hanson, W. B., McElroy, M. B., Seiff, A. and Spencer, N. W. (1972) 'Entry science experiments for Viking 1975', *Icarus,* Vol 16, No 1, pp 74-91.

Nørnberg, P., Gunnlaugsson, H. P., Merrison, J. P. and Vendelboe, A. L. (2009) 'Salten Skov I: A Martian magnetic dust analogue', *Planetary and Space Science,* Vol 57, No 5, pp 628-631.

Nousiainen, T. (2009) 'Optical Modeling of Mineral Dust Particles: A Review', *Journal of Quantitative Spectroscopy & RadiativeTransfer,* Vol 110, No 14-16, pp 1261-1279.

Ockert-Bell, M. E., Bell, J. F., Pollack, J. B., McKay, C. P. and Forget, F. (1997) 'Absorption and scattering properties of the Martian dust in the solar wavelengths', *Journal of Geophysical Research,* Vol 102, No E4, pp 9039-9050.

Otter, S. (2010) *Simulation of the Radiative Flux at the Martian Surface between 180 and 1100nm, Planetary and Space Science Research Institue,* Thesis, The Open University.

Owen, T. (1992) 'The composition and early history of the atmosphere of Mars'. *Mars*, tucson, The University of Arizona Press.

Parkinson, T. D. and Hunten, D. M. (1972) 'Martian dust storm: its depth on 25 November 1971', *Science,* Vol 175, pp 323.

Patel, M. R. (2003) *Modelling the Ultraviolet Environment at the Surface of Mars and Design of the Beagle 2 UV Sensor,* Thesis, The Open University.

Patel, M. R., Christou, A. A., Cockell, C. S., Ringrose, T. J. and Zarnecki, J. C. (2004) 'The UV environment of the Beagle 2 landing site: detailed investigations and detection of atmospheric state', *Icarus,* Vol 168, No 1, pp 93-115.

Patel, M. R., Zarnecki, J. C. and Catling, D. C. (2002) 'Ultraviolet radiation on the surface of Mars and the Beagle 2 UV sensor', *Planetary and Space Science,* Vol 50, No 9, pp 915-927.

Patterson, E. M., Gillette, D. A. and Stockton, B. H. (1977) 'Complex index of refraction between 300 and 700 nm for Saharan aerosols', *Journal of Geophysical Research,* Vol 82, No 21, pp 3153-3160.

Pearl, J. C., Smith, M. D., Conrath, B. J., Bandfield, J. L. and Christensen, P. R. (2001) 'Observations of martian ice clouds by the Mars Global Surveyor Thermal Emission Spectrometer: the first martian year', *Journal of Geophysical Research,* Vol 106, No 12, pp 325-12.

Petrova, E., Keller, H. U., Markiewicz, W. J., Thomas, N. and Wuttke, M. W. (1996) 'Ice hazes and clouds in the Martian atmosphere as derived from the Phobos/KRFM data', *Planetary and Space Science,* Vol 44, No 10, pp 1163-1176.

Petrova, E. V. (1993) 'Irregular shape of particles and the Martian aerosols' properties', *Planetary and space science,* Vol 41, No 8, pp 587-591.

Pettit, E. and Richardson, R. S. (1955) 'Observations of Mars made at Mount Wilson in 1954', *Publications of the Astronomical Society of the Pacific,* Vol 67, No 395, pp 62-73.

Pollack, J. B., Colburn, D., Kahn, R., Hunter, J. and Van, C. (1977) 'Properties of aerosols in the Martian atmosphere, as inferred from Viking Lander imaging data', *Journal of Geophysical Research,* Vol 82, No 28, pp 4479-4496.

Pollack, J. B., Colburn, D. S., Flasar, F. M., Kahn, R., Carlston, C. E. and Pidek, D. (1979) 'Properties and effects of dust particles suspended in the Martian atmosphere', *Journal of Geophysical Research,* Vol 84, No B6, pp 2929–2945.

Pollack, J. B. and Cuzzi, J. N. (1980) 'Scattering by nonspherical particles of size comparable to wavelength-A new semi-empirical theory and its application to tropospheric aerosols', *Journal of Atmospheric Sciences,* Vol 37, pp 868-881.

Pollack, J. B., Leovy, C. B., Mintz, Y. H. and Van, C. (1976) 'Winds on Mars during the Viking season- Predictions based on a general circulation model with topography', *Geophysical Research Letters,* Vol 3, pp 479-482.

Pollack, J. B., Ockert-Bell, M. E. and Shepard, M. K. (1995) 'Viking lander Image Analysis of Martian Atmospheric Dust', *Journal of Geophysical Research,* Vol 100, No 3, pp 5235-5250.

Purcell, E. M. and Pennypacker, C. R. (1973) 'Scattering and absorption of light by nonspherical dielectric grains', *The Astrophysical Journal,* Vol 186, pp 705-714.

Rayleigh, L. (1918) 'On the scattering of light by a cloud of similar small particles of any shape and oriented at random', *Philosophical magazine,* Vol 35, pp 373-381.

Read, P. L. and Lewis, S. R. (2004) *The Martian climate revisited: atmosphere and environment of a desert planet*, Springer Verlag.

Reid, J. S., Jonsson, H. H., Maring, H. B., Smirnov, A., Savoie, D. L., Cliff, S. S., Reid, E. A., Livingston, J. M., Meier, M. M. and Dubovik, O. (2003) 'Comparison of size and morphological measurements of coarse mode dust particles from Africa', *Journal of Geophysical Research,* Vol 108, No 9, pp 1-9.

Rennó, N. O., Abreu, V. J., Koch, J., Smith, P. H., Hartogensis, O. K., De Bruin, H. A. R., Burose, D., Delory, G. T., Farrell, W. M. and Watts, C. J. (2004) 'MATADOR 2002: A pilot field experiment on convective plumes and dust devils', *Journal of Geophysical Research,* Vol 109, No E7, pp E07001.

Richardson, M. I., Wilson, R. J. and Rodin, A. V. (2002) 'Water ice clouds in the Martian atmosphere: General circulation model experiments with a simple cloud scheme', *Journal of Geophysical Research,* Vol 107, No E9, pp 5064.

Rodin, A. V., Korablev, O. I. and Moroz, V. I. (1997) 'Vertical Distribution of Water in the Near-Equatorial Troposphere of Mars: Water Vapor and Clouds', *Icarus,* Vol 125, No 1, pp 212-229.

Ryan, J. A. (1964) 'Notes on the Martian yellow clouds', *Journal of Geophysical Research,* Vol 69, No 18, pp 3759-3770.

Ryan, J. A. and Carroll, J. J. (1970) 'Dust devil wind velocities: Mature state', *Journal of Geophysical Research,* Vol 75, No 3, pp 531-541.

Sagdeev, R. Z., Balebanov, V. M. and Zakharov, A. V. (1988) 'The Phobos project: scientific objectives and experimental methods', *Astrophysics and Space Physics Reviews,* Vol 6, pp 1-60.

Schiaparelli, G. (1899) 'Observations of the planet Mars', *Science,* Vol 9, No 227, pp 633.

Schofield, J. T., Barnes, J. R., Crisp, D., Haberle, R. M., Larsen, S., Magalhaes, J. A., Murphy, J. R., Seiff, A. and Wilson, G. R. (1997) 'The Mars Pathfinder Atmospheric Structure Investigation/Meteorology (ASI/MET) experiment', *Science,* Vol 278, pp 1752-1757.

Schuerger, A. C., Mancinelli, R. L., Kern, R. G., Rothschild, L. J. and McKay, C. P. (2003) 'Survival of endospores of Bacillus subtilis on spacecraft surfaces under simulated martian environments::: implications for the forward contamination of Mars', *Icarus,* Vol 165, No 2, pp 253-276.

Schuerger, A. C., Richards, J. T., Newcombe, D. A. and Venkateswaran, K. (2006) 'Rapid inactivation of seven Bacillus spp. under simulated Mars UV irradiation', *Icarus,* Vol 181, No 1, pp 52-62.

Shelton, W. R. (1968) *Soviet space exploration: the first decade*, New York, Washington Square Press.

Shettle, E. P. and Fenn, R. W. (1976) 'Models of the atmospheric aerosols and their optical properties',

Sims, M. R., Pillinger, C. T., Wright, I. P., Dowson, J., Whitehead, S., Wells, A., Spragg, J. E., Fraser, G., Richter, L. and Hamacher, H. (1999) 'Beagle 2: a proposed exobiology lander for ESA's 2003 Mars Express mission', *Advances in Space Research,* Vol 23, No 11, pp 1925-1928.

Sinclair, P. C. (1966) *A Quantitative analysis of the dust devil,* Thesis, University of Arizona.

Sinclair, P. C. (1973) 'The lower structure of dust devils', *Journal of Atmospheric Sciences,* Vol 30, pp 1599-1619.

Sinclair, P. C. (1974) *Vertical transport of desert particulates by dust devils and clear thermals,* California University., Livermore (USA). Lawrence Livermore Lab.,

Smith, M. D. (2009) 'THEMIS observations of Mars aerosol optical depth from 2002-2008', *Icarus,* Vol 202, No 2, pp 444-452.

Smith, M. D., Pearl, J. C., Conrath, B. J. and Christensen, P. R. (2001) 'Thermal Emission Spectrometer results- Mars atmospheric thermal structure and aerosol distribution', *Journal of Geophysical Research,* Vol 106, No E10, pp 23929–23945.

Smith, M. D., Wolff, M. J., Spanovich, N., Ghosh, A., Banfield, D., Christensen, P. R., Landis, G. A. and Squyres, S. W. (2006) 'One Martian year of atmospheric observations using MER Mini-TES', *Journal of Geophysical Research,* Vol 111, No E11, pp E12S13.

Smith, P. H., Bell III, J. F., Bridges, N. T., Britt, D. T., Gaddis, L., Greeley, R., Keller, H. U., Herkenhoff, K. E., Jaumann, R., Johnson, J. R., Kirk, R. L., Lemmon, M. T., Maki, J. N., Malin, M. C., Murchie, S. L., Oberst, J., Parker, T. J., Reid, R. J., Sablotny, R. M., Soderblom, L. A., Stoker, C., Sullivan, R., Thomas, N., Tomasko, M. G., Ward, W. and

Wegryn, E. (1997) 'Results from the Mars Pathfinder Camera', *Science,* Vol 278, pp 1758-1764.

Smith, P. H. and Lemmon, M. (1999) 'Opacity of the Martian atmosphere measured by the Imager for Mars Pathfinder', *Journal of Geophysical Research,* Vol 104, No E4, pp 8975–8985.

Smith, P. H., Tamppari, L., Arvidson, R. E., Bass, D., Blaney, D., Boynton, W., Carswell, A., Catling, D., Clark, B. and Duck, T. (2008) 'Introduction to special section on the phoenix mission: landing site characterization experiments, mission overviews, and expected science', *Journal of Geophysical Research,* Vol 113, No E3, pp E00A18.

Smith, P. H., Tamppari, L. K., Arvidson, R. E., Bass, D., Blaney, D., Boynton, W. V., Carswell, A., Catling, D. C., Clark, B. C. and Duck, T. (2009) 'H2O at the Phoenix landing site', *Science,* Vol 325, No 5936, pp 58-61.

Smith, S. A. and Smith, B. A. (1972) 'Diurnal and seasonal behavior of discrete white clouds on Mars', *Icarus,* Vol 16, No 3, pp 509-521.

Smrekar, S., Catling, D., Lorenz, R., Magalhães, J., Moersch, J., Morgan, P., Murphy, J., Murray, B., Presley-Holloway, M. and Yen, A. (1999) 'Deep Space 2: the Mars microprobe mission', *Journal of Geophysical Research,* Vol 104, No E11, pp 27013-27030.

Soffen, G. A. (1977) 'The Viking Project', *Journal of Geophysical Research,* Vol 82, No 28, pp 3959-3970.

Sokolik, I. N. and Toon, O. B. (1999) 'Incorporation of mineralogical composition into models of the radiative properties of mineral aerosol from UV to IR wavelengths', *Journal of Geophysical Research,* Vol 104, No D8, pp 9423-9444.

Squyres, S. W., Arvidson, R. E., Bell Iii, J. F., Brückner, J., Cabrol, N. A., Calvin, W., Carr, M. H., Christensen, P. R., Clark, B. C. and Crumpler, L. (2004a) 'The opportunity rover's athena science investigation at Meridiani Planum, Mars', *Science,* Vol 306, No 5702, pp 1698-1703.

Squyres, S. W., Arvidson, R. E., Bell Iii, J. F., Brückner, J., Cabrol, N. A., Calvin, W., Carr, M. H., Christensen, P. R., Clark, B. C. and Crumpler, L. (2004b) 'The Spirit rover's Athena science investigation at Gusev crater, Mars', *Science,* Vol 305, No 5685, pp 794-799.

Tamppari, L. K., Bass, D., Cantor, B., Daubar, I., Dickinson, C., Fisher, D., Fujii, K., Gunnlauggson, H. P., Hudson, T. L. and Kass, D. (2010) 'Phoenix and MRO coordinated atmospheric measurements', *Journal of Geophysical Research,* Vol 115, pp E00E17.

Thomas, N., Keller, H. U., Britt, D. T., Smith, P. H., Herkenhoff, K. E. and Semenov, B. (1999) 'Observations of Phobos, Deimos, and bright stars with the Imager for Mars Pathfinder', *Journal of Geophysical Research,* Vol 104, No E4, pp 9055-9068.

Thomas, P. and Gierasch, P. J. (1985) 'Dust devils on Mars', *Science,* Vol 230, No 4722, pp 175.

Tomasko, M. G., Doose, L. R., Lemmon, M., Smith, P. H. and Wegryn, E. (1999) 'Properties of dust in the Martian atmosphere from the Imager on Mars Pathfinder', *Journal of Geophysical Research,* Vol 104, No E4, pp 8987-9007.

Van de Hulst, H. C. (1957) *Light scattering by small particles*, Dover Publications.

Vincendon, M. and Langevin, Y. (2010) 'A spherical Monte-Carlo model of aerosols: Validation and first applications to Mars and Titan', *Icarus,* Vol 207, No 2, pp 923-931.

Vincendon, M., Langevin, Y., Poulet, F., Bibring, J. P. and Gondet, B. (2007) 'Recovery of surface reflectance spectra and evaluation of the optical depth of aerosols in the near-IR using a Monte Carlo approach: Application to the OMEGA observations of high-latitude regions of Mars', *Journal of Geophysical Research,* Vol 112, No E8, pp E08S13.

Wang, H. and Ingersoll, A. P. (2002) 'Martian clouds observed by Mars Global Surveyor Mars Orbiter Camera', *Journal of Geophysical Research (Planets,* Vol 107, No E10, pp 5078.

Whelley, P. L. and Greeley, R. (2006) 'Latitudinal dependency in dust devil activity on Mars', *Journal of Geophysical Research,* Vol 111 No E10, pp E10003.

Whiteway, J., Daly, M., Carswell, A., Duck, T., Dickinson, C., Komguem, L. and Cook, C. (2008) 'Lidar on the Phoenix mission to Mars', *Journal of Geophysical Research,* Vol 113, pp E00A08.

Whiteway, J. A., Komguem, L., Dickinson, C., Cook, C., Illnicki, M., Seabrook, J., Popovici, V., Duck, T. J., Davy, R. and Taylor, P. A. (2009) 'Mars water-ice clouds and precipitation', *Science,* Vol 325, No 5936, pp 68-70.

Whitney, B. A. (2011) 'Monte Carlo radiative transfer', *Bulletin of the Astronomical Society of India,* Vol 39, pp 101-127.

Wilson, R. J., Neumann, G. A. and Smith, M. D. (2007) 'Diurnal variation and radiative influence of Martian water ice clouds', *Geophysical Research Letters,* Vol 34, No 2, pp 2710.

Withers, P. and Murphy, J. R. (2009) *MER1/MER2-M-IMU-5-EDL-DERIVED- NASA Planetary Data System*

Withers, P. and Smith, M. D. (2006) 'Atmospheric entry profiles from the Mars exploration Rovers Spirit and Opportunity', *Icarus,* Vol 185, No 1, pp 133-142.

Witt, A. N. (1977) 'Multiple scattering in reflection nebulae. I. A Monte Carlo approach', *Astrophysical Journal Supplement Series,* Vol 35, pp 1-6.

Wolff, M. J., Bell, J. F., James, P. B., Clancy, R. T. and Lee, S. W. (1999) 'Hubble Space Telescope observations of the Martian aphelion cloud belt prior to the Pathfinder mission- Seasonal and interannual variations', *Journal of Geophysical Research,* Vol 104, No E4, pp 9027-9041.

Wolff, M. J. and Clancy, R. T. (2003) 'Constraints on the size of Martian aerosols from Thermal Emission Spectrometer observations', *Journal of Geophysical Research,* Vol 108, No E9, pp 5097.

Wolff, M. J., Smith, M. D., Clancy, R. T., Arvidson, R. and Kahre, M. (2009) 'Wavelength dependence of dust aerosol single scattering albedo as observed by the Compact Reconnaissance Imaging Spectrometer', *Journal of Geophysical Research,* Vol 114, No E2, pp E00D04.

Wolff, M. J., Smith, M. D., Clancy, R. T., Spanovich, N., Whitney, B. A., Lemmon, M. T., Bandfield, J. L., Banfield, D., Ghosh, A. and Landis, G. (2006) 'Constraints on dust aerosols from the Mars Exploration Rovers using MGS overflights and Mini-TES', *Journal of Geophysical Research,* Vol 111, No E12, pp E12S17.

Wolff, M. J., Todd Clancy, R., Goguen, J. D., Malin, M. C. and Cantor, B. A. (2010) 'Ultraviolet dust aerosol properties as observed by MARCI', *Icarus,* Vol 208, No 1, pp 143-155.

Zahnle, K., Freedman, R. S. and Catling, D. C. (2011) 'Is there methane on Mars?', *Icarus,* Vol 212, No 2, pp 493-503.

Zurek, R. W., Barnes, J. R., Haberle, R. M., Pollack, J. B., Tillman, J. E. and Leovy, C. B. (1992) 'Dynamics of the atmosphere of Mars'. *Mars*, Tucson, The University of Arizona Press.